EPFL

Thèse n° 10 046

Magnetic Resonance and Hyperpolarization Methods for Perovskite Photovoltaics

Présentée le 16 décembre 2022

Faculté des sciences de base
Laboratoire de résonance magnétique
Programme doctoral en chimie et génie chimique

pour l'obtention du grade de Docteur ès Sciences

par

Aditya MISHRA

Acceptée sur proposition du jury

Prof. K. Sivula, président du jury
Prof. D. L. Emsley, directeur de thèse
Prof. R. Clément, rapporteuse
Prof. D. Massiot, rapporteur
Prof. R. Buonsanti, rapporteuse

École polytechnique fédérale de Lausanne

2022

Acknowledgements

I would like to thank my supervisor Lyndon Emsley for giving me this golden opportunity to join his team to do my research. All the work presented in this thesis wouldn't have been possible without his constant support, guidance, and encouragements throughout. Being in his team was always an element of encouragement and confidence for me. His approach towards science and emphasis on team work have always encouraged me to improve and get better. The learnings from his group are countless. Thank you, Lyndon.

I thank the members of my thesis committee, Raphaële Clément, Dominique Massiot, Raffaella Buonsanti, and Kevin Sivula for taking time to evaluate my thesis.

I would like to thank Nadia Gauljaux and Anne Lene Odegaard for taking care of all administrative work.

I am grateful to brilliant postdocs in the team, Michael A. Hope, Claudia Avalos, and Dominik J. Kubicki for being actively involved and helping in conducting the research presented in this thesis work. Their constant support and teaching have helped me a lot throughout my doctoral studies.

I would like to thank our collaborators Michael Graetzel, Anders Hagfeldt, Ursula Roethlisberger, and their teams. I am grateful to Zaiwei Wang and Jovana Milić for the discussions.

I would like to appreciate and thank all current and former fantastic colleagues in the group – Pinelopi Moutzouri, Gabriele Stevanato, Pierrick Berruyer, Federico Paruzzo, Albert Hofstetter, Andrea Bertarello, Brennan Walder, Snædis Björgvinsdóttir, Baptiste Busi, Saumya Badoni, Federico De Biasi, Martins Balodis, Amrit Venkatesh, Bruno Simões de Almeida, Anna Morales, Manuel Cordova, Yu Rao, and Daria Torodii.

Lastly but most importantly, I would like to thank my beloved parents for their constant love, care, and support in all sorts of situations of my life. This thesis is the fruit of the countless sacrifices they have made for me. In the end, I would like to thank my brother Manish Mishra for filling the gaps in my absence.

Abstract

Solid-state nuclear magnetic resonance (NMR) can provide a wealth of information about atomic-level microstructure and dynamics in materials, which dictate the properties of diverse functional materials. Conventional methods often cannot determine the material's structure in its native state. This is often the case for polycrystalline and amorphous materials which lack long-range order. Solid-state NMR is a powerful technique that can directly probe the local nuclear environment. Consequently, NMR has been increasingly successful for the rational development of new materials in the domain of energy conversion and storage, CO_2 capture and conversion, and catalysis.

In the last decade, halide perovskites have drawn a tremendous interest. This is due to their intriguing optoelectronic properties, inexpensive solution processing, and bandgap tunability. The versatility and robustness in their functional properties make them particularly suitable for solar cells, LEDs, and photodetectors. In particular, perovskite solar cells have achieved power conversion efficiencies (PCEs) exceeding 25% during the last decade. In contrast to these high PCEs, halide perovskites also show deleterious phenomena such as hysteresis, instability, and degradation under operating conditions. Methods such as compositional engineering, passivation of the perovskite surface, interstitial doping, cation alloying, halide mixing, and optimized crystallization have been successfully introduced to increase stability and reduce degradation of halide perovskite solar cells. While establishing structure-activity relation would be key to rationalize the origin of the technology improvement of these cases, this has so far not been fully amenable with the current analytical techniques. Solid-state NMR should in principle be able to describe the structural changes of stabilized perovskite solar cells and thus been a valuable tool to help to establish rational principles for constructing more efficient perovskite solar cells with longer lifetimes.

One of the main limitation of NMR spectroscopy is the inherently low sensitivity arising from low concentration, low-gyromagnetic ratio, and/or low natural abundance of the NMR active nuclei. Dynamic nuclear polarization (DNP) is a method that allow to significantly increase the sensitivity of NMR spectroscopy. In a magic-angle spinning (MAS) DNP experiment, the sample is impregnated with a solution of paramagnetic species such as a stable radical, which have high electronic spin polarization and can be harnessed to hyperpolarize nuclear spins via microwave irradiation. DNP methods are well established for many materials systems, but have had extremely limited success for the technologically-relevant perovskite materials.

The overall objective of my thesis is to develop and apply solid-state NMR methods to investigate perovskite materials, as well as to extend DNP hyperpolarization techniques to these perovskite systems, which offer various challenges in conventional solid-state NMR. This thesis contains three sections, described below.

In the first section, various examples of the application of solid-state NMR to halide perovskite systems is presented. First, an NMR crystallography approach was developed to determine the supramolecular structure of layered hybrid perovskites with a mixture of two spacer cations. In this multi-component complex material, conventional solid-state NMR, molecular dynamics, and NMR crystallography were combined to determine the structure of the spacer layer. The observed nano-scale phase segregation was proposed to be responsible for providing high efficiency and operational stability. Secondly, using conventional solid-state NMR, the incorporation of the dimethylammonium ion was examined under various conditions. Unusually, solution processed samples were found to have a different metastable structure than mechanosynthesised samples. Finally, the NMR-derived atomic-level microstructure in current state-of-the-art hybrid and inorganic perovskites is presented. Notably, structural hypotheses were thoroughly investigated using mechanosynthesised perovskites and solution-processed thin films. These structural insights have guided the studies to achieve unprecedented solar cell performance.

In the second section, a protocol is developed to investigate cation dynamics in the current state-of-the-art single and multi-cation perovskite systems. This protocol employs quadrupolar relaxometry at high magnetic field under magic angle spinning, combined with a rotational diffusion model, to provide the rate of rotation about each principal axis of the cation. Furthermore, this method has been extended to more challenging multi-cation systems, including the most successful contemporary perovskite compositions to date. All the studied organic cations (methylammonium, formamidinium, and guanidinium) have at least one component of rotation on the picosecond timescale at room temperature, with methyl ammonium and guanidinium ion also having a faster and slower component, respectively. The cation dynamics were found to depend upon the symmetry of the inorganic lattice, but were largely unaffected upon cation alloying. In particular, the reorientation energy landscape of the formamidinium ion was unaffected by cation substitution when sufficiently above the phase transition temperature of the material.

In the third section, a DNP method is developed enabling the structure to be determined for the surface layer of a single perovskite thin-film. This was made possible by identifying the factors that affect DNP enhancements in perovskite-based systems: namely fast nuclear relaxation times, particle morphology, and sample heating. Of these, the fast nuclear relaxation time was found to be the major impediment to a high DNP performance. This can be partially mitigated by optimal deuteration, resulting in enhancement factors approaching 100. Overall, by combining this deuteration strategy with DNP at high magnetic field (21 T) and 0.7 mm outer diameter rotors, the spectrum of a 6 μg surface coating on a single thin-film was obtained and the structure identified.

Keywords

Materials science, atomic-level structure, Nuclear Magnetic Resonance (NMR), Magic-angle spinning (MAS), Dynamics, Perovskite photovoltaics (PV), Perovskite solar cells (PSCs), Dynamic nuclear polarization (DNP).

Résumé

La resonance magnétique nucléaire (RMN) à l'état solide peut fournir une multitude d'informations sur la microstructure et la dynamique des matériaux au niveau atomique. Ces dernières déterminent les propriétés de divers matériaux fonctionnels. Jusqu'à présent, les méthodes analytiques sont limités dans le cas des matériaux polycristallins et amorphes, pour lesquels il n'y a pas d'ordre à grande échelle. La RMN à l'état solide sonde directement l'environnement atomique local et permet ainsi d'établir des relations structure-activité. Par conséquent, la RMN a un succès croissant pour le développement de nouveaux matériaux et leurs applications telles que la conversion et le stockage de l'énergie, la capture et la conversion du CO_2 et la catalyse. Ainsi, la RMN à l'état solide est un outil analytique primordial dans divers domaines de la science des matériaux et de la biologie structurale.

Au cours de la dernière décennie, les pérovskites ont suscité un intérêt considérable en science des matériaux. Cet intérêt est lié à leurs propriétés optoélectroniques, leurs tunabilités, et leurs faible coût. La polyvalence et la robustesse de leurs propriétés fonctionnelles en font des matériaux adaptés aux cellules solaires, aux LED et aux photodétecteurs. Les progrès réalisés au cours de la dernière décennie ont permis de mettre au point des cellules solaires type pérovskite qui atteignent déjà des rendements de conversion de puissance (PCE) supérieurs à 25 %. En dépit de leur succès dans l'obtention de PCE élevés, les cellules photovoltaïques à pérovskite présentent des phénomènes délétères notamment en termes de stabilité dans les conditions d'exploitation. Des méthodes telles que l'ingénierie de la composition, la passivation de la surface de la pérovskite, le dopage interstitiel, l'associationn de cations, le mélange d'halogénures et la cristallisation optimisée ont été introduite avec succès afin d'augmenter la stabilité et limiter la dégradation des cellules photovoltaïques à pérovkites. La RMN à l'état solide peut fournir des informations sur les changements structurels et peut aider à établir des principes rationnels pour la construction de cellules solaires en pérovskite plus efficaces avec des durées de vie plus longues.

La RMN est une méthode intrinsiquement peu sensitive, ce qui en linite son utilisation. La polarisation nucléaire dynamique (DNP) est une méthode d'hyperpolarisation et qui permet d'acquérir des spectres RMN avec une plus grande sensibilité. Dans une expérience de DNP avec rotation à l'angle magique (MAS), l'échantillon est imprégné d'une solution d'espèces paramagnétiques telles qu'un radical organique stable, qui ont une polarisation des spin électronique élevée et peuvent être exploitées pour hyperpolariser les spins nucléaire par irradiation par micro-ondes. Les méthodes DNP sont bien établies pour de nombreux systèmes de matériaux, mais ont eu un succès extrêmement limité pour les matériaux pérovskites technologiquement pertinents.

L'objectif global des travaux décrits dans cette thèse est de développer et d'appliquer des méthodes de RMN à l'état solide pour étudier les matériaux pérovskites, ainsi que d'étendre les applications de la DNP à ces systèmes pérovskites, qui présentent divers défis pour la RMN à l'état solide conventionnelle. Cette thèse comprend trois sections :

La première section présente plusieurs exemples d'application de la RMN à l'état solide aux systèmes de pérovskite à halogénure. Tout d'abord, une approche basée sur la cristallographie RMN a été développée pour déterminer la structure supramoléculaire de pérovskites hybrides stratifiées avec un mélange de deux cations espaceurs. Dans ce matériau complexe à plusieurs composants, la RMN conventionnelle à l'état solide, la dynamique moléculaire et la cristallographie RMN ont été combinées pour déterminer la structure de la couche d'espacement. La ségrégation de phase à l'échelle nanométrique observée a été proposée comme responsable de la haute efficacité des cellules et de leurs stabilité. Ensuite, l'incorporation de l'ion diméthylammonium a été examinée dans plusieurs conditions à l'aide de la RMN conventionnelle à l'état solide. De manière inhabituelle, les échantillons traités en solution avaient une structure métastable différente de celle des échantillons mécanosynthétisés. Enfin, la microstructure au niveau atomique dérivée de la RMN dans les pérovskites hybrides et inorganiques les plus récentes est présentée. En particulier, les hypothèses structurelles ont été étudiées de manière approfondie en utilisant des pérovskites mécanosynthétisées et des films minces mis en solution. Ces connaissances structurelles ont guidé les études pour atteindre des performances de cellules solaires sans précédent.

Dans la deuxième section, un protocole a été développé pour étudier la dynamique des cations dans les systèmes de pérovskite à un ou plusieurs cations actuellement. Ce protocole utilise la relaxométrie quadrupolaire à haut champ magnétique sous rotation à l'angle magique. Il est combiné à un modèle de diffusion rotationnelle afin de fournir la fréquence de rotation autour de chaque axe principal du cation. En outre, cette méthode a été étendue à des systèmes multications plus difficiles, y compris à des compositions de pérovskite récentes. Tous les cations organiques étudiés (méthylammonium, formamidinium et guanidinium) ont au moins une composante de rotation à l'échelle de temps de la picoseconde à température ambiante. Les ions méthylammonium et guanidinium ont respectivement une composante supplémentaire plus rapide et plus lente. La dynamique des cations dépend de la symétrie du réseau inorganique, mais n'est pas affectée par l'alliage des cations. En particulier, le paysage énergétique de réorientation de l'ion

formamidinium n'a pas été affecté par la substitution de cations lorsqu'il était suffisamment supérieur à la température de transition de phase du matériau.

Dans la troisième section, une méthode basée sur la DNP a été développée permettant de déterminer la structure de la couche de surface d'une seule couche mince de pérovskite. Ceci a été rendu possible par l'identification des facteurs qui affectent l'efficacité de la DNP dans les systèmes à base de pérovskite : les temps de relaxation nucléaire rapide, la morphologie des particules et le chauffage de l'échantillon. Parmi ces facteurs, le temps de relaxation nucléaire rapide s'est avéré être le principal obstacle. Ce problème peut être partiellement atténué par deutération, ce qui permet d'obtenir des facteurs d'exaltation DNP proches de 100. Dans l'ensemble, en combinant cette stratégie de deutération avec des hauts champs magétique (21 T), et des rotors de 0,7 mm de diamètre, le spectre d'un revêtement de surface de 0,6 µg sur un mono-film mince a été obtenu et la structure identifiée.

Mots-clés

Science des matériaux, structure au niveau atomique, résonance magnétique nucléaire (RMN), rotation à l'angle magique (MAS), dynamique, photovoltaïque pérovskite (PV), cellules solaires à pérovskites (PSCs), polarization nucléaire dynamique (DNP).

Contents

List of Publications

The contents of this thesis are the result of my work, and this includes the contributions from others where indicated. The thesis includes chapters based on the following publications:

1. Mishra, A.; Kubicki, D. J.; Boziki, A.; Chavan, R. D.; Dankl, M.; Mladenović, M.; Prochowicz, D.; Grey, C. P.; Rothlisberger, U.; Emsley, L., Interplay of Kinetic and Thermodynamic Reaction Control Explains Incorporation of Dimethylammonium Iodide into $CsPbI_3$. *ACS Energy Lett.* **2022**, 2745-2752.
2. Hope, M. A.; Nakamura, T.; Ahlawat, P.; Mishra, A.; Cordova, M.; Jahanbakhshi, F.; Mladenović, M.; Runjhun, R.; Merten, L.; Hinderhofer, A.; Carlsen, B. I.; Kubicki, D. J.; Gershoni-Poranne, R.; Schneeberger, T.; Carbone, L. C.; Liu, Y.; Zakeeruddin, S. M.; Lewinski, J.; Hagfeldt, A.; Schreiber, F.; Rothlisberger, U.; Grätzel, M.; Milić, J. V.; Emsley, L., Nanoscale Phase Segregation in Supramolecular π-Templating for Hybrid Perovskite Photovoltaics from NMR Crystallography. *J. Am. Chem. Soc.* **2021**, 143 (3), 1529–1538.
3. Jeong, J.; Kim, M.; Seo, J.; Lu, H.; Ahlawat, P.; Mishra, A.; Yang, Y.; Hope, M. A.; Eickemeyer, F. T.; Kim, M.; Yoon, Y. J.; Choi, I. W.; Darwich, B. P.; Choi, S. J.; Jo, Y.; Lee, J. H.; Walker, B.; Zakeeruddin, S. M.; Emsley, L.; Rothlisberger, U.; Hagfeldt, A.; Kim, D. S.; Grätzel, M.; Kim, J. Y., Pseudo-halide anion engineering for α-$FAPbI_3$ perovskite solar cells. *Nature* **2021,** *592* (7854), 381–385.
4. Lu, H.; Liu, Y.; Ahlawat, P.; Mishra, A.; Tress, W. R.; Eickemeyer, F. T.; Yang, Y.; Fu, F.; Wang, Z.; Avalos, C. E.; Carlsen, B. I.; Agarwalla, A.; Zhang, X.; Li, X.; Zhan, Y.; Zakeeruddin, S. M.; Emsley, L.; Rothlisberger, U.; Zheng, L.; Hagfeldt, A.; Grätzel, M., Vapor-assisted deposition of highly efficient, stable black-phase $FAPbI_3$ perovskite solar cells. *Science* **2020,** *370* (6512), eabb8985.
5. Zhang, J. H.; Wang, Z. W.; Mishra, A.; Yu, M. L.; Shasti, M.; Tress, W.; Kubicki, D. J.; Avalos, C. E.; Lu, H. Z.; Liu, Y. H.; Carlsen, B. I.; Agarwalla, A.; Wang, Z. S.; Xiang, W. C.; Emsley, L.; Zhang, Z. H.; Gratzel, M.; Guo, W. L.; Hagfeldt, A., Intermediate Phase Enhances Inorganic Perovskite and Metal Oxide Interface for Efficient Photovoltaics. *Joule* **2020**, 4 (1), 222–234.
6. Mishra, A.; Hope, M. A.; Grätzel, M.; Emsley, L., A Complete Picture of Cation Dynamics in Hybrid Perovskite Materials using Solid State NMR Spectroscopy. *(submitted)*
7. Mishra, A.; Hope, M. A.; Almalki, M.; Pfeifer, L.; Zakeeruddin, S. M.; Grätzel, M.; Emsley, L., Dynamic Nuclear Polarization Enables NMR of Surface Passivating Agents on Hybrid Perovskite Thin Films. *J. Am. Chem. Soc.* **2022,** *144* (33), 15175–15184.

In addition, I have also worked on a series of application problems that have served the drive for innovations in the field of perovskite photovoltaics. These applications have led to following set of papers:

8. Ummadisingu, A.; Mishra, A.; Kubicki, D. J.; LaGrange, T.; Dučinskas, A.; Siczek, M.; Bury, W.; Milić, J. V.; Grätzel, M.; Emsley, L., Multi-Length Scale Structure of 2D/3D Dion–Jacobson Hybrid Perovskites Based on an Aromatic Diammonium Spacer. *Small* **2022**, 18 (5), 2104287.
9. Mishra, A.; Ahlawat, P.; Fish, G. C.; Jahanbakhshi, F.; Mladenović, M.; Almalki, M.; Ruiz-Preciado, M. A.; Gelvéz-Rueda, M. C.; Ku-bicki, D. J.; Schouwink, P. A.; Dufoulon, V.; Schneeberger, T.; Aslanzadeh, A.; Grozema, F. C.; Zakeeruddin, S. M.; Moser, J.-E.; Rothlisberger, U.; Emsley, L.; Milić, J. V.; Grätzel, M., Naphthalenediimide/Formamidinium-Based Low-Dimensional Perovskites. *Chem. Mater.* **2021**, 33 (16), 6412–6420.
10. Boziki, A.; Kubicki, D. J.; Mishra, A.; Meloni, S.; Emsley, L.; Grätzel, M.; Rothlisberger, U., Atomistic Origins of the Limited Phase Stability of Cs^+-Rich $FA_xCs_{1-x}PbI3$ Mixtures. *Chem. Mater.* **2020**, 32 (6), 2605–2614.
11. Alanazi, A. Q.; Almalki, M. H.; Mishra, A.; Kubicki, D. J.; Wang, Z.; Merten, L.; Eickemeyer, F. T.; Zhang, H.; Ren, D.; Alyamani, A. Y.; Albrithen, H.; Albadri, A.; Alotaibi, M. H.; Hinderhofer, A.; Zakeeruddin, S. M.; Schreiber, F.; Hagfeldt, A.; Emsley, L.; Milić, J. V.; Graetzel, M., Benzylammonium-Mediated Formamidinium Lead Iodide Perovskite Phase Stabilization for Photovoltaics. *Adv. Funct. Mater.* **2021**, 31 (30), 2101163.
12. Dučinskas, A.; Kim, G. Y.; Moia, D.; Senocrate, A.; Wang, Y.-R.; Hope, M. A.; Mishra, A.; Kubicki, D. J.; Siczek, M.; Bury, W.; Schneeberger, T.; Emsley, L.; Milić, J. V.; Maier, J.; Grätzel, M., Unravelling the Behavior of Dion–Jacobson Layered Hybrid Perov-skites in Humid Environments. *ACS Energy Lett.* **2021**, 6 (2), 337–344.
13. Zhang, H.; Eickemeyer, F. T.; Zhou, Z.; Mladenović, M.; Jahanbakhshi, F.; Merten, L.; Hinderhofer, A.; Hope, M. A.; Ouellette, O.; Mishra, A.; Ahlawat, P.; Ren, D.; Su, T.-S.; Krishna, A.; Wang, Z.; Dong, Z.; Guo, J.; Zakeeruddin, S. M.; Schreiber, F.; Hagfeldt, A.; Emsley, L.; Rothlisberger, U.; Milić, J. V.; Grätzel, M., Multimodal host–guest complexation for efficient and stable perovskite photovoltaics. *Nature Commun.* **2021**, 12 (1), 3383.
14. Su, T.-S.; Eickemeyer, F. T.; Hope, M. A.; Jahanbakhshi, F.; Mladenović, M.; Li, J.; Zhou, Z.; Mishra, A.; Yum, J.-H.; Ren, D.; Krish-na, A.; Ouellette, O.; Wei, T.-C.; Zhou, H.; Huang, H.-H.; Mensi, M. D.; Sivula, K.; Zakeeruddin, S. M.; Milić, J.

V.; Hagfeldt, A.; Rothlisberger, U.; Emsley, L.; Zhang, H.; Grätzel, M., Crown Ether Modulation Enables over 23% Efficient Formamidinium-Based Perovskite Solar Cells. *J. Am. Chem. Soc.* **2020**, 142 (47), 19980–19991.

15. Alharbi E.A., Krishna A., Lempesis N., Dankl M., Lois M., Hope M.A., Baumeler T.P., Kakavelakis G., Mishra A., Eickemeyer F., Ouellette O., Chawanpunyawat T., Hagfeldt A., Zakeeruddin S.M., Emsley L., Pfeifer L., Rothelisberger U., Grätzel M., Cooperative Passivation of Perovskite Solar Cells by Alkyldimethylammonium Halide Amphiphiles, *(accepted in Joule).*

Chapter 1 Introduction

Materials are an integral part of human life, whether it be the "chair" on which I am sitting and conveniently writing this thesis or the "screen" which is allowing me to evaluate text. These are just two examples, but we are all surrounded by an uncountable number of objects made up of a wide range of materials. These materials exhibit electrical, mechanical, optical, magnetic, chemical, and structural properties adapted to particular functions. These functional properties emerge from the underlying structure of the material. Structure refers to the spatial arrangement of its internal components, which can be classified from an atomic level ($\sim 10^{-10}$ m) to a macroscopic level ($\sim$ m). An atomic-level understanding of the material is essential to design materials with improved functional properties. This understanding establishes the structure–property relationship, which is the core motivation of materials science.

Given that atomic-level structure dictates the material's properties, determining this structure is one of the key challenges in modern materials science.[1-3] X-ray diffraction is the most valuable method for single crystals, which can give a complete structure. In fact, it has determined over one million structures deposited on the Cambridge Structural Database and, as a result, led to an explosion in materials science.[4-6] However, this technique is less valuable for studying polycrystalline materials or powders. Other methods range from X-ray photoelectron spectroscopy (XPS) and grazing incidence wide-angle X-ray scattering (GIWAXS) to neutron and electron diffraction,[7-9] which each have associated strengths and weaknesses.

On the other hand, nuclear magnetic resonance (NMR) spectroscopy could provide a method of choice to study materials with short-range order. It is sensitive to the nuclear site's local electronic environment and therefore gives the underlying atomic-level information. Further, more than one nuclear site can be investigated by NMR, which can be harnessed to determine the interatomic distances and potentially could provide the global picture of the material. Moreover, NMR is also quite sensitive in providing quantitative information about dynamic processes occurring from picoseconds to seconds time-scale, thereby providing the motion's nature and timescale.

In 1959, Andrew[10] and Lowe[11] discovered the concept of magic-angle spinning (MAS) NMR. The full theoretical description of NMR of rotating solids was presented by Maricq and Waugh in 1979.[12] However, in the early days, because of the limited instrumental capabilities, NMR on materials was conducted on static samples where inherently low-resolution spectra are usually obtained due to anisotropic interactions. As a result, single crystals samples were often chosen for such experiments, making the studies quite cumbersome and the growth of solid-state NMR for materials minimal. However, the advent of high field superconducting magnets and reliable MAS instrumental capabilities have revolutionized the field of solid-state NMR. Today MAS NMR has been extensively used in various kinds of materials such as energy materials,[13-20] halide perovskites,[21-24] bio-materials,[25-27] catalytic materials,[28-30] polymeric materials,[31-36] metal organic-frameworks (MOFs),[37-44] and cementitious materials.[45-49]

In this Ph.D. thesis, I will be capitalizing on MAS NMR along with dynamic nuclear polarization (DNP) to develop new methods to study the structure and dynamics of perovskites. In the following sections, I will set the scene by introducing key theoretical and experimental concepts used in the later chapters.

1.1 Solid-state NMR

As mentioned above, NMR provides site-specific information. Now the question is, what do I mean by site-specificity? For example, the high-resolution ^{1}H MAS NMR spectrum of a powdered sample of alanine presented in Figure 1-1 shows three distinct peaks corresponding to the three distinct ^{1}H-sites in alanine. In solid-state NMR, the desired spectral resolution needed to distinguish site-specific sites is given by MAS, since without MAS the spectrum would be a single resonance around ~150 ppm broad. Therefore, the MAS technique was used in all the work presented in this thesis.

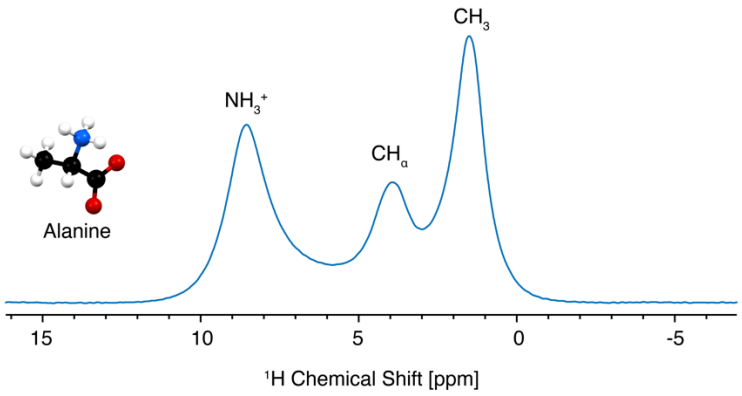

Figure 1-1. Echo-detected ^{1}H NMR spectrum of alanine at 298 K and 50 kHz MAS frequency.

1.1.1 Spin-½ Nuclei

The NMR spectrum manifests various magnetic interactions present in the system. In particular, the peak position in an NMR spectrum corresponds to the transition frequency between nuclear spin states modulated by internal NMR interactions. The nature and magnitudes of interactions determine this modulation in frequency. The interactions involved in the simplest case of a spin-½ nucleus are discussed below. This will be the case for ^{1}H, ^{13}C, ^{207}Pb, and ^{15}N nuclei, used in the later chapters.

Zeeman Interaction

The Zeeman interaction results from direct interaction between the magnetic moment ($\vec{\mu}$) and the applied magnetic field ($\vec{B}$). This interaction can be computed from the classical interaction energy of a bar magnet in a magnetic field as follows

$$E = -\vec{\mu}.\vec{B} \tag{1-1}$$

This classical interaction energy can be converted to the corresponding Hamiltonian with definition of microscopic magnetic moment associated with each nuclear spin[50-52]

$$\hat{H}_{Zeeman} = -\hat{\mu}.\vec{B} = -\gamma_n h\,\hat{I}.\vec{B} \tag{1-2}$$

where γ_n is the nuclear gyromagnetic ratio (specified in Hz T^{-1}), h is the Planck's constant and $\hat{I}$ is the spin angular momentum operator. However, most commonly, the Zeeman interaction is represented in terms of the Larmor frequency (ω_0) as follows

$$\hat{H}_{Zeeman} = -\gamma_n h B_0 \hat{I}_z = \omega_0 \hat{I}_z \tag{1-3}$$

Chemical Shift or Chemical Shielding Interaction

In addition to the main magnetic field of an NMR spectrometer, each nuclear spin also interacts with an anisotropic local magnetic field with strength B_i given by[50-52]

$$\vec{B}_i = -\hat{\sigma}_i . \vec{B}_0 \tag{1-4}$$

Therefore, the Hamiltonian arising from the local electronic environment can be written as[50-52]

$$\hat{H}_{CS} = -\hat{\mu}.\vec{B}_i = \hat{\mu}\,.\,\hat{\sigma}_i\,.\,\vec{B}_0 \quad 1\text{-}5$$

where $\vec{\mu}$ and $\vec{B}_0$ are vectors, and $\hat{\sigma}_i$ is a second-rank tensor (9 independent components) called the shielding tensor. This gives the chemical shift Hamiltonian

$$\hat{H}_{CS} = \gamma_n.h.\begin{bmatrix}\hat{I}_x & \hat{I}_y & \hat{I}_z\end{bmatrix}.\begin{bmatrix}\sigma_{xx} & \sigma_{xy} & \sigma_{xz}\\ \sigma_{yx} & \sigma_{yy} & \sigma_{yz}\\ \sigma_{zx} & \sigma_{zy} & \sigma_{zz}\end{bmatrix}.\begin{bmatrix}B_x\\ B_y\\ B_z\end{bmatrix} \quad 1\text{-}6$$

This Hamiltonian can be decomposed into the two operators corresponding to the spatial-part or the spin-part as follows

$$\hat{H}_{CS} = C_{shift}\,\hat{\sigma}_i\,.\,\hat{X} \quad 1\text{-}7$$

with $C_{shift} = \gamma_n.h$ and $\hat{X}$ is called the spin-field interaction tensor as it is formed by taking the dyadic product of two vectors, namely, the spin angular momentum vector ($\vec{I}$) and the magnetic field ($\vec{B}$).

Dipolar Interaction

In general, each spin behaves like a bar magnet. In a large ensemble of spins, each spin experiences the magnetic field caused by the neighboring nuclear spins. This dipolar coupling between spins is a through-space interaction. Therefore, this interaction energy of two spins i and j, having a position vector ($\vec{r}_i$) and ($\vec{r}_j$), magnetic moments as $\vec{\mu}_i$ and $\vec{\mu}_j$, and internuclear vector $\vec{r}_{ij} = \vec{r}_j - \vec{r}_i$ is given by

$$E = \frac{\vec{\mu}_i.\vec{\mu}_j}{r_{ij}^3} - 3.\frac{(\vec{\mu}_i.\vec{r}_{ij})\,.\,(\vec{\mu}_j.\vec{r}_{ij})}{r_{ij}^5} \quad 1\text{-}8$$

This classical energy can be used to generate corresponding Hamiltonian as follows[50-52]

$$\hat{H}_{DD} = \frac{\mu_0}{4\pi}\frac{\gamma_i.\gamma_j.h^2}{r_{ij}^3}\left[\hat{I}_i.\hat{I}_j - 3.\frac{(\hat{I}_i.\vec{r}_{ij})\,.\,(\hat{I}_j.\vec{r}_{ij})}{r_{ij}^2}\right] = \frac{\mu_0}{4\pi}\frac{\gamma_i.\gamma_j.h^2}{r_{ij}^3}\left[\hat{I}_i.\hat{I}_j - 3.(\hat{I}_i.\hat{e}_{ij})\,.\,(\hat{I}_j.\hat{e}_{ij})\right] = \frac{\mu_0}{4\pi}\frac{\gamma_i.\gamma_j.h^2}{r_{ij}^3}\left[\hat{I}_i.\hat{\mathbb{1}}.\hat{I}_j - 3.(\hat{I}_i.\hat{e}_{ij}.\hat{I}_j)\right]$$

$$\hat{H}_{DD} = \frac{\mu_0}{4\pi}\frac{\gamma_i.\gamma_j.h^2}{r_{ij}^3}\left[\hat{I}_i.\hat{D}.\hat{I}_j\right] \quad 1\text{-}9$$

In this equation, $\hat{e}_{ij}$ is the unit vector along $\vec{r}_{ij}$ and the dipolar coupling tensor ($\hat{D}$) is a second rank tensor (9-components) of the following form[50-52]

$$\hat{D} = \begin{pmatrix}1-3e_{xx} & -3e_{xy} & -3e_{xz}\\ -3e_{yx} & 1-3e_{yy} & -3e_{yz}\\ -3e_{zx} & -3e_{zy} & 1-3e_{zz}\end{pmatrix} = \begin{pmatrix}1-\frac{3x^2}{r^2} & \frac{-3xy}{r^2} & \frac{-3xz}{r^2}\\ \frac{-3xy}{r^2} & 1-\frac{3y^2}{r^2} & \frac{-3yz}{r^2}\\ \frac{-3zx}{r^2} & \frac{-3zy}{r^2} & 1-\frac{3z^2}{r^2}\end{pmatrix} \quad 1\text{-}10$$

The form of $\hat{D}$ shows that it is an inherently *traceless* and *symmetric* tensor and therefore can be uniquely characterized by only 5 components, instead of 9 components as for the case of general second-rank tensor. The Hamiltonian presented in equation 1-9 can be decomposed into the two operators corresponding to the spatial-part and the spin-part as follows[50-52]

$$\hat{H}_{DD} = C_{dipole}\,\hat{D}.\hat{X} \quad 1\text{-}11$$

$$C_{dipole} = \frac{\mu_0}{4\pi}\frac{\gamma_i.\gamma_j.h^2}{r_{ij}^3} \quad 1\text{-}12$$

$\hat{X}$ is called the spin-spin interaction tensor as it is formed by taking the dyadic product of two spin angular momentum vectors associated with interacting spins i and j.

Scalar Interaction or J-coupling

The mutual coupling between spins not only arises from the through-space interaction, but also through bonding electrons. This coupling is given by[50-52]

$$\hat{H}_J = h \cdot \left(\hat{I}_i . \hat{J} . \hat{I}_j\right) = C_J \hat{J} . \hat{X} \quad \text{1-13}$$

In the above equation $\hat{X}$ is the same as in the dipolar coupling case.[50-52]

Averaging of Anisotropic Interactions

So far, I have discussed the origin and form of various NMR interactions manifested in an NMR spectrum. The anisotropic part of these NMR interactions can be shown to follow a 2nd order Legendre polynomial dependence $(3\cos^2\theta - 1)$, where θ is the angle between the principal axis of the interaction and the magnetic field (B_0).[53] For liquid samples, rapid molecular tumbling averages this anisotropic part of the interactions to zero because the rate of molecular tumbling is faster than the strength of the NMR interaction, resulting in narrow lines in the spectrum.

The absence of tumbling in the solid-state results in broad NMR lines masking the resolution in the spectrum. However, if the sample is spun at an angle β to the magnetic field, the average value of the 2nd order Legendre polynomial dependence for a given interaction is modified as shown in 1-14, where χ is the angle between sample axis and the interaction axis.[53-55] Therefore, the $(3\cos^2\theta - 1)$ dependence can be removed by spinning the sample at the magic angle (β = 54.17°). The spinning rate defines the extent of averaging, and, in an ideal scenario, the spinning at an infinite speed will result in complete averaging. Today, >100 kHz spinning can be achieved on commercially available MAS probes.[56-58] The experiments presented in this thesis were performed at MAS rates ranging from 10 – 50 kHz.

$$\langle 3\cos^2\theta - 1\rangle = \frac{1}{2}(3\cos^2\beta - 1)(3\cos^2\chi - 1) \quad \text{1-14}$$

In this subsection, I have introduced the interactions that are manifested in the spectrum of spin-½ nucleus and this will be the case for ^{1}H, ^{13}C, ^{15}N, and ^{207}Pb NMR experiments presented in this thesis. However, a major part of my thesis work concerns another category of nuclei, which will be the subject of the next subsection.

1.1.2 Quadrupolar Nuclei

Nuclei with a non-spherical (but axially symmetric) charge distribution, in addition to a non-zero nuclear magnetic moment, also have an electrical quadrupole moment. This electric quadrupole moment can be either positive (prolate) or negative (oblate). In fact, more than 70% of the elements in the periodic table have quadrupolar stable isotopes. These nuclear isotopes are characterized by having a spin quantum number I > ½. Properties (spin quantum number and quadrupolar moment) of quadrupolar nuclei studied in this thesis are summarized in Table 1-1. NMR properties of quadrupolar nuclei are substantially different from those of spin-½ nuclei. These properties are manifested in the form of quadrupolar couplings which I will briefly discuss below.

Table 1-1. Spin quantum number (*I*) and electric quadrupolar moment (Q) of the nuclei studies in this thesis.

Nuclei	*I*	Q (fm^2)
^{2}H	1	0.286
^{14}N	1	2.044
^{133}Cs	7/2	-0.343

In NMR, quadrupolar coupling is the interaction of the nuclear electric quadrupolar moment (Q) with an electric field gradient (EFG) present at the nuclear site. The interaction strength is given by the size of the quadrupolar moment (eQ, where e is the unit charge) and the EFG, characterized by a second-rank tensor **V**

$$\hat{H}_Q = \frac{eQ}{2I(2I-1)} \hat{\mathbf{I}} . \mathbf{V} . \hat{\mathbf{I}} \quad \text{1-15}$$

In general, the EFG tensor (**V**) is described by a symmetric and traceless matrix, with 5 independent components. In the principal axis frame (PAF), the EFG tensor is diagonal with

$$V_{xx} + V_{yy} + V_{zz} = 0$$

$$|V_{xx}| \leq |V_{yy}| \leq |V_{zz}|$$

and is uniquely characterized by the largest principal axis component V_{zz} and the asymmetry parameter (η), as well as the three Euler angles defining the orientation of the PAF.

$$\eta = \frac{V_{xx} - V_{yy}}{V_{zz}} \text{ and } 0 \leq \eta \leq 1 \quad \text{1-16}$$

The magnitude of the quadrupolar coupling is typically reported in the form of the quadrupolar coupling constant (C_Q) measured in Hz

$$C_Q = \frac{eQV_{zz}}{h} \quad \text{1-17}$$

and the asymmetry parameter (η). Using these parameters, the quadrupolar interaction in the PAF is given by the following equation

$$\hat{H}_Q = \frac{C_Q}{4I(2I-1)}\left[3\hat{I}_z^2 - \hat{I}^2 + \frac{\eta}{2}\left(\hat{I}_+^2 + \hat{I}_-^2\right)\right] \quad \text{1-18}$$

When this quadrupolar Hamiltonian is transformed into the lab frame involving the angles (θ,φ), which define the orientation of B_0 in the quadrupolar PAF, we have

$$\begin{aligned}\hat{H}_Q = \frac{C_Q}{4I(2I-1)}\Big[&\frac{1}{2}(3\cos^2\theta - 1)\left(3\hat{I}_z^2 - \hat{I}^2\right)\\ &+\frac{1}{4}(3\sin^2\theta - \eta\cos^2\theta\cos 2\varphi - \eta\cos 2\varphi)\left(\hat{I}_+^2 + \hat{I}_-^2\right) + \frac{\eta}{2i}\cos\theta\sin 2\varphi\left(\hat{I}_+^2 - \hat{I}_-^2\right)\\ &-\frac{1}{2}\cos\theta\sin\theta\,(3 + \eta\cos 2\varphi)\left(\hat{I}_z(\hat{I}_+ + \hat{I}_-) + (\hat{I}_+ + \hat{I}_-)\hat{I}_z\right)\\ &+\frac{\eta}{2i}\sin\theta\sin 2\varphi\left(\hat{I}_z(\hat{I}_+ - \hat{I}_-) + (\hat{I}_+ - \hat{I}_-)\hat{I}_z\right)\Big]\end{aligned} \quad \text{1-19}$$

When the NMR sample is placed in a large magnetic field, the Zeeman interaction (the interaction between the nuclear magnetic moment and the magnetic field) dominates, being typically orders of magnitude stronger than the quadrupolar interaction. In this case, the quadrupolar Hamiltonian can be treated as a perturbation. To first order, only the secular terms involving I_z and I^2 that commute with the Zeeman interaction remain, which gives rise to a first order correction to the Zeeman energy states, depending on the z component of the nuclear spin, m[59]

$$E_Q^{(1)} = \frac{(3m^2 - I(I+1))C_Q}{8I(2I-1)}\left[\,3\cos^2\theta - 1 + \eta\sin^2\theta\cos 2\varphi\,\right] \quad \text{1-20}$$

Equation 1-20 illustrates that since the shift in the Zeeman energy states depend upon m^2, it shifts the energy levels involved in the central transition, -½ → ½, for ½-integer quadrupolar nuclei by the same amount. Therefore, the central transition frequency is unaffected to first order, regardless of the orientation (i.e., for all crystallites). In the special case of an axially symmetric nuclear quadrupolar site, η = 0, the energy levels of all the crystallites are affected, except the ones which are at the magic-angle (θ = 54.44°). In general, the correction to the single quantum transition frequencies are to 1[st] order expressed as follows[59]

$$\nu_{Q,(m-1)\to m}^{(1)} = \frac{3(2m-1)C_Q}{8I\,(2I-1)}\left[\,3\cos^2\theta - 1 + \eta\sin^2\theta\cos 2\varphi\right] \quad \text{1-21}$$

The other allowed NMR transitions (satellite transitions) for ½-integer quadrupolar nuclei strongly depend upon (θ,φ). In polycrystalline samples, the satellite transitions will be spread over a large frequency range and, therefore, they might not be visible for large C_Q.

When the quadrupolar coupling constants are larger than ~1% of the Zeeman term, then just considering the first order correction does not reproduce the experimental spectrum. In this scenario, non-secular terms, i.e., terms involving I_+ and I_- result in second-order shifts to the energy levels. These terms also introduce mixing of states and, therefore, pure nuclear Zeeman states are no

longer eigenstates of the overall Hamiltonian.[55] The form of those second order correction terms involve the 4th-order Legendre polynomial and the exact forms can be found in reference textbooks.[59-61] Briefly, the second order quadrupolar coupling scales as $(C_Q)^2/B_0$, indicating that a larger C_Q will introduce a larger second-order contribution. This can be mitigated to some extent by going to high external magnetic fields. Moreover, the second order coupling not only affects the satellite transitions but also the central transition. Furthermore, a 0th-rank component in the second-order correction to the central transition results in a shift of the isotropic resonance. Removal of these large second-order coupling effects require advanced methods such as dynamic angle spinning (DAS), double rotation NMR, or multiple quantum MAS ; these methods are the subject of reviews in the literature.[60, 61]

In summary, the static NMR spectrum of a half-integer quadrupolar nucleus possesses a narrow central transition and satellite transitions with powder patterns. Under MAS, the powder patterns are averaged and split into spinning side bands due to the averaging of the 2nd-order Legendre polynomial.[55] I will be using ^{133}Cs NMR in later chapters, which is a spin-7/2 nucleus. As can be seen in Table 1-1, ^{133}Cs has a very small quadrupolar moment, therefore, it behaves as a pseudo spin-½ nucleus.

Integer-spin Quadrupolar Nuclei

Integer spin nuclei (e.g., ^{2}H, ^{14}N, ^{6}Li etc.) do not have a central transition, therefore the spectral manifold will be broadened by 1st order quadrupolar coupling.[55] In this thesis, some of the work deals with ^{2}H and ^{14}N MAS NMR. As can be seen from equation 1.6, for a spin-1 site, the two possible Δm = ±1 transitions have opposite signs of the quadrupolar coupling, with no central transition, i.e., $\nu_{-1\to0} = -\nu_{0\to1}$.[55] Therefore, a polycrystalline sample will exhibit a pattern broadened by 1st order quadrupolar coupling with a separation between the outer singularities is $3C_Q/2$ as shown in Figure 1-2 (left panel). Under MAS, this first-order quadrupolar coupling will be averaged and this will result in a manifold of spinning sidebands for each deuterium site in the spectrum as shown in Figure 1-2 (right panel).[55, 60] In fact, this will be the case for ^{2}H and ^{14}N spectra shown in the later chapters.

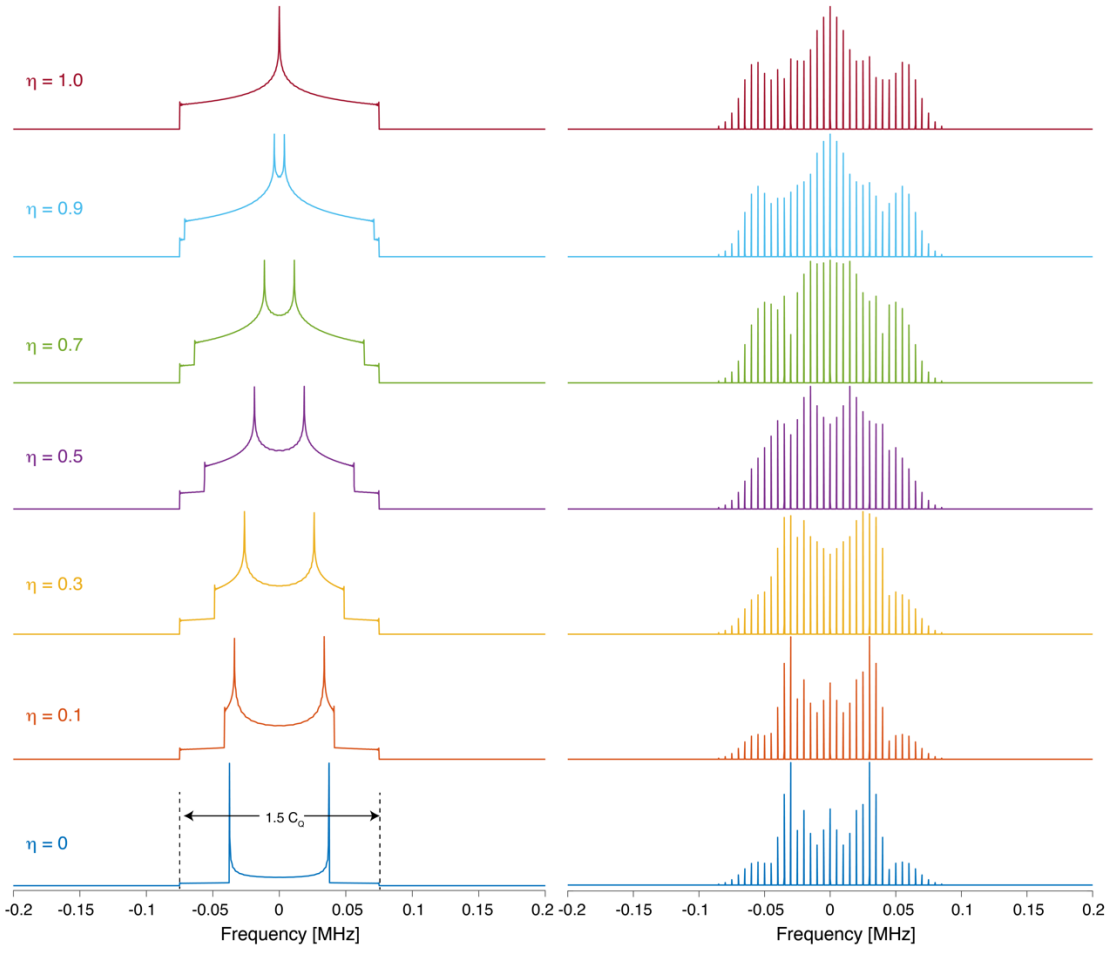

Figure 1-2. Simulated powder pattern (left panel) and MAS pattern (5 kHz) for spin-1 nucleus as a function of η with C_Q = 100 kHz

In this subsection, I have talked about the basics of quadrupolar NMR, upon which subsequent chapters will be based. In the beginning, I mentioned that NMR is useful for probing dynamics. This dynamical information is accessed by multi-field and variable temperature nuclear relaxation measurements. In this thesis, I will be relating ^{2}H and ^{14}N nuclear relaxation times to the motional parameters. Therefore, I will discuss relaxation and its relation to the motional parameters in the following subsection.

1.1.3 Relaxation

Relaxation is the process by which non-equilibrium bulk magnetization returns to equilibrium. This equilibrium state of bulk magnetization consists of zero magnetization in the x-y plane (transverse), and Boltzmann magnetization along the z-direction (longitudinal). Therefore, relaxation is the process by which the transverse magnetization decays to zero, and the longitudinal magnetization returns to its equilibrium value after any perturbation from equilibrium.[62-64] If we assume that relaxation to be mono-exponential, then if at $\tau = 0$, we have $M_z = M_z^{eq}$ and $M_{x,y} = M_0$, the return to equilibrium is given as

$$M_z(\tau) = M_z^{eq}\left(1 - \exp\left(-\frac{\tau}{T_1}\right)\right) \quad 1\text{-}22$$

$$M_{x,y}(\tau) = M_0 \exp\left(-\frac{\tau}{T_2}\right) \quad 1\text{-}23$$

This relaxation is characterized by two-time constants, T_1 and T_2, for the longitudinal and transverse relaxation, respectively. Alternatively, in NMR literature sometimes the corresponding relaxation rates are considered, $R_1 = 1/T_1$ and $R_2 = 1/T_2$.

T_1 Relaxation

Longitudinal relaxation (T_1) originates from local transverse magnetic fields fluctuating at or near the Larmor frequency. These fluctuations are often caused by the random stochastic thermal motion of molecules in dynamical systems, which modulates the anisotropic (orientationally dependent) part of the involved NMR interactions. This can be either chemical shift anisotropy (CSA), dipolar or scalar coupling (homonuclear or heteronuclear), or quadrupolar coupling.[63, 65, 66] For example, fluctuation of chemical shift due to rotational motion, or similarly, fluctuations in dipolar coupling due to the overall molecular tumbling. When motion drives the T_1 relaxation, the temperature dependence of T_1 relaxation times can be used as a probe of the molecular motions' magnitude, rate, and activation energy.[66]

A dynamical system can exhibit motion on a range of timescales. In general, this can include vibration, rotational and translational motion. All these motions can provide the necessary fluctuations in the local fields, however, not all these time dependences drive the T_1 relaxation. In order to identify what motions are driving the relaxation, a measure is required of quantifying the random motion that provides the relevant time dependence to the local fields.[65, 66]

The time dependence of the random thermal motion is conveniently characterized with the correlation function ($G(\tau)$). If we assume that the correlation function decays exponentially, as is often the case,[55, 63, 65, 66] then

$$G(\tau) = G(0)\exp\left(-\frac{\tau}{\tau_c}\right) \quad 1\text{-}24$$

This decay time is called the correlation time of a molecule (τ_c). For rotation, this corresponds to the average time that a molecule takes to rotate by 1 radian, for example. In this equation G(0) is the variance (σ^2) or the mean-square amplitude of the fluctuating interaction.

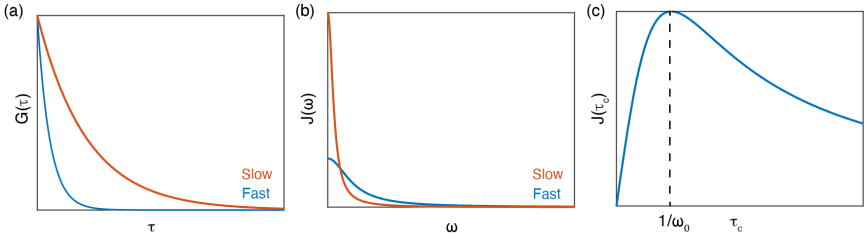

Figure 1-3. (a) Correlation function as a function of time (τ), and spectral density as a function of (b) frequency (ω), and (c) correlation time (τ_c).

Now, in order to find out what frequency components are present in a motion, Fourier transformation of the correlation function provides the spectral density of the motion.[65, 66] In the case of an exponential correlation function, the spectral density takes the form of a Lorentzian centered at $\omega = 0$ with the form given as[64, 66]

$$J(\omega) = G(0).\frac{2\,\tau_c}{(1 + \omega^2\tau_c^2)} \quad 1\text{-}25$$

This form of the spectral density function demonstrates that as τ_c becomes shorter and the motion becomes faster, the spectral density extends to higher frequency components, as shown in Figure 1-3b.

As shown in Figure 1-3c, motion with a correlation time $\tau_c = 1/\omega_0$ provides the highest spectral density at the Larmor frequency thereby providing the most efficient relaxation (except for quadrupolar and dipolar relaxation, for which most efficient relaxation occurs when $\tau_c = 0.606/\omega_0$).[63, 66] Two limiting extremes can be identified when the motion is much faster or slower than the Larmor frequency, where the spectral density adopts the following form[63]

Fast motion or extreme narrowing limit ($\tau_c << 1/\omega_0$)

$$J(\omega_0) = G(0).2\tau_c \quad 1\text{-}26$$

Slow motion or rigid lattice limit ($\tau_c >> 1/\omega_0$)

$$J(\omega_0) = G(0).\frac{2}{\omega_0^2}.\frac{1}{\tau_c} \quad 1\text{-}27$$

When motion induces fluctuations in the chemical shift anisotropy (CSA), the T_1 relaxation has the following form,[65, 66]

$$R_1^{CSA} = \frac{1}{T_1^{CSA}} = A\,[J(\omega_0)] \quad 1\text{-}28$$

When motion induces fluctuations in the dipolar (DD) or quadrupolar coupling (Q), the T_1 relaxation has the following form,[65, 66]

$$R_1^{DD,Q} = \frac{1}{T_1^{DD,Q}} = A\,[J(\omega_0) + 4.J(2\omega_0)] \quad 1\text{-}29$$

The form of A depends upon the strength of the interaction and nature of the motions (or symmetry of the motion). In the case of isotropic reorientations of the molecule with a single correlation time, A is given in the table below[63, 66]

Table 1-2. Form of pre-factors in determining relaxation times.

Mechanisms	A (Hz)	Conventions
CSA	$\frac{3}{5}\gamma_I^2 B_0^2 \delta^2 \left(1+\frac{\eta^2}{3}\right)$	$\delta = \delta_{zz} - \delta_{iso}$ $\delta_{zz} - \delta_{iso} \geq \delta_{xx} - \delta_{iso} \geq \delta_{yy} - \delta_{iso}$ $\eta = \frac{\delta_{yy} - \delta_{xx}}{\delta}$
DD (Homonuclear)	$\frac{3\mu_0^2 \hbar^2 \gamma_I^4}{160\pi^3 r^6}$	-
Q	$\frac{3\,(2I+3)}{400I^2(2I-1)}\left(1+\frac{1}{3}\eta_Q^2\right)C_Q^2$	$C_Q = eqV_{zz}$ $V_{zz} \geq V_{xx} \geq V_{yy}$ $\eta_Q = \frac{V_{xx} - V_{yy}}{V_{zz}}$

In this thesis, I will be measuring relaxation of ^{2}H and ^{14}N nuclei. Quadrupolar nuclei with spin quantum number *I* have 2*I*+1 nuclear spin states.[67] The population distribution of these states is given by 2*I* differential equations, and therefore 2*I* relaxation time constants. The analysis of T_1 relaxation of quadrupolar nuclei is generally rather complicated and has been described in the literature.[60, 67] However, for I = 1 nuclei (e.g., ^{2}H and ^{14}N), the population distribution is characterized by only two rate constants which correspond to the Zeeman order (T_{1z}) and quadrupolar order (T_{1Q}). Moreover, for the case of *I* = 1, T_1 relaxation shows mono-exponential behavior. Since the T_1 behavior varies according to motional regimes, it is worth stating the behavior of T_1 relaxation in the limiting motional regimes[63, 66]

Fast motion or extreme narrowing limit ($\tau_c << 1/\omega_0$)

$$R_1^Q = \frac{1}{T_1^Q} = 10\,A\,\tau_c \qquad 1\text{-}30$$

Slow motion or rigid lattice limit ($\tau_c >> 1/\omega_0$)

$$R_1^Q = \frac{1}{T_1^Q} = \frac{4\,A\,\tau_c}{\omega_0^2\,\tau_c} \qquad 1\text{-}31$$

Between these two limits, T_1 exhibits a minimum when $\tau_c = 0.616/\omega_0$ as shown in Figure 1-4. Further, in the cases where the correlation time of the molecule (τ_c) follows an Arrhenius temperature dependence with activation energy of the motion (E_a)

$$\tau_c = \tau_0 \exp\left(\frac{E_a}{k_B T}\right) \qquad 1\text{-}32$$

T_1 relaxation is typically measured by saturation recovery or inversion recovery experiments (Figure 1-5). In the former, magnetization is first saturated and subsequently detected after a variable delay. In the latter, magnetization is inverted and then detected with variable delays. The choice of these two methods depends upon T_1, available rf powers and other experimental factors. In this thesis, in most scenarios ^{2}H and ^{1}H T_1 constants are measured with saturation recovery experiments and ^{14}N T_1 constants are measured with inversion recovery experiments.

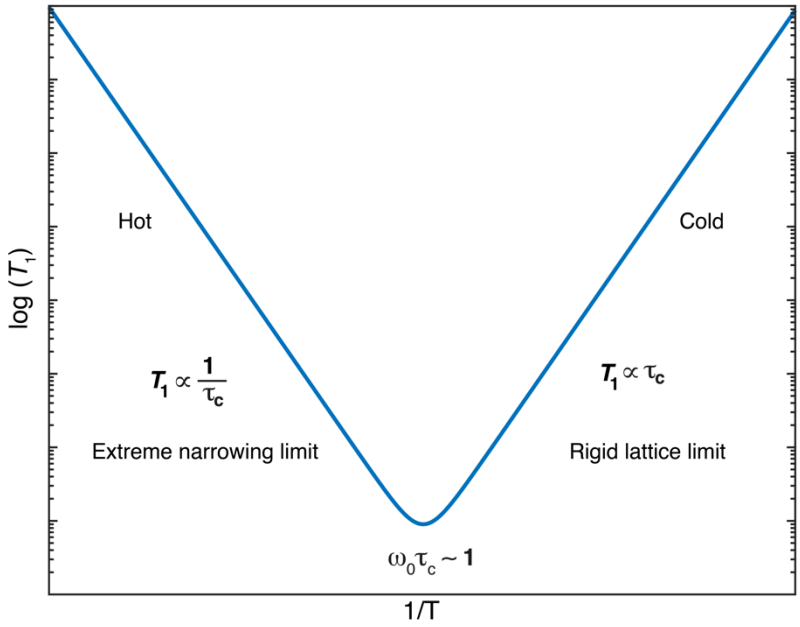

Figure 1-4. Plot showing the dependence of longitudinal relaxation time (T_1) with inverse temperature.

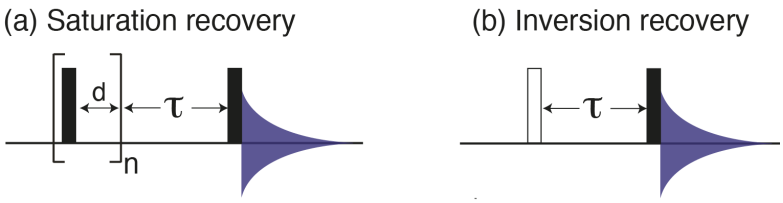

Figure 1-5. Pulse sequences for T_1 measurements (a) Saturation recovery (b) Inversion recovery. Filled and open rectangles are 90° and 180° pulses, respectively.

The above discussion describes the case where motion drives the T_1 relaxation. However, nuclear T_1 relaxation can also be induced by the fast relaxation of coupled nuclei (e.g., quadrupolar nuclei or paramagnetic electrons) in cases where motion is not the dominant source of relaxation, which is known as scalar relaxation of 2nd-kind. Scalar relaxation of the 1st-kind results from the fluctuating coupling between spins, e.g., due to motion.[62, 66, 68, 69] Moreover, T_1 relaxation can also occur by spin diffusion (see chapter 3/section 3.2.5) from fast relaxing spins near a relaxation sink (e.g., a paramagnetic center) to the rest of the sample.

$T_{1\rho}$ Relaxation

Spin-lattice relaxation in the rotating frame is characterized by a time constant $T_{1\rho}$ which describes the decay of transverse magnetization in the presence of a spin-locking radio frequency field.[55, 62] This decay of the transverse magnetization depends upon the strength of the spin-locking field which is often on the order of ~100 kHz. Spectral density at this spin-locking frequency drives this relaxation. Estimation and interpretation of $T_{1\rho}$ relaxation is not used in this work.

T_2 Relaxation

As mentioned in the introduction, spin–spin relaxation or T_2 relaxation is the decay of magnetization in the transverse plane. Dephasing of spins also appears like a T_2 relaxation, but this dephasing can result from frequency distribution which are not caused by spin–spin interactions.[55, 70] Similar to T_1 relaxation, T_2 relaxation is also caused by local fields fluctuating at or near the Larmor frequency, however, T_2 relaxation is also caused by spectral density at zero frequency.[55, 62, 63, 65, 66]

In the case of a specific single nuclear environment where transverse decay is purely due to T_2 relaxation, i.e., *solely* caused by fluctuating local fields at that nuclear site or environment, with no other dephasing contribution (a distribution of chemical shifts, diffusion, chemical exchange, or, B_0 inhomogeneity), then the decay constant of the free induction decay (FID) is the T_2 relaxation time. In that scenario, the full-width-at-half-maximum (Δ) of that Lorentzian shaped NMR signal in the frequency domain is related to the T_2 as follows[55, 63, 70]

$$\Delta = \frac{1}{\pi T_2} \qquad 1\text{-}33$$

In the solids, the observed linewidth (Δ^*) is the result of broadening coming from other sources as well: (1) residual dipolar coupling or CSA; (2) local magnetic field inhomogeneity (B_0 inhomogeneity and anisotropic bulk magnetic susceptibility); (3) degree of disorder (4) stochastically fluctuating local fields that drives the T_2 relaxation.[55, 70] These sources can be characterized as homogenous or inhomogeneous. In an observed NMR lineshape, homogenous broadened lines can't be distinguished from each other as they respond to pulse all together. The origin of homogenous broadening is spin-spin interactions.[55] However, inhomogeneous broadened lines are a "continuum of independent lines", that can be handled individually. Such broadening originates from chemical shift distribution and B_0 inhomogeneity.[55, 70]

The Carr–Purcell spin echo experiment refocuses (removes) the inhomogeneous line broadening coming from all the interactions which are linear in I_z, such as heteronuclear dipolar coupling, 2nd-order quadrupolar coupling and B_0 inhomogeneity. The decay constant in a variable-length spin-echo experiment denoted by T_2' corresponds to Δ' i.e., the non-refocusable linewidth (according to equation 1-33).[55, 70] In liquid state NMR, usually this refocused linewidth is dominated by T_2 relaxation i.e., in liquids, $T_2 = T_2'$. On the other hand, solid-echo experiment removes (refocuses) the broadening arises from terms which are bilinear in I_z, such as homonuclear dipolar couplings and 1st-order quadrupolar couplings.[55, 70] Both Carr-Purcell spin echo and solid-echo experiments can still (and often do) give T_2' which is shorter than the *true* T_2', for example when both bilinear and linear interactions are present or pulse imperfections lead to B_1 inhomogeneity.[55, 70]

In summary, I have described in this subsection how dynamics can be probed using nuclear relaxation and in the following chapters I will be use these concepts.

So far, I have talked about standard methods for NMR in the solid-state, which works beautifully to elucidate structural and dynamic information. It would have been perfect if all those NMR methods performed equally well, irrespective of the type and concentration of nuclei of interest. However, these possibilities only exist in an ideal world. In reality, this is not the case, and there are limits for the usage of NMR to investigate surfaces, interfaces, and others. In the following subsection, I will discuss why this is so.

1.1.4 The Problem of Insensitivity in NMR

In an NMR experiment, bulk nuclear magnetization arising from the sample is measured via perturbing the equilibrium state of magnetization using radio frequency pulses. This bulk magnetization originates from the small magnetic moment associated with nuclear spins. The small magnetic moment makes NMR as intrinsically insensitive technique. As an example, when a spin–½ nucleus with gyromagnetic ratio $\gamma_n > 0$ (in units of Hz/T), is placed in a static magnetic field B_0, the nuclear spin states become non-degenerate and the difference in the corresponding energy states is given by

$$\Delta E = E_{-1/2} - E_{+1/2} = \frac{h\gamma_n B_0}{2} - \left(-\frac{h\gamma_n B_0}{2}\right) = h\gamma_n B_0 \qquad 1\text{-}34$$

Where h is the Planck constant. The populations of these energy states are given by the Boltzmann distribution

$$\frac{N_{+1/2}}{N_{-1/2}} = \frac{\exp\left(\frac{-E_{+1/2}}{k_B T}\right)}{\exp\left(\frac{-E_{-1/2}}{k_B T}\right)} = \exp\left(\frac{-E_{+\frac{1}{2}} + E_{-\frac{1}{2}}}{k_B T}\right) = \exp\left(\frac{-\Delta E}{k_B T}\right) \qquad 1\text{-}35$$

where k_B is the Boltzmann constant and T is the temperature.

The NMR signal is proportional to the polarization which is defined as the net (relative) population difference between the spin states as deduced below:

$$P = \frac{N_{+1/2} - N_{-1/2}}{N_{+1/2} + N_{-1/2}} = \frac{\exp\left(\frac{-E_{+\frac{1}{2}}}{k_B T}\right) - \exp\left(\frac{-E_{-\frac{1}{2}}}{k_B T}\right)}{\exp\left(\frac{-E_{+\frac{1}{2}}}{k_B T}\right) + \exp\left(\frac{-E_{-\frac{1}{2}}}{k_B T}\right)} = \frac{1 - \exp\left(\frac{-E_{-1/2} + E_{+1/2}}{k_B T}\right)}{1 + \exp\left(\frac{-E_{-1/2} + E_{+1/2}}{k_B T}\right)} = \frac{1 - \exp\left(\frac{-\Delta E}{k_B T}\right)}{1 + \exp\left(\frac{-\Delta E}{k_B T}\right)} = \tanh\left(\frac{h\gamma_n B_0}{2k_B T}\right)$$

This polarization depends on the external factors of temperature and applied magnetic field as well as the internal factor of the gyromagnetic ratio. At a moderate magnetic field of 9.4 T and a temperature of 300 K for hydrogen (proton spins) with γ_n = 42.577 $\times$ 10^6 Hz/T, the polarization is P = 3.2 $\times$ 10^{-5}, which is much less than one. This implies that for one million spins, only 32 spins will contribute to the NMR signal. This demonstrates the inherently insensitive nature of NMR spectroscopy. In order to increase the polarization in NMR spectroscopy, it is evident that one either needs to increase the applied magnetic field or decrease the temperature by several orders of magnitude, as shown in Figure 1-6. However, this is not physical to achieve with current technology as the highest achievable magnetic field today is 35 T. Moreover, at extremely low temperatures (~mK) the longitudinal relaxation times of the spins become excessively long which impedes the faster acquisition of NMR spectra.

Therefore, in practice, nuclei cannot be hyperpolarized just by a brute force approach with these unavoidable, major technological challenges.

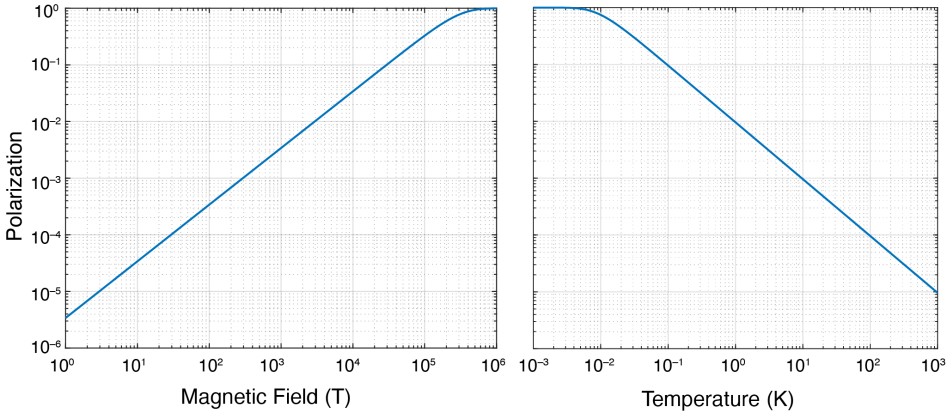

Figure 1-6. ^{1}H spin polarization (left) as a function of magnetic field at 300 K and (right) as a function of temperature at 9.4 T.

In this subsection, I have talked about the insensitivity of NMR and illustrated why it works better for some nuclei than others. I have also mentioned how it is impossible to put all nuclei on an equal footing with current technological advancements. In the next section, I will discuss about how nuclear polarization can be enhanced using other methods.

1.2 Dynamic Nuclear Polarization (DNP)

Various methods have been developed in last two decades to increase nuclear polarization which include spin-exchange optical pumping,[71] parahydrogen-induced polarization,[72] chemically-induced dynamic nuclear polarization,[73] and dynamic nuclear polarization.[74, 75] Dynamic nuclear polarization was first predicted by Overhauser in 1953,[74] who considered that nuclear spins can be polarized using electron spins by exploiting electron–nuclear magnetic interactions. Soon after, Carver and Slichter demonstrated the first DNP phenomenon in lithium metal.[75] These seminal works laid the foundation stone for DNP. However, DNP experiments were limited to low magnetic fields until high power microwave source such as gyrotrons were available to perform DNP at high field.[76-79] Today, MAS DNP methods have been increasingly successful to increase sensitivity and address challenges in structural biology and materials science.[80-86] This method will be used later in this thesis.

Polarization transfer is an important concept in NMR, which exploits the magnetic interactions (either dipolar coupling or J-coupling) among nuclei to enhance the signal from low-γ nuclei by transferring the high polarization from high-γ nuclei. Electrons have a much higher gyromagnetic ratio than nuclear spins (658 times higher than ^{1}H spins), and therefore have a higher polarization, as compared to ^{1}H and ^{13}C in Figure 1-7. If this high electron polarization can be harnessed then a maximum theoretical ^{1}H enhancement can be achieved of

$$\varepsilon = \frac{P_{e^-}}{P_{1_H}} = \frac{\tanh\left(\frac{\gamma_e h B_0}{2 k_B T}\right)}{\tanh\left(\frac{\gamma_n h B_0}{2 k_B T}\right)} = 657.33 \qquad 1\text{-}36$$

This ratio is approximately constant for the realistic temperature ranges >10 K as shown in Figure 1-7. The high electronic polarization is the core of dynamic nuclear polarization methods and the mechanisms by which this high electronic polarization can be harnessed to induce nuclear hyperpolarization will be discussed in the next subsection.

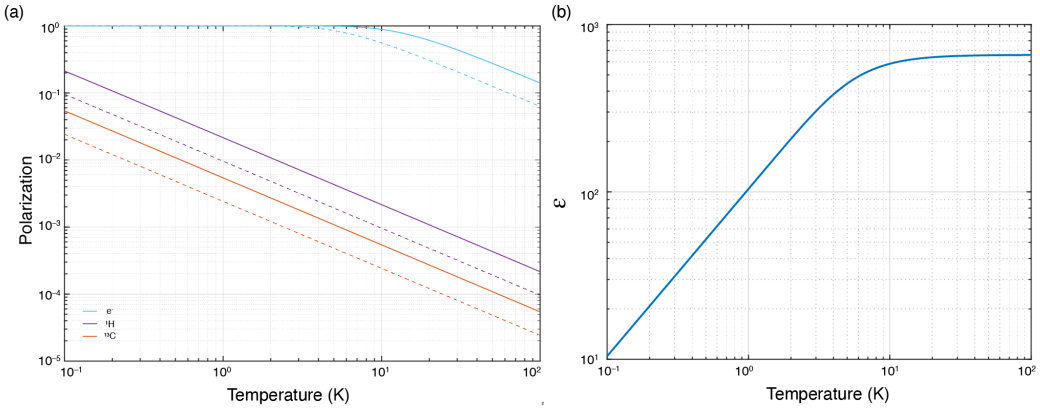

Figure 1-7. Polarization of electron spins, ^{1}H spins and ^{13}C spins as a function of temperature at 9.4 T (dashed lines) and 21.1 (solid lines) (b) Maximum theoretical enhancement (ε) for ^{1}H spins using electron polarization as a function of temperature.

1.2.1 DNP – Mechanisms

The operational mechanism responsible for DNP depends upon the relative magnitudes of three parameters as listed below

1. Larmor frequency of the nucleus – ω_{0I}
2. EPR linewidth (homogenous) – δ
3. EPR linewidth (inhomogeneous) – Δ

Solid Effect (SE)

Solid effect operates when $\omega_{0I} >> \delta$, and $\omega_{0I} >> \Delta$. This is case for, e.g., the trityl radical (Figure 1-8(a); top EPR spectra). Hu et al calculated that for the trityl radical[87], $\delta < \Delta = 42$ MHz with $\omega_{0I} = 210$ MHz at 5T, as shown in Figure 1-8 (a). Under microwave irradiation with frequency ω_{mw}, for an EPR resonance frequency ω_{0S} of the paramagnetic species, the **solid effect** occurs when either $\omega_{mw} = \omega_{0I}$

+ ω_{0S} or $\omega_{mw} = \omega_{0I} - \omega_{0S}$, giving rise to negative and positive enhancements, respectively (Figure 1-8c and Figure 1-8d).The maximum DNP enhancements are achieved at $\pm\omega_{0I}$, 211 MHz away from the center of EPR resonance frequency (ω_{0S}) Figure 1-8a. These matching conditions drive the polarization transfer via quantum mechanically forbidden transitions in the electron-nucleus two-level spin system.

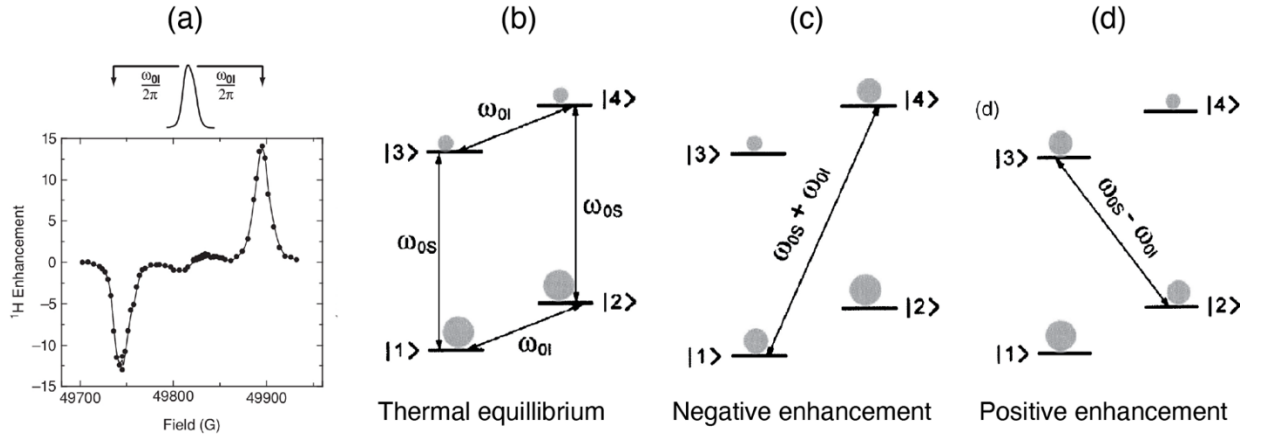

Figure 1-8 ^{1}H enhancement field profile for the solid-effect of the trityl radical; the EPR spectrum of the trityl radical is shown at the top of the figure. Reproduced with permission from original work.[88] Population distribution in the electron–nucleus two-level system for the solid-effect DNP mechanism. (b) Populations in thermal equilibrium with the EPR (vertical) and NMR (oblique) transitions. (c) State of the system after saturating the double-quantum forbidden transition to give a negative enhancement on the nucleus. (d) State of the system after saturating the zero-quantum forbidden transition corresponding to a positive enhancement on the nucleus. Reproduced with permission from the original work.[79]

Cross Effect (CE)

Cross effect operates when $\delta < \omega_{0I} < \Delta$. This is the case for example for the TOTAPOL radical as shown in (Figure 1-9a); top EPR spectra).[88] Contrary to SE, CE occurs due to quantum-mechanically allowed transitions in a three-level spin system. In this scenario, two unpaired electrons are dipolar coupled with a third nuclear spin. The CE matching condition is met when the difference in the resonance frequencies of these two electron spins is matched with the third nuclear spin as

$$\omega_{0I} = \pm \left(\omega_{0S}^{(1)} - \omega_{0S}^{(2)}\right)$$

In this manner, saturation of one of the electron-spins with $\omega_{mw} = \omega_{0S}^{(1)}$ or $\omega_{mw} = \omega_{0S}^{(2)}$, transfers polarization to the third nuclear spin as illustrated in Figure 1-9. Saturating the transition corresponding to states 1–5, 3-7, 2–6, and 4–8 generate negative polarization on the nuclear spins (Figure 1-9c), whereas saturation of other allowed transition 1–3, 2–4, 5–7, and 6–8 results in positive enhancement (Figure 1-9d). In other words, if $\omega_{0S}^{(1)} > \omega_{0S}^{(2)}$, saturation of electron spin '1' gives a negative enhancement and saturation of electron spin '2' gives a positive enhancement.

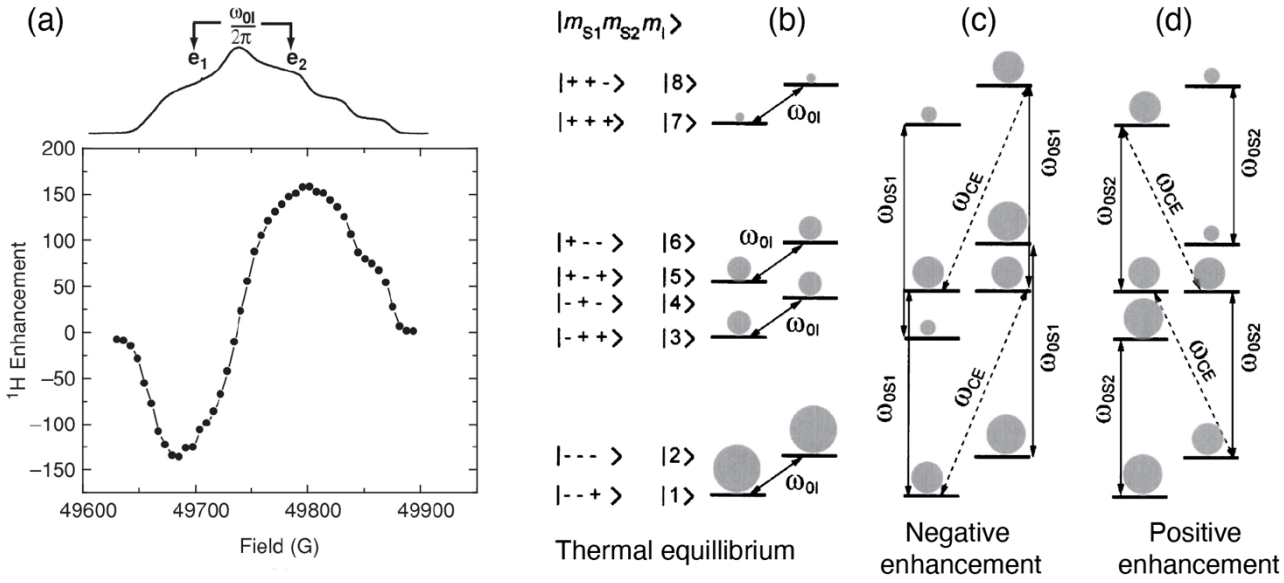

Figure 1-9. ^{1}H enhancement field profile for cross-effect of the TOTAPOL radical. On the top of the figure, the EPR spectrum of the TOTAPOL radical is shown. Reproduced with permission from the original work.[88] Population distribution in the electron-nucleus two-level system for the cross-effect DNP mechanism. (b) Populations in thermal equilibrium with the NMR transitions shown. (c) State of the system after saturating the higher frequency EPR transitions, corresponding to a negative enhancement on the nucleus. (d) State of the system after saturating the lower frequency EPR transitions, corresponding to a positive enhancement on the nucleus. Reproduced with permission from the original work.[79]

Overhauser Effect (OE)

The Overhauser effect operates on an electron–nucleus two-level spin system similar to the SE, however, contrary to the SE, the OE transfers the polarization through saturation of the single quantum EPR transitions $\omega_{mw} = \omega_{0s}$. This saturation perturbs the equilibrium electron population and then polarization is transferred from the electron spins to the nuclear spins by cross relaxation. (Figure 1-10). As in the nuclear Overhauser effect (NOE), the sign of the nuclear enhancement in OE is dictated by the relative magnitudes of the zero-quantum (ZQ) and double-quantum (DQ) rate constants. These DQ and ZQ rates depend upon dipolar and Fermi contact contributions to the hyperfine couplings. This mechanism is observed for metals or liquids as the cross relaxation requires spectral density at the ZQ or DQ frequencies; it is not typically present in insulating solids, which lack motion at sufficiently high frequency. Usually, OE is present at low field however, it has been seen in the BDPA radical and its derivatives at high-fields.[89]

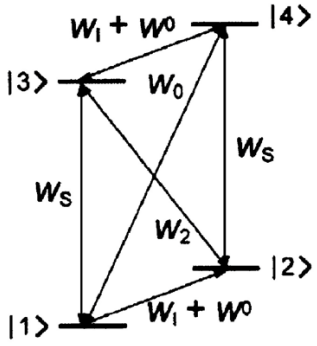

Figure 1-10. Energy level diagram and transition rates for the Overhauser effect. Reproduced with permission form the original work.[79]

In summary, the field profiles for all three mechanisms are shown in the Figure 1-11. There are many excellent reviews for the DNP mechanisms incorporating full quantum mechanical treatments.[88, 90-93] The formalism describing how these DNP mechanisms translate to the case of magic-angle spinning case has been investigated thoroughly and can be found elsewhere.[88, 90-95]

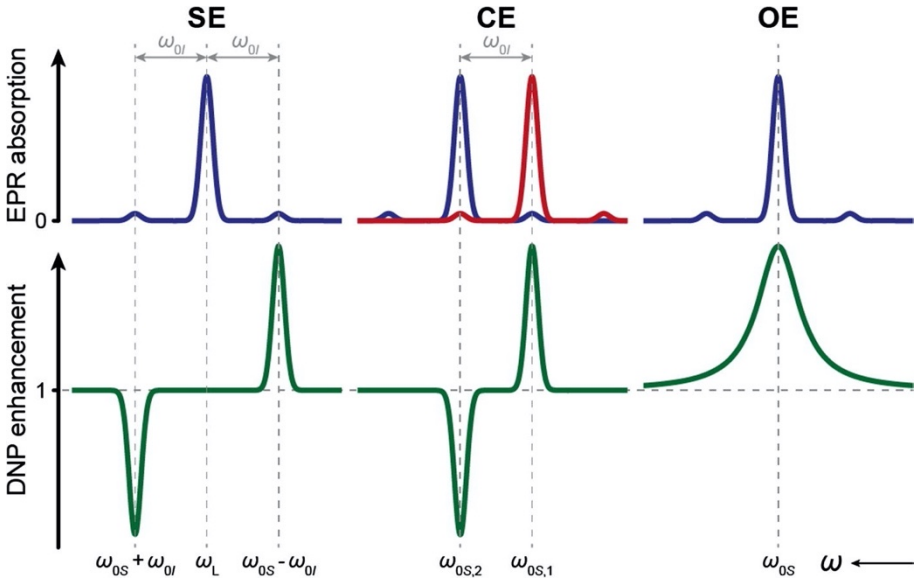

Figure 1-11. Field Profiles for the solid effect (SE), cross effect (CE), and Overhauser effect (OE). Reproduced with permission from the original work.[94]

Enhancement Quantification

The aim of DNP is to hyperpolarize nuclear spins and enhance the NMR signal. Therefore, metrics have been reported to quantify the DNP enhancements in real systems, to compare different polarizing agents, and to rationalize the principles to improve MAS DNP.

In the simplest approach, the DNP enhancement (ε) is measured as the ratio of the peak or integrated signal intensities (I) with and without microwave irradiation:

$$\varepsilon = \frac{I_{ON}}{I_{OFF}} \qquad 1\text{-}37$$

Although this measure shows the change in sensitivity with and without the DNP mechanism, it does not account for the effect of adding the radical to the sample. To compare the sensitivity between a neat sample and the DNP-enhanced spectrum of a sample impregnated with a solution of radicals, there is another quantitative measure of absolute enhancement (Σ) defined as[96]

$$\Sigma = \varepsilon \,.\, \theta \,.\, \sqrt{\frac{T_1}{T_b}} = \varepsilon \,.\, \theta \,.\, \sqrt{\kappa} \qquad 1\text{-}38$$

ε – DNP enhancement;

θ – quenching factor;

T_b – Polarization Build-up time *with* polarizing agent and μw on.

T_1 – Polarization Build-up time *without* polarizing agent and μw off.

In this metric, the quenching factor accounts for loss in signal intensity due to introducing the radical species, via two phenomena. First, the spins closest to the radical are subject to large hyperfine couplings, resulting in large broadening and shifts in frequency. These unobservable spins are known as quenched spins. The second process arises from the cross effect itself. In the cross-effect mechanism, saturation of one of the electron spins transfers the difference in polarization of the electron spins to the nucleus. This mechanism still operates in the microwave off condition, however without saturation of the electron spin, there is very little difference in the electron polarizations and therefore the nuclear polarization is transferred to the electrons, reducing the nuclear polarization. This phenomenon is known as the depolarization effect and has been discussed thoroughly in a number of reviews.[97-99] In this thesis, DNP enhancements are reported using the ratio of integrated intensity as shown in the first part of this section.

In this subsection, I have discussed mechanisms of nuclear hyperpolarization and metrics of this hyperpolarization. In the following subsection, I will discuss briefly the experimental procedures and instrumentation.

1.2.2 DNP – Experiments and Instrumentation

There are two major aspects of DNP experiments which have been developed and optimized in the past decade: the sample preparation and the instrumentation.

Sample Preparation

In a DNP experiment, a high polarization source in the form of an EPR active species is required. These EPR active species can be metal ions, stable radicals, or paramagnetic defects. These paramagnetic species are the source of high polarization in the sample and the manner in which they are introduced in the system affects the efficiency of DNP.

In order to analyze the sample employing DNP methods, the target material is wetted by an incipient wetness impregnation (IWI) method with a solution containing a paramagnetic species, which could be a stable organic radical. The solvent is chosen to be an anti-solvent for the target material so that this step does not perturb the structure of the target analyte. In this thesis, tetrachloroethane (TCE) (Figure 1-12) is used as a solvent.

At high fields, CE typically results in higher enhancements than SE because less microwave power is needed. To optimize the enhancement generated by the CE, various polarizing agents have been developed, adapted for the spinning frequency, magnetic field and temperature. Development of polarizing agents to tailor the magnetic interactions favorably is an active area of research and the guiding principles can be found in the literature.[100-104] In this thesis, the CE mechanism will be utilized at 9.4 T and 21.1 T, with the TEKPOL and HyTEK-2 radicals in TCE, which have been specifically developed for these magnetic fields, respectively (Figure 1-12).[100, 105] The HyTEK-2 radical is a combination of a narrow line radical (BDPA) tethered with a nitroxide moiety. In this radical, the bulkiness of the nitroxide moiety is tailored in such a way that an optimum distance between the two radical is obtained which can increase the electronic relaxation times. [100]

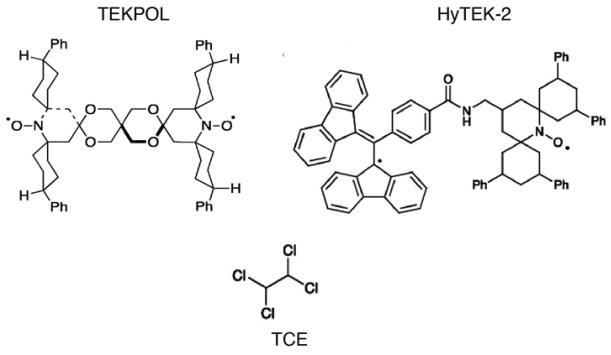

Figure 1-12. Polarization agents and solvent used in this thesis work.

Instrumentation for MAS DNP

In the early years of DNP, the experiments were conducted at low magnetic fields because of the unavailability of high-power microwave sources needed for polarization transfer at high field. However, with the advent of gyrotrons as high-power microwave sources (>20 W output power), DNP at high magnetic fields was introduced by Griffin and coworkers in 1990s.[76, 77, 79] DNP experiments are done at low temperature to slow down the electronic relaxation so that the electrons can be saturated as required in all the DNP mechanisms.

Figure 1-13 shows the components of a commercially available MAS DNP system: (1) Superconducting NMR magnet, (2) MAS cooling system or low-temperature magic angle spinning (LTMAS) cabinet, (3) High-power microwave source – gyrotron with transmission line, (4) LTMAS probe, and (5) Corrugated waveguide. The LTMAS cabinet (2) provides the cold gases to the LTMAS probe (4), which is placed inside the magnet (1) (shown in green in Figure 1-13). The sample temperature is regulated by controlling the flow of the gases and heater powers with the software connected to the spectrometer. The corrugated waveguide (5) (shown in cyan color in Figure 1-13) connects the gyrotron to the stator in the LTMAS probe. The power of the microwaves is controlled through the software and monitored using a calorimeter placed halfway between the probe and the gyrotron. High power microwaves are generated in

the gyrotron using the principle of cyclotron resonance in a magnetic field. A more complete description of MAS DNP instrumentation can be found elsewhere.[106]

Today, there are various commercially available MAS DNP instruments available worldwide for the range of magnetic fields 9.4 – 21.1 T. In this thesis, I will present DNP experiments conducted at 9.4 T and 21.1 T at EPFL.

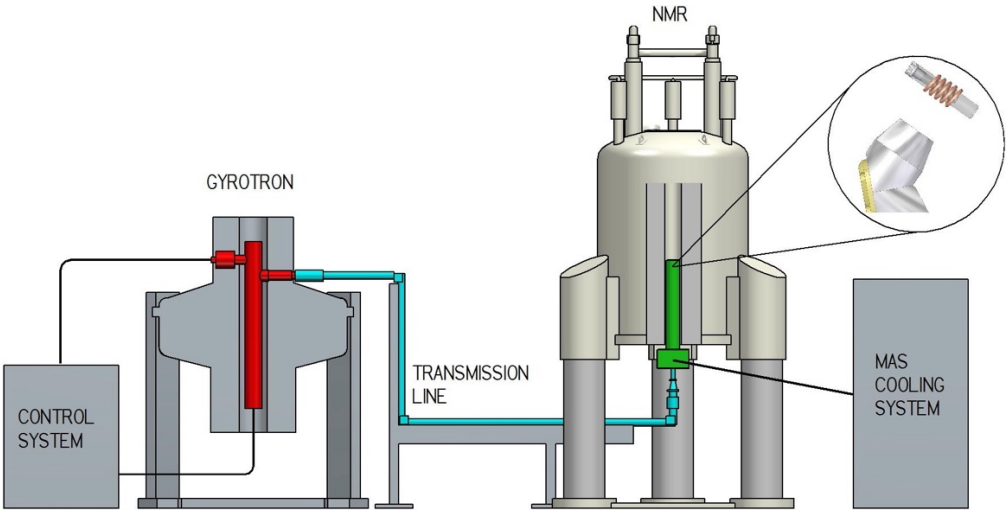

Figure 1-13. Schematic representation of the MAS-DNP system. Reproduced with permission from the original work.[106]

In this subsection, I have described the sample preparation and instrumentation uses in DNP experiments. In the following subsection, I will mention the important concepts that determine the DNP enhancements.

1.2.3 DNP – The Role of Spin-diffusion

As derived in the section 1.1.1, the dipolar coupling Hamiltonian depends upon the gyromagnetic ratio, whether the coupling is homonuclear or heteronuclear, and most importantly the distance between the interacting spins. The secular part of the homonuclear dipolar coupled nuclear spin Hamiltonian can be written as

$$\widehat{H}_{DD} = C_{dipole}\,(1 - 3\cos^2\theta_{ij})(3I_{iz}I_{jz} - \mathbf{I}_J.\mathbf{I}_k) \qquad 1\text{-}39$$

This dipolar coupling is for a static sample. However, in the case of samples spinning at the magic angle $\theta = 54.7°$, the dipolar coupling is averaged out progressively with increasing MAS speed (ν_r) [see section 1.1.1].

The dipolar Hamiltonian (equation 1-39) can be rewritten in terms of shift operators (I^+ and I^-) (equation 1-40); this implies that flip-flop transitions can occur and drive spin diffusion, as discussed below.

$$\widehat{H}_{DD} = C_{dipole}\,(1 - 3\cos^2\theta_{ij})\left(2I_{iz}I_{jz} - \left(\frac{I_i^+I_j^- + I_i^+I_j^-}{2}\right)\right) \qquad 1\text{-}40$$

As the gradient of heat or concentration of a substance in space induces its spontaneous transfer in space, a polarization gradient results in the transfer of polarization in space via spin diffusion. This process occurs because the dipolar Hamiltonian contains flip-flop terms (equation 1-40), often called zero-quantum (ZQ) flip-flop operators. Therefore, spin diffusion requires non-averaged dipolar couplings among spins, as is often the case for protons in solids. These flip-flop transitions are associated with a probability W_{ij} per unit time, which is given in static conditions as[107, 108]

$$W_{ij} = \frac{1}{2}\left(\frac{R_2^{ZQ}}{(\omega_i - \omega_j)^2 - (R_2^{ZQ})^2}\right) d_{ij}^2 \qquad 1\text{-}41$$

where d_{ij} is the coupling constant (C_{dipole}, defined in equation 1-12) between i^{th} and j^{th} spin. In equation 1-41, the bracketed term represents the intensity at zero frequency of the zero-quantum lineshape centered at the difference frequency $\omega_i - \omega_j$, and R_2^{ZQ} is the zero-quantum linewidth, where the lineshape is assumed to be a Lorentzian shape.

However, under MAS, the width of the ZQ lineshape (R_2^{ZQ}) scales inversely with spinning speed.[109, 110] In that case, in order to conserve the area under the ZQ lineshape, the contribution of the ZQ lineshape at zero frequency becomes smaller, reducing the probability of a flip-flop transition.[111]

Both the probability of these flip-flop transitions (W_{ij}) and the distance between the spins are important for spin-diffusion process. The efficiency of spin-diffusion is characterized by a parameter called the "spin-diffusion coefficient" or diffusivity (D). This coefficient is a measure of how fast the polarization is spread in space. D is defined as[68, 111, 112]

$$D = \sum_{i \neq j} W_{ij} . r_{ij}^2 \qquad 1\text{-}42$$

D is typically measured in units of $nm^2.s^{-1}$. The time for polarization transfer to travel a distance r from the source in three-dimensional space is $t = r^2/6D$. Spin diffusion is limited by T_1 relaxation and the characteristic spin-diffusion length is given by $\sqrt{DT_1}$.[113]

Diffusivity for an unknown solid can be estimated from scaling the experimental value from a reference solid. It has been shown that[112] $R_2^{ZQ} \propto r^{-3}\gamma^2$ for abundant high-gamma nuclei, whereas the average distance (r) between two spins with concentration c can be estimated using the Wigner-Seitz radius,[114] which implies that $r \propto c^{-1/3}$. Taken all together the spin-diffusion coefficient (D) follows[108]

$$D \propto \gamma^2 \sqrt[3]{c} \qquad 1\text{-}43$$

The core concept of spin diffusion has already been applied to various kinds of solids such as small molecules,[115, 116] biomolecules,[117, 118] and polymers.[119-122] In this subsection, I explained the concept of spin-diffusion and now in the following subsection, I will describe the how these concepts facilitate the DNP process as used for various applications in material science.

1.2.4 DNP – Applications in Materials Science

After the introduction of gyrotrons as a source of high-power microwave irradiation, the application of DNP methods under MAS at high fields were mostly in the field of biomolecular NMR.[79, 84, 123] In these experiments, biomolecules are dissolved or suspended in the radical containing water-glycerol solution (Figure 1-14a). The water-glycerol works as a cryo-protectant and inhibits formation of radical aggregates and crystallization upon freezing. The sample is packed in a rotor and rapidly cooled down to 100 K to perform DNP experiments. By including the molecule of interest directly in the radical-containing solution, a large DNP effect is observed upon microwave irradiation, enhancing the NMR signals.[79]

However, in many cases it is not possible (or desirable) to dissolve or suspend a material in the radical-containing solution. Instead, the sample must be wetted/impregnated with the solution. This enables the detection of dilute species present on the surface of functional materials, both mesoporous and granular (Figure 1-14b and Figure 1-14c), which is known as DNP surface-enhanced NMR spectroscopy (DNP SENS).[84, 124] This discovery led to application in many areas of material science.[82, 83, 85, 86, 96, 125-129]

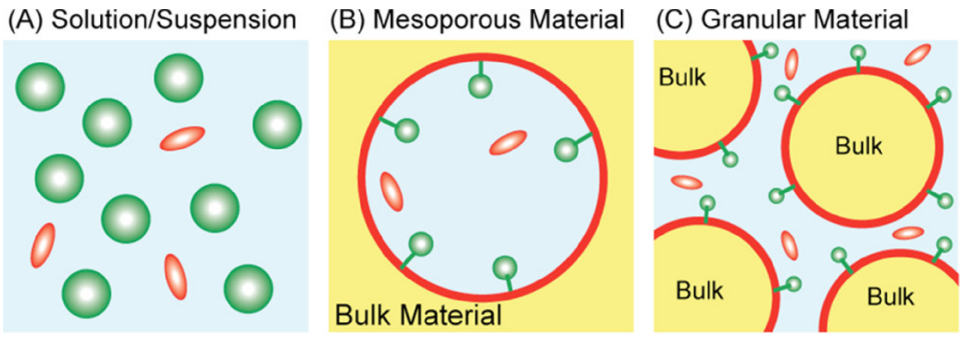

Figure 1-14. Schematic of different ways to introduce polarizing agents for DNP experiments: (a) bulk solution (b) impregnated mesoporous material (c) impregnated non-porous/granular materials. In this figure, red ellipsoids are stable radicals, blue background is the radical containing solution, green spheres are the target analytes, and red lines indicate the surface nuclei. Reproduced with permission from the original article.[84]

DNP Surface-Enhanced NMR Spectroscopy (DNP SENS)

Why is surface structure important?

The properties of many functional materials used for CO_2 capture/conversion, solar energy, gas storage/separation etc. are dictated by their surface structure.[130] For the development of these advanced materials and to rationalize the principles underpinning the properties, atomic-level understanding of the surface structure/sites is necessary. NMR is an invaluable tool to determine the structure of bulk materials at the atomic level. However, often the low surface area of materials and/or the low concentration of dilute species at the surface of material inhibits the use of NMR to detect the surface sites. Heterogeneity at the surface can also result in broad signals. [131, 132] These shortcomings are reflected in very long and impractical acquisition times for an NMR experiment. In order to overcome this limitation, DNP SENS based experimental protocols have been discovered and will be briefly introduced in this section.

Sample preparation

In the quest to analyze the surface structure, surface nuclei are selectively hyperpolarized. Contrary to suspension/dissolution of the sample in the radical-containing solution, in DNP SENS, the target material is wetted by an incipient wetness impregnation method with a stable organic radical containing solution.[84] The solvent is chosen to be an anti-solvent for the target material so that this step does not perturb the target structure. In the case of an organic solvent such as TCE, the sample should be properly degassed using freeze–thaw cycles by inserting and ejecting the rotor in the probe, prior to measurement in order to remove dissolved O_2. In addition, it is recommended to use a small amount of deuterated-EtOH/MeOH to inhibit the crystallization of TCE[133, 134] and to mix a few grains of KBr or sapphire particles in the rotor in order to homogenize the microwave power distribution throughout the sample.[134]

DNP SENS experiments

There are two basic ways to perform DNP SENS experiments

1. Indirect DNP.
2. Direct DNP.

In Direct DNP experiments, the nucleus of interest is hyperpolarized directly by interaction with the radical. In this case, the NMR spectrum is simply acquired in the presence of continuous microwaves as shown in Figure 1-15. This method typically gives a lower enhancement than indirect DNP, due to less efficient DNP polarization transfer and nuclear spin diffusion, but can be used in samples without abundant ^{1}H spins or for which ^{1}H–X polarization transfer is challenging.[135-137]

In Indirect DNP experiments, the hyperpolarization is transferred via abundant ^{1}H spins from the radical to the surface. In this scenario, first the polarization is transferred to the ^{1}H nuclei in the vicinity of the radical. Then this hyperpolarization is propagated farther away through spontaneous ^{1}H-^{1}H spin-diffusion throughout the wetting phase. Finally, the hyperpolarization is transferred to dilute species on the surface via cross-polarization based methods and detected[82-86, 96, 132, 138] (Figure 1-15)

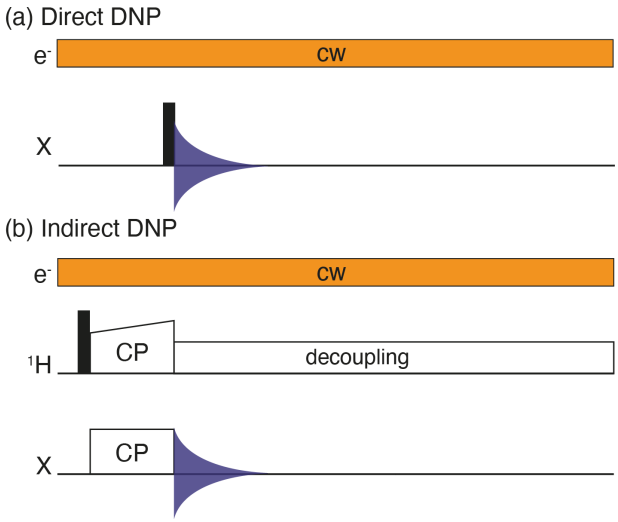

Figure 1-15. DNP Experiments. (a) Direct DNP (b) Indirect DNP.

Applications

DNP SENS has been successfully applied to enhance the sensitivity of NMR experiments for various low-sensitivity nuclei such as ^{13}C,[96] ^{15}N[139] and ^{29}Si,[96, 140] as well as half-integer quadrupolar nuclei such as ^{27}Al[126, 141, 142] and ^{17}O[143-149]. In particular, it has been used to detect the surface species in alumima,[126, 143] and amorphous alumina/silica-based materials for their widespread use in heterogenous catalysis.[141] A number of review articles demonstrate wide applications of DNP SENS in materials science.[83, 84, 132, 138]

Relayed DNP

Solid-state NMR is suitable for bulk characterization of materials, however in the absence of any motion the nuclei can have exceedingly long (min–h) spin lattice relaxation times, especially inorganic solids containing low-gamma and/or low-abundance nuclei. This hampers the use of NMR, due to infeasibly long experimental times from the long magnetization recovery period (on the order of T_1). Relayed DNP can reduce the experimental time significantly by (i) hyperpolarizing the nuclear spins, and (ii) generating polarization faster according to the build-up in the wetting phase. Sample preparation protocols are the same as for DNP SENS.

In relayed DNP, ^1H spins in the wetting phase are hyperpolarized first by DNP and then subsequently spread by ^1H-^1H spin diffusion. In ^1H containing solids, the polarization can be propagated to the bulk via ^1H-^1H spin diffusion. (Figure 1-16a) In non-protonated solids, this high proton polarization from the wetting phase is transferred to nuclei of interest (X) at the surface of the sample with cross polarization methods. The hyperpolarization on the surface nuclei is relayed to the bulk of the particle due to spontaneous spin diffusion (Figure 1-16b). In the case of inorganic solids, pulse cooling methods based upon multiple-contact cross-polarization have been developed to further improve relayed DNP.[150, 151]

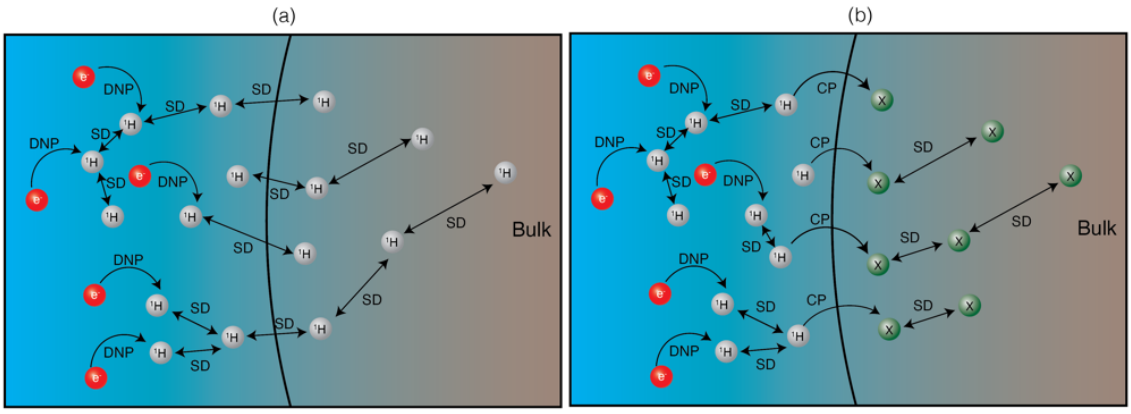

Figure 1-16 Schematic of Relayed DNP in hyperpolarizing (a) a ^1H containing solid, (b) a non-protonated solid. SD = spin diffusion and CP = cross polarization.

Applications

Relayed DNP is necessary to study the bulk of microcrystalline solids where the target analyte cannot be brought closer to the polarizing agents. Relayed DNP is used in various applications such as MOFs,[152, 153] pharmaceuticals,[85, 86, 154] surfactant filled silica,[155] metal substituted zeolites,[156-158] cementitious materials,[159] metal hydroxides,[137] hydroxyapatite,[160] battery materials,[135] wood fibers,[161] and bulk inorganic solids.[135, 150, 151] In this thesis, the concept of relayed DNP has been used to hyperpolarize perovskite materials.

So far, I have talked about the experimental and theoretical concepts of NMR and DNP that will be used later. As the title of my thesis states, I will build on these concepts to develop new methods for perovskites. Now the question arises, what is a perovskite? Why it is important for the research presented in this thesis? In fact, all of this will be the subject of the next section of this chapter.

1.3 Perovskites

In the mineral history, perovskite was first discovered in a piece of chlorite-rich skarn by the Prussian mineralogist Gustav Rose in 1839.[162] The mineral was composed of $CaTiO_3$ and was named after Russian mineralogist Count Lev A. Perobvkiy. Subsequently, many inorganic metal oxides, such as $BaTiO_3$, $PbTiO_3$, $SrTiO_3$, $BiFeO_3$, etc. were also found to have the perovskite structure. Therefore, perovskite compounds were commonly considered as only metal oxides, often with ferroelectric or piezoelectric properties.[163] [163] Perovskite now generally refers to a kind of crystal structure with chemical formula ABX_3, in which A and B are cations and X is an anion. This can be imagined as a cube with the A-cation at the corner positions, the B-cation present at the body-center position, and the X-anion occupying the face-centered positions (Figure 1-17).

Halide perovskites were first investigated by Wells et al. in 1893, where they provided synthesis of the lead halide perovskites employing a Cs^+ cation, i.e. $CsPbX_3$ (X: Cl^-, Br^-, and I^-).[164]

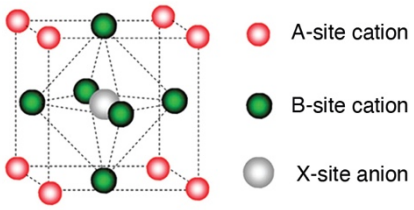

Figure 1-17. Perovskite crystal structure. Reproduced with permission from the original work.[165]

It was not until 2009, that the possibility of using halide perovskites as a sensitizer on the mesoporous TiO_2 in dye-sensitized solar cells (DSSC) was tested.[165] This led to the discovery of the use of halide perovskites as light-absorber materials in the solar cell.[165] Subsequently, halide perovskites have been widely studied using a range of techniques in the last decade or so. These studies have led to improvements in perovskite solar cells, that can now achieve power conversion efficiencies (PCEs) exceeding 25%.[166] These materials have the same ABX_3 structure as oxide perovskites, but monovalent halide ions (Cl^-, Br^-, or I^-) occupy the X sites, monovalent cations occupy the A sites, most commonly cesium (Cs^+), methylammonium – $CH_3NH_3^+$ (MA^+), and formamidinium – $CH(NH_2)_2^+$ (FA^+), and divalent cations occupy the B sites, typically lead (Pb^{2+}) and tin (Sn^{2+}), which are found to have unique optoelectronic properties (Figure 1-18).[167-170] As the lead-based iodide perovskites are the most efficient for solar cell applications,[171] I conducted my research only on lead-based iodide compounds. Nevertheless, I will briefly mention tin-based halide perovskites in the challenges section. These lead iodide perovskite materials possess superior optoelectronic properties in comparison to conventional, covalent semiconductors such as multicrystalline Si or CdTe (Figure 1-19). These properties and their origin have been thoroughly documented elsewhere[172-174] and will not be in the scope of this thesis.

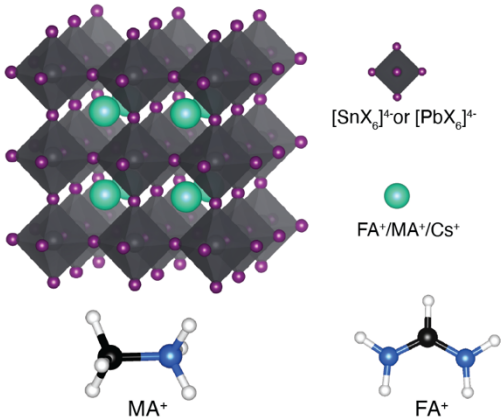

Figure 1-18. Halide perovskite crystal structure and its components with the most commonly employed cations.

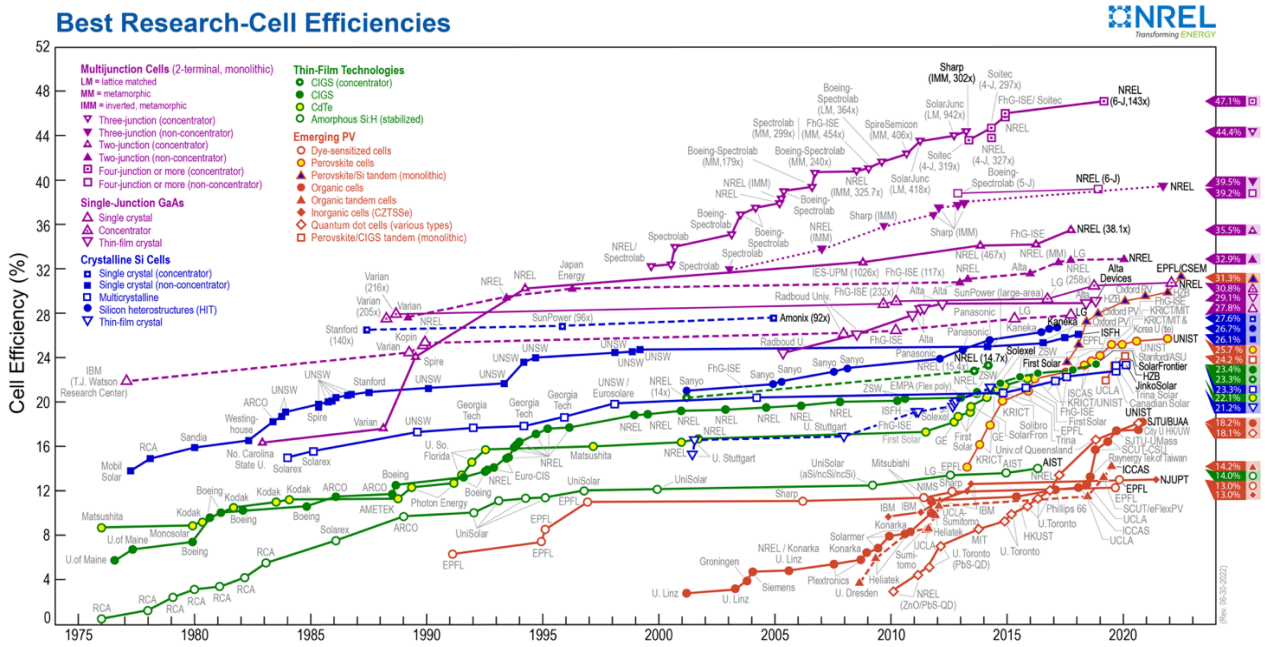

Figure 1-19. National Renewable Energy Laboratory (NREL) chart comparing various solar-cell technologies.[166]

1.3.1 Phase Transitions and Thermodynamic Stability of Halide Perovskites

Phase Transitions

Halide perovskites have been shown to exhibit several structural phase transitions in response to the external conditions such as temperature or pressure. These phase transitions have been studied by a range of techniques including calorimetry, NMR, and neutron scattering. At ambient pressure, these transitions are associated with changes in the optoelectronic properties of the material. Phase transitions of halide perovskites are summarized in the following table.

Table 1-3. Phase transition in the halide perovskite used for optoelectronic applications.

Material	Phase Transition Temperature (K)	Phase Symmetry
$CsPbCl_3$[175-178]	<310 310 – 315 315 – 320 >320	Orthorhombic Orthorhombic Tetragonal Cubic
$CsPbBr_3$[179, 180]	<318 318 – 361 361 – 403 >403	Orthorhombic Orthorhombic Tetragonal Cubic
$CsPbI_3$[167]	<600 (δ ; stable) <448 (γ; metastable) 448 – 533 (β; metastable) >600 (α; stable)	Orthorhombic Orthorhombic Tetragonal Cubic
$FAPbCl_3$[181]	<258 258 – 271 >271	Orthorhombic unknown Cubic
$FAPbBr_3$[181]	<153 153 – 265 >265	Orthorhombic Tetragonal Cubic
$FAPbI_3$[182-184]	<433 (δ) <140 (γ) 240 – 285 (β) >285 (α; metastable)	Hexagonal Tetragonal Tetragonal Cubic
$MAPbCl_3$[185, 186]	<171 171 – 177 >177	Orthorhombic Tetragonal Cubic
$MAPbBr_3$[185, 186]	<148 148 – 154 154 – 235 >235	Orthorhombic Tetragonal Tetragonal Cubic
$MAPbI_3$[185, 186]	<163 163 – 326 >326	Orthorhombic Tetragonal Cubic

Tolerance Factor and Stability

The empirical index which determines the stability of the ABX_3 perovskite structure is called the Goldschmidt tolerance factor, which is given by[187, 188]

$$t = \frac{r_A + r_X}{\sqrt{2}(r_B + r_X)} \qquad 1\text{-}44$$

where r_A, r_B and r_X are the ionic radii of the A-cation, B-cation and X-anion, respectively. A value of *t* between 0.9 and 1.0 favors the three-dimensional cubic crystal structure. As listed above, the choice of cations and anions are Cs^+, FA^+ and MA^+ as the A-site cation, Pb^{2+} and Sn^{2+} as the B-site cation, and I^-, Cl^- and Br^- as the X-site anion. Out of all possible combinations, the most widely used are $MAPbI_3$, $FAPbI_3$, and $CsPbI_3$, given their close to optimum properties for solar cell applications, and therefore will be the main subject this thesis. However, the bromide- and chloride-based higher band gap materials are also used for tandem applications. Using the ionic radii of the various cations listed in the table, $MAPbI_3$, $FAPbI_3$ and $CsPbI_3$ have tolerance factors of 0.9, 1.0, and 0.8, respectively.

Table 1-4. Ionic radii of commonly used ions in the halide perovskites[188]

Ions	Radius (Å)
FA^+	2.53
MA^+	2.17
GUA^+	2.78
Cs^+	1.67
DMA^+	2.67
Pb^{2+}	1.19
I^-	2.20
Br^-	1.96
Cl^-	1.81

1.3.2 Current Challenges

Today, halide perovskites are the subject of research interest of many research groups throughout the world, to overcome the obstacles to commercializing the perovskite technology for the solar cell market.[189] This requires an understanding of the structure, crystallization, optical and electronic properties, stability and efficiency.

With the intense research efforts of the last decade, out of the three most common single-cation lead iodide perovskites, i.e., $MAPbI_3$, $FAPbI_3$ and $CsPbI_3$, $FAPbI_3$ is the most efficient solar cell absorber material as its band gap (E_g = 1.45 eV) is close to the optimum for a single-junction. FA^+ is stable up to 170°C and is not as volatile as MA^+, which is not thermally stable and exhibits various degradation pathways. Furthermore, Cs^+-based iodide perovskites are not thermodynamically stable at room temperature and transition to the non-perovskite δ-$CsPbI_3$ phase, although it is the most stable at elevated temperatures among contemporary candidates. Therefore, FA^+ has fewer intrinsic limitations than Cs^+ and MA^+.

However, $FAPbI_3$ also offers further challenges as its photoactive α-$FAPbI_3$ phase is a metastable phase which can transform into hexagonal δ-$FAPbI_3$. Currently, the highest achievable solar cell efficiencies using $FAPbI_3$ use a small amount of doping with MA^+, Br, Cl^-, and/or Cs^+. These systematic manipulations all slightly reduce the high tolerance factor of $FAPbI_3$, bringing it closer to the optimum value with minimal effect on the electronic structure of the material. To make highly efficient and stable $FAPbI_3$ based perovskite solar cells, a series of efforts have been made and documented in various reviews.[190, 191]

Band gap tunability is one of the most useful properties of halide perovskite which occurs with appropriate mixing of halide precursors. However, it is well established that mixed halide compositions segregate upon light-illumination and form domains with higher concentrations of each halide. The characteristics of the halide segregation have been the subject of various research works which include the determination of rate constants and concentration-dependent halide segregation. A few works also reported how to minimize these detrimental phenomena. For example, Nandi et al. showed that the Cs^+/FA^+ alloyed mixed-halide composition is most robust against light-induced phase segregation.[192]

Lead-based halide perovskites show impressive solar cell conversion efficiency; however, the toxicity and water solubility of the lead remains a concern for the commercialization of perovskite solar cells. In this regard, Sn^{2+} has also emerged as a suitable B-site cation, and $FASnI_3$ perovskite has an appropriate band gap of ~1.4 eV. However, tin-based perovskites suffer from the spontaneous oxidation of Sn^{2+} to Sn^{4+} in ambient air.[193] Various research efforts have been put into suppressing this oxidation, which has been the subject of several review articles.[194-197] Currently the highest power conversion efficiency of a tin-based solar cell is 14.80% using $FASnI_3$ with fluorinated phenyl ethylammonium ($FPEA^+$) in a heterogenous 2D/3D architecture.[198]

The most important concern for 3D halide perovskites is their inferior long-term operational stability, which hampers their use in practical applications. The most promising 3D perovskite, $FAPbI_3$ is not stable in ambient air and transforms to non-perovskite phases as shown in Table 1-3 Moreover, in response to heat, moisture, or light, the photoactive phase can degrade to the precursor compounds or form elemental lead and lose I_2. To improve the operational stability of halide perovskites, various strategies have been used to date, the most common being surface surface and bulk passivation, use of layered perovskites, compositional engineering and encapsulation.

1.3.3 NMR for Perovskite Research

NMR was used to study halide perovskites before their use in solar cell applications in 2009. In 1985, Wasylishen *et al* determined the motional correlation time of the methylammonium ion with static ^{2}H and ^{14}N experiments on methylammonium lead halides[186] and Qiang et al. studied molecular motion and phase transitions of different methylammonium lead halides with ^{1}H NMR and halide NQR in 1991.[199] However, with the growing interest in metal halide perovskites in the materials science field and the quest to rationalize the atomic-level principles behind the exceptional properties of halide perovskites, there have been several NMR-focused studies of hybrid perovskites in recent years. In many cases, solid-state NMR is the only technique that can determine the local structure of these polycrystalline materials, particularly in the cases where the three-dimensional perovskite structure is either doped with elemental or molecular ions or passivated with small organic molecules. These doping and passivation strategies have been used to manipulate the properties of halide perovskites and achieve record solar cell efficiencies of more than 25%. Solid-state NMR has been used to determine cation incorporation,[200-205] phase composition,[203] cation dynamics,[182, 185, 186, 206, 207] atomic-level proximities between various moieties,[208] halide mixing, [209-212] incorporation of paramagnetic dopants,[202, 204] the presence of intermediate phase during growth,[205] phase transitions,[208, 213-215] and cation disorder.[216] These studies have been very well summarized in recent reviews.[21-24, 217] Some of these particular breakthroughs have been possible with the advent of current state-of-the-art NMR instrumentation including the development of fast-spinning and low temperature magic angle spinning probes. Today, many researchers in the solid-state NMR field have contributed towards the understanding of structure–activity relationships in halide perovskites.

1.3.4 Layered Perovskites

As perovskite stability is one of the major concerns preventing the commercialization of halide perovskites,[189] layered perovskites have been considered as an alternative for the solar cell absorber layer. In 2014, Smith et al. showed that layered two-dimensional perovskite-based absorber layers show greater resilience towards ambient air and provide more stability.[218]

The most commonly studied lower dimensional perovskites for optoelectronic applications are the Ruddlesden-Popper (RP) and Dion-Jacobson (DJ) two-dimensional (2D) perovskites.

The RP 2D perovskites are composed of alternating organic and inorganic layers, with the general formula $A_2A'_{n-1}B_nX_{3n+1}$ in which A is the long organic cation with only one anchoring functional group (usually ammonium) separated with lead halide octahedra layers. B is the central metal cation of the octahedra, usually B is either Pb^{2+} or Sn^{2+}, and A' is the central cation in the cuboctahedral cavity[219]. This family of materials has been classified by the number of inorganic layers per organic layer, *n*, as shown in Figure 1-20.

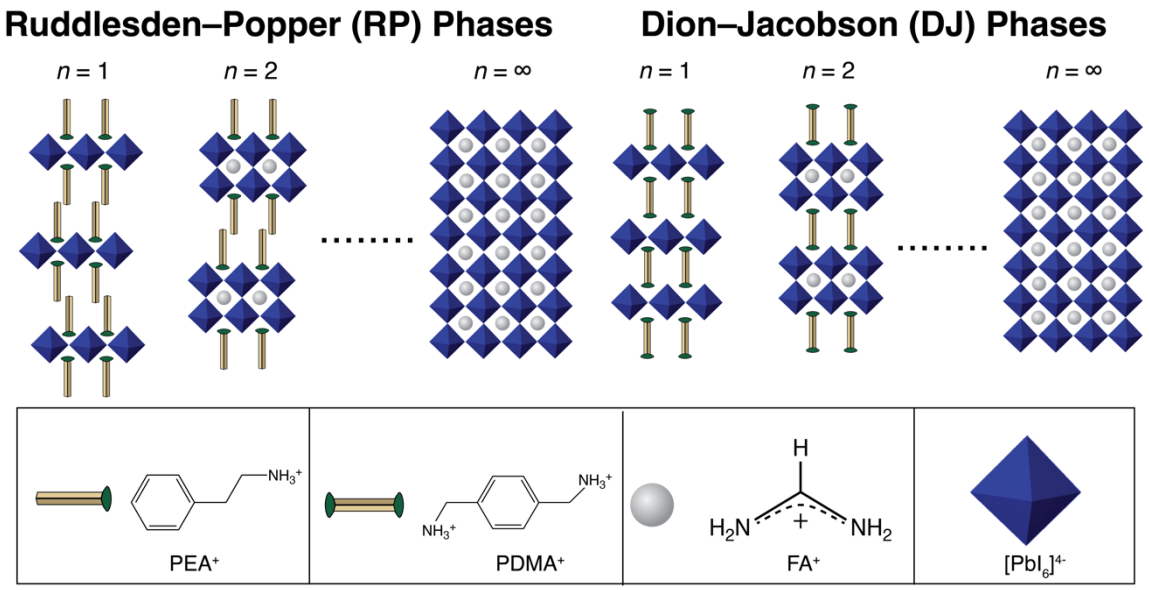

Figure 1-20 Ruddlesden–Popper (RP) and Dion–Jacobson (DJ) two dimensional perovskites.

In contrast, in DJ two-dimensional perovskites, there are A-organic cations with anchoring functional groups (usually ammonium) at both ends which separate the lead halide octahedra layers, resulting in the formula $AA'_{n-1}B_nX_{3n+1}$.[220] This modification can remove

the van del Waals gap between the layers depending upon the length of the cation as shown in Figure 1-20. The other optical and electronic properties of the layered hybrid perovskites have been documented elsewhere.[219, 221-231]

In these layered hybrid perovskite systems, the structure of the organic layer dictates the property of the material.[221] It has been shown that non-covalent interactions within the organic layers can be favorably tuned to improve the functional properties of the materials.[215, 227, 228, 232] In order to favorably tune the interactions in real systems, the atomic level structure of the organic layer needs to be determined. However, these materials offer several challenges to grow single crystals, which limits the utility of diffraction-based techniques. Moreover, the presence of the heavy atoms masks the signatures from the organic layers. In contrast, solid-state NMR methods are well-suited to determine the organic structure, which will be the discussed in the Chapter 2 of this thesis.

1.4 Thesis Outline

In this chapter, I have introduced perovskites and the toolkits of NMR and DNP methodology.

Chapter 2 deals with the *Atomic-level Structure of Hybrid Perovskites*. This chapter is divided into five sections 2.1-2.5. The first two sections focus on new NMR methodologies to study perovskites. Section 2.1 presents the atomic-level structure of DMA^+ doped $CsPbI_3$ perovskite. In this, we show that mixed-cation $Cs_xDMA_{1-x}PbI_3$ only forms when it is kinetically trapped by rapid antisolvent-induced crystallization. Here, we use ^{133}Cs and ^{13}C MAS NMR to show that solid-solutions are thermodynamically unstable and their synthesis under thermodynamic control leads to segregated phases of $DMAPbI_3$ and $CsPbI_3$. In section 2.2, we show how MAS NMR can be combined with computational methods to give the structure of the organic layer in Ruddlesden–Popper based hybrid perovskites. In particular, we demonstrate the use of NMR crystallography in determining the structure of layered hybrid perovskites for a mixed-spacer model composed of 2-phenylethylammonium (PEA^+) and 2-(perfluorophenyl)ethylammonium (FEA^+) moieties, revealing nanoscale phase segregation. We illustrate the application of this structure in perovskite solar cells with power conversion efficiencies that exceed 21%, with enhanced operational stability. The last three sections (2.3–2.5) are application focused, with NMR providing vital guidance on the underlying structure. Section 2.3 presents ^{13}C and ^{207}Pb MAS NMR results which confirm the hypothesis that formate ions passivate defects in $FAPbI_3$, resulting in a solar cell with a record power conversion efficiency. Section 2.4 identifies MA^+ and establishes its atomic-level contacts with FA^+ following the MASCN vapor-assisted perovskite growth. Further, ^{14}N MAS NMR was used to probe the cuboctahedral symmetry of the cation. Finally, in Section 2.5, intermediate-phase engineered $CsPbBr_3$ inorganic perovskite growth was studied. In this, the possibility of incorporation of FA^+ ions in the $CsPbBr_3$ lattice was systematically investigated. Further, the effect of temperature was studied in combination with solution-state NMR. A structural model emerged from these NMR results that provided the link to the improved interfacial contacts in the inorganic perovskite solar cell. In these works, the studied perovskite compositions have enabled highly efficient and stable solar cells in the current literature.

Chapter 3 describes *Dynamics in Hybrid Perovskites*. It presents a complete quantitative picture of cation dynamics for formamidinium based perovskites and contemporary mixed-cation compositions, which are the most prominent solar cell absorber materials today. We used ^2H and ^{14}N quadrupolar solid-state NMR relaxometry under MAS to determine the activation energies (E_a) and correlation times (τ_c) at room temperature for rotation about each principal axis of a series of organic cations. We found that FA^+, MA^+ and GUA^+ all have at least one component of rotation on the picosecond timescale at room temperature, with MA^+ and GUA^+ also having a faster and a slower component, respectively. FA^+ rotation is invariant across all compositions i.e., $FAPbI_3$, $FA_xCs_{1-x-y}MA_yPbI_3$, $FA_xMA_{1-x}PbI_3$. This precise picture that we present will enable better understanding of the relationship between the molecular cations and the optoelectronic properties in hybrid perovskites.

Chapter 4 concerns *DNP in Hybrid Perovskites*. It describes how DNP enables the structure of the surface layer on a perovskite thin-film to be determined. Surface and bulk molecular modulators are often heterogeneous and present with very low sample mass, impeding the use of solid-state NMR on thin films and hampering its utility to establish structure–activity relationships. In this work, we have determined the factors that limit the efficiency of DNP NMR for perovskites by systematically studying a layered perovskite system. We found that the fast-relaxing cation is the major impediment for high DNP efficiency, while microwave absorption and particle morphology also play a secondary role. We found that the former can be mitigated by optimally deuterating the cations, which provides enhancement factors up to 100 that can be harnessed to detect a surface layer on a single thin film. This work extends DNP-enhanced solid-state NMR methods to characterize the local structure of additives and surface treatments for technologically relevant perovskite thin-film compositions.

Chapter 5 summarizes the results obtained in this thesis and provides future prospects for the utilization of NMR and DNP methods in the field of halide perovskites.

Chapter 2 Atomic-level Structure of Perovskites

2.1 Dimethylammonium Incorporation in the $CsPbI_3$ Lattice

This section has been adapted from the following work with the permission from the journal:

Mishra, A.; Kubicki, D. J.; Boziki, A.; Chavan, R. D.; Dankl, M.; Mladenović, M.; Prochowicz, D.; Grey, C. P.; Rothlisberger, U.; Emsley, L., Interplay of Kinetic and Thermodynamic Reaction Control Explains Incorporation of Dimethylammonium Iodide into $CsPbI_3$. *ACS Energy Lett.* **2022**, 2745–2752.

Contribution statement: I designed, conducted, analyzed, interpreted and wrote up the solid-state NMR experiments together with DJK and LE. I collaborated on correcting the whole final manuscript.

Thermal stability of hybrid perovskites has been a major bottleneck due to the volatility of the organic components at elevated temperatures, which leads to irreversible degradation of device performance over time.[233-237] All-inorganic PSC based on cesium lead halides have attracted significant attention owing to their higher thermal stability and have reached PCEs on the order of 20%, albeit typically with various organic additives.[169, 204, 238-244] $CsPbI_3$ has been identified as one of the most promising solar cell materials due to its bandgap (E_g = 1.71 eV) which is close to the radiative efficiency limit.[169, 245] However, its perovskite α phase (*Pm*-3*m*) is thermodynamically stable only above ca. 300°C. On cooling, it transforms first to the tetragonal β phase (P_4/mbm) and then the orthorhombic γ phase (*Pbnm*) with distorted corner-sharing octahedra (Figure 2-1).[167, 169, 246] The metastable perovskite phase (γ-$CsPbI_3$) has been stabilized using several strategies to date to enable its use in optoelectronic devices. These strategies include incorporating Br^- and F^-,[204, 242, 247-249] solvent-controlled growth,[250, 251] the use of intermediate phases,[205] doping with metal ions such as Bi^{3+},[252, 253] Sn^{2+},[248] Sb^{2+},[254] and Eu^{2+},[204, 255] passivation with small organic molecules,[256-258] and addition of hydroiodic acid (HI) to the precursor solution.[240, 259, 260] The last strategy has been remarkably successful and has been adopted as the primary method to fabricate all-inorganic PSCs based on $CsPbI_3$.[261-263] In 2018, Ke *et al*. reported that the addition of HI catalyzes the acidic hydrolysis of the commonly used solvent, dimethylformamide (DMF), leading to dimethylammonium (DMA) as a degradation product. DMA was thought to incorporate into the perovskite structure as an A-site cation leading to $DMA_xCs_{1-x}PbI_3$ phases.[260] Further, Wang *et al*. showed that DMA can affect $CsPbI_3$ crystallization kinetics and thin film morphology.[263] DMA has also been used in hybrid PSC in an attempt to modulate electronic properties,[264] stability,[261-263, 265] and efficiency.[260-263] However, the speciation and microscopic mechanism of action of DMA in mixtures with $CsPbI_3$ in the solid state have been elusive. More recently, Marshall *et al*. concluded that mixed-cation $DMA_xCs_{1-x}PbI_3$ phases form using a combination of optical spectroscopies and XRD.[266] Recent progress in characterizing the role of DMA in perovskite solar cells has recently been reviewed.[267] While those techniques provide insight into the long-range structure and bulk properties of materials, there is a critical need to investigate the local structure of the individual components to assess their structure and role at the atomic level.

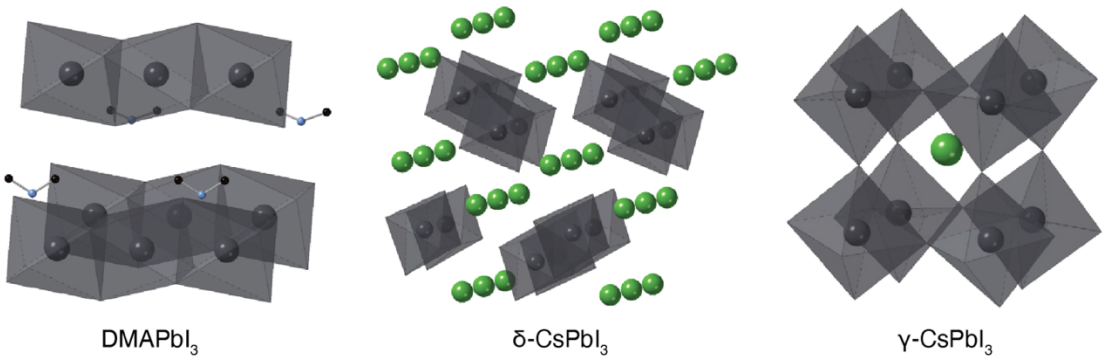

Figure 2-1 Crystal structures of the compositional endmembers ($DMAPbI_3$, δ-$CsPbI_3$, and γ-$CsPbI_3$) showing the PbI_6 connected octahedra in grey, Cs^+ in green, and DMA cations (C – black, N – blue).

Solid-state NMR spectroscopy has emerged as a powerful local structure characterization technique to determine the speciation of dopants.[22-24] Here we use it to show that the formation of mixed-cation iodoplumbates of DMA and Cs, i.e., compositions with the nominal formula $DMA_xCs_{1-x}PbI_3$, is determined by an interplay of kinetic and thermodynamic reaction control factors. We experimentally show that thermodynamic reaction conditions (mechanosynthesis, solution processing without an antisolvent) lead to materials completely segregated into δ-$CsPbI_3$ and $DMAPbI_3$, while kinetic reaction control (spin coating with rapid crystallization induced by antisolvent dripping) leads to a mixed-cation solid solution. From this, we conclude that the atomic-level mechanism of γ-$CsPbI_3$ stabilization with DMAI in thin films processed with an antisolvent involves incorporation of DMA into the perovskite structure. We elucidate and rationalize the composition of the resulting materials using a combination of long-range (X-ray diffraction) and local structure (solid-state NMR) probes, and density functional theory (DFT) based calculations and molecular dynamics (MD) simulations.

Now, I will mention the experimental details followed by the results and discussion.

2.1.1 Experimental

Materials. The following materials were used: dimethylammonium iodide (TCI, >98%), CsI (Sigma, 99.9%), PbI_2 (Sigma, 99%), chlorobenzene (Sigma, anhydrous 99.8%), diethyl ether (Sigma, 99.9%), anhydrous N,N-dimethylformamide (Sigma, 99.8%), dimethyl sulfoxide (Sigma, 99.9%).

Perovskite mechanosynthesis. The materials were prepared using mechanosynthesis following the previously published protocol[268], which was as follows. The precursors were stored and weighed out (±1 mg) into either an agate grinding jar (10 mL) containing an agate ball (⌀10 mm) or 2 mL polypropylene (PP) Eppendorf vial containing a stainless steel (⌀4 mm) ball under argon. We found that both types of grinding vessels lead to the same products, but the latter introduces trace amounts of PP through abrasion, which lead to background in the ^{13}C cross-polarization (CP)[269] spectra. The following stoichiometries were used:

$CsPbI_3$: CsI (129.9 mg, 0.50 mmol), and PbI_2 (230.5 mg, 0.50 mmol),
$DMA_{0.01}Cs_{0.99}PbI_3$: DMAI (0.9 mg, 0.005 mmol), CsI (128.6 mg, 0.495 mmol), and PbI_2 (230.5 mg, 0.50 mmol),
$DMA_{0.10}Cs_{0.90}PbI_3$: DMAI (8.7 mg, 0.05 mmol), CsI (116.9 mg, 0.45 mmol), and PbI_2 (230.5 mg, 0.50 mmol),
$DMA_{0.30}Cs_{0.70}PbI_3$: DMAI (26.0 mg, 0.15 mmol), CsI (90.9 mg, 0.35 mmol), and PbI_2 (230.5 mg, 0.50 mmol),
$DMA_{0.50}Cs_{0.70}PbI_3$: DMAI (43.4 mg, 0.25 mmol), CsI (65.0 mg, 0.25 mmol), and PbI_2 (230.5 mg, 0.50 mmol),
$DMA_{0.70}Cs_{0.70}PbI_3$: DMAI (60.6 mg, 0.35 mmol), CsI (39.0 mg, 0.15 mmol), and PbI_2 (230.5 mg, 0.50 mmol),
$DMAPbI_3$: DMAI (86.5 mg, 0.5 mmol), and PbI_2 (230.5 mg, 0.50 mmol).

The combined precursors were ground in an electric ball mill (Retsch MM−400) for 30 minutes at a vibration frequency of 25 Hz. The resulting powders were scraped off the walls of the grinding jars, transferred into glass vials and annealed for 5 minutes at 100°C to remove grinding-induced defects. In the case of $CsPbI_3$, the annealing temperature was 300 °C to induce the phase transition to the metastable perovskite phase, the sample was heated directly in a rotor using a hot-air blower outside the magnet and quickly transferred to the NMR probe for measurements. The annealing temperature was monitored by attaching the rotor to a thermocouple. Karmakar et al.[210] have previously found that the half-life of the γ phase prepared in this way is on the order of 30 minutes (see Figure S8 therein), and our experience corroborates this result.

Precursor solution preparation. $Cs_{0.8}DMA_{0.2}PbI_3$ perovskite solution was prepared by dissolving CsI (208 mg), DMAI (34.6 mg) and PbI_2 (461 mg) in 1 mL of DMF:DMSO solution (4:1, v/v). The solution was stirred in a nitrogen glovebox at room temperature for 1 hour.

Deposition of solution processed $DMA_{0.2}Cs_{0.8}PbI_3$ (drop cast, without antisolvent). 2 mL of the precursor solution were drop cast using a pipette onto microscope slides kept at 100°C on a hot plate inside an argon glovebox. The solution was allowed to evaporate over 20 minutes and the dry yellow powder was scraped off and packed into a rotor.

Deposition of solution processed $DMA_{0.2}Cs_{0.8}PbI_3$ (spin-coated, with antisolvent). Pre-cleaned FTO glasses were treated with UV-ozone for 15 min. and annealed at 150°C for 60 min. The deposition process and subsequent handling were carried out inside an argon glove box. The perovskite solution was spin-coated onto the substrate at 1000 rpm for 10 s and continuously at 3000 rpm for 30 s. The antisolvent (CB, 200 µl) was dropped on the spinning substrate during the second spin-coating step at 15 s before the end of the procedure, followed by annealing at 100°C for 5 min. The resulting black material was scraped off of the substrates (25 substrates in total) using a razor blade and transferred into a rotor. The sealed rotor was transported from the glovebox to the spectrometer inside an air-tight Schlenk flask and only exposed to ambient air for <1 minute, the time needed to load it into the probe where it was in

dry nitrogen atmosphere. Despite these precautions, we found that the black perovskite phase transitioned to the non-perovskite yellow polymorph within 3-4 hours after starting the NMR measurement (Figure 2-5).

Antisolvent optimization. To fabricate stable high-quality black perovskite films, we tested two deposition approaches, with and without an antisolvent. We found that films fabricated without the use of an antisolvent do not form the black phase. We tested two antisolvents, chlorobenzene (CB) and diethyl ether (DEE). In our hands, the use of CB led to more stable and high-quality black films of $DMA_{0.2}Cs_{0.8}PbI_3$ compared to DEE.

Optimization of annealing temperature. We tested 3 approaches, all carried out inside a nitrogen glovebox:

1. Two-step annealing – the films were annealed for 2 min. at 60°C and then 5 min at 100 °C on a hot plate. In this method, the films were not sufficiently stable (black phase retained about 1 hour)
2. High-temperature annealing - the films were annealed for 2 min at 100°C and then 5 min at 180°C on a hot plate. After the first step, the films were stable but after applying high temperature (180°C), rapid films degradation started due to decomposition of the organic component (DMA^+). This result suggests that the high temperature (180°C) is not suitable for the $DMA_{0.2}Cs_{0.8}PbI_3$ composition, in agreement with previous reports.
3. One-step annealing – the films were annealed for 5 min at 100°C on a hot plate. In this method, the black phase was stable for at least 24 hours. This protocol was used to fabricate the films used in the solid-state NMR experiment. 25 films were fabricated and used in total.

Powder X-ray diffraction. Powder X-ray diffraction patterns were recorded on an X'Pert MPD PRO (Panalytical) diffractometer equipped with a ceramic tube (Cu anode, λ = 1.54060 Å), a secondary graphite (002) monochromator and an RTMS X'Celerator (Panalytical) in an angle range of 2θ = 5° to 40°, by step scanning with a step of 0.02 degree.

NMR measurements. Solid-state MAS NMR spectra of ^{133}Cs (52.6 MHz) were recorded on a Bruker Avance III 9.4 T spectrometer equipped with a 4 mm MAS probe using 62.5 kHz RF field amplitude or a Bruker Avance III 11.7 T spectrometer equipped with a 3.2 mm MAS probe using 50 kHz RF field amplitude (Table 2-1) and referenced to solid CsI (271.05 ppm). The recycle delays to obtain quantitative spectra were set based on the previously measured T_1 values and are given in Table 2-1. Room-temperature ^{13}C MAS and $^1H \rightarrow ^{13}C$ (100.9 MHz) CP MAS spectra were recorded on a Bruker Avance III 9.4 T spectrometer equipped with a 4.0 mm CPMAS probe and referenced to solid adamantane (38.48 ppm for the CH_2 signal). 80 kHz ^1H decoupling was used. The rotors were spun using dry nitrogen.

2.1.2 Results and Discussion

We first focus our attention on compositions corresponding to the nominal formula $DMA_xCs_{1-x}PbI_3$ (x = 0.01, 0.10, 0.30, 0.50, 0.70, 1.0) prepared using solid-state mechanosynthesis followed by high-temperature annealing (see experimental section). All the resulting polycrystalline powders were yellow. Powder X-ray diffraction (pXRD) data show that the mixed DMA/Cs samples are mixtures of two non-perovskite hexagonal phases: $DMAPbI_3$ and δ-$CsPbI_3$ (Figure 2-2a). The composition-dependent evolution can be readily followed in the 2θ = 9-12° region where δ-$CsPbI_3$ yields reflections at 9.8° and 10.0° while $DMAPbI_3$ has a reflection at 11.6°. The diffractograms of mixed DMA/Cs compositions correspond to mixtures of δ-$CsPbI_3$ and $DMAPbI_3$, with no new phases being present.

To gain a more detailed picture of Cs/DMA mixing, we elucidate the local structure of Cs and DMA using magic-angle-spinning (MAS) ^{133}Cs and ^{13}C solid-state NMR, respectively. ^{133}Cs NMR is particularly useful for studying Cs-containing metal halide perovskites (MHPs) as it can be used to evidence Cs incorporation into hybrid MHPs[200] since its shift strongly depends on the structure topology and halide composition.[210]

Figure 2-2b shows the ^{133}Cs MAS NMR spectra of the materials. The reference $CsPbI_3$ sample was annealed at 300 °C before the measurement to capture the metastable γ perovskite phase (158 ppm). The transformation back to the hexagonal δ phase (240 ppm) occurs on the timescale of minutes (half-life of γ-$CsPbI_3$ at room temperature is about 30 minutes),[210] so it possible to record a high-quality spectrum of each phase by taking a measurement immediately after annealing (phase-pure γ-$CsPbI_3$) and after a few hours (phase-pure δ-$CsPbI_3$). For comparison, a spectrum of this material mid-transition is shown as a reference in Figure 2-2b. ^{133}Cs spectra of the compositions formally denoted as $DMA_xCs_{1-x}PbI_3$ (x = 0.01, 0.1, 0.3, 0.5, 0.7) show a single peak corresponding to δ-$CsPbI_3$ with

no substantial shift or line width variation as a function of the DMA/Cs ratio (Table 2-1). The γ phase was not detected in any of the samples, consistent with their yellow appearance.

To elucidate the speciation of DMA, we recorded room-temperature $^{1}H \rightarrow ^{13}C$ cross-polarization (CP) MAS NMR spectra (Figure 2-2c). While the ^{13}C chemical shift of DMA in the $DMA_xCs_{1-x}PbI_3$ (x = 0.1, 0.3, 0.5, 0.7) compositions is consistent with it being present as $DMAPbI_3$, in agreement with the XRD data, we found remarkable variation in line width which is uncorrelated with the DMA/Cs ratio (Table 2-2). For example, the line widths are (0.224 ± 0.006) ppm for $DMAPbI_3$, (1.35 ± 0.03) ppm for $DMA_{0.7}Cs_{0.3}PbI_3$ and (3.48 ± 0.04) ppm for $DMA_{0.01}Cs_{0.99}PbI_3$. Since broader line widths correspond to more disordered local environments, we attribute this effect to the presence of nanosized regions and disorder of $DMAPbI_3$ formed as a result of mechanosynthesis. Interestingly, in the case of the x = 0.01 material, the ^{13}C signal of DMA is shifted to lower frequencies, indicating a substantially different local environment. This effect may result from the interaction of the nanosized grains of $DMAPbI_3$ with the surface of δ-$CsPbI_3$ owing to the high level of dispersion of the hybrid phase within the all-inorganic matrix. The effect is only visible in the most dilute material where we recorded the ^{13}C spectrum over 214 hours. We suggest that this effect could be further investigated using surface-enhanced NMR spectroscopy.[84] Taken together, these XRD and solid-state NMR results show that DMA has no propensity to form thermodynamically stable mixed-cation phases with $CsPbI_3$ and instead forms $DMAPbI_3$, i.e., the two cations do not mix at the atomic level.

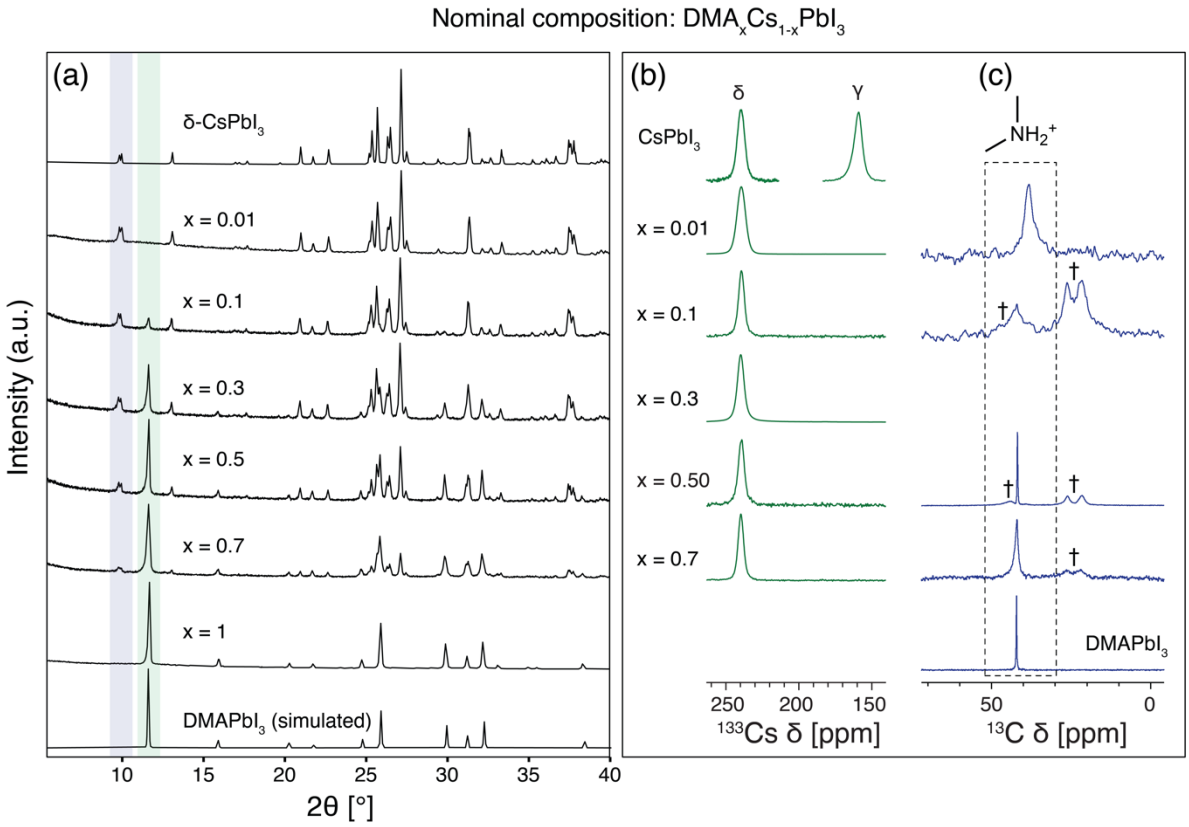

Figure 2-2 Characterization of the $DMA_xCs_{1-x}PbI_3$ materials. (a) powder XRD (see Figure 2-6 for enlarged view), (b) ^{133}Cs MAS and (c) $^{1}H \rightarrow ^{13}C$ CPMAS solid-state NMR spectra. All experiments were carried out at room temperature (ca. 294 K). The NMR spectrum of the x = 0.01 material was recorded using a Hahn echo to avoid baseline distortions. † indicates trace (<2wt% based on the ^{1}H spectrum) polypropylene (PP) used as the grinding jar material, peaks at 21.5, 26.1 and 44.3 ppm. The x = 0.01 material was ground in an agate jar to avoid PP contamination. The full ^{133}Cs spectra and further experimental details are given in Figure 2-4 and Table 2-1 respectively.

However, the formation of black perovskite phase in this phase diagram has been repeatedly reported by multiple groups using solution synthesis,[260, 263] which led us to investigate solution-processed $DMA_{0.20}Cs_{0.80}PbI_3$. We chose this composition because it has a high DMA:Cs ratio while still falling within the stability range of the solid solution reported by Marshall et al.[266] While we have previously shown that qualitative chemical reactivity tends to be identical in solution and mechanosynthesized materials,[200, 270] it appears that in this case solution processing is key to the formation of the black perovskite phase. We first attempted to make the solution-processed material by drop casting without the use of an antisolvent and it behaved in analogy to the materials made by mechanosynthesis, i.e., we observed complete phase segregation into δ-$CsPbI_3$ and $DMAPbI_3$ (Figure 2-2a,c).

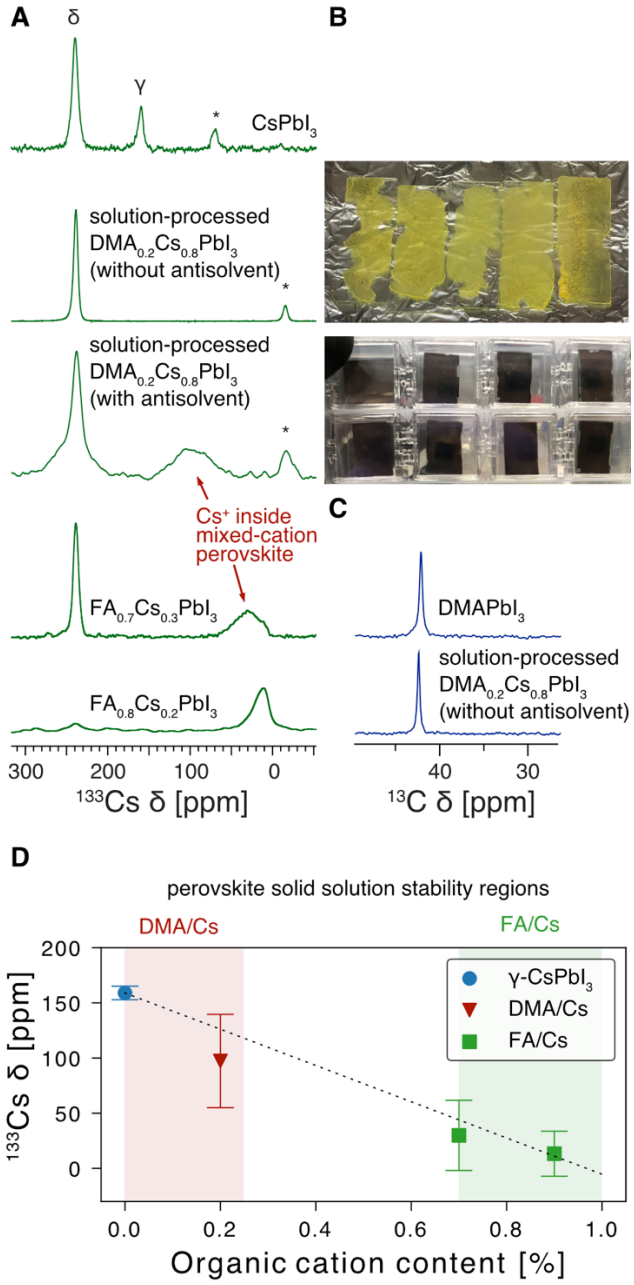

Figure 2-3 Characterization of $DMA_{0.2}Cs_{0.8}PbI_3$ materials prepared by solution processing. (A) ^{133}Cs MAS solid-state NMR spectra of $DMA_{0.2}Cs_{0.8}PbI_3$ made with and without the use of an antisolvent (chlorobenzene). Rapid antisolvent-induced crystallization leads to kinetic trapping of a mixed-cation perovskite with DMA incorporated into the perovskite structure. Its NMR signature its similar to that previously observed for $FA_xCs_{1-x}PbI_3$ solid solutions adapted from the original work [200]. Asterisks (*) indicate spinning sidebands. (B) Photographs of films made with and without the use of an antisolvent. (C) $^{1}H \rightarrow ^{13}C$ CPMAS solid-state NMR spectrum of $DMA_{0.2}Cs_{0.8}PbI_3$ showing that DMA is only present as $DMAPbI_3$. All experiments were carried out at room temperature (ca. 294 K). (D) Correlation between the ^{133}Cs shift of black perovskite solid solutions of $A_xCs_{1-x}PbI_3$ where A = DMA, FA. The error bars are taken as the corresponding full width at half maximum (FWHM) values. The solid-solution stability regions are indicated based on refs.[200, 266] The linear weighed regression equation is δ_{Cs} [ppm] = $-164 \cdot x + 159$.

However, all previous works reporting DMA-assisted formation of a stable black phase used an antisolvent in their deposition process. The role of an antisolvent is to induce rapid crystallization of an intermediate phase by reducing its solubility, which is transformed into the perovskite phase during annealing. Those results suggested to us that the use of an antisolvent may be key to understanding the CsI-DMAI-PbI_2 phase diagram. After optimizing the deposition process (see the Experimental section for details), we found that chlorobenzene reproducibly yields black films, which are stable, if humidity is strictly excluded (Figure 2-3b). The ^{133}Cs MAS NMR spectrum of this black form shows a new very broad peak centered at about 100 ppm with a linewidth of 42 ppm (Figure 2-3a). This NMR signature is reminiscent of Cs^+ incorporated into $FAPbI_3$ (Figure 2-3a, bottom), with the remarkably large linewidth resulting from substantial static disorder, i.e., the presence of a distribution of different nearest and next-nearest neighbor local environments.

For example, in the cubic perovskite aristo type $CsPbI_3$, Cs has 6 nearest neighbors at 6.3 Å (neighboring cuboctahedra), 12 nearest neighbors at 8.9 (across the $[PbI_6]^{4-}$ vertices) and 8 more at 10.9 Å (across the $[PbI_6]^{4-}$ octahedra). Including all the next-nearest neighbors within the 20 Å radius, it has a total of 146 Cs^+ ions surrounding it, each of which can be replaced by DMA, leading to a slight change in ^{133}Cs shift. The convolution of these possibilities leads to the experimentally observed broad lineshape. Despite all the precautions taken (handling inside an argon glovebox, transfer of the rotor in an air-tight Schlenk flask, spinning using dry nitrogen), we found that this phase disappears within 3-4 hours of starting the measurement (Figure 2-5). Figure 2-5 shows the evolution of this spectrum as a function of time. We were unable to record a ^{13}C spectrum of this material (no signal after 8 hours of acquisition), presumably because of the small amount of material and substantial disorder of the degraded phase leading to signal broadening. The spectrum shown in Figure 2-3a is a sum of spectra taken during the first 8 hours of the measurement. Another interesting aspect of this spectrum is that the signal corresponding to δ-$CsPbI_3$ has a broad underlying component, which corresponds to a δ-$CsPbI_3$ in which some Cs was replaced by DMA. This result is similar to what we have previously observed in Cs-rich $FAPbI_3$ compositions such as $FA_{0.16}Cs_{0.84}PbI_3$.[271] These results evidence that DMA can be incorporated into the perovskite phase of $CsPbI_3$, with the strict prerequisite being fast antisolvent-induced crystallization, which leads to kinetic stabilization of the metastable phase. On the other hand, when the material is prepared under thermodynamic conditions[200, 271-273] (mechanosynthesis, slow solvent evaporation), complete phase segregation into δ-$CsPbI_3$ and $DMAPbI_3$ results. This behavior contrasts with that observed for Cs/FA and Cs/GUA, which yield mixed-cation iodoplumbate phases under thermodynamic conditions. The importance of kinetic reaction control also has potential bearing on the role and speciation of Rb^+ and K^+ in hybrid MHPs doped with these cations, where we have previously observed complete segregation of the inorganic dopants under thermodynamic control.[200, 201, 272] The lack of thermodynamic stability of Cs/DMA iodoplumbate phases can be rationalized by the difference in ionic radii of Cs and DMA. The smaller Cs is replaced by the larger DMA, imposing distortions in the lattice. On increasing the DMA:Cs ratio, the volume of the unit cell is expected to increase proportionally. On the one hand, the incorporation of DMA alleviates the initial strain in γ-$CsPbI_3$. On the other, because of the antibonding character of the valence band maximum, the reduction of the lattice distortion leads to an increase in the overlap of the I p and Pb s orbitals, which in turn leads to destabilization of the mixed-cation perovskite phase. We have previously also observed this phenomenon in Cs-rich $Cs_xFA_{1-x}PbI_3$ solid solutions.[271] For reference, based on Bader volume calculations, DMA has an effective radius of 2.67 Å while MA and FA have effective radii of 2.37 Å and 2.48 Å, respectively. Guanidinium (GUA), which has been shown to form mixed GUA/MA and GUA/FA 3D perovskite phases, has an effective radius of 2.68 Å.[272] Finally, we also noticed that the ^{133}Cs shift of the Cs^+ inside the perovskite phase is correlated with the content of the organic cation present in the solid solution (Figure 2-3d). There are two regions corresponding to stable $A_xCs_{1-x}PbI_3$ solid solutions: 0-25 mol% (A=DMA^+, kinetic stability) and >70 mol%) (A = FA, thermodynamic stability). Interestingly, there are currently no known organic cations that lead to stable phases for x in the 25-70 mol% range.

To gain further insights into the potential miscibility of DMA and Cs iodoplumbates, we studied their mixing free energy using DFT calculations. In this energetic and entropic contributions to the free energy of mixing as a function of x for the two phases. For the γ phase and low DMA molar fractions, the replacement of Cs with DMA induces a negligible or slightly positive energetic contribution on the order of 0.01 eV per stoichiometric unit, i.e., energies on the same order of magnitude as the variations between different substitution patterns. Since the values of the mixing free energy for molar fractions of DMA below 37.5 mol % lie within the intrinsic error of the calculations, it is not possible to unambiguously conclude if DMA/Cs mixing in the γ phase leads to marginal stabilization relative to the single-cation end members. On the other hand, for DMA fractions larger than 37.5 % both energetic and entropic contributions favor the formation of mixed-cation phases. Further, in order to assess the relative phase stability at finite temperatures we carried out MD simulations in order to adequately account for vibrational entropy which is absent in calculations done at 0 K. In these simulations, the calculated potential energies per stoichiometric unit of γ and δ phase ($Cs_xDMA_{1-x}PbI_3$) at 300 K suggests that δ phase remains the most thermodynamically stable phase. Given the time scale of first-principles MD simulations (of a few picoseconds) and considering that the systems do not contain any vacancies that might accelerate de-mixing, no spontaneous phase segregation toward the pure phases is expected to be observed, although the calculated mixing free energies show that all mixtures in the δ-phase are unstable with respect to de-mixing.

2.1.3 Conclusions

In conclusion, we have assessed the possibility of incorporating DMA into the $CsPbI_3$ lattice using a combination of long-range and local structure probes, and static and dynamic first principles calculations. Our results show a remarkable dependence on the reaction conditions, with kinetic control leading to stabilization of the mixed-cation $DMA_xCs_{1-x}PbI_3$ perovskite phase and thermodynamic control resulting in complete phase segregation into a physical mixture of δ-$CsPbI_3$ and $DMAPbI_3$. These experimental findings are rationalized by DFT calculations, which show that, overall, the formation of mixed-cation phases is unfavorable. We contend that further multimodal studies into the chemical transformations of $CsPbI_3$ and its solid solutions are urgently needed to improve our understanding of these materials.

2.1.4 Appendix

NMR Acquisition and Processing Details

Table 2-1. ^{133}Cs NMR acquisition and processing parameters for the $DMA_xCs_{1-x}PbI_3$ materials. The FWHM values are given in ppm, in addition to Hz, to allow for a comparison between the two magnetic fields.

x	pulse sequence	Recycle delay [s]	^{133}Cs shift [ppm]	^{133}Cs FWHM [Hz]	^{133}Cs FWHM [ppm]	Magnetic field [T]	MAS rate [kHz]	Apodization [Hz]
0 (δ)	Hahn echo	60	239.5	346 ± 2	5.27 ± 0.03	11.7	8	0
0 (γ)	Hahn echo	30	158.9	404 ± 4	6.15 ± 0.06	11.7	22	0
0.01	Bloch decay	500	239.4	301 ± 3	5.73 ± 0.05	9.4	14	0
0.10	Hahn echo	100	239.3	513 ± 5	4.35 ± 0.04	11.7	20	0
0.30	Hahn echo	100	239.7	435 ± 8	3.68 ± 0.06	11.7	20	0
0.50	Hahn echo	100	239.0	527 ± 6	4.46 ± 0.05	11.7	20	0
0.70	Hahn echo	100	239.7	467 ± 7	3.95 ± 0.06	11.7	20	0

Table 2-2. ^{13}C NMR acquisition and processing parameters for the $DMA_xCs_{1-x}PbI_3$ materials.

x	pulse sequence	Recycle delay [s]	^{13}C chemical shift [ppm]	^{13}C FWHM [Hz]	Magnetic field [T]	MAS rate [kHz]	Apodization [Hz]
0.01	Hahn echo	5	38.1	351 ± 4	9.4	12	50
0.10	CP	4	ca. 42	n/d	9.4	12	50
0.50	CP	7	41.8	24.7 ± 0.8	9.4	12	0
0.70	CP	9	41.9	136 ± 3	9.4	12	10
1.00	Bloch decay	5	42.1	22.6 ± 0.6	9.4	12	0

Table 2-3. ^{133}Cs NMR acquisition and processing parameters for the thin-film $DMA_xCs_{1-x}PbI_3$ materials in Figure 2-3 of the main text. Linewidths were measured without apodization.

x	pulse sequence	Recycle delay [s]	^{133}Cs shift [ppm]	^{13}Cs FWHM [Hz]	Magnetic field [T]	MAS rate [kHz]	Apodization [Hz]
0.20 (drop cast, without antisolvent)	Hahn echo	110	238.7	351 ± 4	14.1	20	50
0.20 (drop cast, with antisolvent)	Hahn echo	21	238.6	520 ± 6 (δ-phase) 3327 ± 54 (perovskite phase)	14.1	20	1000

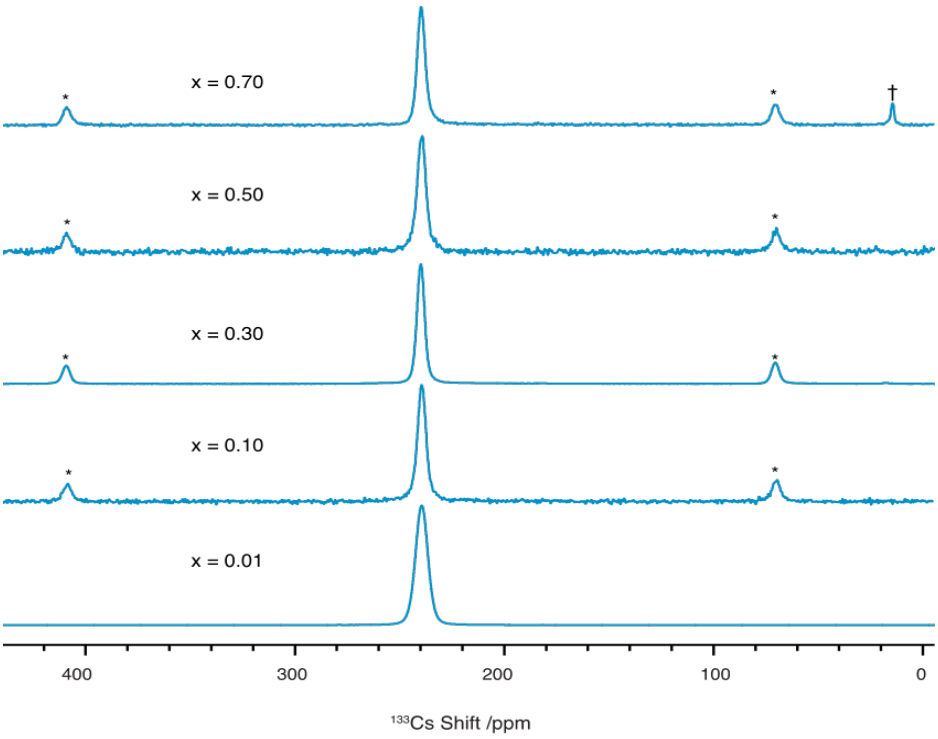

Figure 2-4. ^{133}Cs MAS NMR spectra of $DMA_xCs_{1-x}PbI_3$ materials. Asterisks (*) indicate spinning sidebands, the dagger (†) indicates an unidentified impurity.

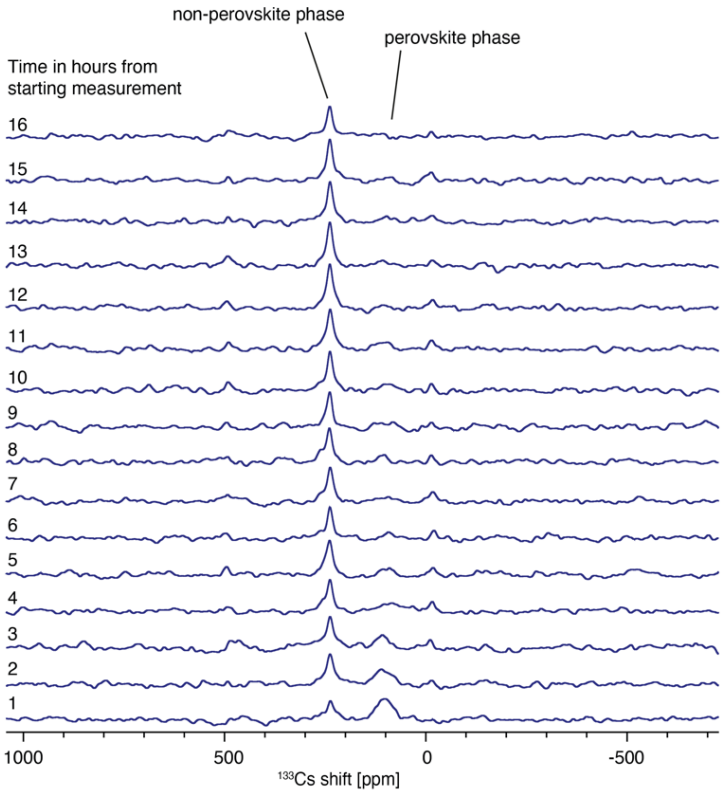

Figure 2-5. ^{133}Cs MAS NMR spectra of $DMA_{0.20}Cs_{0.80}PbI_3$ prepared as solution-processing thin films (25 substrates, spin-coated, with antisolvent) as a function of time. Each spectrum consists of 32 scans with a recycle delay of 110 s (total scan time 59 minutes). Further experimental details are given in table materials. Asterisks (*) indicate spinning sidebands, the dagger (†) indicates an unidentified impurity.

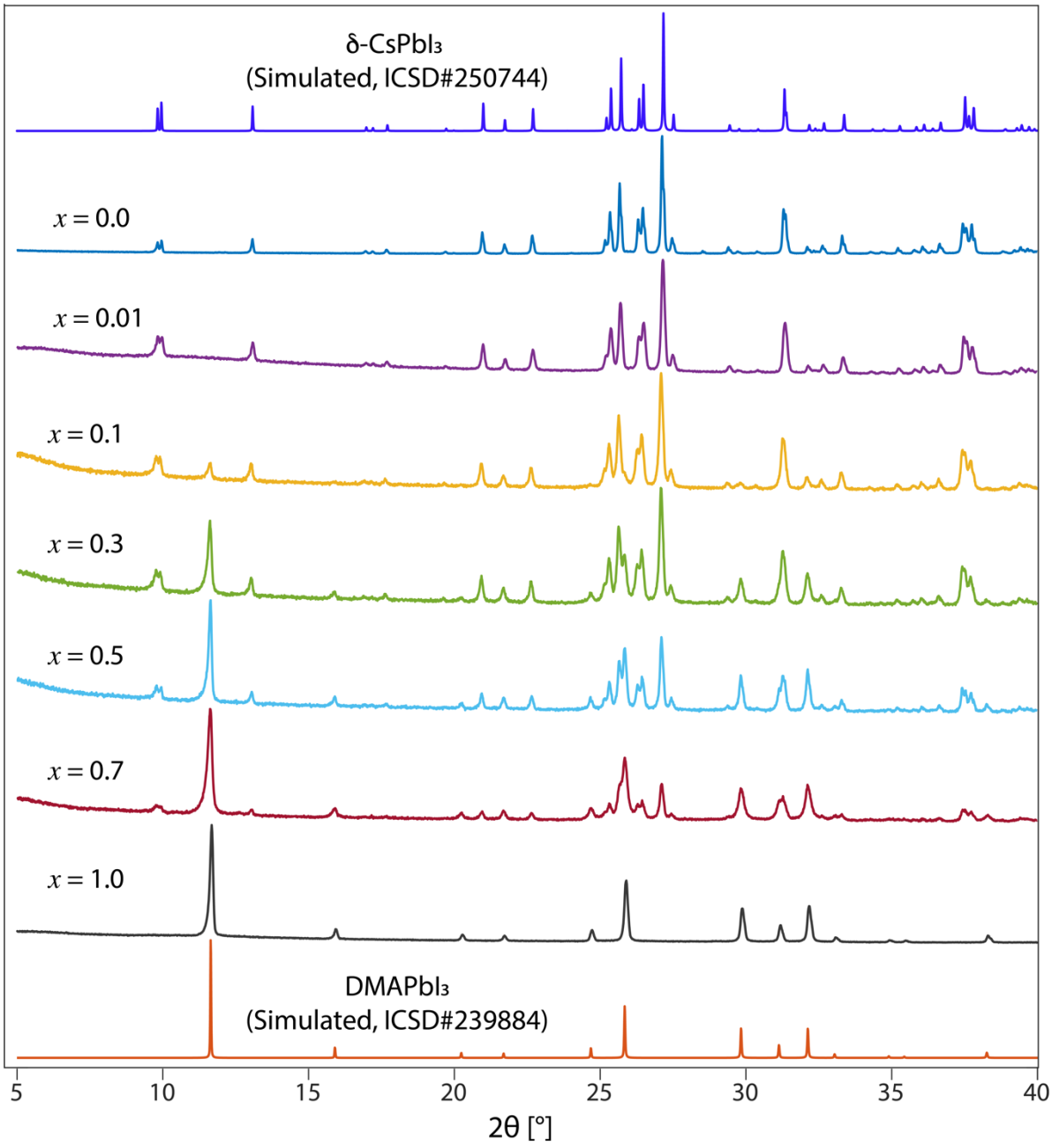

Figure 2-6. Enlarged view of XRD data of $DMA_xCs_{1-x}PbI_3$ as shown in Figure 2-2, including a simulated pattern of δ-$CsPbI_3$ and $DMAPbI_3$.

2.2 NMR Crystallography Determines the Supramolecular Structure of Layered Hybrid Perovskites

This section has been adapted from the following work with the permission from the journal:

Hope, M. A.; Nakamura, T; Ahlawat, P.; Mishra, A.; Cordova, M.; Jahanbakhshi, F.; Mladenović, M.; Runjhun, R.; Merten, L.; Hinderhofer, A.; Carlsen, B. I.; Kubicki, D. J.; Gershoni-Poranne, R.; Schneeberger, T.; Carbone, L. C.; Liu, Y.; Zakeeruddin, S. M.; Lewinski, J.; Hagfeldt, A.; Schreiber, F.; Rothlisberger, U.; Grätzel, M.; Milić, J. V.; Emsley, L., Nanoscale Phase Segregation in Supramolecular π-Templating for Hybrid Perovskite Photovoltaics from NMR Crystallography. *J. Am. Chem. Soc.* 2021, 143 (3), 1529–1538.

Contribution statement: I designed, conducted, analyzed, interpreted and wrote up the solid-state NMR experiments together with MAH, DJK, MC and LE. I collaborated on correcting the whole final manuscript.

Ruddlesden–Popper perovskite phases based on the $A_2A'_{n-1}M_nX_{3n+1}$ composition as shown in the Figure 2-7, where A^+ is a spacer cation.[218, 220, 224, 274] These materials have shown greater resilience to degradation, yet their photovoltaic performance is impaired by the poor electronic properties of the spacer layers and by the lack of ordered supramolecular packing, which impedes overall crystallinity.[220, 224, 275] The interactions between the organic moieties that form the spacer layer directly affect the structure of the resulting materials and, consequently, their optoelectronic properties.[224, 276] While progress has been made in the search for new organic moieties that can form layered perovskites, their assembly can only be controlled by having a thorough understanding of the noncovalent interactions which direct the supramolecular structure, such as hydrogen bonding,[208, 277-279] van der Waals interactions,[218, 280] metal coordination,[281] halogen bonding,[215, 282] and π-based interactions.[283-286] Furthermore, to unravel these interactions, it is vital to accurately determine the atomic structure; this is a challenge for conventional diffraction techniques, due to polycrystallinity and the presence of heavy atoms.[284]

Solid-state nuclear magnetic resonance (NMR) spectroscopy has previously been used to determine the local structure of hybrid perovskites and their composites with various organic molecules.[205, 210, 287, 288] In particular, NMR crystallography, where the structure is determined by comparing the experimental NMR parameters to those calculated for trial structures, is a powerful tool for analyzing the organic assemblies and their templating effects in hybrid perovskite materials.[215, 289]

One of the most widely-employed organic moieties for layered perovskites is 2-phenylethylammonium (PEA^+), which interacts with the hybrid perovskite slabs via ion pairing and hydrogen bonding through the ammonium termini ($-NH_3^+$).[218, 284, 290, 291] The assembly of the organic layer is directed by weaker van der Waals and π-based interactions between the organic moieties (Figure 2-7),[276, 290, 292] which determine the relative orientation of the aromatic rings according to their quadrupole moments.[293, 294] The quadrupole moment of a benzene ring and the corresponding dispersion interactions stabilize two orientations, T-shaped (π_T) and parallel displaced (π_d), which are more favorable than the parallel orientation (π_p; Figure 2-7,inset, top).[293] This is due to areas of positive and negative potential of the aromatic core, which can be visualized by the electronic density distribution or electrostatic potential (ESP) maps (Figure 2-7). Fluoroarenes, such as 2-(perfluorophenyl) ethylammonium (FEA^+, Figure 2-7), feature a reversed quadrupole moment due to the higher electronegativity of fluorine substituents, which favors parallel π interactions (π_p) in benzene–perfluorobenzene systems (Figure 2-7, inset, top).[293] Parallel π–π stacking (Figure 2-7, inset, bottom) of the spacer cations could thus, in principle, be directed by employing alternating arene–fluoroarene moieties.[284, 294] In addition, the presence of fluoroarene moieties could further contribute to the hydrophobicity of the material, improving its resilience to moisture, while fluoroarene anion–π interactions[295] could reduce halide ion migration, increasing the stability under device operating conditions.[296] Therefore, supramolecular π-assemblies of arenes and fluoroarenes could be used to control the properties of hybrid perovskites and their composites, although they remain underexploited in this context.

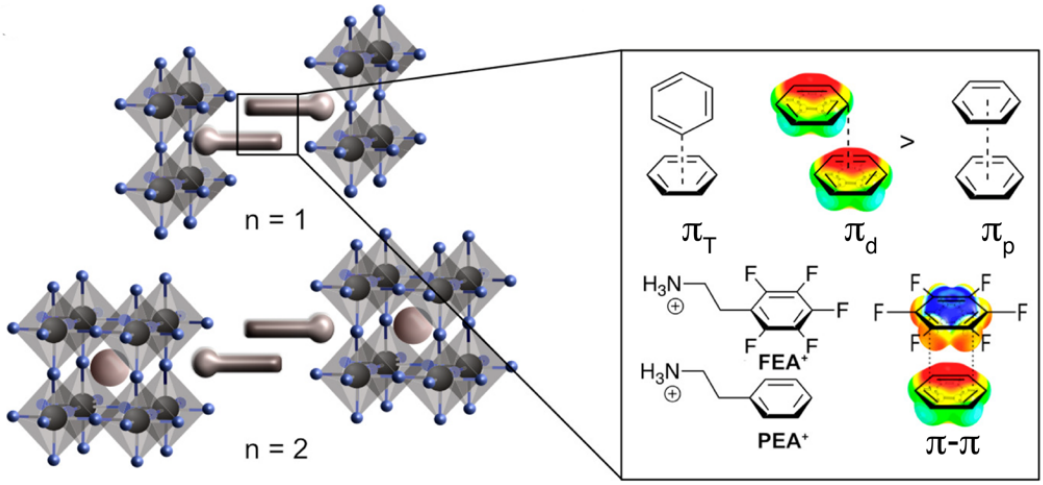

Figure 2-7. Schematic representation of the structure of Ruddlesden–Popper phases of hybrid two-dimensional perovskites based on the $A_2A'_{n-1}M_nX_{3n+1}$ formula (n = 1, 2, etc.) comprised of an organic spacer (A^+) bilayer. (Inset) Top: Overview of possible π–π interaction modes between two arenes with comparable electron-density surfaces, with different interaction strengths ($\pi_T \approx \pi_d > \pi_p$). bottom: Arene–fluoroarene π–π interaction and the spacer cations used in this study: 2-phenylethylamonium (PEA^+) and 2-(perfluorophenyl)ethylammonium (FEA^+). The π_p and π_d interactions of model systems are illustrated by the corresponding electrostatic potential (ESP) maps.

Here, we use NMR crystallography in combination with molecular dynamics (MD) simulations, density functional theory (DFT), and X-ray diffraction to elucidate the atomic-level structure of the spacer cations in a model system that consists of PEA^+ and/or FEA^+ spacers (A^+) in a typical layered 2D perovskite of A_2PbI_4 (n = 1) composition. Contrary to previous reports, we reveal that the arene–fluoroarene interactions of the systems studied here do not lead to templating of a uniform alternating structure, but instead the spacer layers form nanoscale phase-segregated domains. Furthermore, we find that this nanoscale supramolecular structure with mixed-spacers enhances the performance of perovskite solar cells as compared to either of the components alone, which is accompanied by enhanced operational stability. We suggest that nanoscale segregation provides a new route for the design of layered hybrid perovskite systems. This new understanding is provided by the capacity of NMR crystallography to determine the atomic-level structure of the materials, which thus enables rational structure–activity-based design strategies applicable to other hybrid materials.

Now, I will mention the experimental details followed by the results and discussion.

2.2.1 Experimental

Layered perovskite thin films were deposited on microscope glass slides from a 0.5 M precursor solution by spin-coating, followed by annealing at 120°C for 15 mins. 2D/3D thin films similarly prepared by spin-coating with a 1.5 M perovskite precursor solution, followed by annealing at 120°C for 10 min and 100°C for 40 min, before spin-coating an overlayer with a 30 mM solution of the spacer precursor in isopropanol at ambient temperature, followed by annealing at 110°C for 5 min.

Bulk layered perovskite powders were prepared by mechanosynthesis according to previous protocols[268, 297].

Solid state NMR spectra were recorded at 9.4, 11.7 or 21.1 T. Full details are given in Table 2-5. Samples were annealed at 150°C before acquiring the NMR spectra.

Trial structures for the layered perovskites were determined from molecular dynamics simulations and DFT calculations following an analogous procedure as previously reported.[298]

NMR crystallography was used to determine the structure of the organic spacers and the chemical shifts were calculated for the different trial structures using DFT.

2.2.2 Results and Discussion

Hybrid Perovskite Thin Films

This study focuses on the n = 1 model system with PEA^+ and/or FEA^+ spacers (A^+) in a A_2PbI_4 layered 2D perovskite composition. Higher compositional representatives of Ruddlesden–Popper $A_2A'_{n-1}M_nX_{3n+1}$ systems (n > 1) commonly form mixtures of phases (known as quasi-2D perovskites) and are thus not well-defined.[224, 276] Moreover, we assessed 2D/3D composites with overlayers of the organic spacer(s) on the 3D perovskite, which form a thin layer of a 2D phase upon annealing, which are relevant for photovoltaic

applications.[277, 299] For these materials, we have based our investigation on compositions comprising FA^+ as the central A^+ cation due to its higher thermal stability.[300, 301]

Thin films of layered perovskites were prepared based on n = 1 A_2PbI_4 compositions (A^+ = PEA^+, FEA^+ and 1:1 PEA^+:FEA^+ denoted PF) as well as 3D $(Cs_{0.05}FA_{0.95}MA_{0.1})PbI_3$ perovskite thin films with a spacer overlayer of PEAI, FEAI or 1:1 PEAI:FEAI to form 2D/3D perovskite compositions on the surface, in accordance with the previous reports.[299]

The structural properties of the resulting perovskite films were analyzed by X-ray diffraction (XRD) in a Bragg–Brentano configuration. XRD patterns of A_2PbI_4 compositions evidence the capacity of all of the spacers to form well-defined layered perovskite structures (Figure 2-8a). This is revealed by the presence of characteristic periodic patterns and low-angle reflections in the 2θ region below 10° that are associated with the basal (*h00*) planes.[224] The $(FEA)_2PbI_4$ films also show additional reflections (e.g., around 2θ of 12.6°) that are associated with residual PbI_2.

For the 2D/3D perovskites (Figure 2-8b), the overlayers of organic spacers do not substantially change the crystal structure of the 3D perovskite, as the characteristic signals remain unaltered. In Figure 2-8b, grey colored diffractogram refers to the control film, i.e., corresponding to $FAPbI_3$ perovskite thin-film exhibiting the diffraction peaks corresponding to a 3D perovskite. However, the PEA-based system features additional low-angle reflections in the region of 2θ below 10°, which are indicative of the formation of low-dimensional perovskite phases.[224] These signals were not apparent for FEA^+- and PF-treated perovskite thin films, most likely due to orientation or low crystallinity. Grazing-incidence wide-angle X-ray scattering (GIWAXS) showed the low angle signals.[302] The assemblies of the FEA^+ and PF spacers on the 3D perovskite surface were also probed by X-ray photoelectron spectroscopy (XPS), which confirms the presence of FEA^+ on the surface of the hybrid perovskite through the appearance of F 1s core level signals.[302] The F 1s binding energies for FEA^+- and PF-treated samples of 686.89 and 688.09 eV, respectively, indicate that the organic moieties engage in different binding modes on the surface of the hybrid perovskite.[302] However, the spacer layers were not found to significantly alter the optical properties of the 3D perovskite, as demonstrated by the UV-Vis absorption and photoluminescence (PL) spectroscopy of the corresponding films (Figure 2-8c–d). This is beneficial for maintaining favorable optoelectronic features relevant to their application.

In summary, the analysis of perovskite films of A_2PbI_4 (n = 1) composition indicates that the spacer moieties (PEA^+, FEA^+ and their 1:1 mixture, PF) form layered 2D perovskite structures. Moreover, the presence of the spacer overlayer does not substantially affect the optoelectronic properties of the resulting 2D/3D perovskite films, which is beneficial for their application. Although XRD deter-mines the layered 2D nature of the inorganic lattice, it is not sensitive to the structure of the organic spacer cation. The atomic-level structure was therefore investigated by solid-state NMR spectroscopy[200, 287, 303] in conjunction with MD simulations and DFT calculations.

Elucidation of the Supramolecular Structure

To analyze the bulk properties of the materials, powders of A_2PbI_4 composition (n = 1; A^+ = PEA^+, FEA^+ and PF) were prepared mechanochemically.[268, 297] XRD reveal that the crystalline low-dimensional perovskite structure is formed for all compositions, exemplified by the low angle reflections at around 2θ = 5.2° (Figure 2-8e) These correspond to layer spacings of 16.5 Å, 17.5 Å and 16.7 Å for $(PEA)_2PbI_4$, $(FEA)_2PbI_4$ and $(PF)_2PbI_4$, respectively, consistent with the trend observed for calculated structures. Many more reflections are seen than for the thin film samples, due to the lack of preferred orientation. The pattern for $(PEA)_2PbI_4$ is in good agreement with the previously reported crystal structure,[304] and similar patterns are observed for the other samples. The reflections at 2θ values of ~14–15° are consistent with in-plane Pb–Pb distances of ~6.1 Å. The $(FEA)_2PbI_4$ and $(PF)_2PbI_4$ samples show an additional reflection at 2θ of 12.6° which is ascribed to unreacted PbI_2, as also observed for the thin film $(FEA)_2PbI_4$ sample.

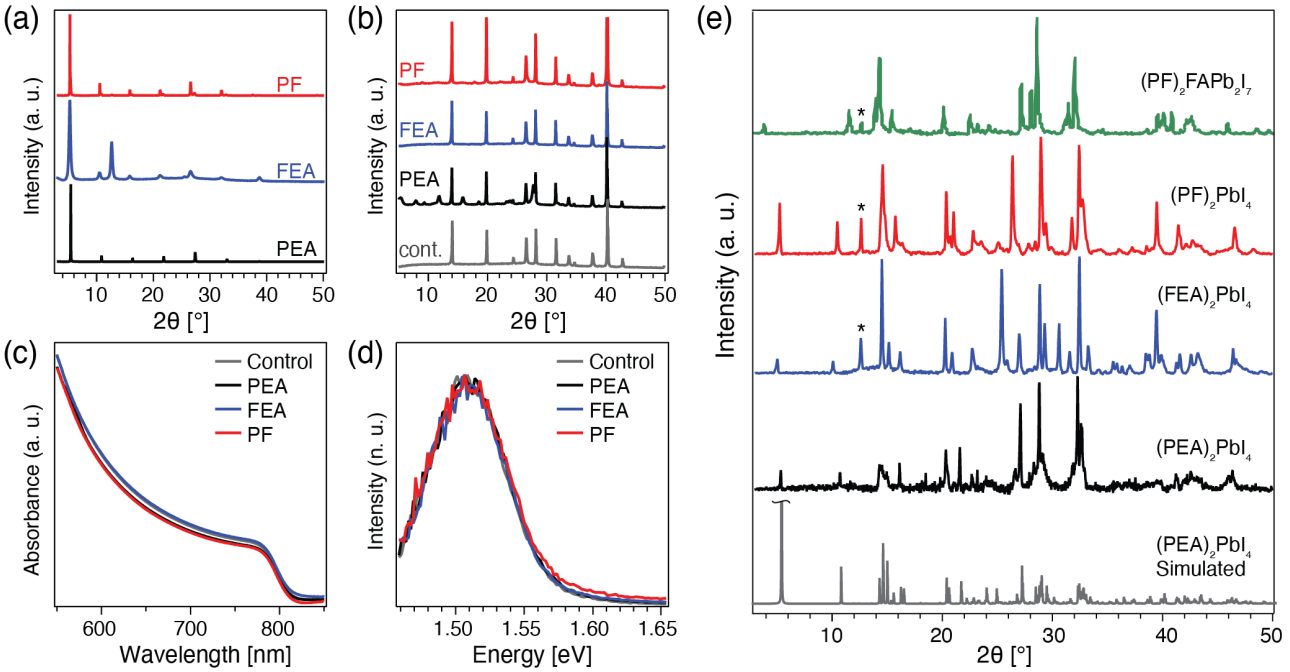

Figure 2-8. Structural and optical properties of the perovskite thin films. X-ray diffraction (XRD) patterns of (a) layered 2D perovskite films of A_2PbI_4 composition and (b) 2D/3D perovskites (A^+ = PEA^+, FEA^+ and 1:1 PEA^+:FEA^+ denoted PF) on microscopic glass slides. (c) UV-Vis absorption spectra and (d) steady-state photo-luminescence (PL) spectra of 2D/3D perovskite films on microscopic glass slide. n.u. = normalized units; cont. = control. (e) PXRD patterns of mechanosynthesized layered hybrid perovskites of $A_2FA_{n-1}Pb_nI_4$ compositions, (A^+ = PEA^+, FEA^+ and 1:1 PEA^+: FEA^+ denoted PF). The simulated pattern for PEA_2PbI_4 is shown for previously reported (twisted) crystal structure.[304] The major PbI_2 reflection is marked with an asterisk.

Comparison of the $^1H/^{19}F \rightarrow ^{13}C$ cross polarization (CP) and direct ^{19}F NMR spectra in the aromatic regions of the spacer cations for the pure PEAI and FEAI precursors and for the layered 2D perovskites (Figure 2-9) shows that the spacer environment changes upon formation of layered 2D perovskites. The ^{19}F spectra for pentafluorophenyl derivatives are well known.[305] the assignment of the ^{13}C signals for FEAI was determined by $^{19}F \rightarrow ^{13}C$ heteronuclear correlation (HETCOR) spectroscopy (Figure 2-13), whereas the assignment of the ^{13}C signals for PEA^+ was found by comparison with the calculated shifts, *vide infra*. Ball-milling a 1:1 mixture of PEAI and FEAI under comparable conditions to the mechanochemical preparation of the layered perovskite systems causes only relatively minor changes to the NMR spectra (Figure 2-9,red spectra, bottom panels). This indicates that the sample adopts a similar structure to the neat spacer precursors. The atomic-level mixing between the phenyl moieties of the two components in the PEAI:FEAI sample is nevertheless clearly evidenced by the signal arising from the PEA^+ carbons (labelled *a*–*c*, Figure 2-9a) in the $^{19}F \rightarrow ^{13}C$ CP spectrum (Figure 2-9, dashed box). The ^{19}F spectrum for PEAI:FEAI (Figure 2-9d) exhibits slightly different shifts compared to pure FEAI, due to the sensitivity of the ^{19}F shifts to the modified structure. For the layered perovskites, clear differences are observed in the NMR spectra of the spacer cations, implying the formation of a new supramolecular structure (Figure 2-9b–d, top panels). The spectra for $(FP)_2Pb_2I_4$ (n = 1) and $(FP)_2FAPb_2I_7$ (n = 2) compositions are comparable, which implies that the organic structures are also very similar; this is expected, since the presence of a second layer of lead iodide octahedra should not significantly influence the spacer cations. Furthermore, for both systems the PEA^+ carbons can be observed in the $^{19}F \rightarrow ^{13}C$ CP spectra (Figure 2-9c, dashed boxes), indicating atomic-scale mixing of the spacer cations, since CP transfer relies on through-space dipole–dipole interactions at the sub-nano meter length scale. However, the layered perovskites containing only a single type of spacer cation, namely $(PEA)_2PbI_4$ and $(FEA)_2PbI_4$, exhibit very similar spectra to the samples with mixed spacers. These observations can be explained by nanoscale segregation due to self-recognition or "narcissistic" self-sorting,[306] which would result in the local environments remaining similar to the individual spacer structures, while still affording the atomic-level contact observed by $^{19}F \rightarrow ^{13}C$ CP. The broader signals in the mixed samples may thus correspond to the broader distribution of slightly different possible local environments experienced within nanodomains of the different spacer cations.

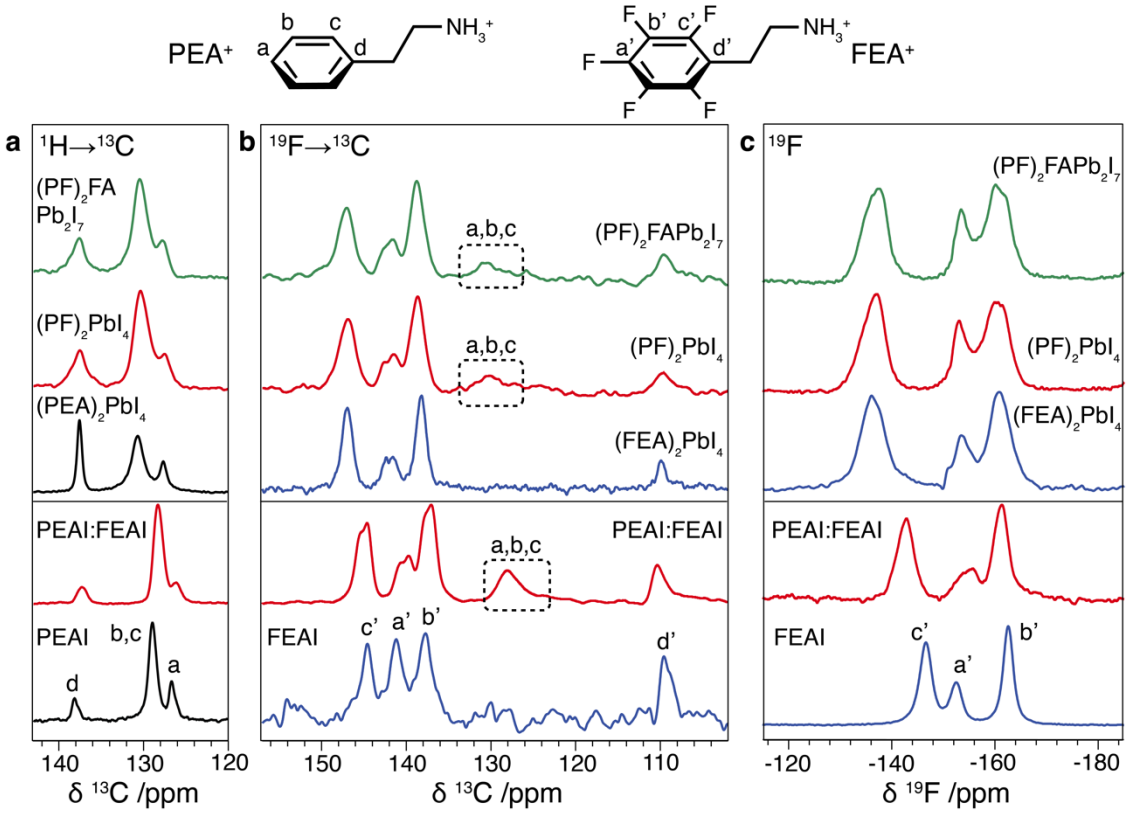

Figure 2-9. Solid-state NMR spectra of the spacer cations. (a) Structure of PEA^+ and FEA^+ cations with the corresponding ^{13}C and ^{19}F sites labelled. (b) $^{1}H\rightarrow^{13}C$ CP, (c) $^{19}F\rightarrow^{13}C$ CP and (d) direct ^{19}F MAS NMR spectra. The top half of the panels are spectra from the layered hybrid perovskites whereas the bottom half are from the neat spacer salts and their 1:1 mixture, following ball-milling. PF = 1:1 PEA^+:FEA^+. Signals arising from PEA^+ in the $^{19}F\rightarrow^{13}C$ CP spectra are highlighted in dashed boxes. Experimental parameters are given in Table 2-5. Full ^{13}C spectra are shown in Figure 2-12.

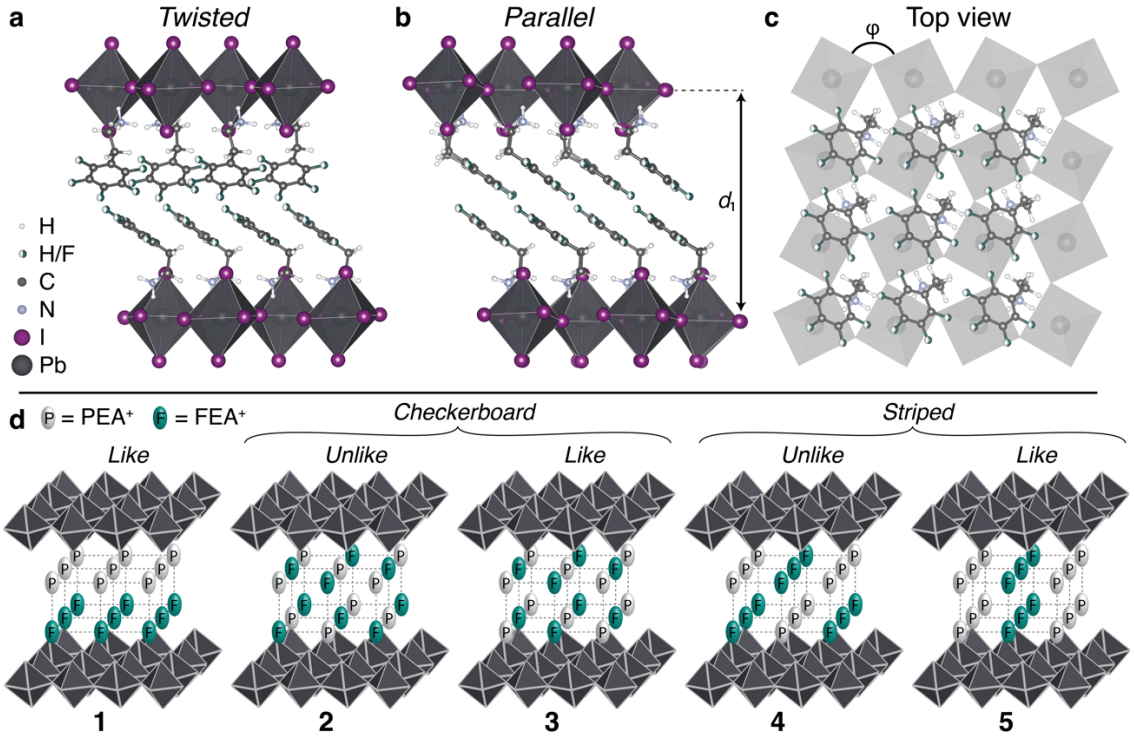

Figure 2-10. Trial structures for DFT calculations and NMR crystallography of A'_2PbI_4 layered perovskites. (a, b) *Twisted* and *parallel* relative orientations of the aromatic rings in adjacent layers, and (c) top view of the spacer layer, showing the square lattice of interstices in the inorganic layer, all shown for the PEA_2PbI_4 composition. The interlayer spacing (d_1) and octahedral tilting (ϕ) are also indicated. (d) Schematic of different

possible arrangements (**1**–**5**) of PEA^+ (P) and FEA^+ (F) moieties on the two opposing lattices representing the spacer bilayer within the layered perovskite.

To test whether the results obtained for the bulk mechanosynthesised samples are also applicable to solution-processed thin films, the $^1H \rightarrow ^{13}C$ spectrum was recorded for a thin film sample of $(FP)_2PbI_4$ after scraping off the substrate (Figure 2-12, top). Although the signal-to-noise ratio is relatively low due to the low sample mass, the aromatic signals for the spacer cations are observed with the same shifts as for the bulk $(FP)_2PbI_4$ sample, within a root-mean-squared error of 0.45 ppm. This indicates that the same supramolecular structure is adopted here for both the bulk and thin film layered perovskites.

To illuminate the atomic-level structure using the NMR data, the predicted chemical shieldings were calculated using DFT for different trial structures. These were then converted to chemical shifts using a regression obtained from a set of reference organic structures containing fluorine and iodine (for details in the appendix). The $n = 1$ structure was used for the comparison, since the organic cation structure is shared by higher order 2D/3D homologues. Trial structures were generated by selecting low energy structures from molecular dynamics simulations (details in appendix), some of which were based on previously reported crystal structures,[218, 304, 307, 308] prior to geometry optimization using DFT. Structures with two different relative orientations of the spacer cation aromatic rings were considered: the "*twisted*" structure (Figure 2-10a), with a twist between the aromatic rings in the two opposing layers, resulting in predominantly π_T interactions and the "*parallel*" structure (Figure 2-10b), with aromatic rings from opposite layers aligned in parallel planes at 180° between the layers, allowing displaced parallel π_d interactions. For $(PEA)_2PbI_4$, the experimental ^{13}C shifts agree with the calculated shifts for the *twisted* structure better than for the *parallel* structure (Table 2-6). This observation is in agreement with the previously reported single crystal structure (CCDC no. 1542461)[304] and the slightly lower calculated DFT energy (details in appendix). For this analysis, only the aromatic carbons in the spacer cations were considered because the aliphatic carbons are close to the heavy Pb and I atoms and may require full relativistic treatment to obtain accurate shieldings. In contrast, for $(FEA)_2PbI_4$ the calculated ^{13}C and ^{19}F shifts for the *parallel* structure are in better agreement with experiment (Table 2-6), in accordance with the fact that the DFT energy is lower for the *parallel* structure (details in appendix).

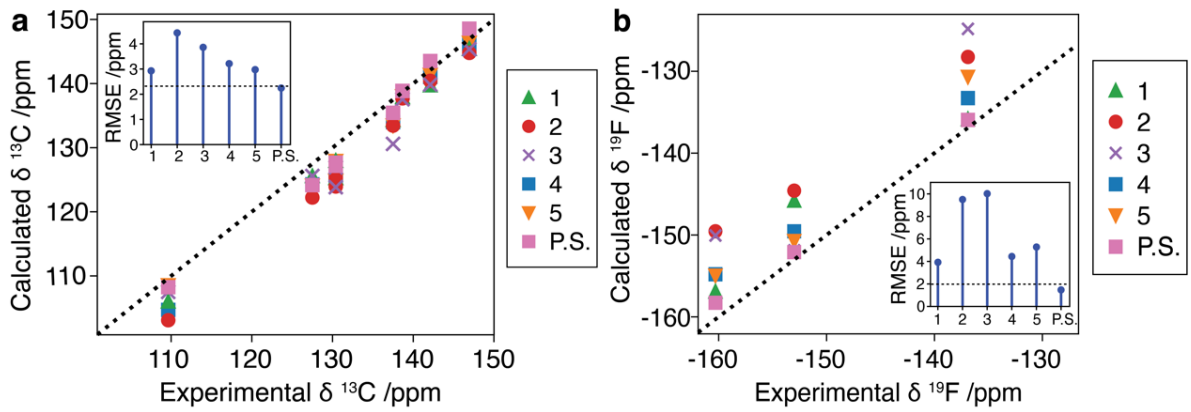

Figure 2-11. NMR shift calculations. Calculated aromatic (a) ^{13}C and (b) ^{19}F chemical shifts plotted against the experimental $(FP)_2PbI_4$ chemical shifts for structures **1**–**5** Figure 2-10d) and a phase segregated model (P.S., the calculated shifts for pure $(PEA)_2PbI_4$ and $(FEA)_2PbI_4$). The dashed diagonal lines indicate exact agreement. The inserts show the root-mean-squared error (RMSE) between the calculated and experimental chemical shifts for each structure, and the horizontal lines are the expected error in DFT calculated shifts given by the RMSE in the regression set.

For the mixed $(PF)_2PbI_4$ layered perovskite, there are many possible arrangements of the PEA^+ and FEA^+ spacers. Each lead iodide layer contains an array of tilted corner-sharing octahedra, resulting in a square lattice of rhombic interstices on each face in which the spacer cations reside (Figure 2-10c). We have considered the simplest representative examples of tiling the spacer cations over the two opposing lattices to form five trial structures (Figure 2-10d). In structure **1** each face comprises only a single type of spacer, while structures **2** and **3** have "*checkerboard*" arrangements of the cations on each face. In structure **2** the arrangements are offset so that *unlike* spacers are opposite each other (i.e., PEA^+ is opposite FEA^+), while structure **3** has *like* spacers opposing. Finally, structures **4** and **5** have *striped* arrangements of the spacers on each face with *unlike*- and *like*-pairing arrangements of the opposing spacers, respectively. In addition, we also consider a segregated model, where the shifts are calculated for the separate pure *twisted* $(PEA)_2PbI_4$ and *parallel* $(FEA)_2PbI_4$ structures to imitate the environments in a nanoscale segregated structure that would form as a result of predominantly narcissistic self-sorting.

Figure 2-11 compares the experimental and calculated ^{13}C and ^{19}F chemical shifts for the five mixed $(PF)_2PbI_4$ structures, and the segregated model with the shifts from the pure $(PEA)_2PbI_4$ and $(FEA)_2PbI_4$ structures. The best agreement was found for a segregated model, and this is the only case for which the root-mean-squared errors (RMSE) between the calculated and experimental chemical

shifts (Figure 2-11, insets) are less than the expected root-mean-squared error in DFT calculated shifts: 2.32 and 1.98 ppm for ^{13}C and ^{19}F, respectively, as estimated by the error in the calculated shifts for the external reference set (details in appendix). Bayesian analysis of the data with the Bayesian NMR tool[309] indicates that the segregated system matches the experimental data with 99.9% probability, which is also consistent with the experimental shifts for $(FP)_2PbI_4$ being very similar to those for $(PEA)_2PbI_4$ and $(FEA)_2PbI_4$.

We therefore conclude that the layered hybrid perovskite structured formed by mixed PEA^+ and FEA^+ spacers comprises segregated domains of the two spacer moieties; however, since the PEA^+ ^{13}C signals are observed in the $^{19}F\rightarrow^{13}C$ CP spectrum (Figure 2-9c), the domains must be limited to the nanoscale. Although the opposite quadrupolar moments of the aromatic systems were expected to favor PEA^+–FEA^+ π interactions, the segregation may reflect the differing preferences of the two spacer cations to form *twisted* and *parallel* aromatic contacts, respectively (Figure 2-10a, b). Nevertheless, nanoscale mixing of the two spacers is observed, which may be entropically driven and is further supported by the single basal reflection observed by XRD (Figure 2-8), despite the pure layered 2D perovskites having different layer spacings (*vide supra*). As a result, the photovoltaic performance of the mixed system could be affected as compared to the pure system (*vide infra*) through a synergistic effect.

The photovoltaic performance of hybrid perovskites with overlayers of layered perovskites with the differen.t spacer cations was investigated. The mixed-spacer treated device, which we have determined to have a nanoscale-segregated structure of the spacer cations, shows a higher power conversion efficiency than with either spacer individually. We note, however, that the photovoltaic performances were not the primary objective of this study and were instead analyzed to illustrate the utility of this class of hybrid perovskites; therefore, further optimization of the corresponding devices can be envisaged. Moreover, We further examined the effect of the overlayer on the operational stability of unencapsulated devices by monitoring the evolution of their maximum power point (MPP) under continuous irradiation of 1 sun in a nitrogen atmosphere, which has previously been found to play a role in suppressing the degradation under operational conditions.[310, 311] While the initial performance of the control devices dropped to values below 80% after just 20 h of operation, the treated devices showed improved stability during this period of time, maintaining around 90% of their initial performance value after 100 h of operation. These performance and stability improvements indicate the potential of such mixed-spacer layered perovskites in perovskite photovoltaics, which should stimulate further investigations.

2.2.3 Conclusions

In summary, we present a systematic NMR crystallography approach based on solid-state NMR spectroscopy and computational analysis to elucidate the supramolecular structure of the organic spacer layer for layered hybrid perovskites. Specifically, a mixed arene–fluoroarene model system was studied, for which we find that although there is atomic-level contact between the spacers, the structures most closely resemble those of the endmembers, implying nanoscale segregation. We illustrate the application of this system in enhancing the performance and stability of perovskite solar cells and demonstrate that the performance is greater than for either of the spacers individually. In general, we envisage that NMR crystallography will play an important role in determining the supramolecular structure of layered hybrid perovskites, facilitating molecular design of spacer systems driven by an understanding of their assemblies, thereby advancing the properties and applications of hybrid materials.

2.2.4 Appendix

2.2.4.1 Chemical Shift Calculations

GIPAW Chemical Shifts of Candidate Structures

All NMR computations were carried out using the plane-wave density functional theory (DFT) software Quantum ESPRESSO, version 6.5.[312] To allow comparison with the reference structures, the trial structures were first relaxed, including cell parameters, at the PBE level of theory using Grimme D2 dispersion correction and projector augmented wave scalar relativistic pseudopotentials obtained from PS library version 1.0.0.[313, 314] In these pseudopotentials, semi core d electron states are included for Pb and I, and nonlinear core-correction is used except for H. Wavefunction and charge density energy cutoffs were set to 100 Ry and 400 Ry, respectively. A Monkhorst-Pack grid of k-points corresponding to a maximum spacing of 0.05 $Å^{-1}$ in reciprocal space was used.[315] After relaxing the structures, a single-point computation was performed using the same parameters, and chemical shieldings were computed using the GIPAW method.[316, 317] Structures were visualized with the VESTA software package.[318]

External Referencing for ^{19}F GIPAW Chemical Shifts

The reference structures used to convert shielding to chemical shifts were obtained from Ruiz-Preciado et al.[215] and GIPAW chemical shifts were obtained as described in the previous section. The reference structures considered and their corresponding experimental shift references are listed in Table 2-4. Linear regression was performed between the isotropic ^{19}F experimental shifts δ_{exp} and computed isotropic shieldings σ_{comp}. The obtained parameters were used to predict isotropic chemical shifts δ_{pred} of the candidate structures. The conversion is defined by the following equation.

$$\delta_{\mathrm{pred,19F}} = -0.918\sigma_{\mathrm{comp,19F}} + 129.062\ \mathrm{ppm}$$

For ^{13}C, the computed chemical shieldings of carbon atoms bound to iodine were found to significantly deviate from the linear relationship between computed isotropic shieldings and experimental isotropic shifts, as previously reported by Szell et al.[319] They were thus not taken into account to perform the linear regression. The equation obtained for the conversion is given below.

$$\delta_{\mathrm{pred,13C}} = -0.975\sigma_{\mathrm{comp,13C}} + 164.524\ \mathrm{ppm}$$

Table 2-4. $^{19}F/^{13}C$ Experimental chemical shifts of reference materials.

Material name	Experimental ^{19}F chemical shift reference	Experimental ^{13}C chemical shift reference
Fluorouracil	Viger-Gravel et al.[320]	Viger-Gravel et al.[320]
Perfluoronapthalene	Robbins et al.[321]	-
Sym-TFTIB	Szell et al.[319]	Szell et al.[319]
ACD-TFDIB	Szell et al.[319]	Szell et al.[319]
ACD-TFTIB	Szell et al.[319]	Szell et al.[319]
PHN-TFDIB	Szell et al.[319]	Szell et al.[319]
PHN-TFTIB	Szell et al.[319]	Szell et al.[319]
TMP-TFDIB	Szell et al.[319]	Szell et al.[319]
TMP-TFTIB	Szell et al.[319]	Szell et al.[319]
HMT-TFDIB	Szell et al.[319]	Szell et al.[319]
HMT-TFTIB	Szell et al.[319]	Szell et al.[319]

Probabilistic Analysis of the Best Fitting Structure

In order to determine which structure matches best the experiment and to assess the confidence of the result, the Bayesian framework introduced by Engel et al.[309] was applied to the set of candidate structures. ^{19}F and ^{13}C chemical shifts were considered for the probabilistic analysis. The external reference described in the previous section was used to obtain the computed ^{19}F isotropic chemical shifts, while a least-square regression between computed ^{13}C isotropic shieldings and experimental isotropic shifts was performed for each candidate.

Table 2-5. Experiments parameters for the spectra in Figure 2-9 and Figure 2-12.
The bracketed numbers are for the scraped thin film sample.

Material	Parameters	$^{1}H \rightarrow ^{13}C$ CP	$^{19}F \rightarrow ^{13}C$ CP	Direct ^{19}F
PEAI	Field /T	21.1		
	Scans	108		
	Recycle delay /s	5		
	Contact time /ms	1		
	MAS rate /kHz	15		
FEAI	Field /T	21.1	21.1	9.4
	Scans	128	32	8
	Recycle delay /s	5	40	30
	Contact time /ms	2	2	–
	MAS rate /kHz	15	20	20
1:1 FEAI:PEAI	Field /T	21.1	21.1	11.7
	Scans	600	960	64
	Recycle delay /s	2.6	30	15
	Contact time /ms	2	4	–
	MAS rate /kHz	15	20	50
$(PEA)_2PbI_4$	Field /T	11.7		
	Scans	2372		
	Recycle delay /s	5		
	Contact time /ms	2		
	MAS rate /kHz	15		
$(FEA)_2PbI_4$	Field /T	11.7	21.1	9.4
	Scans	2726	1080	640
	Recycle delay /s	5	30	1
	Contact time /ms	2	4	–
	MAS rate /kHz	15	20	20
$n = 1$ $(FP)_2PbI_4$	Field /T	21.1	21.1	9.4
	Scans	128 (44776)	600	16
	Recycle delay /s	5	30	30
	Contact time /ms	2	4	–
	MAS rate /kHz	15 (50)	20	20
$n = 2$ $(FP)_2FAPb_2I_7$	Field /T	21.1	21.1	9.4
	Scans	128	1408	16
	Recycle delay /s	5	25	30
	Contact time /ms	2	4	–
	MAS rate /kHz	15	20	20

Table 2-6. Root-mean-square-errors (RMSE) between the experimental and calculated ^{13}C and ^{19}F chemical shifts for the *parallel* and *Twisted* structures of $(PEA)_2PbI_4$ and $(FEA)_2PbI_4$. The squared error is calculated for each atom in the calculated supercell, from which the RMSE is calculated.

		RMSE /ppm	
		Parallel	*Twisted*
$(PEA)_2PbI_4$	^{13}C	**3.57**	4.81
$(FEA)_2PbI_4$	^{13}C	1.82	**1.40**
	^{19}F	3.14	**2.35**

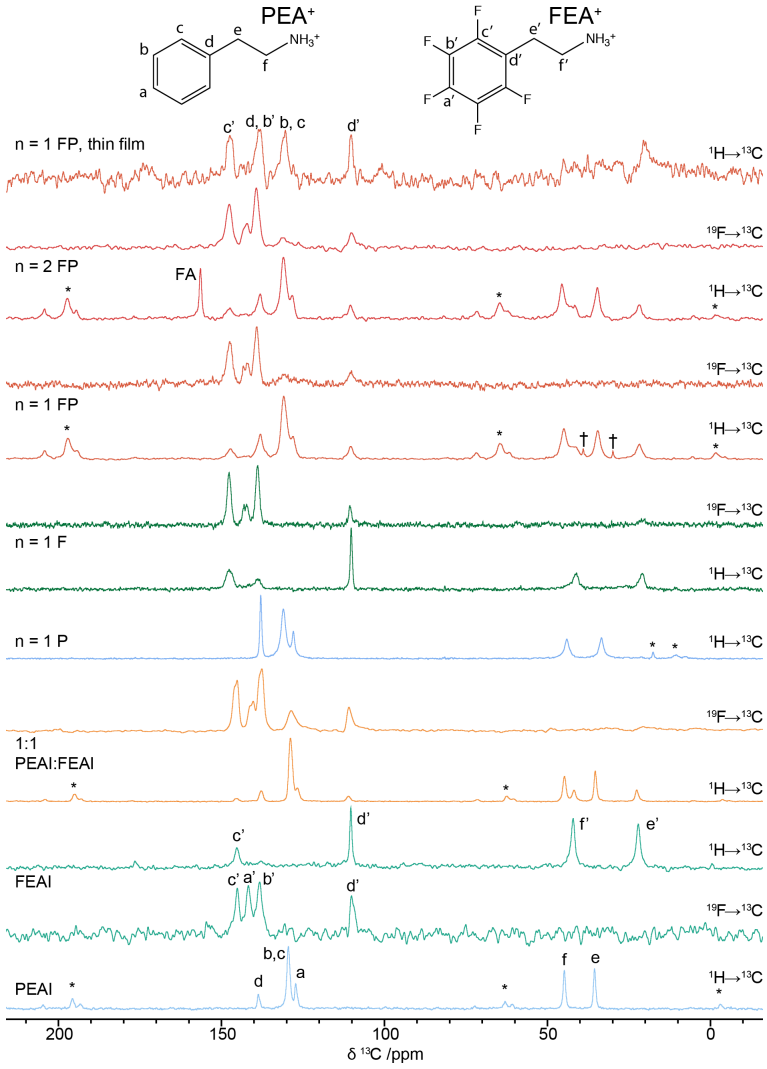

Figure 2-12. $^{1}H \rightarrow ^{13}C$ and $^{19}F \rightarrow ^{13}C$ CP spectra of the spacer cations, showing the whole spectra. Asterisks denote spinning sidebands. The peaks marked with † are due to contamination of the sample with adamantane. The peak marked FA is due to the carbon in the formamidinium cation, present only in the *n* = 2 sample; this is not visible in the $^{19}F \rightarrow ^{13}C$ spectrum since the fluorine atoms are a significant distance from the FA^+ cations.

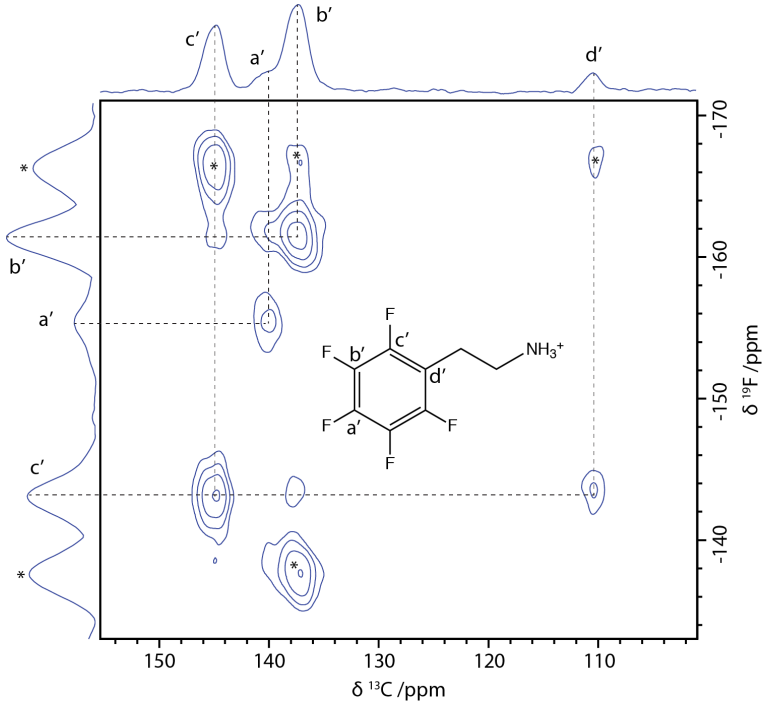

Figure 2-13. $^{19}F \rightarrow ^{13}C$ HETCOR spectrum of a ball-milled 1:1 mixture of PEAI:FEAI recorded at 21.1 T with 20 kHz MAS, a recycle delay of 30 s, a 1 ms contact time, 240 scans and 80, 25 µs increments in the indirect dimension.

2.3 NMR Explores the Formate Ion as a Pseudo-halide in α-$FAPbI_3$

This section has been adapted from the following work with the permission from the journal:

Jeong, J.; Kim, M.; Seo, J.; Lu, H.; Ahlawat, P.; Mishra, A.; Yang, Y.; Hope, M. A.; Eickemeyer, F. T.; Kim, M.; Yoon, Y. J.; Choi, I. W.; Darwich, B. P.; Choi, S. J.; Jo, Y.; Lee, J. H.; Walker, B.; Zakeeruddin, S. M.; Emsley, L.; Rothlisberger, U.; Hagfeldt, A.; Kim, D. S.; Grätzel, M.; Kim, J. Y., Pseudo-halide anion engineering for α-$FAPbI_3$ perovskite solar cells. *Nature* **2021,** *592* (7854), 381–385.

Contribution statement: I designed, conducted, analyzed, interpreted and wrote up the solid-state NMR experiments together with MAH and LE. I collaborated on correcting the whole final manuscript.

Compositional engineering plays a key role in achieving highly-efficient and stable PSCs. In particular, mixtures of methylammonium lead triiodide ($MAPbI_3$) with formamidinium lead triiodide ($FAPbI_3$) have been extensively studied.[190, 322] Compared to $MAPbI_3$, $FAPbI_3$ is thermally more stable and has a bandgap closer to the Shockley-Queisser limit,[323] rendering $FAPbI_3$ the most attractive perovskite layer for single junction PSCs. Unfortunately, thin $FAPbI_3$ films undergo a phase-transition from the black α-phase to a photoinactive yellow δ-phase below a temperature of 150°C. Previous approaches to overcome this problem include mixing $FAPbI_3$ with a combination of MA^+, Cs^+ and Br^- ions, at the cost of blue-shifted absorbance and phase segregation under operational conditions.[322, 324-326]

Br^-, Cl^-, and thiocyanate (SCN^-) anions have commonly been used to improve the crystallinity and stability of perovskite films.[324, 325, 327-333] Another pseudo-halide anion, formate ($HCOO^-$), has been investigated in connection with $MAPbI_3$ based PSCs.[334-337] Two studies[334, 335] reported that methylammonium formate improves the quality of $MAPbI_3$ films by controlling the perovskite crystal growth, while others[336, 337] reported that formic acid accelerates the crystallization of MA^+ cations. Previous work has therefore mainly dealt with the effect of formate on the morphology, nucleation and growth of $MAPbI_3$. There has also been a recent report of a highly fluorescent methylammonium lead bromide and formate mixture in water.[338] However, a fundamental understanding of the effects of formate on perovskite films has yet to be achieved.

Here, we uncover the key role of $HCOO^-$ anions in removing halide vacancies, which are the predominant lattice defects in $FAPbI_3$ perovskite films. This enables the PCE of the PSC to exceed 25%, combined with a high operational stability. Iodide vacancies are also the principal cause for the unwanted ionic conductivity of metal halide perovskites which exerts a deleterious effect on their operational stability. We provide insight into the mode of formate intervention. Formate is small enough to fit in the iodide vacancy,[333] thereby eliminating a prevalent and notorious defect in the metal halide perovskite that accelerates the nonradiative recombination of photogenerated charge carriers. In addition, $FAPbI_3$ perovskite films with improved crystallinity and larger grain size were achieved by introducing 2% FAHCOO into the precursor solution. The defect passivation and the improved crystallinity are essential to attain the record efficiency and excellent stability demonstrated by our $FAPbI_3$-based PSCs.

2.3.1 Experimental

Low-temperature (100 K) $^1H \rightarrow ^{13}C$ cross-polarization and directly detected ^{13}C (125.8 MHz) NMR spectra, and room-temperature ^{207}Pb (104.7 MHz) NMR spectra were recorded on a Bruker Avance III 11.7 T spectrometer equipped with a 3.2-mm low-temperature CPMAS probe. ^{207}Pb and ^{13}C spectra were referenced to lead nitrate at -3492 ppm and the CH_2 resonance of solid adamantane at 38.48 ppm, respectively, at room temperature. Room temperature ^{207}Pb spectra were recorded with a Hahn echo and an effective recycle delay of 17 ms. The low-temperature $^1H \rightarrow ^{13}C$ cross-polarization spectra of δ-$FAPbI_3$ and α-$FAPbI_3$ were recorded with 1 ms contact time, recycle delays of 1.5 s and 4 s, respectively, and 12 kHz MAS. The low-temperature $^1H \rightarrow ^{13}C$ spectra of FAHCOO and Fo-$FAPbI_3$ were recorded with 2 ms contact time, 10 s recycle delay and 12 kHz MAS. The quantitative, directly detected ^{13}C experiment on a scraped 2% Fo-$FAPbI_3$ film was performed with a single pulse experiment, 12 kHz MAS and a 10 s recycle delay, which is more than 5 times the longitudinal relaxation time of ^{13}C (1 s). All ^{13}C spectra were acquired with 100 kHz ^1H decoupling. The low-temperature $^1H \rightarrow ^{13}C$ cross-polarization spectrum of scraped 2% Fo-FAPbI3 thin-film was measured with 2 ms contact time, 4 s recycle delay and 12 kHz MAS. NMR characterization was performed with 5% Fo-FAPbI3, because the greater amount of formate in the sample provides higher sensitivity compared to 2% Fo-$FAPbI_3$. MACl was not included in the mechanosynthesized samples for NMR spectroscopy, because this would lead to broadening of the ^{13}C and ^{207}Pb resonances of $FAPbI_3$,[207] owing to different local environments with slightly different chemical shifts that arise from MA^+ substitution of nearest-neighbor and more distant A-site cations. This broadening would obscure the small changes in the ^{207}Pb and ^{13}C resonances that arise from the incorporation of formate. However, given that the incorporation of MA^+ ions have a minimal effect on the lattice structure, these findings also apply to the MA^+-doped composition studied in this work.

2.3.2 Results and Discussion

NMR Enabling the Atomic-level Structure

We prepared the samples by mixing FAI and PbI_2 powders with 5 mol% extra $FAHCOO^-$ using a mechano-synthesis method. MACl was not added to avoid broadening of resonances, affording greater resolution and therefore sensitivity to the local environments. The ^{207}Pb spectrum is sensitive to the nature of the anions coordinated to Pb^{2+} in the perovskite;[210] Figure 2-14 shows the ^{207}Pb spectrum of α-$FAPbI_3$ which resonances at 1543 ppm. The addition of 5% FABr results in a notable shoulder on the low-frequency side of the ^{207}Pb resonance, as shown in Figure 2-14b. Since $FAPbBr_3$ resonates at 510 ppm, the new ^{207}Pb environment has a slightly lower frequency than α-$FAPbI_3$. However, the ^{207}Pb resonance of the α-$FAPbI_3$ remained the same after adding 5% FAHCOO in the synthesis, which is strong evidence that $HCOO^-$ does not substitute for iodide anions on the α-$FAPbI_3$ lattice. This is also further supported by the density functional theory (DFT) calculations of the formation energy.[171]

To explore the local environment of the $HCOO^-$ anions in the Formate-$FAPbI_3$ perovskite, $^1H \rightarrow ^{13}C$ cross-polarization experiments were performed at 100 K.[207] Figure 2-14(d) shows ^{13}C resonance signals at 167.8 ppm and 158.5 ppm for the $HCOO^-$ and FA^+ environments in FAHCOO. Figure 2-14, (e) and (f) show the α-$FAPbI_3$ and δ-$FAPbI_3$ ^{13}C resonances at 153.4 ppm and 157.6 ppm, respectively. Upon mixing 5 mol% FAHCOO with $FAPbI_3$, the ^{13}C signal of α-$FAPbI_3$ remained unchanged, at 153.4 ppm, shown in Figure 2-14(g), which further corroborates the lack of substitution of iodide by $HCOO^-$ inside the $FAPbI_3$ lattice. The $HCOO^-$ peak, however, exhibited significant broadening, indicative of a distribution of local environments which could arise from interaction of the $HCOO^-$ anion with Pb^{2+} at the surface or grain boundaries of the perovskite, in contrast to the well-defined environment in crystalline FAHCOO. For the spin-coated 2% Fo-$FAPbI_3$ thin films, the formate ^{13}C signal is less intense, appearing as a shoulder on the peak of α-$FAPbI_3$ (Figure 2-15). This is due to a combination of the lower initial formate concentration and potentially greater evaporation of formate during annealing in the thin films compared to powders since the exposed area is greater, although the CP spectra are not quantitative. We further quantified the composition of the spin-coated 2% Formate-$FAPbI_3$ films using directly-detected ^{13}C NMR at 100 K (Table 2-7).

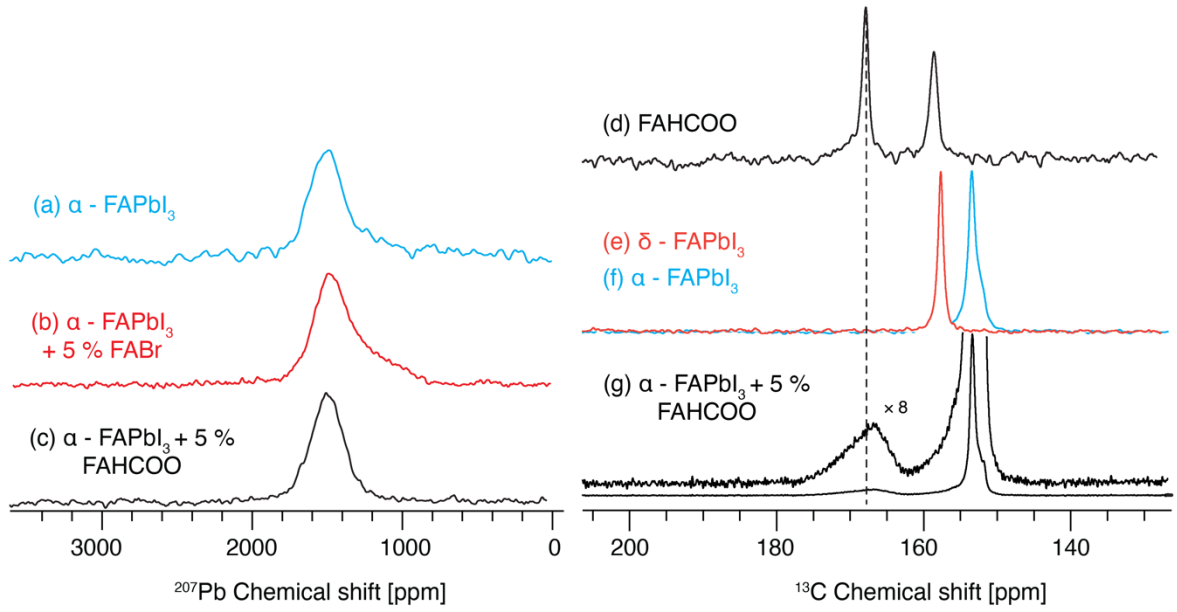

Figure 2-14. ^{207}Pb Solid-state NMR spectra recorded at 298 K and MAS rate of 15 kHz of (a) α-$FAPbI_3$ (b) α-$FAPbI_3$ + 5% FABr (c) α-$FAPbI_3$ + 5% FAHCOO. In a small amount of delta-phase can be seen, but this is distinct from the shoulder seen in (b). ^{13}C solid state NMR spectra recorded at 100 K and 12 kHz MAS of (d) FAHCOO (e) δ-$FAPbI_3$ (f) α-$FAPbI_3$, and (g) α-$FAPbI_3$ + 5% FAHCOO.

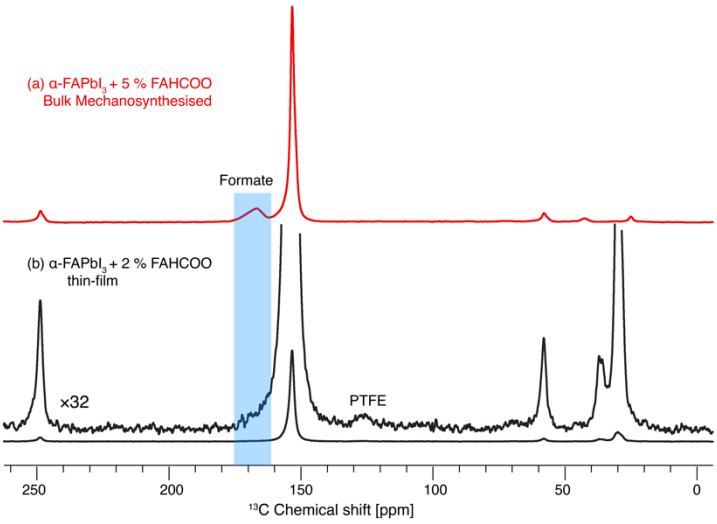

Figure 2-15. $^{1}H \rightarrow ^{13}C$ cross-polarization spectra of mechanosynthesized $FAPbI_3$ with 5% FAHCOO (a), and a scraped thin-film of 2% FAHCOO-$FAPbI_3$, recorded at 12 kHz MAS and 100 K.

Quantification of MA^+ in the 2% Fo-$FAPbI_3$ Thin Film

To quantify the amount of MA in the sample, the resonances in Figure 2-16 were integrated. The NMR signal of the FA includes two spinning sidebands, which are added to the integration of the central FA^+ peak. The percentage of MA^+ relative to FA^+ is then calculated from the ratio of the integrated NMR intensities, noting that a quantitative recycle delay of >5× the longest T_1 relaxation constant was used.

Table 2-7. Quantification of MA^+.

^{13}C Peak	Integral value
MA^+	2.5653
FA^+	46.5746
Spinning side band 1	0.4654
Spinning side band 2	0.3796

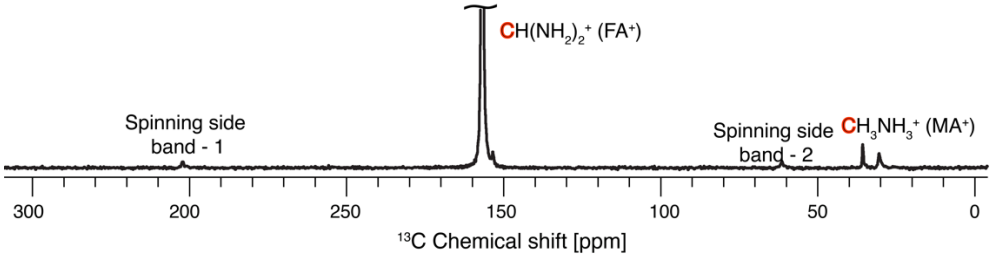

Figure 2-16. Quantitative directly detected ^{13}C solid-state NMR spectra of 2% Fo-$FAPbI_3$ scaped thin film at 12 kHz MAS and 100 K.

2.3.3 Conclusions

In conclusion, we demonstrate α-$FAPbI_3$ -based PSCs with a PCE of 25.6% (certified 25.2%) and high stability, achieved through solution processing by introducing 2% formamidinium formate into the $FAPbI_3$ perovskite precursor solution. Our solid-state NMR spectroscopy measurements together with molecular dynamics simulations analysis provide an understanding of the role of $HCOO^-$ anions as passivating agents for $FAPbI_3$ perovskites. Our findings pave the way for facile access to high-performance PSCs approaching their theoretical efficiency limit.

2.4 Local Structure and Quantification in Vapor-assisted Perovskite Growth

This section has been adapted from the following work with the permission from the journal:

Lu, H.; Liu, Y.; Ahlawat, P.; Mishra, A.; Tress, W. R.; Eickemeyer, F. T.; Yang, Y.; Fu, F.; Wang, Z.; Avalos, C. E.; Carlsen, B. I.; Agarwalla, A.; Zhang, X.; Li, X.; Zhan, Y.; Zakeeruddin, S. M.; Emsley, L.; Rothlisberger, U.; Zheng, L.; Hagfeldt, A.; Grätzel, M., Vapor-assisted deposition of highly efficient, stable black-phase $FAPbI_3$ perovskite solar cells. *Science* **2020,** *370* (6512), eabb8985.

Contribution statement: I designed, conducted, analyzed, interpreted and wrote up the solid-state NMR experiments together with CEA and LE. I collaborated on correcting the whole final manuscript.

The photoinactive δ form of $FAPbI_3$ is the most stable phase at room temperature, and the crystallinity of $FAPbI_3$ film is normally poor even after high temperature annealing. To avoid formation of the δ-phase and improve the crystallinity, various complex perovskite compositions have been developed. For example, a combination of MA^+, Cs^+, or Br^- are commonly mixed with $FAPbI_3$, especially for the record high efficiency PSCs.[339-342] However, these mixed perovskite compositions show an unwanted blue-shift in their light absorption. Moreover, MA^+ is thermally unstable,[343, 344] whereas Br^-/I^- mixtures suffer from severe ion segregations under long-term light illuminations.[345] Thus, a mixing strategy may be unfavorable regarding long-term operational stability. Hence obtaining efficient, phase pure and stable $FAPbI_3$ perovskite layers is of vital importance for the perovskite research field.

In contrast to the previous mixing strategies, manipulation of surface energy has been reported to stabilize the perovskite phases and modify the gain growth orientations.[238, 346-349] For example, templated growth of oriented layered perovskites has been demonstrated for 2D perovskites,[348] and epitaxial growth and stabilization of α-$FAPbI_3$ has been reported recently.[349] Swarnkar et al. showed that α-$CsPbI_3$ can be stabilized in the form of colloidal quantum dots because of a large contribution of surface energy.[238] Fu et al. reported that functionalizing the surface of $FAPbI_3$ with large organic molecules could lower the formation energy to stabilize the α-$FAPbI_3$ at room temperature.[347] However, the performance, stability, or both of these systems are still poor comparing with those of mixed-cation-halide PSCs.[346]

Motivated by these promising strategies of surface-energy manipulations and our recent work using polyiodide vapor for scalable perovskites,[350] we developed a methylammonium thiocyanate (MASCN) vapor treatment method for preparing efficient and stable α-$FAPbI_3$ PSCs. Yellow-color δ-$FAPbI_3$ film was obtained by spin-coating a precursor solution of equal molar FAI and PbI_2 mixture. The as-fabricated δ-$FAPbI_3$ film was annealed at 100°C for 1 min. Then, the annealed film was put in a MASCN vapor environment for ~5 s until the yellow color changed to black. This vapor treatment was done under normal pressure as MASCN has a sublimation point < 100°C, which rendered the entire treatment process low-cost and of practical interest for industrial scale-up applications.

2.4.1 Experimental

Room-temperature ^1H (900 MHz) and ^{14}N (65.04 MHz) NMR spectra were recorded on a Bruker Avance Neo 21.1 T spectrometer equipped with a 3.2 mm low-temperature CPMAS probe. ^1H chemical shifts were referenced to solid adamantane (δ_H=1.91 ppm). ^{14}N chemical shifts were referenced to solid NH_4Cl (δ = 0 ppm). Echo-detected quantitative ^1H spectra used a recycle delay of ~200 s. Peak widths were fitted in Topspin 3.2 and the uncertainties were given at one standard deviation.

2.4.2 Results and Discussion

NMR Establishes Atomic-level Proximities

In order to unravel the role of MASCN during the vapor treatment solid-state nuclear magnetic resonance spectroscopy measurements were performed. We first carried out ^{14}N magic angle spinning (MAS) NMR measurements to investigate the effect of atomic-level interaction from the MASCN presence on the intrinsic crystallographic symmetry of the parent $FAPbI_3$ lattice. The ^{14}N MAS NMR spectra of $FAPbI_3$ features a ^{14}N spinning sideband (SSB) pattern, which corresponds to FA^+ reorientation on the picosecond timescale. Figure 2-17a and Figure 2-17b indicate that the SSB width is altered by the MASCN surface treatment. It has been shown previously that the width of the ^{14}N SSB manifold is correlated with the symmetry of the cuboctahedra cavity in which FA^+ reorientation takes place, whereby a narrower manifold indicates a symmetry closer to cubic.[214] MASCN treated $FAPbI_3$ thin film features 3-4 orders of SSB less in ^{14}N spectrum compared to the reference $FAPbI_3$, indicative that FA is in a more symmetric environment. Noting that, for both the reference and the treated $FAPbI_3$, the central peak of the ^{14}N MAS NMR spectra has identical shift. We conclude that MASCN is most likely interacting with the surface of the $FAPbI_3$ perovskites. We carried out ^1H MAS NMR experiments to assess the amount

of MA cation that is present in $FAPbI_3$ after the MASCN treatment. Figure 2-17c shows the ^1H spectrum of MASCN salt which identifies two distinct ^1H environments corresponding to CH_3 at 3.05 and NH_3^+ at 7.45 ppm. $MAPbI_3$ and reference $FAPbI_3$ perovskites yielded signals at 3.5, 6.5 ppm corresponding to MA^+ (Figure 2-17d) and at 7.5, 8.2 ppm corresponding to FA^+ (Figure 2-17e). Figure 2-17f shows the ^1H spectrum of treated $FAPbI_3$ perovskites, which for the FA^+ protons is identical to that of the reference $FAPbI_3$. When the signal is enhanced 8 times, small additional peaks at 3.5 and 6.3 ppm confirm that MA^+ is present in small quantities within the $MA_xFA_{1-x}PbI_3$ environment, and not present as MASCN or any other form of MA^+. This observation is further corroborated by two-dimensional ^1H-^1H spin diffusion measurements on MASCN treated $FAPbI_3$ film (Figure 2-17g), where the appearance of the cross-peak between MA^+ and FA^+ suggests that MA^+ and FA^+ moieties are within 10 Å of each other. Moreover, to quantify the amount of MA in the treated $FAPbI_3$ film, we carried out quantitative solid-state one-dimensional measurements where the integral over the peak suggests the amount of the respective species. Herein, the integral over the MA^+ peak suggests up to 1.8% of MA^+ in this vapor treated $FAPbI_3$ films. We conclude that during the first stage of the MASCN vapor treatment, MA^+ is incorporated into the surface of $FAPbI_3$ films, which initialized the phase transformation process.

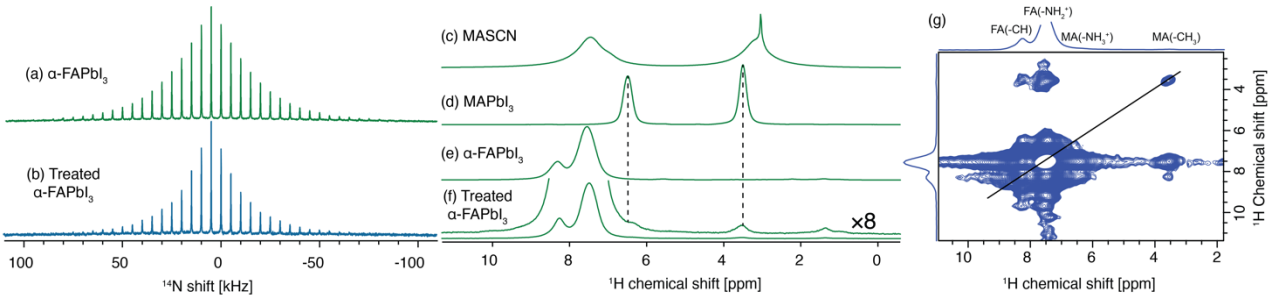

Figure 2-17. Solid state NMR measurements. Echo-detected ^{14}N NMR at 5 kHz MAS (a) α-$FAPbI_3$, (b) MASCN treated $FAPbI_3$. Echo detected ^1H MAS NMR (c) MASCN salt (d) $MAPbI_3$ (e) α-$FAPbI_3$ (f) MASCN treated $FAPbI_3$ (g) ^1H-^1H spin-diffusion experiment with 1 s of mixing interval.

2.4.3 Conclusions

In conclusion, we show a complete conversion from δ- to α-$FAPbI_3$ at 100°C using the MASCN vapor treatment method. This phase transition can also be achieved using FASCN vapor. The vapor-treated $FAPbI_3$ film remained in its pure black phase even after 500 hours of annealing at 85°C, whereas the reference $FAPbI_3$ film formed mainly PbI_2 during the heat exposure. X-ray diffraction data showed an improved crystallinity and preferred orientation of the $FAPbI_3$ films after vapor treatment. One-and two-dimensional NMR experiments were used to probe changes in symmetry and quantify the incorporation of MA^+ into the perovskite framework. We used these low-defect-density α-$FAPbI_3$ films to make PSCs with >23% PCE, long-term operational stability.

2.5 Intermediate Phase Formation during Perovskite Growth Revealed using NMR

This section has been adapted from the following work with the permission from the journal:

Zhang, J. H.; Wang, Z. W.; Mishra, A.; Yu, M. L.; Shasti, M.; Tress, W.; Kubicki, D. J.; Avalos, C. E.; Lu, H. Z.; Liu, Y. H.; Carlsen, B. I.; Agarwalla, A.; Wang, Z. S.; Xiang, W. C.; Emsley, L.; Zhang, Z. H.; Gratzel, M.; Guo, W. L.; Hagfeldt, A., Intermediate Phase Enhances Inorganic Perovskite and Metal Oxide Interface for Efficient Photovoltaics. *Joule* **2020**, 4 (1), 222–234.

Contribution statement: I designed, conducted, analyzed, interpreted and wrote up the solid-state NMR experiments together with DJK, CEA, and LE. I collaborated on correcting the whole final manuscript.

The unique properties of halide perovskite materials including long charge carrier diffusion length, high light-harvesting efficiency, and tunable band gap make them ideal materials for photoelectronic applications.[165, 168, 327, 351-353] To date, the certified PCE of organic-inorganic hybrid PSCs has reached 25%, which is higher than that of polycrystalline silicon solar cells.[354-357] Despite the encouraging PCE, the intrinsic instability of organic-inorganic hybrid perovskite (OIHP) materials, such as the degradation under moisture and heat, is hindering further industrialization of PSCs.[235, 311] By replacing the volatile organic cations with an inorganic cesium cation (Cs^+), the inorganic cesium lead halide perovskites, denoted as $CsPbX_3$ (X = Br, I), are attracting extensive research interests due to their potential to improve the stability of PSCs fundamentally.[358, 359] Interfacial contact plays an important role in high performance organic-inorganic PSCs.[360, 361] However, it has not been thoroughly studied in inorganic PSCs, especially the interfacial contact of inorganic perovskite and the metal oxide charge transport layer (such as TiO_2 and SnO_2).

Density-functional theory (DFT) calculations and X-ray photoelectron spectroscopy (XPS) measurements indicate that the inorganic perovskite has a weaker interaction with metal oxide due to the lack of hydrogen bonds at the interface as compared to OIHPs. The interfacial contact is closely related to the chemical interaction between the perovskite and metal oxide layers.[360] This leads to a potentially larger challenge in the inorganic perovskite/metal oxide interfacial contact compared to that of OIHP. Various organic additives have been employed to modify the interfacial contact and improve the efficiency in PSCs.[362] However, in inorganic perovskites, the existence of organic components compromises the original premise of preserving outstanding thermal stability.[363]

Here, we report an intermediate phase engineering strategy by introducing volatile acetate organic salts such as Formamidinium acetate (FAOAc) into the inorganic perovskite precursor solution, leading to the formation of an OIHP intermediate phase with strong hydrogen bonding at the perovskite/metal oxide interface. It optimizes the interfacial contact between all-inorganic perovskite and metal oxide of mesoscopic (meso-) and planar architectures, and also retains the thermal stability of all-inorganic perovskite without organic residues. With this strategy, the PCE of the champion device based on $CsPb(I_{0.75}Br_{0.25})_3$ is 17.0%. The open-circuit voltage (V_{oc}) of 1.34 V for this champion device in planar tin oxide (SnO_2) architecture is up to 86% of the theoretical V_{oc}, which is also the highest reported ratio in inorganic PSCs.

2.5.1 Experimental

Solid state NMR measurements. Room temperature ^{133}Cs (118.04 MHz and 65.58 MHz) NMR spectra were recorded on a Bruker Avance Neo 21.1 T spectrometer and Bruker Avance III 11.7 T spectrometer equipped with a 3.2 mm low-temperature CPMAS probe. ^{133}Cs shifts were referenced to 1 M aqueous solution of CsCl, using solid CsI (δ=271.05 ppm) as a secondary reference. ^1H chemical shifts were referenced to solid adamantane (δ_H = 1.91 ppm). Quantitative echo-detected ^{133}Cs spectra were recorded with recycle delay between 24 s to 100 s. 1H spectra were acquired with recycle delays between 3 and 10 s. Peak widths were fitted in Topspin 3.2.

Perovskite mechanosynthesis. Starting materials were stored inside a glove box under argon. Perovskite powders were synthesized by grinding the reactants in an electric ball mill (Retsch Ball Mill MM-200) using a grinding jar (10 ml) and a ball (⌀10 mm) for 60 min at 25 Hz. The resulting powders were annealed for 20 minutes at temperature specified below. The amounts of reagents taken into the synthesis were as follows:

$CsPbBr_3$: 0.212 g CsBr (1.00 mmol) and 0.367 g $PbBr_2$ (1.00 mmol). The material was annealed at 250°C.

$Cs_{0.95}FA_{0.05}PbBr_3$: 0.202 g of CsBr (0.95 mmol), 0.006 g of FABr (0.05 mmol) and 0.367 g $PbBr_2$(1.00 mmol). The material was annealed at 150°C.

$Cs_{0.90}FA_{0.10}PbBr_3$: 0.191 g of CsBr (0.90 mmol), 0.012 g of FABr (0.10 mmol) and 0.367 g $PbBr_2$ (1.00 mmol). The material was annealed at 150°C.

$Cs_{0.85}FA_{0.15}PbBr_3$: 0.180 g of CsBr (0.85 mmol), 0.018 g of FABr (0.15 mmol) and 0.367 g $PbBr_2$ (1.00 mmol). The material was annealed at 150°C.

$Cs_{0.80}FA_{0.20}PbBr_3$: 0.170 g of CsBr (0.80 mmol), 0.024 g of FABr (0.20 mmol) and 0.367 g $PbBr_2$ (1.00 mmol). The material was annealed at 150°C.

$Cs_{0.75}FA_{0.25}PbBr_3$: 0.159 g of CsBr (0.75 mmol), 0.031 g of FABr (0.25 mmol) and 0.367 g ($PbBr_2$1.00 mmol). The material was annealed at 150°C.

$Cs_{0.50}FA_{0.50}PbBr_3$: 0.106 g of CsBr (0.50 mmol), 0.062 g of FABr (0.50 mmol) and 0.367 g $PbBr_2$ (1.00 mmol). The material was annealed at 150°C.

$CsPbBr_3$-0.2$Pb(OAc)_2$: 0.212 g CsBr (1.00 mmol), 0.367 g $PbBr_2$ (1.00 mmol) and 0.065 g of $Pb(OAc)_2$ (0.2 mmol). The material was annealed at 150°C.

$CsPbBr_3$-0.5$Pb(OAc)_2$: 0.212 g CsBr (1.00 mmol), 0.367 g $PbBr_2$ (1.00 mmol) and 0.162 g of $Pb(OAc)_2$ (0.5 mmol). The material was annealed at 150°C.

$Cs_{0.80}FA_{0.20}OAc$: 0.154 g CsOAc (0.8 mmol), 20.82 g FAOAc (0.2 mmol).

$CsPbBr_3$-0.5FAOAc: 0.212 g CsBr (1.00 mmol), 0.367 g $PbBr_2$ (1.00 mmol) and 0.052 g of FAOAc (0.5 mmol). The material was annealed at two temperatures: 80°C and 280°C. The former is as the initial $CsPbBr_3$-0.5FAOAc powder. The latter is as the annealed $CsPbBr_3$-0.5FAOAc powder.

$Cs_{0.50}MA_{0.50}PbBr_3$: 0.106 g of CsBr (0.50 mmol), 0.056 g of MABr (0.50 mmol) and 0.367 g $PbBr_2$ (1.00 mmol). The material was annealed at 150°C.

$Cs_{0.90}(NH_4)_{0.10}PbBr3$: 0.191 g of CsBr (0.90 mmol), 0.0098 g of NH_4Br (0.10 mmol) and 0.367 g $PbBr_2$ (1.00 mmol). The material was annealed at 150°C.

$Cs_{0.90}BA_{0.10}PbBr_3$: 0.191 g of CsBr (0.90 mmol), 0.015 g of BABr (0.10 mmol) and 0.367 g $PbBr_2$ (1.00 mmol). The material was annealed at 150°C.

Perovskite powder from solution processing. The initial perovskite films were prepared by spin-coating the precursor solutions at 1000 rpm for 50 s, and annealing at 80°C for 30s to remove the excess DMSO. Then these films were scratched off for NMR characterization. The annealed perovskite films were prepared by spin-coating the precursor solutions at 1000 rpm for 50 s, and annealed at 280°C for 8 mins. Then these films were scratched off for NMR measurements.

The vaporized components from $CsPbBr_3$-0.5FAOAc powder. During the initial $CsPbBr_3$-0.5FAOAc powder annealed at 280°C, a glass slide is put on the crucible of the initial $CsPbBr_3$-0.5FAOAc powder to collected the vaporized components. Then the vaporized components are dissolved in the DMSO-d_6 for liquid-state ^{1}H NMR measurements.

2.5.2 Results and Discussion

Intermediate Phase Characterization using NMR

In order to verify the existence of an intermediate phase process, we carried out solid-state magic angle spinning (MAS) nuclear magnetic resonance (NMR) measurements on bulk mechanochemical perovskites as well as thin films. Here, we use $CsPbBr_3$ as a model perovskite because it is structurally similar to $CsPb(I_{0.75}Br_{0.25})_3$. Moreover, spectral features in $CsPbBr_3$ are well-resolved, unlike in $CsPb(I_{0.75}Br_{0.25})_3$ where chemical disorder leads to very broad ^{133}Cs resonances.[204]

We first check whether the doping with FAOAc leads to the incorporation of FA^+ or OAc^- (as a pseudohalide[333]) into the perovskite lattice of $CsPbBr_3$. Figure 2-18a shows ^{133}Cs MAS NMR spectra of $Cs_{1-x}FA_xPbBr_3$ (x = 0, 0.05, 0.10, 0.25, 0.50). The undoped $CsPbBr_3$ exhibits a relatively narrow (full width at half maximum of 400 Hz) peak at 101.7 ppm. Upon addition of FA^+, the peak shifts to lower ppm values and progressively broadens (the fitted values in Table 2-8), indicating the formation of mixed Cs^+/FA^+ perovskite phases.

The broadening is due to the presence of cesium sites with different numbers of nearest neighbor FA^+ in the neighboring cubo-octahedral cages. There are no other peaks present in the spectra, indicating that the mixed Cs^+/FA^+ alloys are phase pure. We have thus shown that FA^+ can be incorporated into the $CsPbBr_3$ perovskite lattice up to at least 50 mol%.

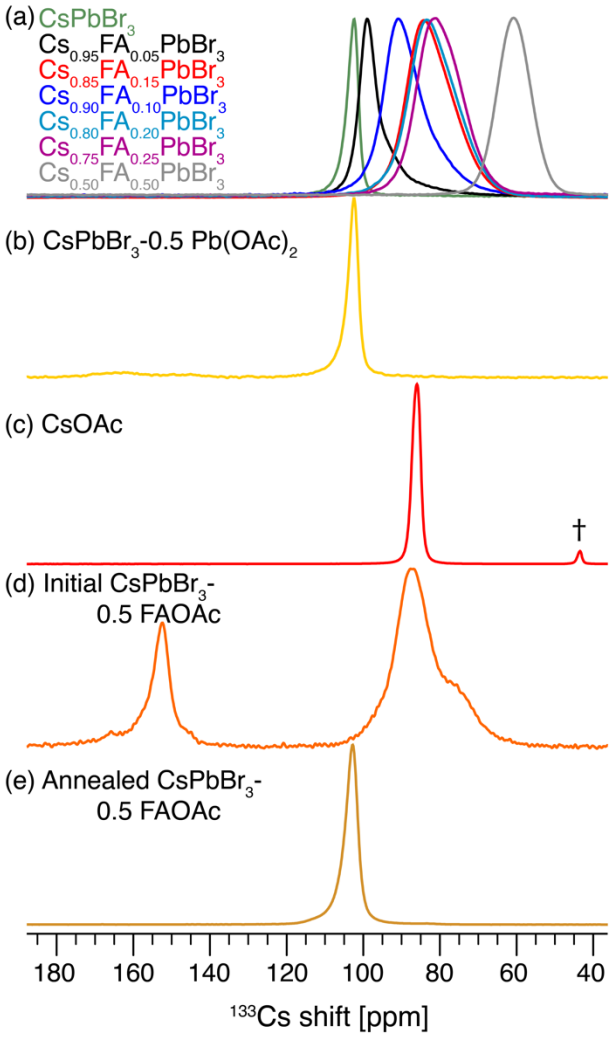

Figure 2-18. Solid-state MAS nuclear magnetic resonance (NMR) characterization of the materials. Echo-detected ^{133}Cs spectra at 21.1 T, 298 K, and 20 kHz MAS of (a) $Cs_xFA_{1-x}PbBr3$, (x = 1.0,0.05, 0.10, 0.15, 0.20, 0.25, 0.50) (b) $CsPbBr_3$- 0.5 $Pb(OAc)_2$ (c) CsOAc (d) Initial $CsPbBr_3$-0.5 FAOAc, and (e) Annealed $CsPbBr_3$-0.5 FAOAc. The dagger symbol (†) indicates an impurity.

Figure 2-18b shows the ^{133}Cs NMR spectrum of $CsPbBr_3$ doped with 50 mol% of $Pb(OAc)_2$ ($CsPbBr_3$-0.5 $Pb(OAc)_2$). The peak position (~102 ppm) and its width (~400 Hz) are within error unchanged with respect to neat $CsPbBr_3$, indicating that the OAc^- is not incorporated into the perovskite lattice. In addition, we do not observe the formation of CsOAc, which would lead to the appearance of a peak at 86 ppm as shown in Figure 2-18c. We have therefore clearly shown that the acetate ion has no propensity to incorporate into $CsPbBr_3$ as a pseudohalide. The ^{133}Cs spectrum of $Cs_{0.80}FA_{0.20}OAc$ in Figure 2-19 (left panel) shows that the peak position (86 ppm) and its width (173±9 Hz) are within the experimental error unchanged with respect to those of neat CsOAc (86 ppm and 155±6 Hz, respectively), indicating that the FA is not incorporated into the CsOAc lattice.

We then look at $CsPbBr_3$-0.5 FAOAc, corresponding to the optimized composition in this work. The mechanochemical initial $CsPbBr_3$-0.5 FAOAc composition exhibits three peaks: at 78 (broad shoulder), 88 and 152 ppm (Figure 2-18). The first two broadening peaks located between these of $CsPbBr_3$ and $Cs_{0.5}FA_{0.5}PbBr_3$ and near that of CsOAc correspond to the disordered mixed-cation $Cs_{1-x}FA_x$-$PbBr_3$ 3D perovskite ($0<x<0.5$) and CsOAc. The peak at 152 ppm does not correspond to any of the known phases in the CsBr-$PbBr_2$ family. Since its position (152 ppm) is intermediate with respect to the pure 3D $CsPbBr_3$ perovskite (101.7 ppm) and the 0D non-perovskite Cs_4PbBr_6 phase (224.9 ppm),[210] we suggest it might be an intermediate of a not fully assembled 3D-like phase since structural heterogeneity is expected in insufficiently annealed samples. The annealed $CsPbBr_3$-0.5 FAOAc leads to the emergence of only one peak at 103 ppm, which corresponds to undoped $CsPbBr_3$.

In order to investigate the composition of the thermally decomposed organic products formed during annealing at 280°C, we collected the vaporized components on a glass slide and acquired a liquid-state ^{1}H NMR spectrum in DMSO-d_6 (Figure 2-19; right panel). The spectrum matches that of FAOAc (Figure 2-19; right panel), indicating that FAOAc volatilizes during high-temperature annealing.

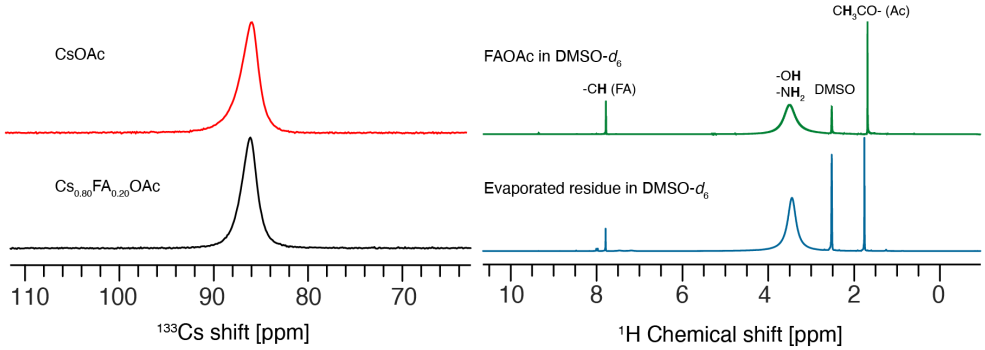

Figure 2-19. Left Panel - Echo-detected ^{133}Cs spectra at 11.74 T, 298 K and 20 kHz MAS of CsOAc and $Cs_{0.80}FA_{0.20}OAc$. Right panel - Liquid-state ^{1}H spectra at 9.4 T and 298 K of (I) neat FAOAc in DMSO-d_6, (II) the evaporated component formed during annealing at 280°C of $CsPbBr_3$-0.5FAOAc, dissolved in DMSO-d_6.

In addition, we collected the powders from $CsPb(I_{0.75}Br_{0.25})_3$-0.5 FAOAc thin films to investigate the fate of FAOAc during annealing in the mixed-halide composition used for device fabrication in this work by using solid-state ^{1}H MAS NMR (Figure 2-19–right panel). The powder from the initial $CsPb(I_{0.75}Br_{0.25})_3$-0.5 FAOAc films shows a peak corresponding to unreacted FAOAc at 2.0 ppm and a very narrow peak of residual DMSO at ~3.2 ppm. Annealing at 280°C leads to the disappearance of both these peaks, indicating that FAOAc is no longer present in the material. High-temperature annealing therefore leads to the removal of FA^+ from the perovskite lattice of $CsPb(I_{0.75}Br_{0.25})_3$ and a recovery of the parent all-inorganic structure.

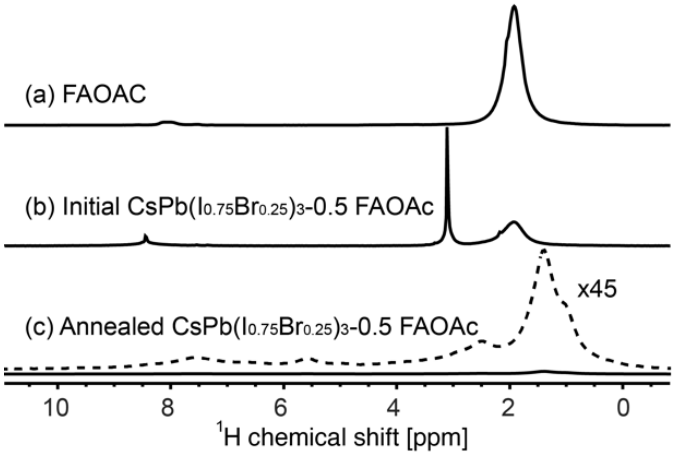

Figure 2-20. Echo-detected ^{1}H MAS NMR spectra at 21.1 T, 298 K and 20 kHz MAS of (a) neat FAOAc, (b) initial $CsPb(I_{0.75}Br_{0.25})_3$-0.5 FAOAc powder from solution processing, (c) annealed $CsPb(I_{0.75}Br_{0.25})_3$-0.5 FAOAc powder from solution processing. The dashed line is the spectrum magnified 45-fold to show the trace residual protons in the sample.

Besides FAOAc, volatile acetate salts with three different cations, methylammonium acetate (MAOAc), ammonium acetate (NH_4OAc) and butylammonium acetate (BAOAc) were further investigated as additives for $CsPb(I_{0.75}Br_{0.25})_3$. The annealed films of $CsPb(I_{0.75}Br_{0.25})_3$-0.5 MAOAc, $CsPb(I_{0.75}Br_{0.25})_3$-0.5 NH_4OAc and $CsPb(I_{0.75}Br_{0.25})_3$-0.5 BAOAc are uniform and pinhole-free as seen in the top-view SEM images. However, the cross-sectional SEM images of PSCs based on the three films show that only the $CsPb(I_{0.75}Br_{0.25})_3$-0.5 MAOAc perovskite completely penetrated into meso-TiO_2, while voids exist at the perovskite/meso-TiO_2 interfaces of the others. The $CsPb(I_{0.75}Br_{0.25})_3$-0.5 MAOAc device has an improved efficiency of 13.5%, and the $CsPb(I_{0.75}Br_{0.25})_3$-0.5 NH_4OAc and $CsPb(I_{0.75}Br_{0.25})_3$-0.5 BAOAc devices show low efficiencies of 11.56% and 11.11%, respectively. We carried out ^{133}Cs solid-state NMR experiments on $Cs_{0.5}MA_{0.5}PbBr_3$, $Cs_{0.9}(NH_4)_{0.1}PbBr_3$, and $Cs_{0.9}BA_{0.1}PbBr_3$ to establish whether MA^+, $NH4^+$, and BA^+ can dope into the $CsPbBr_3$ perovskite lattice. Upon addition of MA^+, the peak of $CsPbBr_3$ shifts to lower ppm values and broadens (Figure 2-21), indicating the formation of a mixed Cs^+/MA^+ 3D perovskite phase, analogous to the behavior previously reported for Cs^+/FA^+ 3D iodoplumbate[200] and above for 3D bromoplumbate perovskites. Again, the presence of only one peak evidences that the mixed Cs^+/MA^+ material is phase pure. Therefore, MA^+ has the capacity to replace at least 50 mol% Cs^+ in the $CsPbBr_3$ perovskite lattice with no phase

segregation. Doping with NH_4^+ and BA^+ leads to a different behavior: the distribution of Cs^+ in $Cs_{0.9}(NH_4)_{0.1}PbBr_3$, and $Cs_{0.9}BA_{0.1}PbBr_3$ is heterogeneous, indicative of phase segregation. The 3D perovskite peak of $CsPbBr_3$ in the two mixtures is largely unchanged as compared to neat $CsPbBr_3$, whilst a broad overlapping component appears in both cases indicating the formation of mixed Cs^+/NH_4^+ and Cs^+/BA^+ bromoplumbate phases. These secondary phases are likely 1D[364] and 2D,[365] respectively, analogous to their undoped counterparts. Further, the XRD peaks of the $CsPb(I_{0.75}Br_{0.25})_3$-0.5 MAOAc initial film are shifted left compared to those of the initial control film, which confirms the formation of an OIHP intermediate phase $Cs_{1-x}MA_xPb(I_{0.75}Br_{0.25})_3$ as MA^+ dopes into the perovskite lattice.[200] This result is expected, as the radii of NH_4^+ and BA^+ are not compatible with a cubic 3D perovskite lattice.

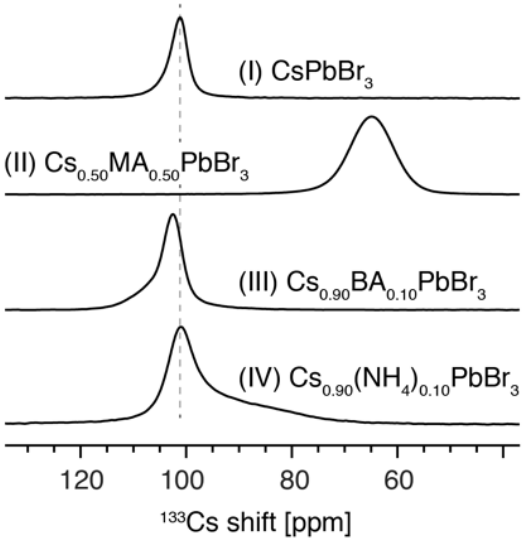

Figure 2-21. Echo-detected ^{133}Cs spectra at 21.1 T, 298 K, and 20 kHz MAS of $CsPbBr_3$, $Cs_{0.5}MA_{0.5}PbBr_3$, $Cs_{0.9}(NH_4)_{0.1}PbBr_3$, and $Cs_{0.9}BA_{0.1}PbBr_3$.

2.5.3 Conclusions

In conclusion, we have developed a novel intermediate phase engineering strategy to enhance the interfacial contact between the all-inorganic perovskite and metal oxide by introducing organic volatile salts into the inorganic perovskite precursor solution. According to our thorough investigation of volatile salts with different cations and anions using solid state NMR, we found that the introduction of organic cations (such as MA^+ and FA^+) which can be doped into the cubic perovskite lattice, lead to the formation of an OIHP intermediate phase in the initial film. These results enabled us to come up with structural model presented in the Figure 2-22. Meanwhile, the strong hydrogen bonding between OIHP intermediate phase and metal oxide promotes the high-quality interfacial contact. With this strategy, the champion planar-device achieves a PCE of 17.0% with a V_{oc} of 1.34 V. The PCE and V_{oc} are 66% and 86% of their Shockley-Queisser limits, which are the highest values reported for inorganic PSCs.

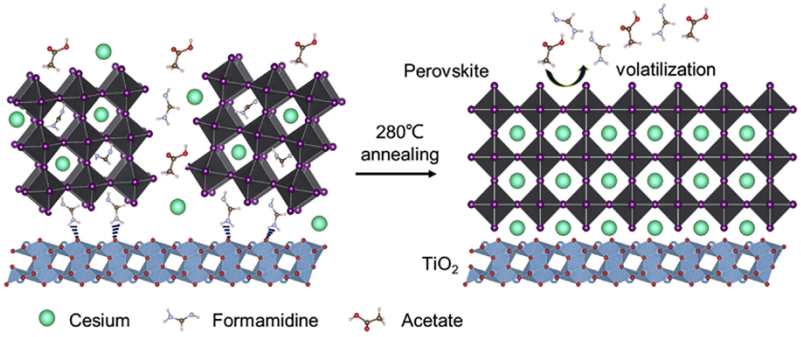

Figure 2-22. Schematic illustration of the Intermediate phase engineering (IPE) process.

Table 2-8. ^{133}Cs shift and peak width of the NMR spectra reported in this work.

Material	^{133}Cs Shift [ppm]	FWHM [Hz]
$CsPbBr_3$	101.7	400
$Cs_{0.95}FA_{0.05}PbBr_3$	99.2	650
$Cs_{0.90}FA_{0.10}PbBr_3$	91.1	1330
$Cs_{0.85}FA_{0.15}PbBr_3$	84.2	1650
$Cs_{0.80}FA_{0.20}PbBr_3$	82.8	1690
$Cs_{0.75}FA_{0.25}PbBr_3$	80.5	1630
$Cs_{0.50}FA_{0.50}PbBr_3$	60.2	1210
$CsPbBr_3$-20% $Pb(OAc)_2$	102.1	410
$CsPbBr_3$-50% $Pb(OAc)_2$	101.9	380
CsOAc	86	156
$Cs_{0.80}FA_{0.20}OAc$	86	173
Initial $CsPbBr_3$-50% FAOAc	78 88 152	1084 1269.4 567.5
Annealed $CsPbBr_3$-50% FAOAc	102.1	440
$Cs_{0.50}MA_{0.50}PbBr_3$	64.9	532
$Cs_{0.90}(NH_4)_{0.10}PbBr_3$	Component 1: 102.2 Component 2: 106.2	277 565
$Cs_{0.90}BA_{0.10}PbBr_3$	Component 1: 101.0 Component 2: 92.6	381 1428

In conclusion, this chapter includes a few examples of applications of NMR in hybrid perovskites. During my PhD, I have also worked on other applications that can be found in literature.[270, 271, 366-369]

Chapter 3 Dynamics in Hybrid Perovskites

This chapter has been adapted from the following work with the permission from the journal:

Mishra, A.; Hope, M. A.; Grätzel, M.; Emsley, L., A Complete Picture of Cation Dynamics in Hybrid Perovskite Materials using Solid State NMR Spectroscopy. *(submitted)*

Contribution statement: I designed, conducted, analyzed, interpreted and wrote up the manuscript together with MAH and LE.

Hybrid perovskites exhibit a variety of complex atomic-level motions spanning a wide range of frequencies. This includes ion migration on long time scales (milliseconds to hours),[370, 371] low energy polar (optical) vibrational modes of the metal-halide sublattice (up to ps),[372, 373] and reorientation of the A-site cation within the cuboctahedral cavities of the inorganic lattice on a similar timescale (~0.1-1 ps).[182, 186, 374, 375] These multi-timescale structural dynamics affect key electronic properties such as exciton binding energies and charge-carrier mobilities.[376-383] The rotation of the A-site cation is particularly important because it has also been shown to be linked with key phenomena such as efficient charge separation,[384] tolerance to intrinsic point defects,[385] and dynamic splitting of band extrema.[386]

MA^+ cation dynamics have been widely explored through a range of techniques including quasi-elastic and inelastic neutron scattering,[387-391] dielectric spectroscopy,[370] millimeter-wave spectroscopy,[392] two-dimensional infrared spectroscopy,[393, 394] and NMR spectroscopy.[22, 185, 186, 199, 207] The MA^+ cation dynamics have been further found to correlate strongly with the crystallographic perovskite phase evolution.[168] Amongst these techniques, NMR relaxometry and linewidth analysis have proved to be sensitive probes of both the nature and rate of motion.[185, 186, 199, 206, 207] Notably, ^2H and ^{14}N quadrupolar relaxation measurements performed under static conditions have been used to determine the correlation times about each of the two unique principal axes of the MA^+ ion as shown in Figure 3-1a.[185]

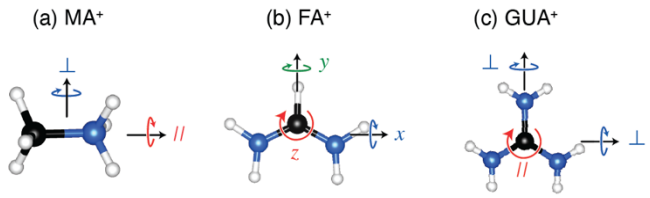

Figure 3-1. The Principal axes of rotation of most commonly employed cations. (a) Methylammonium ion (MA^+) (b) Formamidinium ion (FA^+) (c) Guanidinium ion (GUA^+). H, C, N atoms are represented by white, black and blue balls, respectively.

In contrast, there has been much less focus on dynamics of the FA^+ cation, despite it being the most widely used in optoelectronic applications.[171, 395] Experimental studies using two-dimensional infrared spectroscopy[396] and low temperature neutron scattering[397] rely heavily on molecular dynamic simulations to aid interpretation. ^1H NMR relaxometry[182, 398] and ^{14}N linewidth analysis[207] have been used to study FA^+ dynamics, but with simple motional models that rely on a series of assumptions (Bloembergen-Purcell-Pound theory and model free analysis) and that yield only a single correlation time, while FA^+ motion is notably characterized by rotational rates about three distinct principal axes (Figure 3-1b). Device-relevant multi-cation systems introduce additional experimental complexity. As a result, a complete picture of the dynamics in $FAPbI_3$ and mixed-cation perovskites is lacking.

Here, we use variable temperature, multi-nuclear ^2H and ^{14}N NMR relaxometry under magic-angle-spinning (MAS) to determine the rotational rates and activation energies for each distinct axis of FA^+, MA^+ and GUA^+ in a series of contemporary multi-cation perovskite compositions. MAS critically facilitates the study of lower symmetry cations and mixtures. We discover noticeably faster rotational dynamics for MA^+ in mixed FA^+/MA^+ compositions, whereas the FA^+ dynamics are essentially unaffected. In contrast, we find that the addition of Cs^+ into the FA^+ matrix does change the FA^+ motion at room temperature significantly, largely because of changes in the phase transition temperature. Further, extending the approach to a mixed GUA^+/MA^+ perovskite, we find that MA^+ rotation is again faster than in $MAPbI_3$, and that surprisingly GUA^+ also exhibits fast picosecond rotation, despite its bulky nature.

Now, I will mention the experimental details followed by the results and discussion.

3.1 Experimental

Materials. The following materials were used: formamidinium iodide (Sigma, >99%), PbI_2 (Sigma, 99%), methylammonium iodide (Sigma, >99%), d-FAI (Cortecnet, 85% CD), and d_5-FAI (Cortecnet, 85% CD deuterated, 90% ND_2 deuterated). d_4-FAI and d_3-MAI were prepared by dissolving in heavy water (1:40 mol/mol ratio), followed by evaporation. This yielded ~50% deuterium on the FAI and MAI. Highly deuterated MAI was prepared by repeating 5 times the dissolution and evaporation steps to yield about ~90% deuteration.

Bulk sample preparation. The perovskite materials were prepared using mechanosynthesis following the previously published protocol.[268] The precursors (PbI_2, FAI, *d*-FAI/d_4-FAI/d_5-FAI, CsI, d_6-GUAI and d_3-MAI/MAI, ~100 mg total) were mixed in the appropriate molar ratio and ground in an electric ball mill (Retsch MM-400) using a PTFE jar (10ml) and stainless-steel ball (⌀10 mm) for 30 minutes at 25 Hz. In order to prepare a low-deuterated $MAPbI_3$ sample, protonated MAI was appropriately mixed. $FAPbI_3$ and FA^+/Cs^+ compositions were then annealed at 150°C for 20 mins; FA^+/MA^+, $FA^+/MA^+/Cs^+$ and MA^+/GUA^+ compositions were annealed at 120°C for 20 mins, and $MAPbI_3$ samples were annealed at 60°C for 10 mins.

High purity sample preparation. High-purity partially deuterated $FA_{0.78}MA_{0.22}PbI_3$ was prepared using a solution-based antisolvent method. A 1.5 M solution was prepared by dissolving d_4-FAI (96 mg), d_3-MAI (38 mg) and PbI_2 (365 mg) in gamma-butyrolactone (0.53 mL) at 50 °C. Acetonitrile (0.5 mL) was added and the temperature increased to 60 °C for an hour before collecting over vacuum and washing with acetonitrile.

Solid-state NMR measurements. Most NMR experiments (^{2}H, ^{14}N and ^{133}Cs) were performed on a 900 MHz (21.1 T) Avance Neo Bruker NMR spectrometer equipped with a low temperature magic angle spinning (LTMAS) 3.2 mm triple resonance probe with zirconia rotors spinning at 10 kHz MAS, unless otherwise stated. Temperature measurements were performed at each variable temperature point by measuring the ^{207}Pb chemical shift of $Pb(NO_3)_2$,[399] and therefore a few grains of $Pb(NO_3)_2$ was put on the top of the sample, separated from the sample with PTFE tape**.** Further ^{2}H and ^{1}H T_1 measurements were performed on a Bruker Avance III 500 MHz (11.7 T) NMR spectrometer equipped with a 3.2 mm triple resonance LTMAS probe with zirconia rotors spinning at 10 kHz or 15 kHz. High temperature ^{2}H and ^{1}H T_1 experiments were performed on a Bruker Avance III 400 MHz (9.4 T) NMR spectrometer equipped with a 2.5 mm triple resonance room-temperature magic angle spinning probe with zirconia rotors spinning at 5 kHz. ^{1}H, ^{2}H, ^{14}N and ^{133}Cs spectra were referenced to adamantane at 1.91 ppm, D_2O at 4.8 ppm, NH_4Cl at 0 ppm, and CsI at 271 ppm, respectively. ^{1}H and ^{2}H T_1 measurements were performed using saturation recovery experiments. ^{14}N T_1 measurements were performed using a Hahn-echo-detected inversion recovery sequence to avoid excessive heating by the higher power saturation pulses at the low ^{14}N frequency. For GUA^+, the ^{14}N T_1 was measured using an echo-detected saturation recovery experiment with a long 10 rotor-period, 17 kHz, phase-modulated saturation pulse[400] because the broad quadrupolar pattern could not be saturated or inverted with hard pulses. Typical radiofrequency powers of 54 kHz and 42 kHz were used for ^{2}H and ^{14}N, respectively.

3.2 Results

3.2.1 Symmetry and Phase Transitions in $FAPbI_3$

^2H and ^{14}N are quadrupolar nuclei (I = 1) which yield NMR spectra that are very sensitive to the local symmetry.[22, 401] To perform deuterium NMR measurements, deuterated $FAPbI_3$ was synthesized using *d*-FAI and d_4-FAI, with substitution of the CH and NH_2 hydrogens, respectively. Figure 3-2a and Figure 3-2b show the ^2H MAS spectra of *d*-$FAPbI_3$ and d_4-$FAPbI_3$ at room temperature in the metastable, cubic black phase (α, $Pm\bar{3}m$). *d*-$FAPbI_3$ shows one peak at 8.5 ppm, as expected (inset, Figure 3-2a), whereas two isotropic shifts are observed for d_4-$FAPbI_3$, corresponding to the two inequivalent deuterons arising from restricted rotation of the C-N bond, as also seen by solution NMR.[402] These can be assigned in the fully deuterated d_5-$FAPbI_3$ sample using a ^2H–^2H EXSY experiment on the basis of their proximity to the CD deuteron (Figure 3-12).

Figure 2e shows the ^{14}N MAS spectrum at room temperature, where the quadrupolar coupling results in a spinning sideband manifold over a width (FWHM) of ~20 kHz, which can be approximately fitted using a Czjzek model[403] (Figure 3-13), with an average C_Q of 27 kHz. This narrow width compared to the ^{14}N quadrupolar coupling constant (C_Q) for FA^+ of ~2.7 MHz in the absence of any motion indicates that the cation undergoes almost, but not quite, isotropic reorientation, as expected at room temperature in the cubic cavity.

The residual anisotropy is also visible as low-intensity spinning sidebands in the ^2H spectra (Figure 3-14), but the anisotropy is smaller for CD and the trans ND_2 deuteron than for the *cis* deuteron. This indicates that the anisotropy predominantly arises from preferred orientation of the x and z axes (using the axis scheme shown in Figure 3-1b), i.e., the S_{xx} and S_{zz} components of the order tensor are larger than the S_{yy} term, although the residual orientational order is very small, with $|S|$ on the order of 0.01. The similarity of the anisotropies for CD and the parallel ND_2 further corroborates the assignment of the ND_2 deuterons since they have similar orientations within the molecule (noting that quadrupolar coupling is invariant to a 180° rotation).

Black $FAPbI_3$ is known to undergo a phase transition at ~285 K from the cubic phase to the tetragonal phase (β, $P4_2/mbm$).[182, 404] This reduction is symmetry is clearly observed in the ^2H spectrum which shows a significantly broader sideband manifold at 260 K (Figure 3-2 c,d). This is associated with a distribution of quadrupolar coupling tensors corresponding to a distribution of motions with different orientational anisotropies. Due to the larger quadrupolar moment of ^{14}N, the ^{14}N spectrum becomes challenging to measure with conventional techniques in the β phase because the quadrupolar pattern becomes very broad.[398]

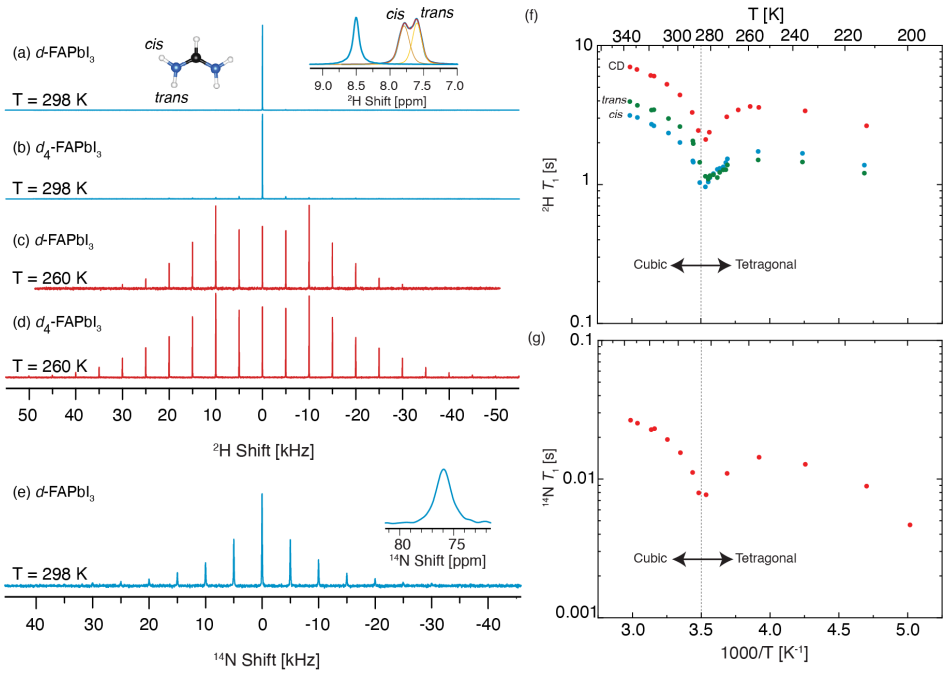

Figure 3-2. Single pulse solid-state ^2H MAS NMR spectra in the cubic phase of *d*-$FAPbI_3$ (a) and d_4-$FAPbI_3$ (b). The inset shows a zoom of isotropic resonances and the resolved peaks of the two ND_2 deuterons. ^2H MAS NMR spectra in the tetragonal phase (at 260 K) of *d*-$FAPbI_3$ (c) and d_4-$FAPbI_3$ (d). Hahn-echo detected ^{14}N MAS NMR spectra of *d*-$FAPbI_3$ (e). The inset shows the zoom of central peak. All spectra were recorded at 5 kHz MAS.

further details are in experimental details section. Measured ^{2}H and ^{14}N longitudinal relaxation time constants (T_1) of black $FAPbI_3$ as a function of temperature (f) and (g). The discontinuities in the T_1 behavior are indicative of phase transition in the material.

Motion on a similar timescale to the nuclear Larmor frequency (~10^8 Hz) induces longitudinal nuclear spin relaxation (T_1). ^{2}H and ^{14}N T_1 relaxation times are pertinent probes to investigate rotation as they depend upon the orientation of the electric field gradient (EFG) tensor with respect to the principal axes of rotation, and can therefore differentiate the correlation times about different axes. Figure 3-2f and Figure 3-2g show the measured ^{2}H and ^{14}N T_1 constants for $FAPbI_3$, which are observed to decrease with decreasing temperature, indicating that the cation rotation is in the so-called fast motion regime, (faster than the Larmor frequency). As the characteristic timescale of the rotational motion slows down at lower temperatures, it becomes closer to the Larmor frequency and induces relaxation more effectively. Superimposed on this general trend, we observe discontinuities at 285 K corresponding to the $\alpha\leftrightarrow\beta$ first-order phase transition. In the following we analyze the NMR relaxometry data in depth, exploiting the sensitivity of the T_1 relaxation to motion on this timescale to extract a detailed picture of the cation dynamics.

3.2.2 Rotational Dynamics in $FAPbI_3$

In order to extract motional rates from the relaxation data, a motional model is required. Here, we use the rotational diffusion model of Huntress et al. in which the orientation of the molecule is assumed to change randomly, resulting in overall rotational diffusion, analogously to the random translation that results in overall translational diffusion.[405] This rotational diffusion is characterized by rotational diffusion constants (D_i) about the three principal axes of the molecule, which are in turn related to angular correlation times about the corresponding axes by $D = 1/(6\tau_c)$.[405] When the principal axes are not equivalent by symmetry, the rotational diffusion rates about these axes are different. Note that, even with different rotational rates about the three axes, this rotational diffusion model assumes an isotropic orientational distribution.[405] Although as discussed above the orientation of FA^+ in $FAPbI_3$ is not quite isotropic, the very small residual orientational order would be a negligibly minor correction to the model. We note that the rotational diffusion model has previously been applied to $MAPbI_3$ in the tetragonal phase which has a much larger residual orientational order.[185]

Quadrupolar T_1 relaxation depends on the rotational diffusion rate about each axis, the size of the quadrupolar coupling, and the orientation of the quadrupolar coupling tensor with respect to the principal axes of the rotational diffusion tensor. Expressions for quadrupolar relaxation under rotational diffusion have been derived by Huntress;[405] in the case of the planar FA^+ cation, the ^{2}H relaxation is given by

$$\frac{1}{T_1(^{2}\mathrm{H})} = \frac{1}{32}\frac{(2\pi C_\mathrm{Q})^2}{D_r}\left\{\left[4D_x + (\eta-1)^2 D_y + (\eta+1)^2 D_\mathrm{z}\right]\cos^2\phi \;+\left[4D_y + (\eta-1)^2 D_x + (\eta+1)^2 D_\mathrm{z}\right]\sin^2\phi - \frac{(\eta-3)^2}{3}\frac{(D_x - D_y)^2}{D_\mathrm{z} + D_s}\cos^2\phi\sin^2\phi\right\} \tag{3.1}$$

$$D_r = D_x D_y + D_x D_\mathrm{z} + D_y D_\mathrm{z}$$

$$D_s = \frac{1}{3}(D_x + D_y + D_z)$$

where C_Q is the quadrupolar coupling constant in units of Hz, η is the quadrupolar asymmetry, ϕ is the angle between the EFG principal axis $V_{zz}^{2\mathrm{H}}$ (along the deuterium bond) and the x-axis of the diffusion tensor. For ^{14}N, where the principal component of the EFG tensor is perpendicular to the plane, T_1 is given by

$$\frac{1}{T_1(^{14}\mathrm{N})} = \frac{1}{32}\frac{(2\pi C_\mathrm{Q})^2}{D_r}\left\{\left[4D_z + (\eta+1)^2 D_y + (\eta-1)^2 D_x\right]\cos^2\phi' \;+\left[4D_z + (\eta+1)^2 D_x + (\eta-1)^2 D_y\right]\sin^2\phi' - \frac{4\eta^2}{3}\frac{(D_x - D_y)^2}{D_z + D_s}\cos^2\phi'\sin^2\phi'\right\} \tag{3.2}$$

where ϕ' is the angle between $V_{xx}^{14\mathrm{N}}$ and the x-axis of the diffusion tensor.

Table 3-1. Nuclear quadrupolar tensor parameters for FA^+

Nucleus	C_Q (MHz)	η	ϕ (°)
^{14}N	2.7 ± 0.2	0.26	55.5
^{2}H-CD	0.165 ± 0.005	0.16	90
^{2}H-ND_2- *trans*	0.207 ± 0.005	0.17	-84.2
^{2}H-ND_2- *cis*	0.207 ± 0.005	0.17	32.8

The quadrupolar parameters used here for the ^{2}H and ^{14}N nuclei in FA^+ are given in Table 3-1 (see also Figure 3-29) It is the quadrupolar coupling constant in the absence of motion that dictates the quadrupolar relaxation and to measure this experimentally, all motion must be frozen out. However, in $FAPbI_3$, even at ~100 K, the motion is not completely arrested (see Figure 3-15). To counter this, we measured the ^{2}H quadrupolar couplings in *d*-FAI and d_4-FAI at 100 K (Figure 3-16 and Figure 3-17), and use those values as proxies. The ^{14}N quadrupolar coupling is challenging to measure due to the large width of the quadrupolar pattern. Therefore, we have used the value calculated from density functional theory (DFT) by Kubicki et al.[207] of 2.7 MHz. We note that Mozur et al.[398] calculated a C_Q of 2.8 MHz in $FAPbBr_3$ and we have calculated C_Q = 2.4 MHz in FACl; therefore, we estimate an uncertainty of ~0.2 MHz.

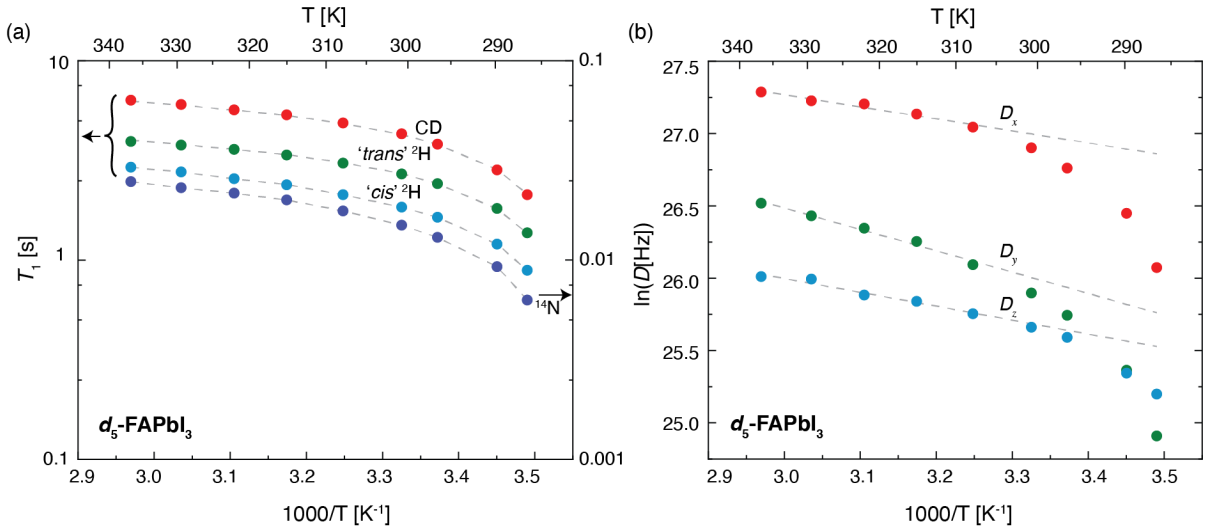

Figure 3-3. d_5-$FAPbI_3$ NMR relaxometry and rotational diffusion rates. (a) The three ^{2}H and one ^{14}N T_1 constants measured as a function of temperature in the cubic phase. Grey lines indicate the fit to the rotational diffusion model. (b) Arrhenius plot of rotational diffusion constants derived from (a). Grey lines indicate the fit to the Arrhenius behavior. Only the five highest temperature points were considered in the Arrhenius fit as the phase transition at ~ 285 K cause deviation from Arrhenius behavior.

To extract the rotational rates about the three axes, the T_1 constants of all three deuterons and ^{14}N must be combined, therefore we measured these for perdeuterated d_5-$FAPbI_3$ (Figure 3-3a). As the cubic α-$FAPbI_3$ phase is the most relevant to photovoltaic applications, we focus on the temperature range 290 – 340 K. At each temperature, the four T_1 constants were combined to give D_x, D_y, and D_z using the above equations (Figure 3-3b). The resulting T_1 constants (dashed lines in Figure 3-3a) match the experimental data extremely well, lending confidence in the model. The determined rotational diffusion constants show an Arrhenius dependence above 305 K, below which deviation is observed due to the nearby first-order phase transition (cf. Figure 3-2). Arrhenius analysis gives the activation energies (E_a) about each axis independently (Table 3-2). Using the relation $D = 1/(6\tau_c)$, the correlation time about each axis was calculated at 298 K (Table 3-2). from the data shown in Figure 3-3a; note that due to non-Arrhenius behavior near the phase transition, the correlation time was interpolated directly from the adjacent data, not taken from the Arrhenius analysis. The motion about all three axes is on the picosecond timescale, with rotation fastest about the *x*-axis, as predicted by Fabini et al. using molecular dynamics simulations[182] and in line with the relative moments of inertia $I_x < I_y < I_z$.[406]

Table 3-2. Activation energy (E_a) and correlation time (τ_c) at 298 K determined in this work for rotation about each axis FA^+ in $FAPbI_3$

Axis	E_a (meV)	τ_c(ps), 298 K
x	62 ± 17	0.38 ± 0.08
y	130 ± 16	1.05 ± 0.24
z	99 ± 26	1.3 ± 0.5

3.2.3 FA^+ Dynamics in FA^+/Cs^+-alloyed Perovskites

Alloying $FAPbI_3$ with a small amount of Cs^+ is the best strategy to-date to suppress the detrimental processes of ion migration, and light-induced phase segregation in mixed-halide perovskites, which limit device performance and lifetimes.[192, 367, 395, 407-410] In order to assess the changes in the FA^+ dynamics on Cs^+ substitution, d_5-$FAPbI_3$ was substituted with 5% Cs^+ as confirmed by ^{133}Cs MAS NMR (Figure 3-18).[200] Compared to pristine $FAPbI_3$, we note that the phase transition temperature was raised to 300 K, consistent with prior work.[404] The ^{2}H T_1 is shorter for the Cs^+/FA^+ composition around room temperature, indicating that the motion is slower due to the vicinity of the phase transition (Figure 3-4 and Figure 3-38, Table 3-7). However, at higher temperatures, the T_1 time constants for $FAPbI_3$ and $Cs_{0.05}FA_{0.95}PbI_3$ are the same to within error, suggesting that there is no significant change in the energy landscape for FA^+ rotation (Figure 3-35).

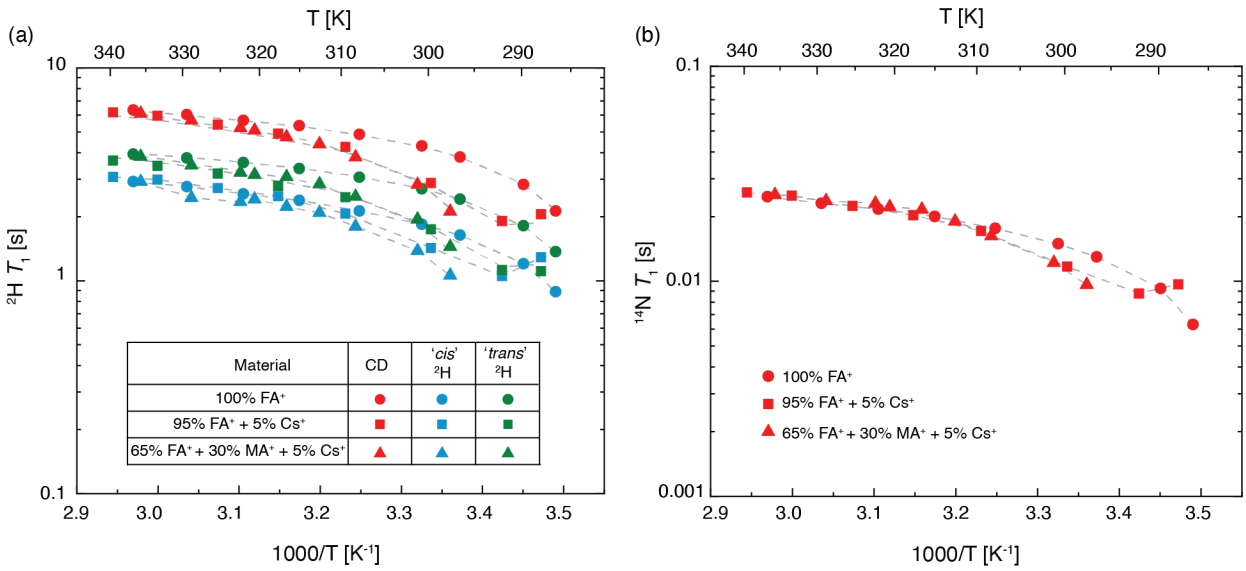

Figure 3-4. FA^+ dynamics in Cs-alloyed perovskite compositions. Experimentally measured (a) ^{2}H, (b) ^{14}N T_1 as a function of inverse temperature. Dashed lines represent fitted T_1 values using the rotational diffusion model.

Further alloying with MA^+ to yield a triple-cation composition[326] does not significantly change the experimental FA^+ T_1 values (Figure 3-4). We conclude that FA^+ dynamics are similar in the single, double and triple cation compositions.

3.2.4 FA^+ Dynamics in FA^+/MA^+ Perovskites

To explore the effect of MA^+ doping on the cation dynamics directly, we synthesized deuterated $FA_xMA_{1-x}PbI_3$ perovskite compositions. First, we determine the FA^+ dynamics. As shown in Figure 3-5a, all four deuterium signals are resolvable allowing all the necessary ^{2}H and ^{14}N T_1 constants to be measured. The ^{14}N sideband manifold of FA^+ is broader than in pure $FAPbI_3$ (Figure 3-19) because MA^+ substitution breaks the local cubic symmetry. The ^{14}N sideband manifold of MA^+ is narrower than FA^+ due to the smaller C_Q of the former, but still broader than the isotropic signal observed in the cubic phase of pure $MAPbI_3$ due to the presence of FA^+. As shown in Figure 3-5b,c the ^{2}H and ^{14}N relaxation times for FA^+ are largely unchanged as the composition is changed to include up to 40% MA^+, indicating that the FA^+ cation dynamics in the cubic phase are essentially unaltered by MA^+ substitution (Figure 3-35 and

Figure 3-36). Unlike for Cs^+ doping, there is little change in the α ⟷ β phase transition temperature for $FAPbI_3$ upon MA^+ substitution.[397, 411]

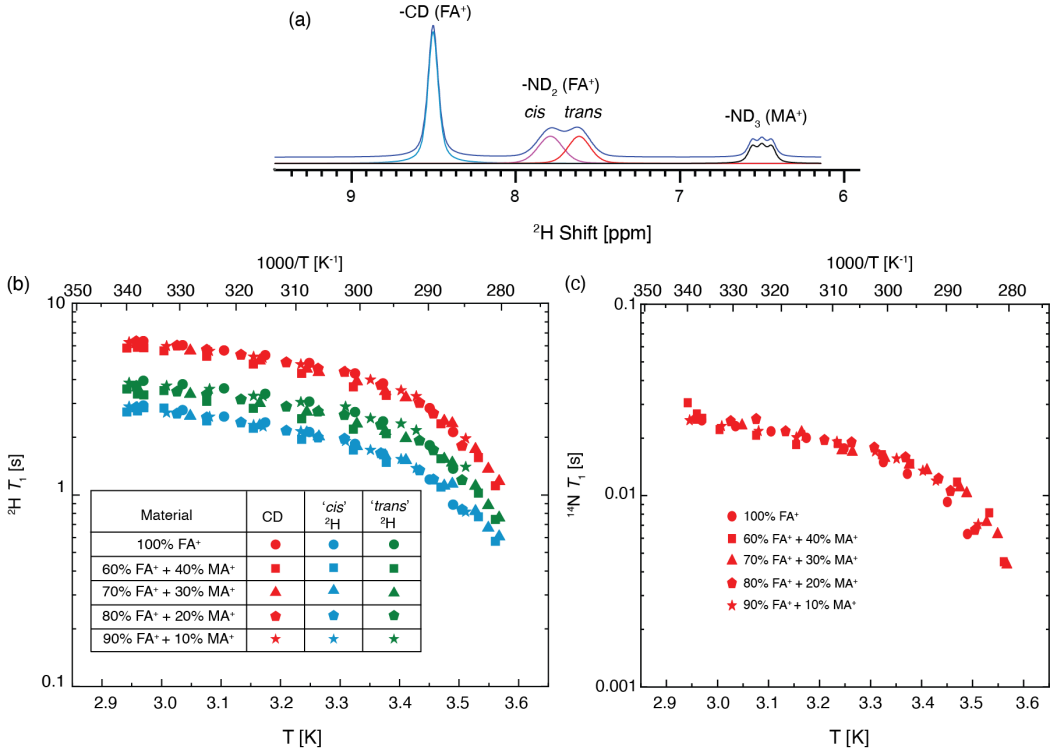

Figure 3-5 FA^+ dynamics in $FA_xMA_{1-x}PbI_3$ perovskite compositions. (a) Single pulse solid-state ^2H MAS NMR spectra of the cubic phase of $FA_{0.70}MA_{0.30}PbI_3$. The MA^+ peak shows J-coupling of $^1J(^2H\text{-}^{14}N)$ = 8.25 Hz. The deconvolution of all four sites is shown below the spectrum. Experimentally measured(b) ^2H and, (c) ^{14}N T_1 as a function of inverse temperature and as a function of x in $FA_xMA_{1-x}PbI_3$.

3.2.5 MA^+ Dynamics in FA^+/MA^+ Perovskites

Having analyzed the FA^+ dynamics in mixed compositions, we now turn to MA^+. Surprisingly, mechanosynthesized $FA_{0.7}MA_{0.3}PbI_3$ exhibits a maximum in the ^2H T_1 at 310 K (Figure 3-6). As discussed above, the cations are rotating faster than the Larmor frequency ($\omega_0\tau_c \ll 1$) and this fast-motion limit is characterized by a T_1 that increases with increasing temperature. However, above 310 K, T_1 decreases. This intriguing effect is consistently observed across different batches and different FA^+/MA^+ compositions (Figure 3-20, Figure 3-21, Figure 3-22, and Figure 3-23).

T_1 maxima have previously been observed for ^1H, ^{13}C and ^{15}N in pure $MAPbI_3$ and were ascribed to the contribution of spin–rotation relaxation, which becomes more efficient at high temperatures.[206] However, since the spin–rotational relaxation rate is proportional to the square of the nuclear magnetic moment, protons on the MA^+ which are subject to the same rotation should relax $\left(\gamma_{1H}/\gamma_{2H}\right)^2$ = 42 times faster than deuterium spins.[412] Contrary to this, we observed that MA^+ ^1H relaxation is slower than ^2H relaxation, even after accounting for the equilibration of T_1 by fast spin-diffusion between MA^+ and FA^+ moieties (Figure 3-24 and Figure 3-25). This clearly rules out an appreciable contribution of spin–rotation to the ^2H T_1.

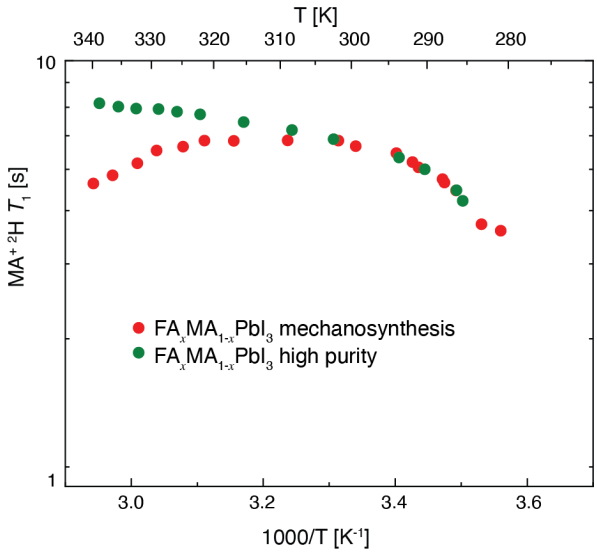

Figure 3-6. ^{2}H relaxation times (T_1) of MA$^+$ in $FA_xMA_{1-x}PbI_3$ prepared using either mechanosynthesis or a solution-based high-purity protocol as described in the text.

Alternatively, the T_1 maximum could be caused by a separate slow-motion process that becomes dominant above 310 K, since in the slow-motion regime, T_1 decreases with increasing temperature. This can be readily checked by testing the expected $T_1 \propto \omega_0^2$ field dependence of a slow-motion process.[66] However, the measured ^{2}H T_1 constants at 21.1 T and 11.7 T are essentially identical (Figure 3-26). Therefore, a slow-motion contribution to the ^{2}H T_1 can also be ruled out.

To propose a mechanism for the ^{2}H T_1 maximum, we consider that the measured ^{1}H relaxation times in solids are often limited by ^{1}H–^{1}H spin-diffusion to relaxation sinks such as paramagnetic impurities, which cause rapid relaxation of nearby protons.[413] We find this to be the case for mechanosynthesized $MAPbI_3$, for which the ^{1}H T_1 can be increased by deuteration to suppress ^{1}H–^{1}H spin diffusion (Figure 3-27). Furthermore, above the T_1 maximum the ^{2}H T_1 varies somewhat between samples and over time (Figure 3-21, Figure 3-22, and Figure 3-23), suggesting the role of defects or impurities. Although ^{2}H–^{2}H spin-diffusion is very slow (owing to the lower gyromagnetic ratio and lower concentration), physical diffusion of MA$^+$ and/or H$^+$ is a well known in the literature and could potentially cause a similar effect. At higher temperature, physical diffusion becomes faster, so that a deuteron would encounter a paramagnetic defect more quickly, on average, resulting in a shorter relaxation time. We note that this proposed mechanism would be field independent, because although the diffusion is slower than the Larmor frequency, it is not the spectral density of motion driving the relaxation, but rather it is the interaction with paramagnetic defects. To test this hypothesis, we prepared a high purity sample by solution processing (see experimental) with a lower concentration of paramagnetic relaxation sinks as evidenced by the longer ^{1}H T_1 (Figure 3-28). At lower temperatures, the ^{2}H T_1 constants of the two samples are the same (Figure 3-6), but the high purity sample does not exhibit a T_1 maximum and the T_1 increases monotonically with temperature. This corroborates the proposed mechanism of physical diffusion to paramagnetic defects for the ^{2}H T_1 maximum in the mechanosynthesized sample. See the appendix note 2 for further discussion of this effect.

Having removed the unusual ^{2}H T_1 maximum, the ^{2}H T_1 of the high purity mixed FA$^+$/MA$^+$ sample is now induced purely by quadrupolar relaxation and can be used as a straightforward reporter of dynamics. We measured the ^{2}H and ^{14}N T_1 as a function of temperature and compared them with pristine $MAPbI_3$, as shown in Figure 3-7. Note that in MA$^+$, the ^{14}N T_1 only depends upon motion of the C-N bond (caused by the perpendicular rotation illustrated in Figure 3-1a) as the EFG tensor is axially symmetric along the C-N bond and invariant to the C_3-rotation (Figure 3-29) whereas the ^{2}H T_1 is induced by both parallel and perpendicular rotation.[185] Unlike the FA$^+$ motion, which was unaffected by MA$^+$ substitution, we observed that both the ^{2}H T_1 and ^{14}N T_1 of MA$^+$ in $FA_{0.78}MA_{0.22}PbI_3$ are higher than in pristine $MAPbI_3$. In order to extract the rates about both axes, we applied the rotational diffusion model, using the equations of Bernard et al. (see Table 3-6 and equations 3.5, 3.6). As shown in Figure 3-7, the rotational diffusional model reproduces very well the experimental data. The activation energies from Arrhenius analysis and the correlation times at 298 K are shown in Table 3-3 for each axis. The parallel (C_3) rotation rate is unchanged for MA$^+$ in the mixed sample and, as previously found by Bernard et al. for pure $MAPbI_3$, appears to be an essentially unactivated process. This shows that in both materials, the parallel rotation of MA$^+$ is unhindered. Since the perpendicular rotation can be determined from the ^{14}N T_1 alone (and the ^{14}N relaxation is too fast to be affected by paramagnetic defects as observed above for ^{2}H), this was measured for all the mechanosynthesized compositions (Table 3-3). We find that while the activation energy for perpendicular rotation of MA$^+$ is similar for pure $MAPbI_3$ and $MA_xFA_{1-x}PbI_3$, the motion is

faster by a factor of ~2 when MA^+ is substituted into $FAPbI_3$, with τ_c (298 K) changing from 1.95 ps to ~1.0 ps. Furthermore, the correlation time is found to be independent of the MA^+ concentration up to 40% MA^+.

Table 3-3. Dynamic parameters of MA^+ in $FA_xMA_{1-x}PbI_3$

Material	E_a (meV)	τ_c(ps), 298 K
$MAPbI_3$	⊥: 156 ± 7 ∥: ~0	⊥: 1.95 ± 0.04 ∥: 0.15 ± 0.04
$FA_{0.78}MA_{0.22}PbI_3$ (high-purity)	⊥: 141 ± 10 ∥: ~0	⊥: 1.06 ± 0.03 ∥: 0.16 ± 0.03
$FA_{0.90}MA_{0.10}PbI_3$ (Mechanosynthesis)	-	⊥:0.96 ± 0.02
$FA_{0.80}MA_{0.20}PbI_3$ (Mechanosynthesis)	-	⊥:0.98 ± 0.01
$FA_{0.70}MA_{0.30}PbI_3$ (Mechanosynthesis)	-	⊥:0.99 ± 0.02
$FA_{0.60}MA_{0.40}PbI_3$ (Mechanosynthesis)	-	⊥: 1.10 ± 0.02

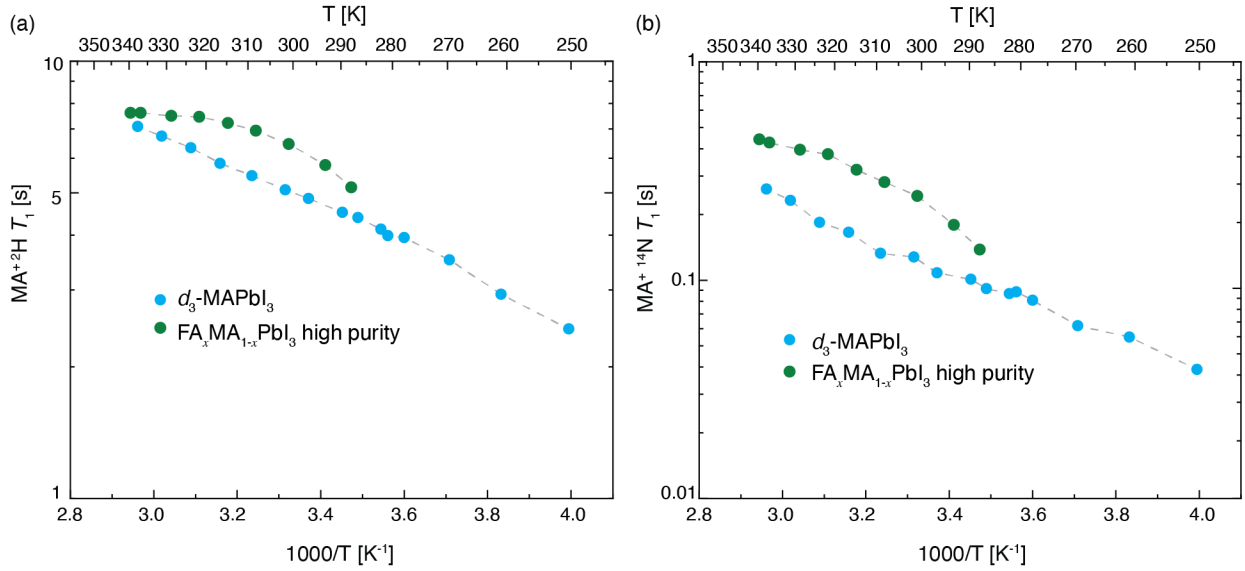

Figure 3-7. Experimentally measured (a) ^2H and (b) ^{14}N T_1 constants as a function of inverse temperature in $MAPbI_3$ and high purity $FA_{0.78}MA_{0.22}PbI_3$. Dashed lines indicate fits to the rotational diffusion model.

3.2.6 MA^+ Dynamics in $MA_xGUA_{1-x}PbI_3$ Perovskites

Incorporation of the GUA^+ ion in the $MAPbI_3$ perovskite has been shown to provide improved performance, specifically long charge carrier lifetimes,[414] high open-circuit voltage,[414, 415] efficient charge transfer,[416] and increased stability.[417] This may be related to the absence of dipole moment in GUA^+, which has been suggested computationally to minimize the hysteresis in perovskite solar cells caused by cation motion.[418]

Here, we investigated the GUA^+ and MA^+ dynamics for the $MA_{0.75}GUA_{0.25}PbI_3$ composition. Although the room temperature phase of $MAPbI_3$ is tetragonal, substitution with the GUA^+ ion has been shown to decrease the phase transition temperature from 326 K to 280 K for 20% GUA^+. However, despite the global cubic symmetry at room temperature, substitution with GUA^+ breaks the local symmetry, resulting in orientational anisotropy for both MA^+ and GUA^+. This anisotropy can clearly be seen from the large residual quadrupolar coupling in the ^2H and ^{14}N spectra (Figure 3-30 and Figure 3-31). Nevertheless, the signals from GUA^+ and MA^+ can be distinguished in both the ^2H and ^{14}N NMR spectra (Figure 3-32). Due to the considerable residual ^{14}N quadrupolar coupling for GUA^+,

it is challenging to saturate the spectrum in order to measure the ^{14}N T_1. Therefore, we used a long phase-modulated pulse[400] to saturate the broad ^{14}N pattern (details in experimental section).

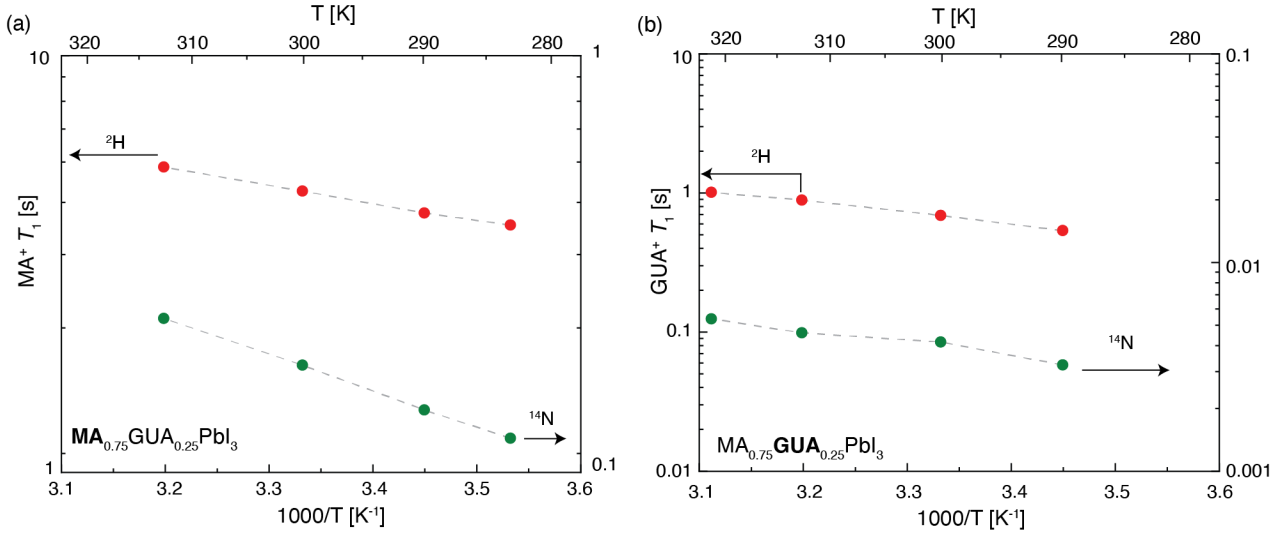

Figure 3-8 ^{2}H and ^{14}N T_1 constants of (a) MA$^+$ and (b) GUA$^+$ as a function of inverse temperature in $MA_{0.75}GUA_{0.25}PbI_3$ at 20 kHz MAS. Dashed lines indicate fits to the rotational diffusion model.

Figure 3-8 shows the experimentally measured ^{2}H and ^{14}N T_1 relaxation times of MA$^+$ as a function of temperature in the room temperature phase. The T_1 behavior is consistent with the expected MA$^+$ motion in the fast motion limit. Applying the rotational diffusion model to this relaxation data, we found that, similarly to mixed MA$^+$/FA$^+$ compositions, the MA$^+$ parallel motion remains unactivated and at a similar rate upon GUA$^+$ substitution as in the pure MA$^+$ formulation (Table 3-4). The perpendicular motion also has a similar activation energy barrier as in $MAPbI_3$ (Table 3-4), however again we found that the correlation time for perpendicular motion at 298 K becomes faster with GUA$^+$ doping, as observed for MA$^+$ in the MA$^+$/FA$^+$ compositions.

Table 3-4. Dynamic parameters of MA$^+$ and GUA$^+$ in $MA_xGUA_{1-x}PbI_3$

Material	E_a (meV)	τ_c(ps), 298 K
MAPbI_3	⊥: 156 ± 7 ∥: ~0	⊥: 1.95 ± 0.04 ∥: 0.15 ± 0.04
MA$_{0.75}GUA_{0.25}PbI_3$	⊥: 168 ± 11 ∥: ~0	⊥: 1.32 ± 0.03 ∥: 0.25 ± 0.03
$MA_{0.75}$**GUA**$_{0.25}PbI_3$	⊥: 121 ± 30 ∥: – –	⊥: 1.27 ± 0.08 ∥: 14 ± 8

Table 3-5. Nuclear quadrupolar tensor parameters for GUA$^+$ ion.

Nucleus	C_Q (MHz)	η
^{14}N*	3.5 ± 0.3	0.4
^{2}H†	0.20 ± 0.01	0.14

*Averaged from nuclear quadrupolar resonance experiments in different guanidinium salts.[419]
†Experimental value from guanidinium chloride. [420]

Now we consider the motion of the guanidinium cation. GUA$^+$ is characterized by two distinct principal axes (Figure 3-1c) owing to the C_3 symmetry. The ^{14}N and ^{2}H quadrupolar relaxation constants are determined by the rotation about these axes according to,

$$\frac{1}{T_1^{\mathrm{Q}}(^2\mathrm{H})} = \frac{1}{32}\frac{(2\pi C_q)^2}{D_r}[4D_\perp + (\eta-1)^2 D_\perp + (\eta+1)^2 D_\parallel] \tag{3.3}$$

$$\frac{1}{T_1^{\mathrm{Q}}(^{14}\mathrm{N})} = \frac{1}{16}\frac{(2\pi C_q)^2}{D_r}[2D_\parallel + (\eta^2+1)D_\perp] \tag{3.4}$$

where, C_Q is the quadrupolar coupling constant in units of Hz, η is the quadrupolar asymmetry. The GUA^+ quadrupolar parameters used here are shown in Table 3-5.

Figure 3-8 shows the ^{2}H and ^{14}N T_1 relaxation data along with fits to the rotational diffusion model of equation (3.3) and (3.4). The resulting activation energies and correlation times at 298 K are shown in Table 3-4. We find that the perpendicular rotation is on the picosecond timescale, which is similar to the other cations considered above. The parallel motion is slower than the perpendicular motion, which is consistent with the larger moment of inertia. However, we note that the parallel motion determined by this model is extremely sensitive to the input parameters, in particular the experimentally measured ^{14}N T_1 and the value of the static ^{14}N C_Q, which are both associated with large uncertainties. As discussed above, the ^{14}N spectrum of GUA^+ has a very broad pattern, resulting in a low signal-to-noise ratio and difficulties in accurately measuring T_1. Moreover, the ^{14}N static C_Q parameters are averaged from experimental nuclear quadrupole resonance studies for different guanidinium compounds, which could change to some degree in this sample. Consequently, there is a large uncertainty in the parallel correlation time at room temperature, and it was not possible to determine an activation energy for the parallel motion.

3.3 Discussion

In summary, we have experimentally determined the rotational rates about each axis in FA^+, MA^+, and GUA^+ for different perovskite compositions (Figure 3-9).

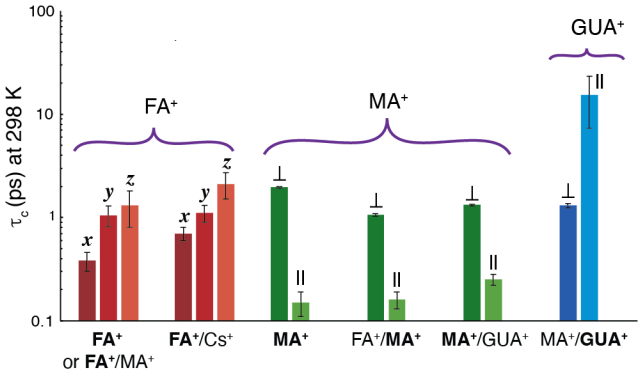

Figure 3-9 Comparison of experimentally measured rotational correlation times at room temperature of MA^+, FA^+, GUA^+ cations in the various iodoplumbate perovskite compositions studied in this work. The corresponding activation energies are shown in Figure 3-33.

Despite these observed difference in rotation about the internal axes, there is at least one component of rotation for all three cations on the pico-second timescale. This similar timescale of the motion is surprising given the differences in dipole moment (GUA^+: 0 D, FA^+: 0.2 D, and MA^+: 2.3 D),[384] effective ionic radius (GUA^+: 278 pm, FA^+: 253 pm, and MA^+:217 pm), and lattice parameters (Table 3-8).[188, 195] The fastest motion we observe is the C_3 parallel rotation of MA^+ ($\tau_c = 0.16 \pm 0.03$ ps), which is consistent with it having the smallest moment of inertia and the apparent absence of any energy barrier to rotation. The slowest motion is the C_3 parallel rotation of GUA^+ ($\tau_c = 15 \pm 8$ ps), which is consistent with it having the largest moment of inertia, although we note the large error associated with this value.

Fabini et al.[182] also noted the similarity of the rotational rates of MA^+ and FA^+, based on a single correlation time determined from ^{1}H NMR relaxometry. However, their values (8 and 7 ps for FA^+ and MA^+ at room temperature, respectively) were significantly larger than those determined using ^{2}H and ^{14}N relaxometry here (and by Bernard et al. for $MAPbI_3$). We propose that while this reflects the same physical phenomenon, i.e. the similarity of the rotational dynamics, the numerical discrepancy may arise from considering a single correlation time or the challenges in applying BPP theory away from the T_1 minimum.[421]

Here we note that we have analyzed our data using an anisotropic rotational diffusion model, which corresponds to an isotropic continuum of possible cation orientations, but with different rotational rates about each axis. This is in line with MD simulations of MA^+ rotation in $MAPbI_3$.[422] In contrast, Chen et al. reported that a $C_3 \otimes C_4$ jump model, combining three-fold jumps about the parallel axis and four-fold jumps about the perpendicular axis (Figure 1b), was a better fit to their neutron scattering data than an isotropic rotational model[389] (a $C_3 \otimes O$ model with octahedral perpendicular jumps also gave indistinguishable results in the cubic phase). Based on the completely averaged ^{2}H and ^{14}N quadrupolar tensors in the experimental spectra of $MAPbI_3$ in the cubic phase, the perpendicular motion must have cubic or higher symmetry, but it is not possible to distinguish between octahedral jumps or rotation diffusion on this basis. To compare, we modeled the ^{2}H and ^{14}N T_1 relaxation of MA^+ in $MAPbI_3$ at 330 K using a jump model, as implemented in the Express software package.[423] However, this yielded an unphysical correlation time for the C_3 jumps of 0.008 ps (See appendix note 3). Therefore, we conclude that the rotational diffusion model is a better fit to the experimental data. Nevertheless, at the current level of our analysis, we cannot discount a preferred orientation of the cations within the cage during rotational diffusion, if this preferred orientation has cubic symmetry.

To utilize ^{2}H NMR relaxometry, (partially) deuterated cations were used in this work and it is important to note that the greater moment of inertia will result in slower cation rotation.[388] This effect is greatest for the C_3 (parallel) rotation of MA^+, since the moment of inertia is entirely determined by the hydrogens, whereas the effect is significantly smaller for the perpendicular MA^+ rotation and for the other cations. The increase in moment of inertia is also mitigated here by the use of relatively low deuteration, typically ~20%. Changes in the phase transition temperatures[424] and coupling to the inorganic lattice[388, 425] have been observed in other hybrid perovskites on deuteration, however since here we focus on the dynamics in the cubic phase near room temperature, this is not expected to have a significant effect. In particular, we note that there is no observable difference in the ^{2}H T_1 constants for two different levels of deuteration in $MAPbI_3$, to within the accuracy of the measurements (Figure 3-27), suggesting any isotope effect is small. We believe that the trends we identify here are directly relevant to the fully protonated analogues used in photovoltaic devices.

Kubicki et al. previously reported that the MA^+ and FA^+ dynamics in $FA_{0.67}MA_{0.33}PbI_3$ are the same as in $MAPbI_3$ and $FAPbI_3$, respectively.[207] However, the correlation times deduced for MA^+ were 2–3 orders of magnitude longer than those determined here and by Bernard et al.[185] We ascribe this discrepancy to difficulties in relating measured ^{14}N linewidths to the motionally-induced T_2 relaxation in their model-free analysis.

Considering the different compositions together, consistently it appears that cation substitution does not directly affect the cation dynamics. Both the FA^+ and MA^+ dynamics are unchanged throughout the mixed $FA_xMA_{1-x}PbI_3$ compositions studied, up to x = 40%. Similarly, the FA^+ dynamics in FA^+/Cs^+ and $FA^+/MA^+/Cs^+$ are unchanged from pure $FAPbI_3$, when sufficiently above the phase transition temperature. This implies that the cation dynamics (for these cations) are insensitive to both direct and indirect cation–cation interactions, perhaps due to the picosecond timescale of the rotation. The invariance of the FA^+ dynamics across different compositions aligns with the unchanged favorable optoelectronic properties compared to pristine $FAPbI_3$.

In contrast, the cation dynamics are affected by the underlying symmetry of the inorganic lattice. The rotational rates of FA^+ are suppressed in the vicinity of the cubic/tetragonal phase transition and, therefore, the increase in the phase transition temperature on Cs^+ substitution causes changes in the room temperature dynamics. Furthermore, we find that the perpendicular rotation of MA^+ is faster at room temperature in cubic FA^+/MA^+ and MA^+/GUA^+ compositions, as compared to tetragonal $MAPbI_3$. Given that most device-relevant perovskite compositions possess this faster perpendicular rotation of MA^+, we speculate that it might be linked with improved optoelectronic properties of the material.

3.4 Conclusions

We have developed a protocol to experimentally determine the activation energies (E_a) and correlation times (τ_c) for rotation about each principal axis of the formamidinium ion (FA^+) separately, by measuring all the ^2H and ^{14}N T_1 relaxation constants as a function of temperature and applying a rotational diffusional model.

We then extended this method to study state-of-the-art multi-cation FA^+/Cs^+, FA^+/MA^+, $FA^+/MA^+/Cs^+$, and MA^+/GUA^+ compositions. We find that in all cases, there is at least one component of rotation for all three cations on the pico-second timescale at room temperature. MA^+ also has a faster component (0.1 ps) and GUA^+ also has a slower component (~10 ps).

Notably, the observed motion is sensitive to the symmetry of the inorganic lattice, but not directly to the degree of substitution. In particular, the FA^+ dynamics were found to be unchanged in all samples, except for slower rotation at room temperature upon Cs^+ substitution due to the higher phase-transition temperature. However, the perpendicular rotation of MA^+ is approximately a factor of two faster at room temperature in cubic $FA_xMA_{1-x}PbI_3$, as compared to tetragonal $MAPbI_3$.

Surprisingly, we found that for mechanosynthesized $FA_xMA_{1-x}PbI_3$, the ^2H relaxation of MA^+ is dominated at high temperature by physical diffusion of MA^+ to paramagnetic defects. This phenomenon could be used in future to study ion-migration and the formation of paramagnetic defects. Importantly, high-purity solution-processed samples did not exhibit this effect.

Having demonstrated this relaxometry methodology for MA^+, FA^+ and GUA^+, we note that it can be readily extended to understand the dynamics of other relevant cations used in hybrid perovskites, such as dimethylammonium ion (DMA^+)[426-428] and methylenediammonium (MDA^+).[329, 395] Overall, the complete picture of the cation dynamics presented here will help reveal the underlying causes of the beneficial optoelectronic properties seen in some hybrid perovskite formulations, and thereby aid the design of perovskite solar cells with higher efficiencies in the future.

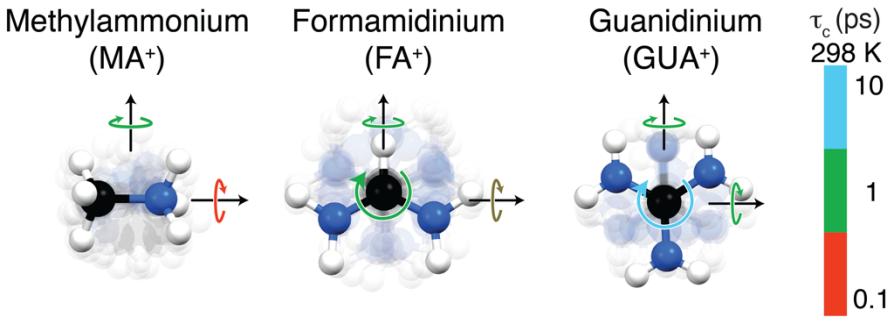

Figure 3-10. Schematic of cation dynamics of most prototypical cations in perovskite photovoltaics.

3.5 Appendix

3.5.1 Relaxation Analysis

At each temperature point, the ^{2}H and ^{14}N T_1 constants were combined to give the rotational diffusion constants about each axis, by using the equations corresponding to that cation along with the static quadrupolar parameters (Table 3-6, Table 3-1, Table 3-5 and equations 3.1 –3.6). This yields the diffusion constants about each axis of the cation at each temperature. Fitting the linear region of an Arrhenius plot of the diffusion constant as a function of temperature behavior, gives the activation energies (E_a) about each axis. Further, using the relation $D = 1/(6\tau_c)$, the correlation time about each axis was calculated at 298 K from the experimental data. Due to non-Arrhenius behavior near the phase transition, the correlation time was interpolated directly from the rotational diffusion constants at adjacent temperature points, not taken from the Arrhenius analysis.

To determine the error in the activation energy and correlation time, Monte Carlo analysis was used. The input relaxation times and quadrupolar coupling constants were varied randomly according to their experimental uncertainties for 1000 trials, and the corresponding activation energies and correlation times calculated for each trial. The errors in these values were then taken as the standard deviation of the resulting distribution. This error in the relaxation time was obtained from the experimental noise, which was calculated at each composition, for each cation, at a temperature point. The uncertainties in the quadrupolar coupling constants are given in the corresponding tables.

For the MA$^+$ cation, the equations of Bernard et al. was used[185]:

$$\frac{1}{T_1^{14\mathrm{N}}} = \frac{3(2\pi C_Q)^2}{8}\,\frac{1}{6D_\perp} \tag{3.5}$$

$$\frac{1}{T_1^{2\mathrm{H}}} = \frac{3(2\pi C_Q)^2}{8}\left(\frac{1/9}{6D_\perp} + \frac{8/27}{5D_\perp + D_\parallel} + \frac{16/27}{2D_\perp + 4D_\parallel}\right) \tag{3.6}$$

Table 3-6 Nuclear quadrupolar tensor parameters for MA$^+$

Nucleus	C_Q (MHz)	η
^{14}N	0.550 ± 0.005	0
^{2}H	0.160 ± 0.001	0

3.5.2 MA$^+$ ^{2}H T_1 Maximum in $FA_xMA_{1-x}PbI_3$

Here, we estimate the physical diffusion (H$^+$ or MA$^+$) rate and defect concentration that would be required for the MA$^+$ ^{2}H T_1 to be limited by physical diffusion to paramagnetic defects, as discussed in the main text.

In general, perovskite materials are very prone to defects, including paramagnetic defects such as Pb^{3+}, paramagnetic oxygen at surfaces/grain boundaries, and cation-centered radicals. Their concentrations depend upon external factors such as light, humidity, and processing routes. In our samples, we can speculate that the high defect concentration arises from the ball-milling procedure. Prior literature suggests that the defect density in hybrid perovskites can be as high as 10^{17} cm^{-3},[429] and this value can be even higher when the materials are prepared using mechanosynthesis.[168, 297] For mono-exponential T_1 relaxation behaviour as observed experimentally, the diffusion length must be larger than the average distance to a paramagnetic defect. For a defect density of 10^{17} cm^{-3}, the Wigner–Seitz radius (r_{ws}) of each defect is 13 nm. At 336 K, the ^{2}H T_1 for the mechanosynthesised $FA_{0.7}MA_{0.3}PbI_3$ sample is 4.7 s, requiring a diffusivity $D \approx r_{ws}^2/T_1 \approx 4 \times 10^{-13}$ cm^2 s^{-1}. Now we consider MA$^+$ and H$^+$ diffusion mechanisms in more detail, and whether the required diffusivity could be achieved.

Case 1: MA$^+$ diffusion. In hybrid perovskites, both cations (MA$^+$, Pb^{2+}) and anions (I^-) have been shown to exhibit migration due to the presence of vacancies and interstitials. In the literature, ion-drift measurements demonstrated a diffusivity of MA$^+$ ions at room temperature of ~10^{-12} cm^2 s^{-1},[430] higher than the estimated requirement for this relaxation mechanism. However, NMR tracer diffusion results indicate that this diffusivity corresponds to the diffusion of MA$^+$ vacancies, whereas the diffusivity of MA$^+$ itself is found to be <10^{-15} cm^2 s^{-1} at 343 K.[431] This value for MA$^+$ diffusion in $MAPbI_3$ is too low for the proposed mechanism based on the estimate above; however, a ^{2}H T_1 maximum is not observed for pure $MAPbI_3$ (Figure 3-27), only for mixed FA$^+$/MA$^+$. This could be explained by faster physical diffusion of MA$^+$ in mixed MA$^+$/FA$^+$ due to the slightly larger lattice. As shown in Figure 3-5 and Figure 3-20–Figure 3-23, a ^{2}H T_1 maximum is not observed for FA$^+$ in $MA_xFA_{1-x}PbI_3$; this can be explained for this mechanism by faster physical diffusion of MA$^+$ than of FA$^+$, in line with the larger size of FA$^+$. This observation also rules out physical diffusion of the defects themselves, as

this would affect both FA^+ and MA^+. For diffusion of MA^+ to paramagnetic defects, similar relaxation would be expected for ^1H and ^2H. However due to fast spin diffusion, the ^1H T_1 equalises between MA^+ and the FA^+ ions which do not diffuse physically on this timescale; consequently, the measured ^1H T_1 would be increased by ~2.4×. The experimental ^1H T_1 at 336 K of 10.5 s (Figure 3-28) is therefore reasonably consistent with the ^2H T_1 of 4.7 s, if there is physical diffusion of MA^+.

Case 2: H^+ diffusion. Interstitial H^+ ions (either $^1H^+$ or $^2H^+$) are another common defect in hybrid perovskites that arise from deprotonation of the organic cation and reaction with H_2O.[432, 433] Interstitial H^+ ions are in equilibrium with the organic cations, providing a mechanism of exchange between cations which has been demonstrated by isotope-exchange[433, 434] and dielectric response[435] measurements. The diffusivity of interstitial H^+ is estimated to be about 5×10^{-10} cm^2 s^{-1} at room temperature.[433] This is significantly faster than the required estimate above, although this diffusivity was measured with a high relative humidity. The diffusion for deuterium has been shown to be higher than for protons due to an inverse kinetic isotope effect,[435] which would explain why the ^1H T_1 is longer than the ^2H T_1. Furthermore, the dissociation energy for deprotonation of FA^+ is higher than for MA^+, which would explain why the ^2H T_1 maximum is only observed for MA^+ and not FA^+ in mixed MA^+/FA^+. The fact that the ^2H T_1 maximum is observed only in mixed $MA_{1-x}FA_xPbI_3$ and not pure $MAPbI_3$ could be due to a higher defect density in the former, or an increased likelihood for MA^+/H^+ exchange with a lower MA^+ concentration for the same interstitial H^+ concentration.
Based on this discussion, we believe that physical diffusion of either MA^+ or $^2H^+$ to paramagnetic defects are feasible mechanisms for the unusual ^2H T_1 maximum in $MA_{1-x}FA_xPbI_3$. Although we cannot distinguish between the two possibilities with the experiments done here, on balance, the $^2H^+$-mediated mechanism appears more likely given the higher measured diffusivity in the literature.

Finally, since a ^2H T_1 maximum was not observed for any $MAPbI_3$ samples (Figure 3-27), but a ^1H T_1 maximum was observed for high-purity samples of $MAPbI_3$ (Figure 3-25, and by Senocrate et al.[206]), spin–rotation relaxation remains the most likely mechanism for the ^1H T_1 maximum in pure $MAPbI_3$.

3.5.3 Jump Model for $MAPbI_3$

In order to compare the rotational diffusion model with a jump model for the ^2H and ^{14}N T_1 relaxation of $MAPbI_3$, we tested a jump model using the Express software. We considered octahedral jumps of the C-N bond at a rate $k_\perp$ and three-fold jumps of the C-H bonds at a rate $k_\parallel$ (Figure S28). As the ^{14}N EFG is axially symmetric about the C-N bond as shown in Figure 3-29, the octahedral jump rate uniquely determines the ^{14}N T_1. The ^2H T_1 is given by the combination of the octahedral and C_3 jump rates.

This model is tested in the cubic phase of $MAPbI_3$ at 331.2 K, to avoid any effects of anisotropy, for which the experimentally measured values are ^2H T_1 = 7.08 s and ^{14}N T_1 = 0.261 s. First, we determined an octahedral jump rate of $k_\perp = 1.17 \times 10^{12}$ s^{-1} to reproduce the ^{14}N T_1. Taking this octahedral jump rate, a C_3 jump rate of $k_\parallel = 5.85 \times 10^{13}$ s^{-1} is required to reproduce the experimental ^2H T_1. Converting these rates to rotational correlation times (i.e., the average time to rotate by 1 radian) gives $\tau_{c,\perp} = 0.544$ ps and $\tau_{c,\parallel} = 0.008$ ps, compared to $\tau_{c,\perp}$ = 1 ps and $\tau_{c,\parallel}$ = 0.2 ps from the rotational diffusion model. Although the perpendicular rate is similar for the two models, the parallel rate is unphysically fast in the jump model.

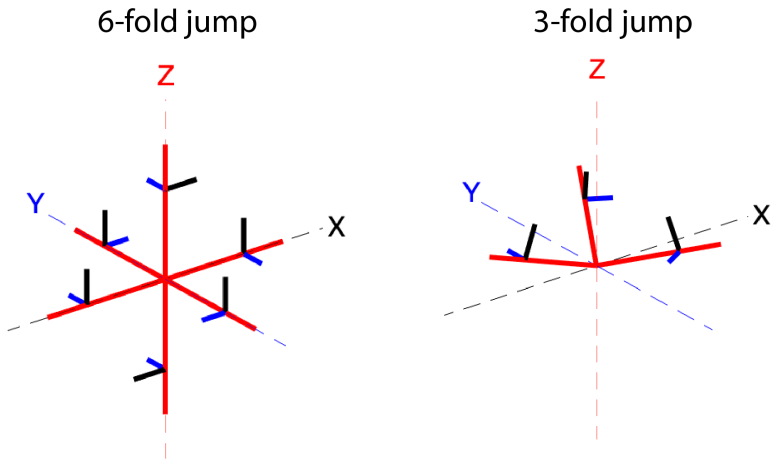

Figure 3-11. 6-fold and 3-fold jump with the shown sites in the considered jump model for $MAPbI_3$.

Table 3-7. Correlation time of FA^+ at room temperature about each axis in Cs-alloyed FA^+–based materials

Material	$\tau_{c,x}$ (ps), 298K	$\tau_{c,y}$ (ps), 298K	$\tau_{c,z}$ (ps), 298K
$FAPbI_3$	0.38 ± 0.08	1.05 ± 0.24	1.3 ± 0.5
$FA_{0.95}Cs_{0.05}PbI_3$	0.7 ± 0.1	1.1 ± 0.2	2.1 ± 0.6
$FA_{0.65}Cs_{0.05}MA_{0.30}PbI_3$	0.6 ± 0.1	1.2 ± 0.2	2.5 ± 1.1

Table 3-8. Pseudo-cubic lattice parameter (*a*) obtained from the profile fitting of powder XRD diffractograms.

Material	*a*/Å
$FAPbI_3$	6.364
$FA_{0.70}MA_{0.30}PbI_3$	6.336
$MA_{0.75}GUA_{0.25}PbI_3$	6.329
$FA_{0.95}Cs_{0.05}PbI_3$	6.357
$FA_{0.65}Cs_{0.05}MA_{0.30}PbI_3$	6.335

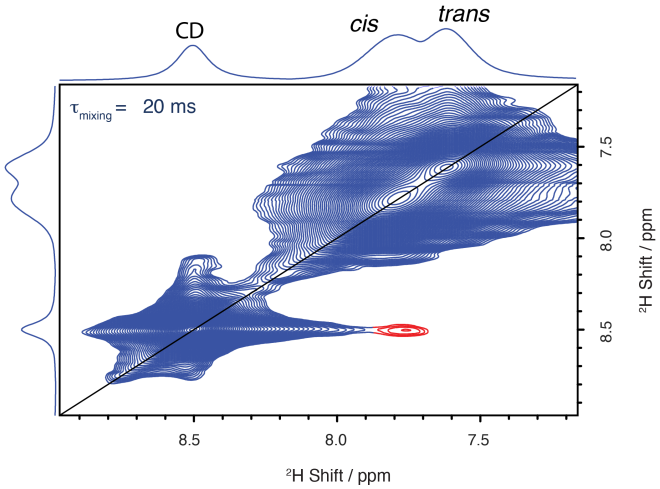

Figure 3-12. ^2H–^2H spin-diffusion experiment on d_5-$FAPbI_3$ at 20 kHz MAS and 21.1 T. The cross peak between the CD and *cis*-ND_2 deuterons is shown in red.

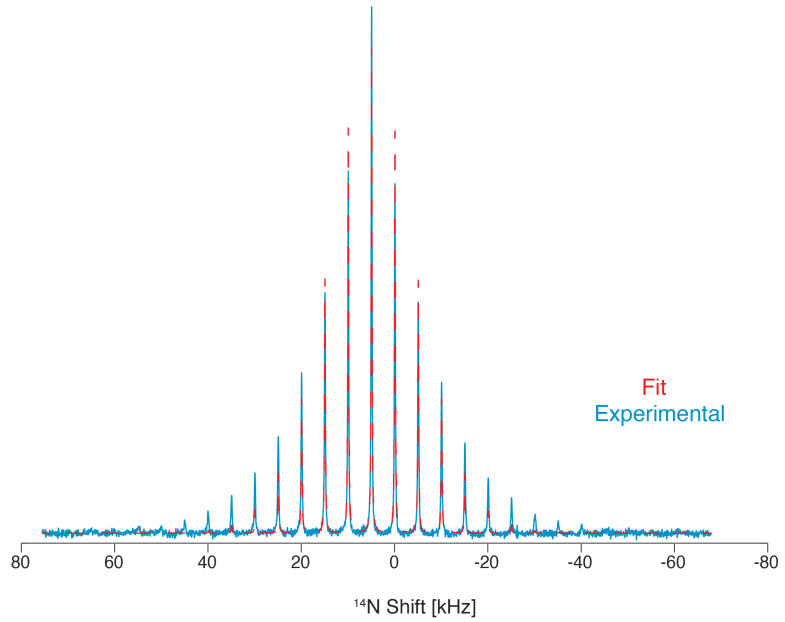

Figure 3-13. $FAPbI_3$ ^{14}N spectrum fit using a Czjzek model[403] with a peak quadrupolar coupling of 27 kHz.

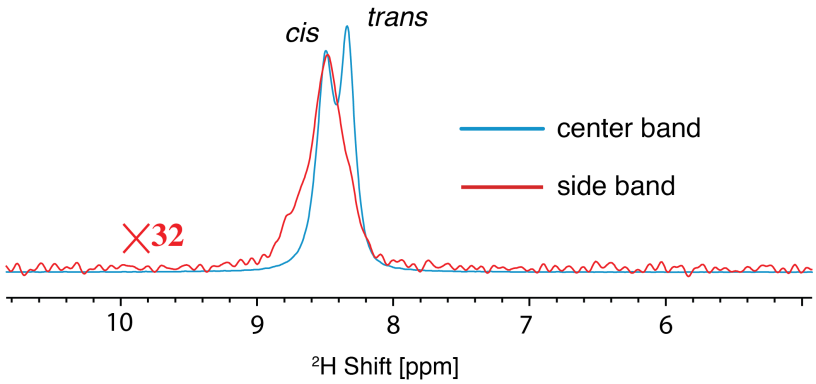

Figure 3-14. Comparison of the center-band and first-order sideband for the ND_2 signals in the echo-detected ^{2}H MAS NMR spectrum of d_4-$FAPbI_3$. The sideband spectrum has been offset by the spinning frequency (5 kHz) to compare the isotropic shifts. Although the sideband signal is broader, indicating a greater distribution of local environments for the more anisotropic component, the shift aligns with that of the cis ND_2. We therefore conclude that the residual anisotropy is greater for the cis ND_2 than the trans ND_2, consistent with the smaller residual anisotropy of the CD deuteron.

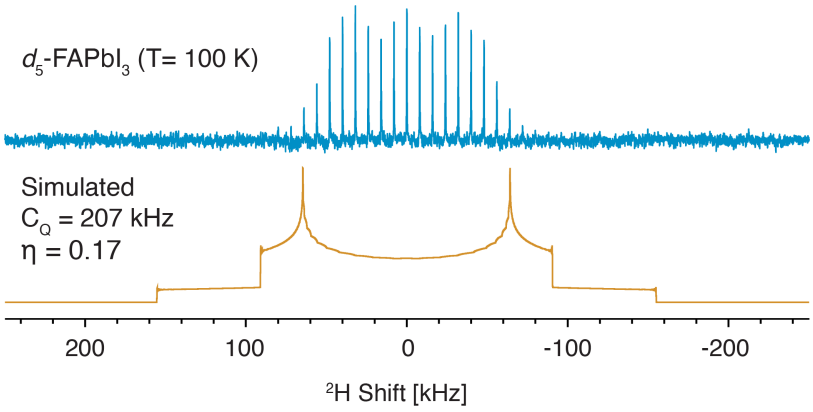

Figure 3-15. Echo-detected ^{2}H MAS NMR spectrum of d_5-$FAPbI_3$ at 8 kHz MAS at 9.4 T and 100 K. Bottom spectrum is the simulated ^{2}H NMR spectrum in the absence of any motion.

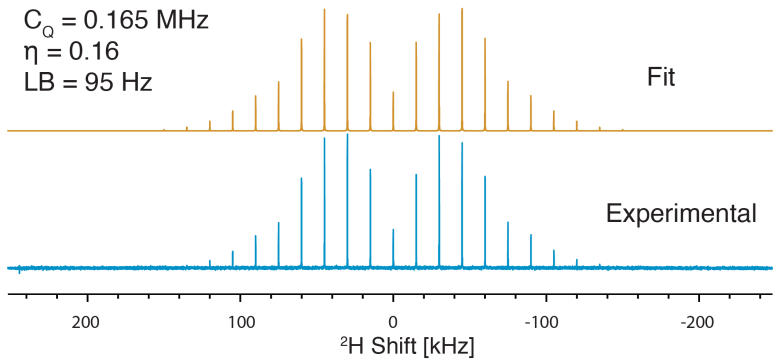

Figure 3-16. Experimental and fitted ^{2}H spectrum of *d*-FAI at 100 K, 15 kHz MAS, and 9.4 T.

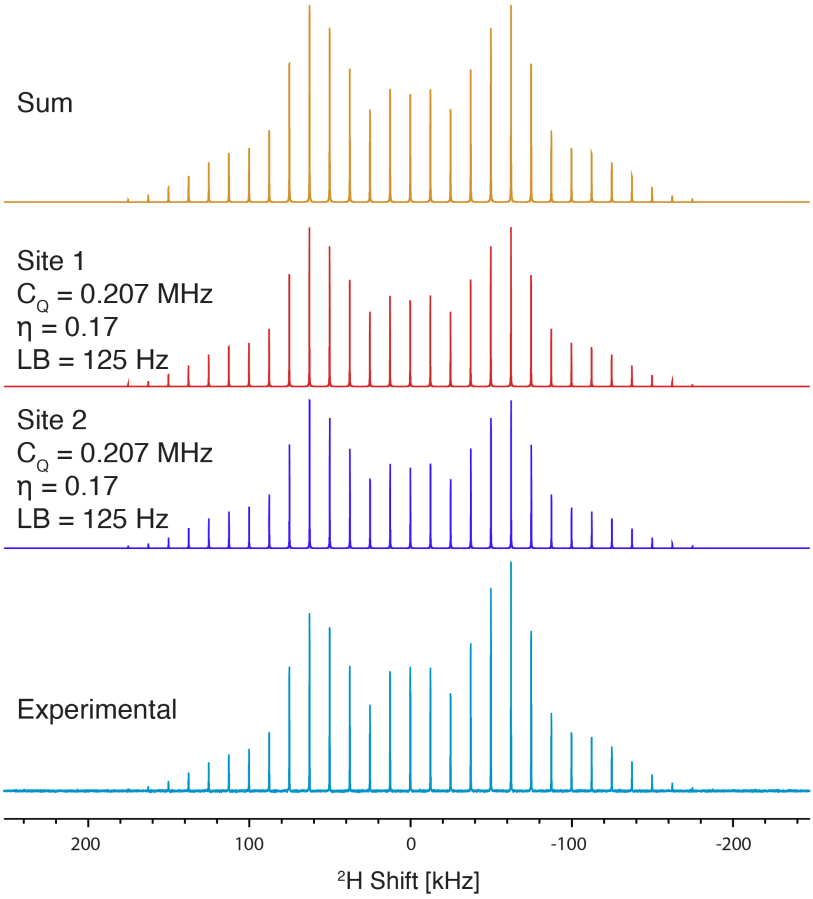

Figure 3-17. Experimental and fitted ^{2}H spectrum of d_4-FAI at 100 K, 12.5 kHz MAS, and 9.4 T.

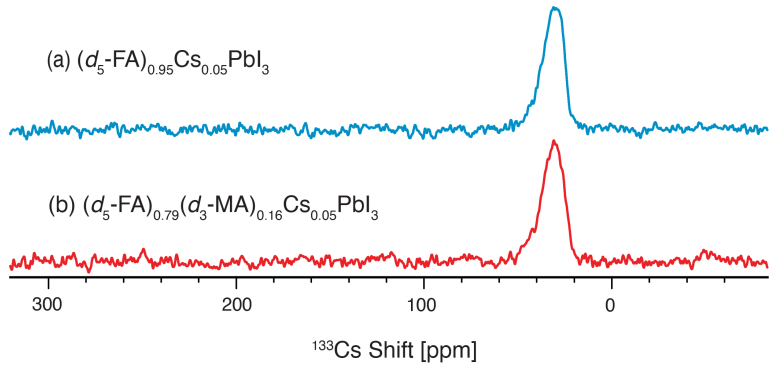

Figure 3-18. ^{133}Cs MAS NMR spectra at 10 kHz MAS, 21.1 T, and 297 K of (a) $(d_5\text{-FA})_{0.95}Cs_{0.05}PbI_3$ and (b) $(d_5\text{-FA})_{0.79}(d_3\text{-MA})_{0.16}Cs_{0.05}PbI_3$.

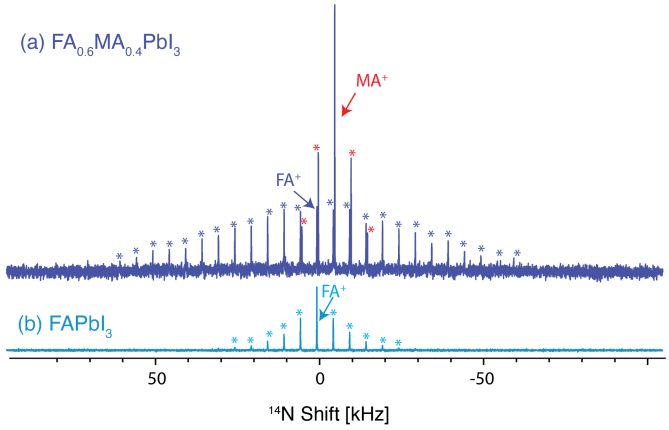

Figure 3-19. Hahn-echo detected ^{14}N MAS NMR spectra of $FAPbI_3$ and $FA_{0.6}MA_{0.4}PbI_3$ at 5 kHz MAS, 21.1 T and room temperature. The intensities have been normalized to give the same FA^+ center-band intensity, in order to highlight the broader manifold of FA^+ in $FA_{0.6}MA_{0.4}PbI_3$. Asterisks denote spinning sidebands and are colored by the corresponding species.

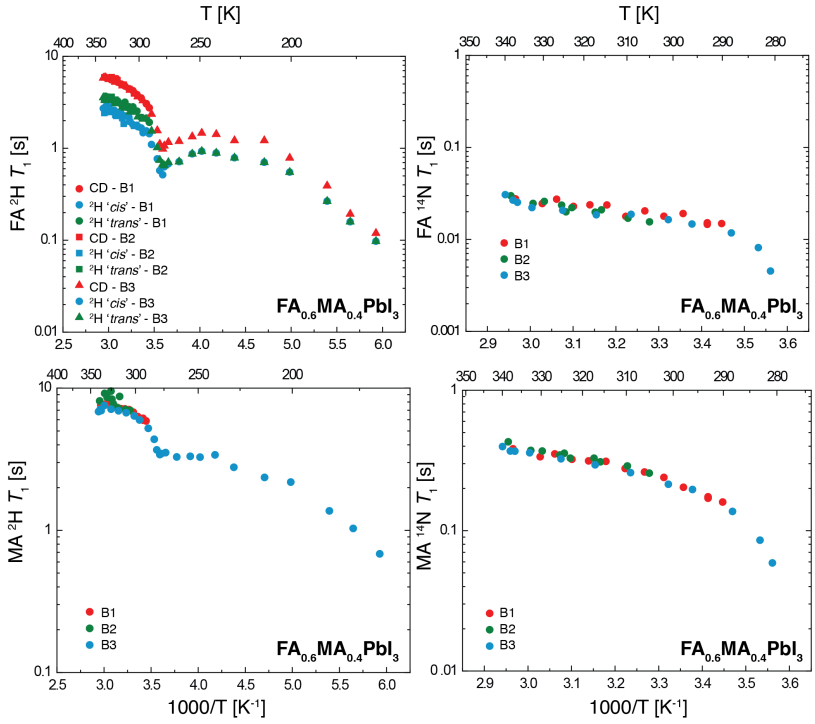

Figure 3-20. Experimentally measured ^{2}H and ^{14}N relaxation times as a function of inverse temperature at 21.1 T and 10 kHz MAS of MA^+ and FA^+ cations in $FA_{0.6}MA_{0.4}PbI_3$ across different batches (B1, B2, B3).

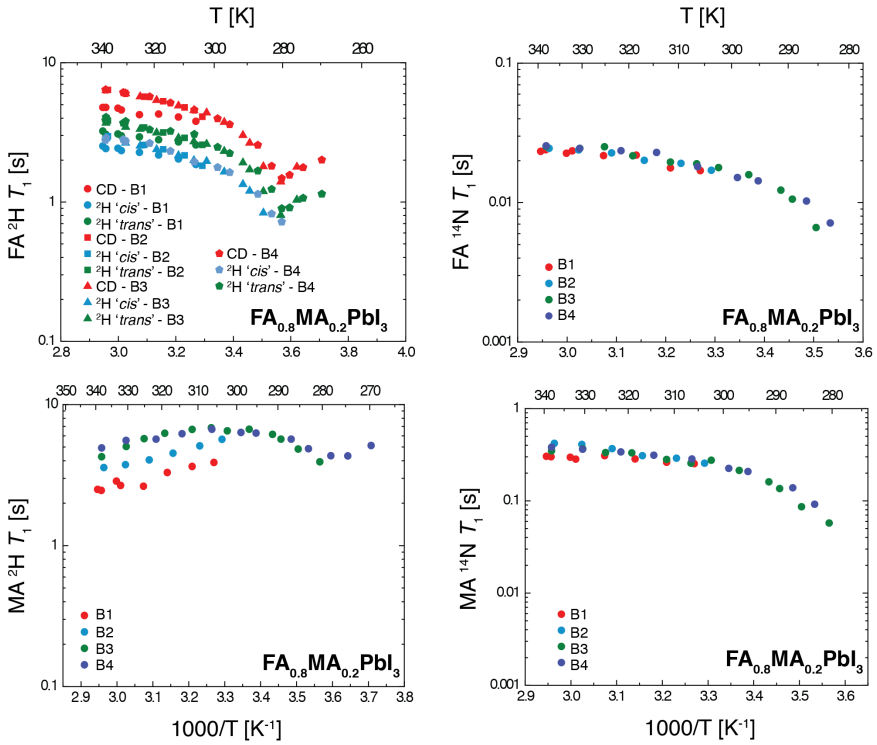

Figure 3-21. Experimentally measured ^{2}H and ^{14}N relaxation times as a function of inverse temperature at 21.1 T and 10 kHz MAS of MA^+ and FA^+ cations in $FA_{0.8}MA_{0.2}PbI_3$ across different batches (B1–B4). Note the batch-to-batch variation in the MA ^{2}H T_1 above the T_1 maximum (~300 K), presumably due to variations in defect density or diffusivity.

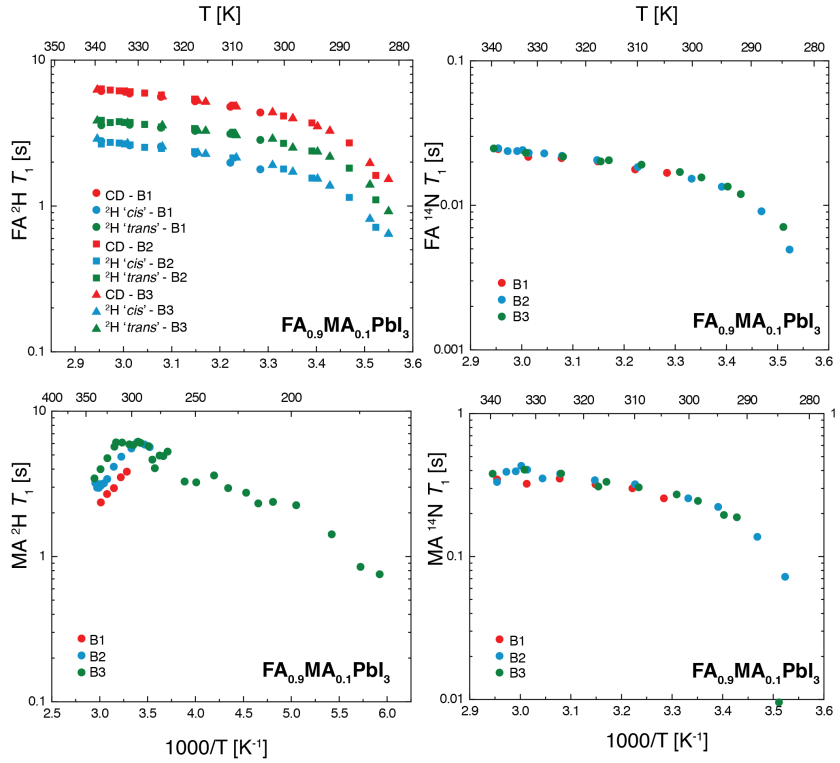

Figure 3-22. Experimentally measured ^{2}H and ^{14}N relaxation times as a function of inverse temperature at 21.1 T and 10 kHz MAS of MA^+ and FA^+ cations in $FA_{0.9}MA_{0.1}PbI_3$ across different batches (B1, B2, B3).

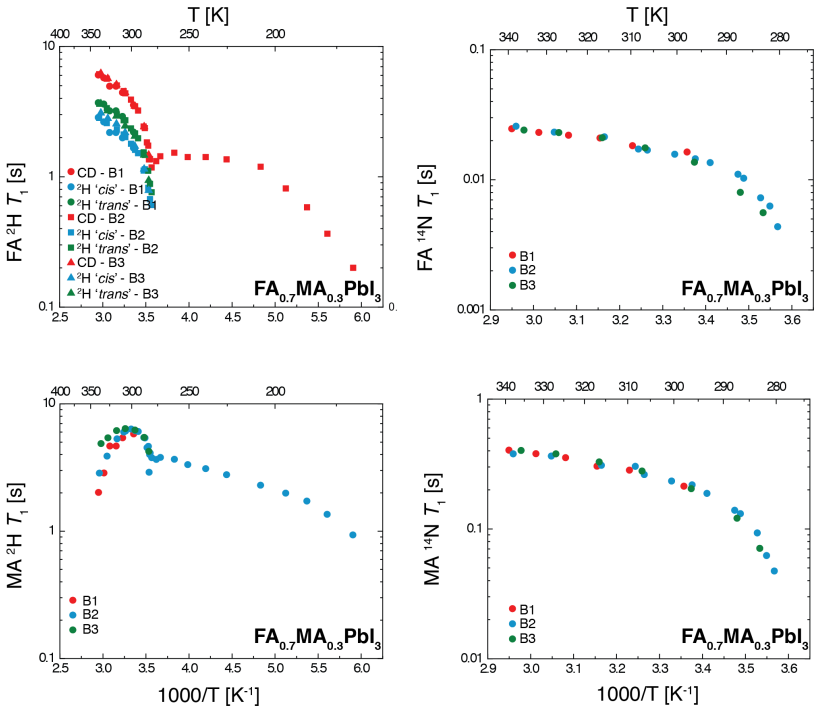

Figure 3-23. Experimentally measured ^{2}H and ^{14}N relaxation times as a function of inverse temperature at 21.1 T and 10 kHz MAS of MA^+ and FA^+ cations in $FA_{0.9}MA_{0.1}PbI_3$ across different batches (B1, B2, B3). Note the batch-to-batch variation in the MA ^{2}H T_1 above the T_1 maximum (~300 K), presumably due to variations in defect density or diffusivity.

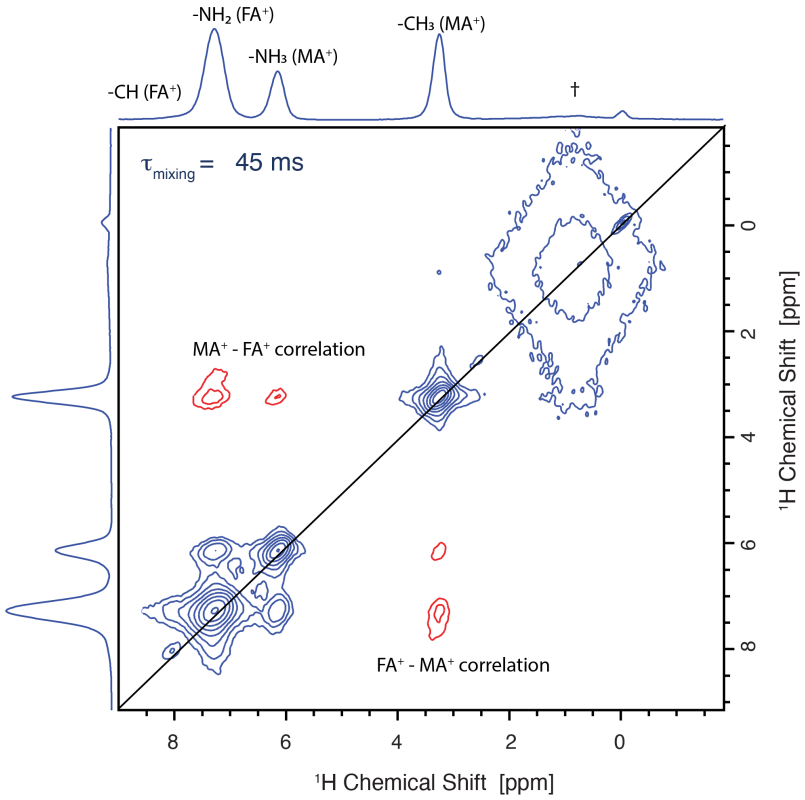

Figure 3-24. Echo-detected ^{1}H–^{1}H spin-diffusion spectrum of $FA_{0.7}MA_{0.3}PbI_3$ at 298 K, 20kHz MAS, and 21.1 T. The signal marked with † is due to polypropylene (PP) from the Eppendorf used for mechanosynthesis.

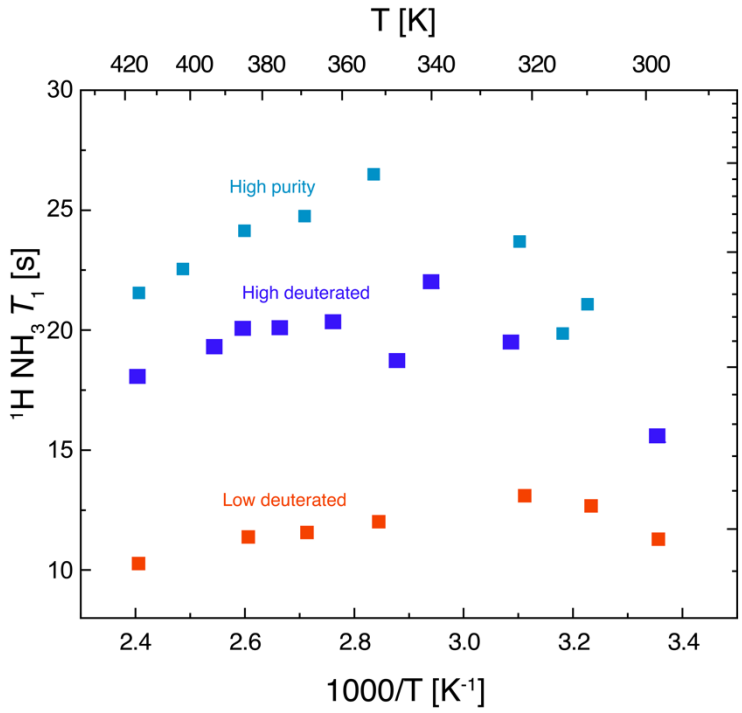

Figure 3-25. Experimentally measured ^{1}H T_1 of $MAPbI_3$ as a function of temperature at 9.4 T and 5 kHz MAS. High deuterated and low deuterated $MAPbI_3$ corresponds to ~90%, and ~15% deuteration, respectively. The T_1 increases for higher deuteration and for the higher purity sample, indicated that relaxation is limited by spin diffusion to relaxation sinks. The T_1 maximum is only visible when this mechanism has been suppressed.

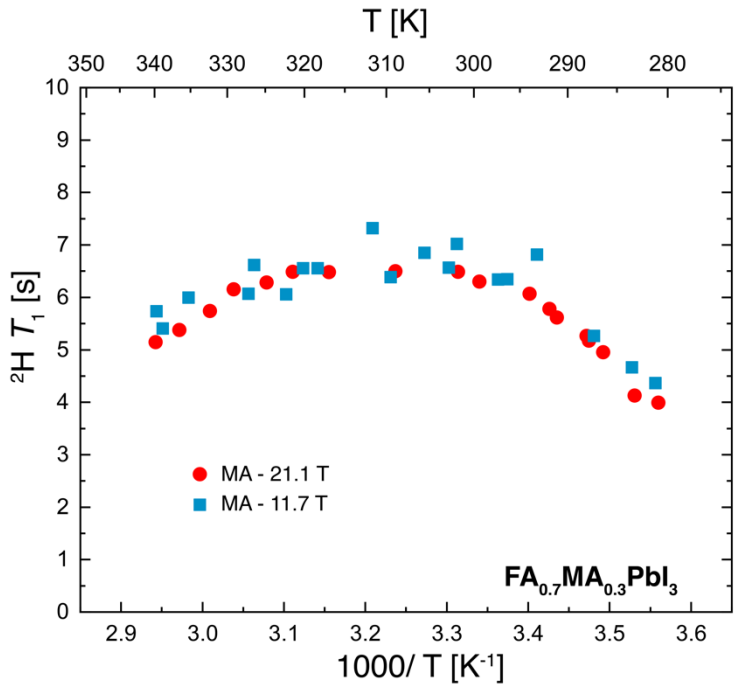

Figure 3-26. Comparison of the experimentally measured ^{2}H T_1 constants for $FA_{0.7}MA_{0.3}PbI_3$ as a function of temperature at two different magnetic fields.

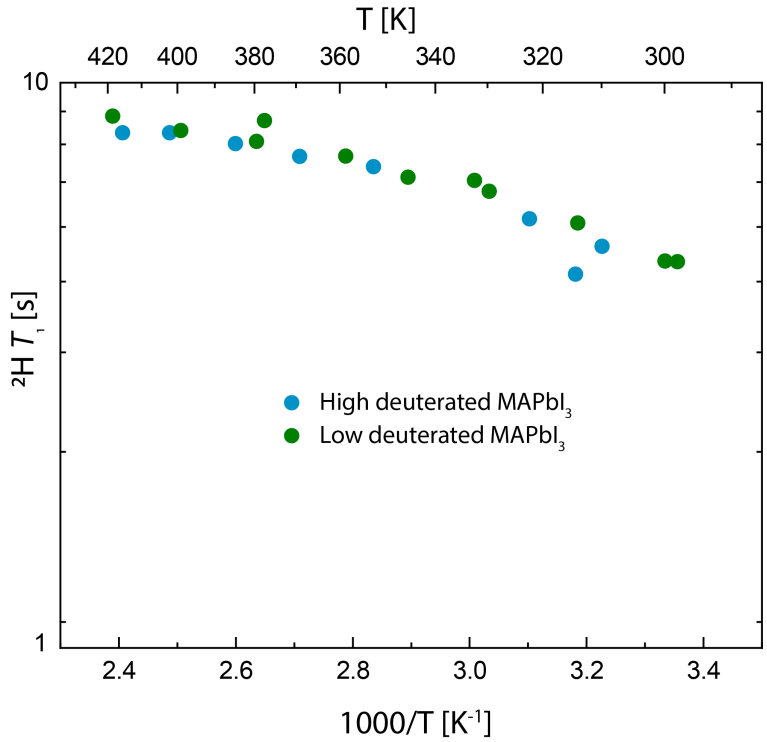

Figure 3-27. Experimentally measured ^{2}H T_1 of $MAPbI_3$ as a function of temperature at 9.4 T and 5 kHz MAS. High deuteration and low deuteration corresponds to ~90%, and ~15% deuteration, respectively. Note the lack of T_1 maximum.

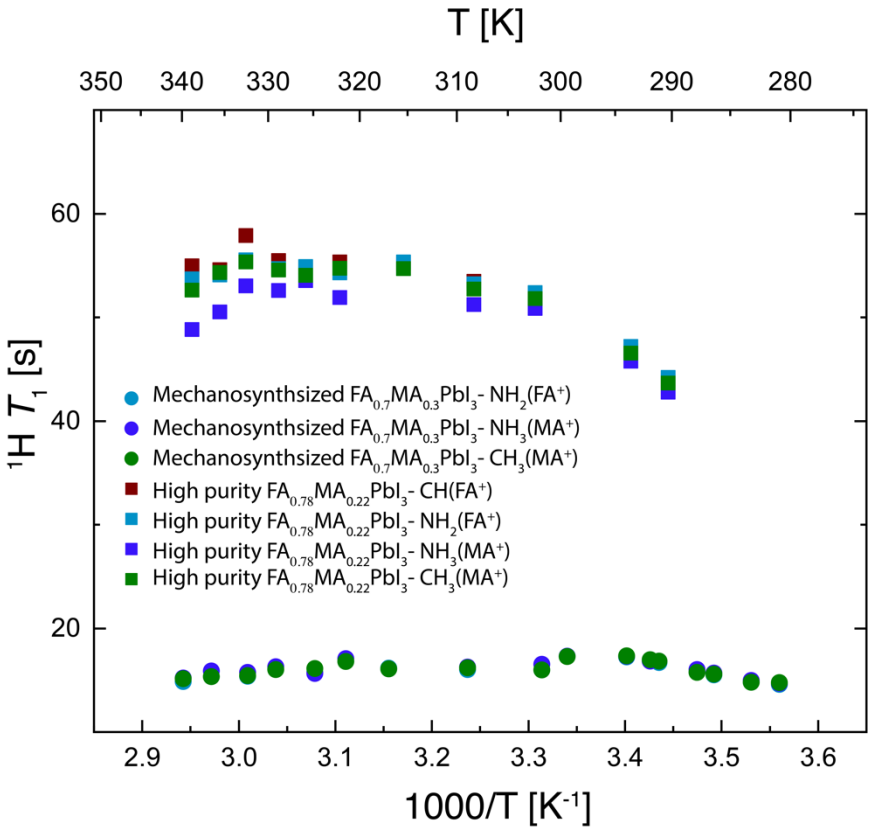

Figure 3-28. Experimentally measured ^{1}H T_1 of $FA_xMA_{1-x}PbI_3$ as a function of temperature at 21.1 T and 10 kHz MAS for mechanosynthesised and high purity samples. The T_1 increases significantly for the high purity sample, indicating that the T_1 is limited by paramagnetic defects. The T_1 maximum can only be seen for the high purity sample.

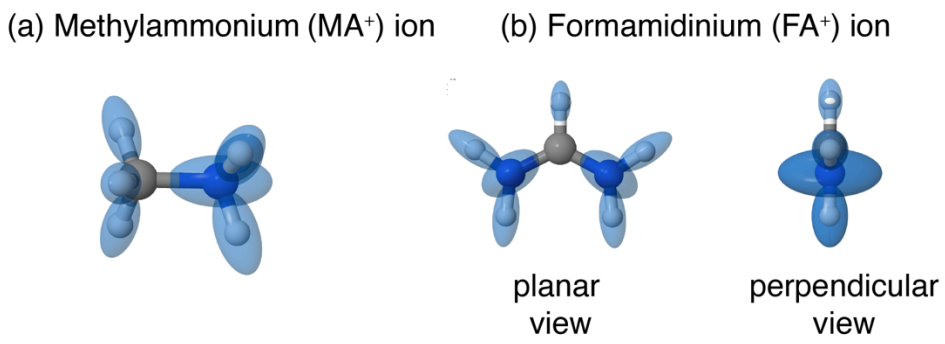

Figure 3-29. Orientation of the local quadrupolar coupling tensors in methylammonium (MA^+) and formamidinium (FA^+) ion. The scaling factor of the tensor magnitude is different for both ions. The tensors were visualised using MagresView.[436]

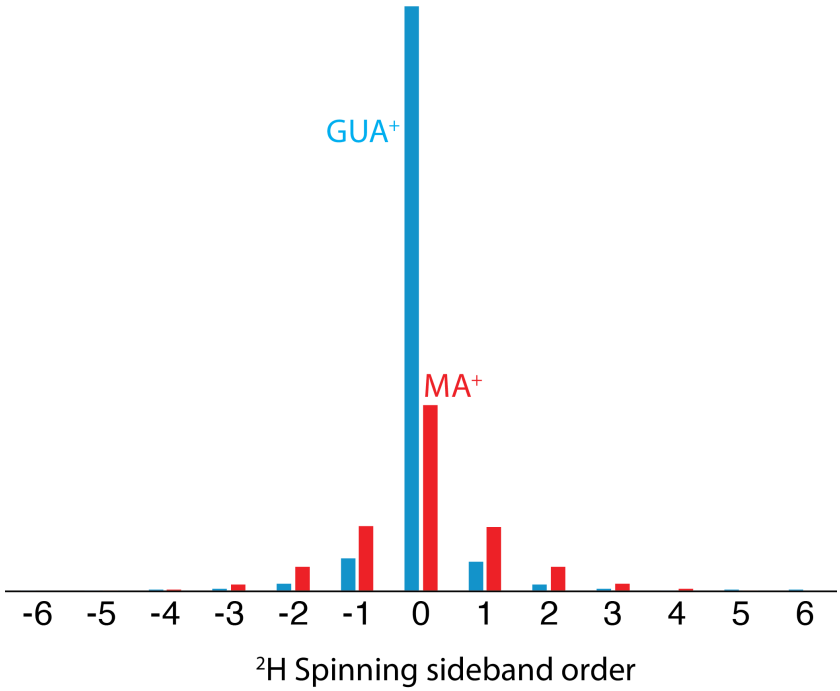

Figure 3-30. Intensity of the GUA^+ and MA^+ ^2H peaks in $MA_{0.75}GUA_{0.25}PbI_3$ as a function of spinning sideband order at 5 kHz MAS and 21.1 T.

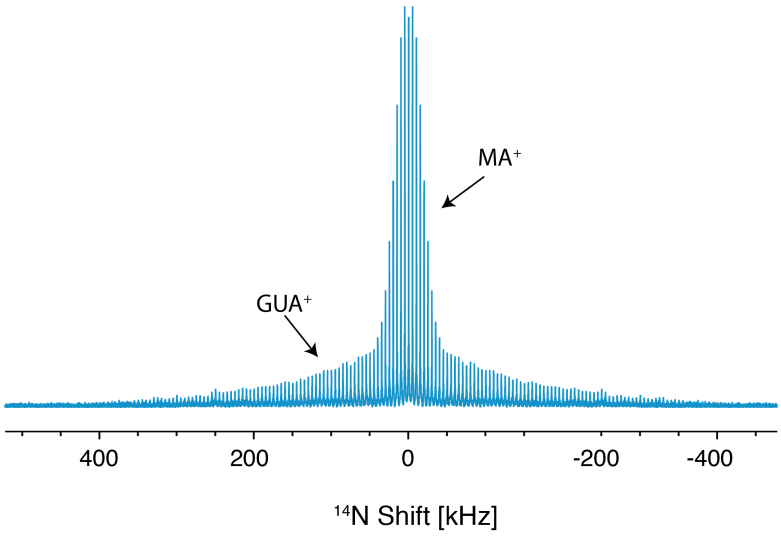

Figure 3-31. ^{14}N static NMR wideline spectrum of $MA_{0.75}GUA_{0.25}PbI_3$ measured with the WURST-QCPMG sequence, at 21.1 T and 298 K. The broad and narrow envelopes correspond to GUA^+ and MA^+, respectively. 100 echoes of 200 µs duration were recorded, giving a spikelet spacing of 5 kHz. 50 µs

WURST-80 pulses were used with 22 kHz radiofrequency power and a sweepwidth of 500 kHz. Two spectra were recorded sweeping the frequency from high-to-low and low-to-high frequency, respectively, and the spectra summed. For each spectrum, 25600 scans were recorded with a recycle delay of 50 ms. 50 Hz of exponential linebroadening was applied. The carrier frequency was 200 kHz and the full symmetric spectrum was generated by reflecting about the origin.

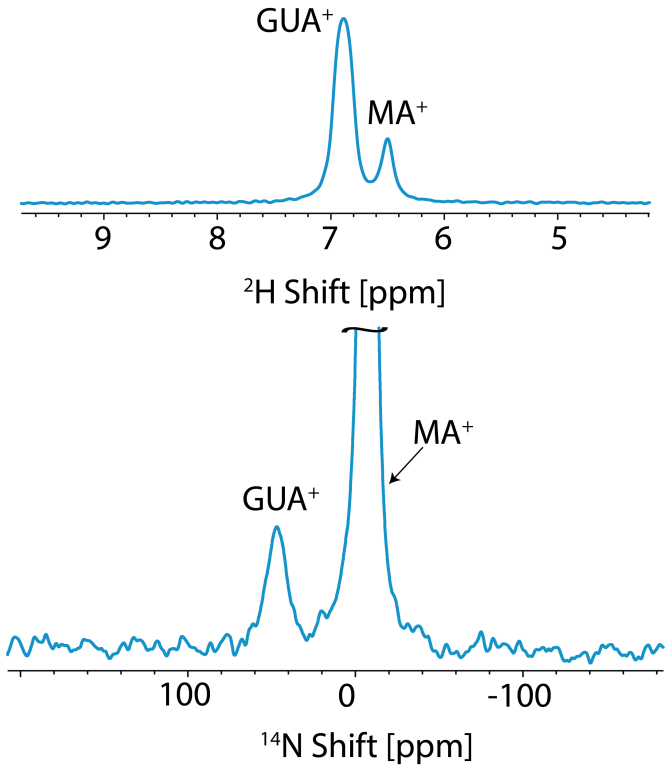

Figure 3-32. ^{2}H and ^{14}N isotropic resonances of $MA_{0.75}GUA_{0.25}PbI_3$ at 5kHz MAS and 20kHz MAS, respectively.

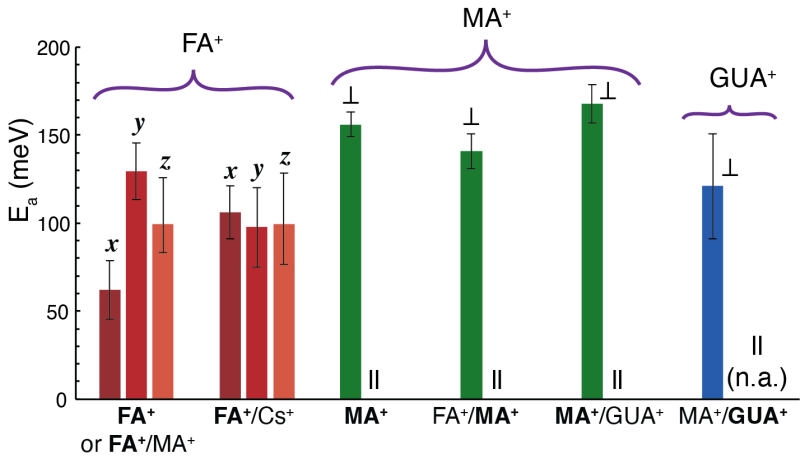

Figure 3-33. Activation energy about each axis of the cation's studied in this work (axes shown in Figure 1).

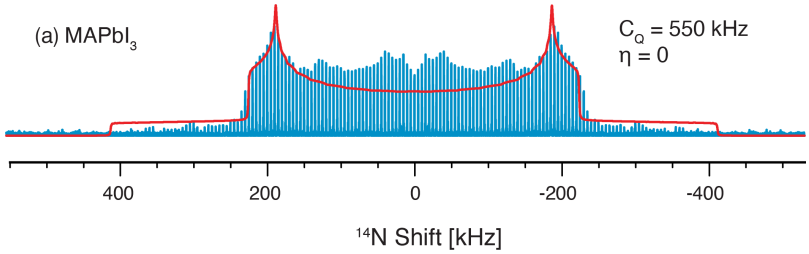

Figure 3-34. ^{14}N static NMR wideline spectrum of $MAPbI_3$ measured with the WURST-QCPMG sequence, at 21.1 T and 110 K. 75 echoes of 200 µs duration were recorded, giving a spikelet spacing of 5 kHz. 50 µs WURST-80 pulses were used with 15 kHz radiofrequency power and a sweepwidth of 500 kHz. Two spectra were recorded sweeping the frequency from high-to-low and low-to-high frequency, respectively, and the spectra summed. For each spectrum, 600000 scans were recorded with a total recycle delay of 50 ms. The first three echoes were discarded to remove the signal from N_2 gas with a short T_2 and 100 Hz of exponential linebroadening was applied. The carrier frequency was −200 kHz and the full symmetric spectrum was generated by reflecting about the origin.

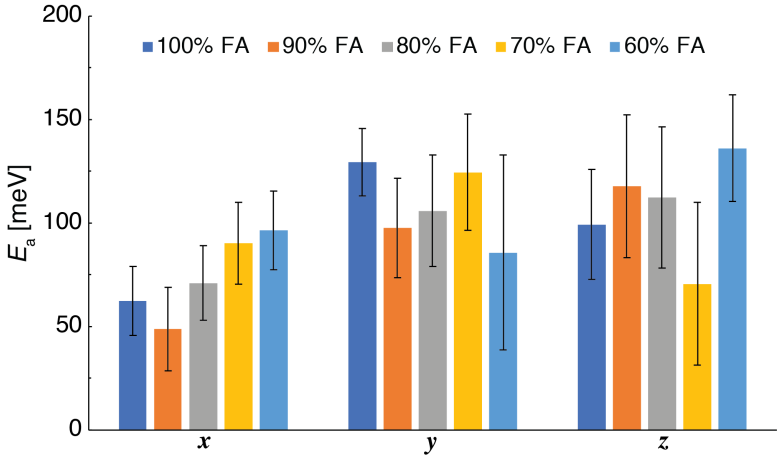

Figure 3-35. Reorientation activation energies (E_a) about each axis of FA^+ in $FA_xMA_{1-x}PbI_3$ (x = 1.0, 0.9, 0.8, 0.7, 0.6). Within error, the activation energies are independent of MA substitution up to 40%.

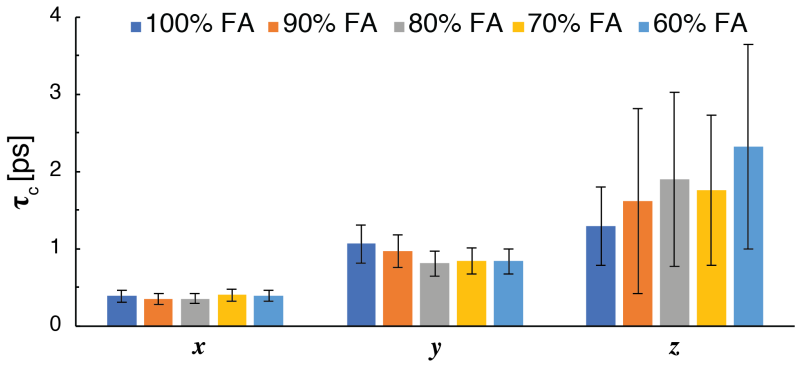

Figure 3-36. Reorientation activation energies (E_a) about each axis of FA molecule in presence of MA^+ substitution in the $FAPbI_3$ lattice.

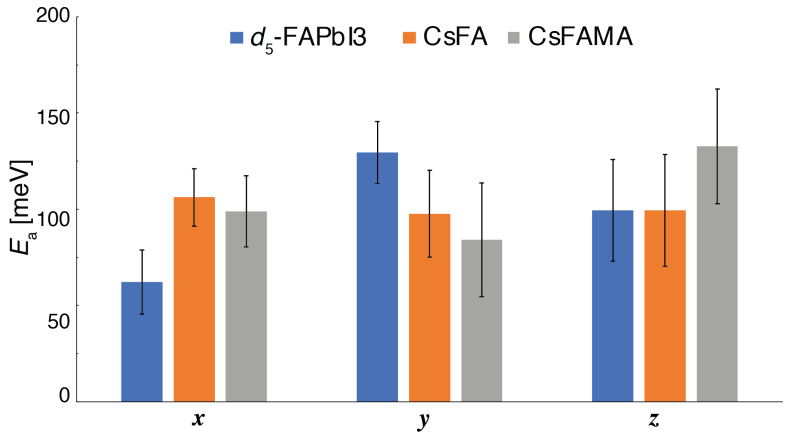

Figure 3-37. The effect of Cs^+ substitution on the activation energies (E_a) for reorientation about each axis of FA^+. The presence of Cs^+ does appear to have a minor effect on the activation energies, however, the change in the cubic/tetragonal phase transition temperature on caesiation makes direct comparison between the samples difficult. Including MA^+ has no effect on the activation energies within error, consistent with the results on pure FA^+/MA^+ compositions.

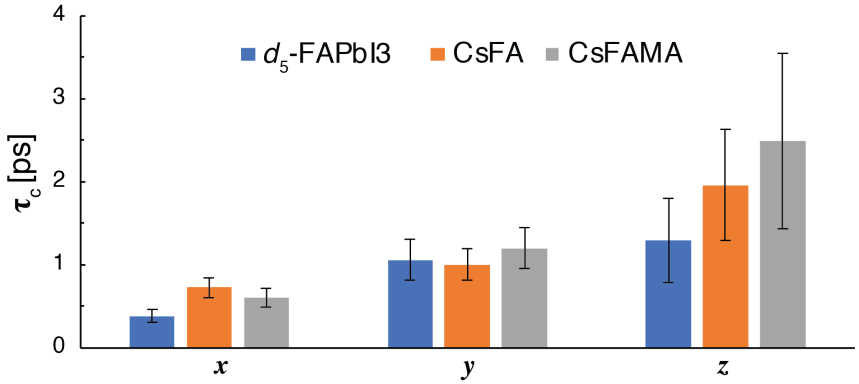

Figure 3-38. Correlation times (τ_c) about each axis of FA molecule in presence of Cs^+ substitution in the $FAPbI_3$ lattice.

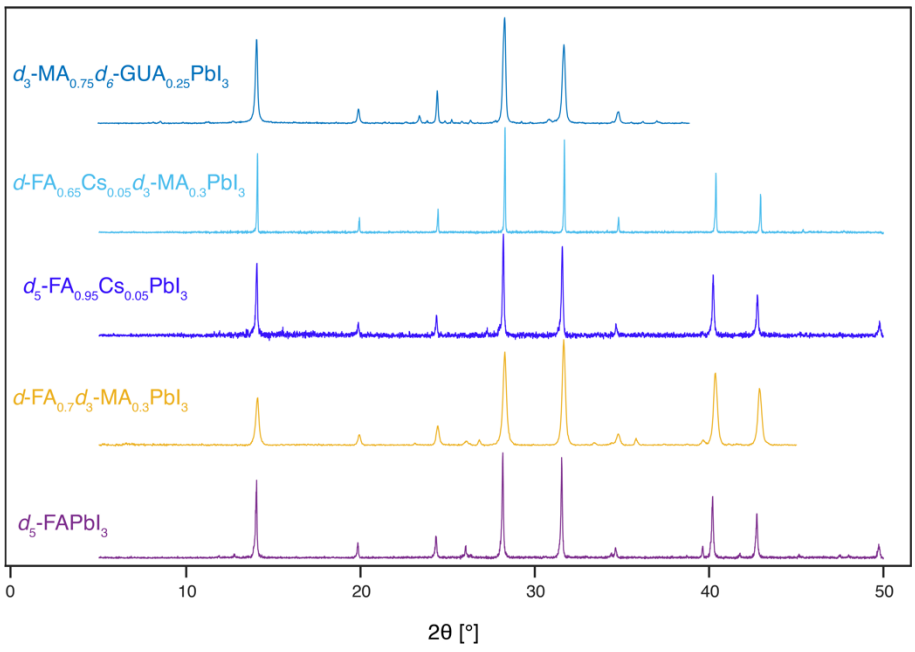

Figure 3-39. Powder XRD diffractograms of representative perovskite compositions used in this work. Lattice parameters are given in Table 3-8.

Chapter 4 Hyperpolarization in Hybrid Perovskites

This section has been adapted from the following work with the permission from the journal:

Mishra, A.; Hope, M. A.; Almalki, M.; Pfeifer, L.; Zakeeruddin, S. M.; Grätzel, M.; Emsley, L., Dynamic Nuclear Polarization Enables NMR of Surface Passivating Agents on Hybrid Perovskite Thin Films. *J. Am. Chem. Soc.* **2022,** *144* (33), 15175–15184.

Contribution statement: I designed, conducted, analyzed, interpreted and wrote up the manuscript together with MAH and LE.

The intrinsic insensitivity of NMR limits its utility to study thin-film samples as used in perovskite devices, owing to the very low sample mass. This insensitivity is compounded for the study of dopants and additives, which comprise only a small fraction of the sample. Consequently, in the majority of previous studies, either several thick films or mechanosynthesized powders were used to enable NMR experiments to be performed. Thus, key challenges relating to NMR sensitivity in hybrid perovskites remain,[22] with spectra from surface and interface species in thin films still largely out of reach.

Sensitivity-enhancing protocols for hybrid perovskites have been investigated by Hanrahan et al.[209] For the detection of ^{207}Pb spectra, they found the most promising technique to be proton detection, while MAS DNP was surprisingly inefficient for both the organic and inorganic components: signal enhancements were typically < 10, especially in the case of the most technologically relevant iodide perovskite.[209] A clear understanding of the underlying challenges in applying DNP to organic–inorganic perovskites, and methodologies to overcome them, are still lacking. Here, we demonstrate efficient DNP for the organic moieties in layered hybrid organic–inorganic perovskites. Specifically, we systematically investigate a class of 2D perovskite homologues to determine that the dynamic A-site cations are the main cause of poor DNP performance. We then demonstrate how to overcome this with deuteration strategies, enabling ^{1}H DNP enhancement factors of up to a factor 100. Finally, using the DNP methodology developed for the layered perovskite combined with high magnetic field and small sample volumes, we have successfully recorded the NMR spectrum of the surface coating (~20 nm) deposited on a single $FAPbI_3$ perovskite thin-film sample (2 × 2 cm^2 area). This opens the door to detailed atomic-level structural studies of surface treatments on technologically relevant samples.

Now, I will mention the experimental details followed by the results and discussion.

4.1 Experimental

Materials. The following materials were used: Formamidinium iodide (Sigma, >99%), PbI_2 (Sigma, 99%), Phenylethylammonium iodide (Greatcell Solar Materials), anhydrous dimethylformamide (99.8%, Acros), dimethylsulphoxide (99.7%, Acros), acetone (99.6%, Acros), chlorobenzene (99.8%, Acros), isopropanol (99.5%, Acros), d_5-FAI (Cortecnet, 85% CD deuterated, 90% ND_2 deuterated). d_4-FAI and d_3-PEAI were prepared by dissolving in heavy water (1:40 mol/mol ratio), followed by evaporation. This yielded ~50% and ~70% deuterium on the FAI and PEAI respectively.

Bulk sample preparation. The perovskite materials were prepared using mechanosynthesis following the previously published protocol.[268] The precursors (PbI_2, PEAI, and FAI, ~ 200 mg total) were mixed in the appropriate molar ratio and ground in an electric ball mill (Retsch MM−400) using an agate grinding jar (10 ml) and agate ball (⌀10 mm) for 60 minutes at 25 Hz. The resulting materials were then annealed at 150°C for 20 mins.

Surface-coated thin-film fabrication. A 1.4 M solution of d_4-$FAPbI_3$ in 4:1 (v:v) DMF:DMSO ratio was spin-coated onto a glass slide (2 × 2 cm^2) with a two-step program at 1000 and 4000 r.p.m. for 10 and 30 s, respectively. During the second step, 200 µl of chlorobenzene (99.8%, Acros) was dropped onto the spinning substrate 10 s prior to the end of the program and the film was annealed at 150°C for 20 minutes. After cooling down the substrate to room temperature, a thin surface layer of d_3-PEAI (5 mg in 1 mL of acetone) was spin-coated on the perovskite layer at 5000 rpm for 30 sec followed by annealing at 100°C for 5 minutes.

DNP-enhanced solid-state NMR measurements. DNP formulations, except for the 0.7 mm DNP samples, were prepared according to standard protocols for impregnation DNP[84, 85, 124] by wetting ~50 mg of the perovskite materials with ~50 µl of 16 mM TEKPol[105] in tetrachloroethane (TCE). 1% d_6-EtOH ethanol was included to improve glass formation.[133] For the thin-film formulation, powder was scraped off from the thin-film, packed into the 0.7 mm rotor, and then a 32 mM solution of HyTEK-2[100] in TCE was added to the sample by centrifugation at 6000 rpm for a minute.

The majority of the DNP-enhanced spectra were acquired on a commercial Bruker Avance III 400 MHz (9.4 T) NMR spectrometer equipped with a 263 GHz gyrotron microwave source using a 3.2 mm triple resonance low-temperature magic angle spinning (LTMAS) probe with sapphire rotors spinning at 8 kHz. A few grains of KBr were mixed into the material before the impregnation step and the temperature was measured from the ^{79}Br T_1 constant.[437] Before measuring the DNP enhanced NMR spectra, samples were degassed by performing three insert–eject cycles, waiting for ~1 min at each step. The DNP enhancement factors were measured from the intensity ratio of the $^1H \rightarrow ^{13}C$ cross polarization (CP)[269] spectra acquired under microwave-on and -off conditions with 100 kHz of SPINAL-64 decoupling.[438] A microwave power of ~12 W was used for all DNP experiments, as measured by a calorimeter halfway along the waveguide. ^{13}C chemical shifts were referenced to the TCE peak at 74 ppm at ~100 K.[85, 439] The TCE enhancement is reported for a recycle delay of 5 s and the PEA^+/FA^+ enhancements for a recycle delay of 100 s. The ^{1}H build-up time-constants (T_{DNP}) were measured using a saturation-recovery $^1H \rightarrow ^{13}C$ experiment. Errors in the time-constants were calculated using Monte-Carlo analysis based on the experimental noise level.
High-field fast-spinning DNP solid-state NMR experiments were performed on a 900 MHz (21.1 T) Avance Neo Bruker NMR spectrometer. The spectrometer is equipped with a LTMAS 0.7 mm triple resonance probe coupled with a Bruker gyrotron producing 593 GHz continuous microwaves. The frequency of the gyrotron was tuned to give the previously observed maximum enhancement for cross-effect DNP with HyTEK-2[100] by modifying the gyrotron cavity temperature to 28°C. The DNP enhancement factors were measured from the intensity ratio of the $^1H \rightarrow ^{13}C$ cross polarization (CP) spectra acquired under microwave-on and -off conditions with 110 kHz of SPINAL-64 decoupling. Details specific to particular spectra are given in Table S2 and the figure captions.

X-ray diffraction measurements. Powder XRD patterns of mechanosynthesized layered and 3D perovskites were recorded with a Bruker D8 Discover Vario Diffractometer with a Cu Kα monochromator (1.5406 Å) from 2θ = 2–50°.

Scanning electron microscopy (SEM) measurements. For the SEM images mechanosynthesized powders were deposited on a standard SEM sample stub with conductive carbon adhesive tabs. A Zeiss Merlin SEM was used and images were acquired at 0.8 kV beam energy using low currents (20–40 pA) detecting secondary electrons with an in-lens detector. SEM images were analysed using the ImageJ software.

4.2 Results and Discussion

First, we determined the DNP enhancements that can be achieved for the organic FA^+ cation in bulk $FAPbI_3$ using a conventional DNP formulation, i.e., impregnation of the materials with 16 mM TEKPol[105] in tetrachloroethane (TCE) at ~100 K[85, 105] (note that $FAPbI_3$ undergoes phase transitions at ~140 K and ~285 K).[182, 404] As seen in Figure 4-1, although the enhancement factor upon microwave irradiation for the ^1H of the TCE is 114 (as measured through the ^{13}C signal intensity in a $^1H \rightarrow ^{13}C$ cross-polarization (CP) spectrum), the FA^+ cation signal exhibits an enhancement of only ~3. While this does correspond to an experimental time saving by an order of magnitude, for typical surfaces or even for bulk micro-crystalline solids, ^1H DNP enhancement factors > 30 can routinely be achieved today.[86, 125, 144] Furthermore, the solvent enhancement is also lower than the expected factor of ~200 for this formulation. Overall, DNP experiments do not work as well as expected in this hybrid perovskite.

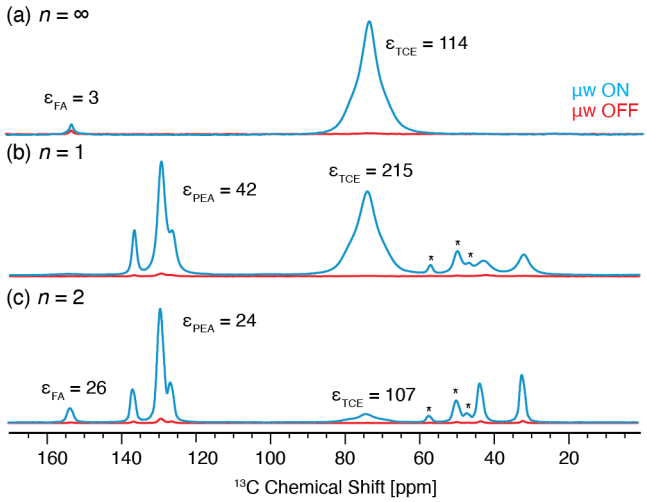

Figure 4-1. (a-c) DNP-enhanced $^1H \rightarrow ^{13}C$ CP spectra with and without microwave (μw) irradiation of (a) $FAPbI_3$ ($n = \infty$) at 133 K, (b) PEA_2PbI_4 ($n = 1$) at 119 K, and (c) $PEA_2FAPb_2I_7$ ($n = 2$) at 130 K. All temperatures are given within ± 2 K. Asterisks indicate spinning sidebands. The μw on spectra shown in the figure were recorded with 8 ($n = \infty$), 64 ($n = 1$), and 4 ($n = 2$) scans each and a polarization delay of 100 s between scans. The full details are given in the appendix.

There are several factors that could explain the poor DNP performance in α-$FAPbI_3$. It is well established that the organic cation which occupies the cuboctahedral cavity in organic–inorganic perovskites is highly dynamic.[182, 185, 207] At 100 K, this motion occurs on a similar timescale to the ^1H Larmor frequency (~1 ns), resulting in fast ^1H relaxation ($T_1 \approx 1$ s). As a result, the cations can act as polarization sinks, causing the hyperpolarization to relax before it can diffuse significantly into the particles. Alternatively, the perovskite material could absorb the microwave radiation itself due to the contribution of the dynamic cation to the dielectric properties.[392] This can have two main consequences: (i) an overall reduction in the available microwave energy to drive the ESR transitions, and/or (ii) a significant increase in the sample temperature, resulting in shorter electron spin relaxation times and less efficient DNP (note that while the increased temperature does affect the cation dynamics, there is little change in the ^1H T_1 due to the proximity to the T_1 minimum; Figure 4-12). Each of these factors could play a significant role in determining the overall enhancement in the perovskite materials and in the following we disentangle their relative contributions.

In order to distinguish between these factors, we performed experiments on samples of two-dimensional Ruddlesden–Popper layered perovskites containing phenylethylammonium (PEA^+) spacers,[440, 441] which allow the dynamic FA^+ cation to be removed and systematically reintroduced in the different homologues. These low-dimensional perovskites are characterized by the number of inorganic layers per organic layer (n), as shown in Figure 1-20. In this convention, α-$FAPbI_3$ can be considered as $n = \infty$. Notably, the $n = 1$ member is unique in that it does not contain an A-site cation and therefore offers the advantage to selectively investigate the effects of the mobile FA cation.

Figure 4-1c shows the DNP enhanced $^1H \rightarrow ^{13}C$ CP spectrum of $n = 1$ (PEA_2PbI_4) where we observe enhancement factors of 215 and 43 for the solvent and PEA^+ signals, respectively (see Figure 4-7 for the spectral assignment). This is around the maximum solvent enhancement that can be achieved for this formulation, and the perovskite enhancement is far higher than for pure α-$FAPbI_3$ (see summary in Figure 4-2a). The lower enhancement of PEA^+ compared to the solvent is expected since the high polarization from the wetting phase has to diffuse into the particle.[82, 85, 113] For the $n = 2$ ($PEA_2FAPb_2I_7$) composition (Figure 4-1c), the solvent enhancement is significantly lower (107), whereas the perovskite enhancements are still appreciable (around 25). Notably, the FA^+ and PEA^+ moieties show very similar enhancement factors within error since they are in atomic-scale proximity and fast ^1H–^1H spin-diffusion

equalizes the nuclear hyperpolarization.[82, 113] These large DNP enhancements for both the n = 1 and n = 2 perovskites further allow $^{1}H \rightarrow ^{15}N$ CP spectra to be measured within minutes (Figure 4-8).

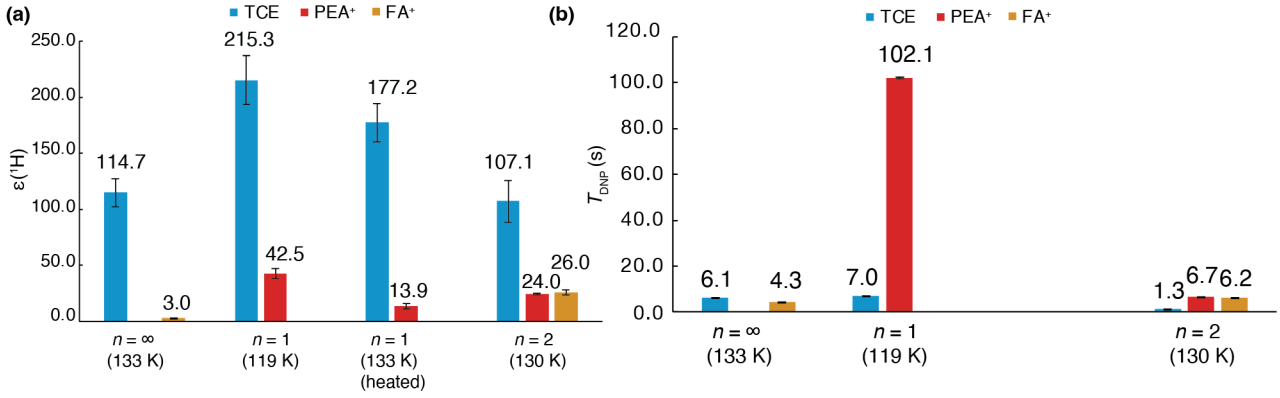

Figure 4-2. Comparison of (a) ^{1}H DNP enhancement factors and (b) T_{DNP} values measured via $^{1}H \rightarrow ^{13}C$ CP spectra of n = ∞ ($FAPbI_3$), n = 1 (PEA_2PbI_4), and n = 2 ($PEA_2FAPb_2I_7$) at the specified temperatures. Temperatures are given to within ± 2 K.

The observation that the solvent enhancements for the n = 2 and n = ∞ samples are similar, while that for n = 1 is higher, is consistent with the presence of dynamic FA^+ cations in the former; we now examine the mechanism for this. First, we consider microwave heating: for n = 2 and n = ∞, the microwaves induce heating by 30 ± 2 K and 33 ± 2 K, respectively, resulting in a minimum achievable temperature of 133 ± 2 K, whereas for n = 1 the heating is only 19 ± 2 K, resulting in a minimum achievable temperature of 119 ± 2 K. Clearly the presence of the dynamic FA^+ cation does induce greater sample heating. However, when the sample temperature is deliberately increased to 130 ± 2 K for the n = 1 sample by heating the incident gas flows, the solvent enhancement decreases only to 177, still far higher than for the n = 2 and n = ∞ perovskites. Therefore, while sample heating does play a role, it is not the major cause of the differing DNP performance.

Further detail on the DNP behavior can be inferred from the build-up of nuclear polarization under microwave irradiation, as characterized by the time constant T_{DNP} (Figure 4-2b). The long T_{DNP} for the n = 1 sample is consistent with the high enhancement, since there is more time to accumulate polarization, which relaxes more slowly. T_{DNP} is significantly shorter for the n = 2 and n = ∞ perovskites, consistent with the presence of fast-relaxing FA cations. However, despite the similar build-up behavior the enhancement is far higher for n = 2 than for n = ∞. This difference can be explained by considering another crucial factor for DNP of impregnated solids, the particle size and morphology;[82, 113] therefore, scanning electron microscopy (SEM) images were obtained as shown in Figure 4-3.

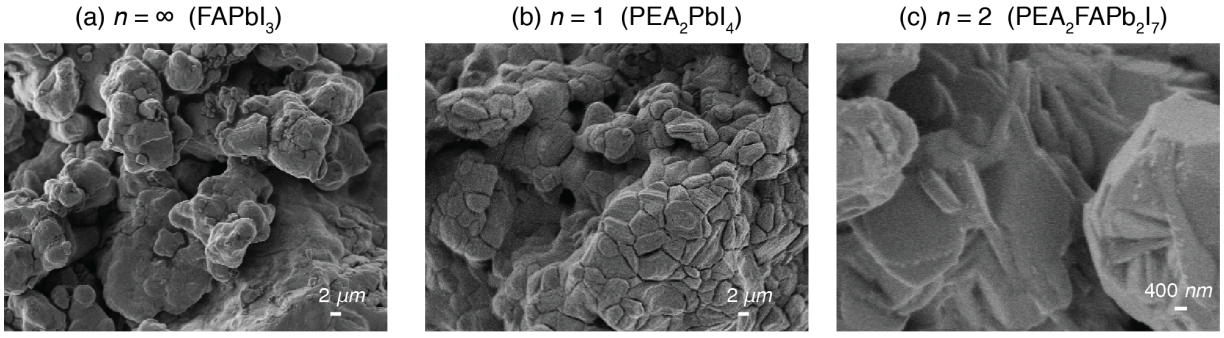

Figure 4-3. SEM images of mechanosynthesized (a) n = ∞ ($FAPbI_3$), (b) n = 1 (PEA_2PbI_4), and (c) n = 2 ($PEA_2FAPb_2I_7$) perovskites.

The n = ∞ and n = 1 compositions show loosely agglomerated secondary particles composed of approximately spherical primary particles with an average particle size of 0.7 ± 0.2 μm (Figure 4-3a, Figure 4-3b). In contrast, the n = 2 sample (Figure 4-3c) exhibits platelet-like primary particles, as commonly observed for layered materials,[442] with a thickness of 0.13 ± 0.05 μm. The morphology in the n = 2 sample favors the propagation of polarization to the bulk owing to the increased surface-to-volume ratio and the shorter diffusion lengths required.[82, 113] Therefore, although the FA^+ cation reduces the T_1 and therefore the spin-diffusion length for the n = 2 homologue, the favorable thin particle size nevertheless allows appreciable hyperpolarization to be relayed to the perovskite.

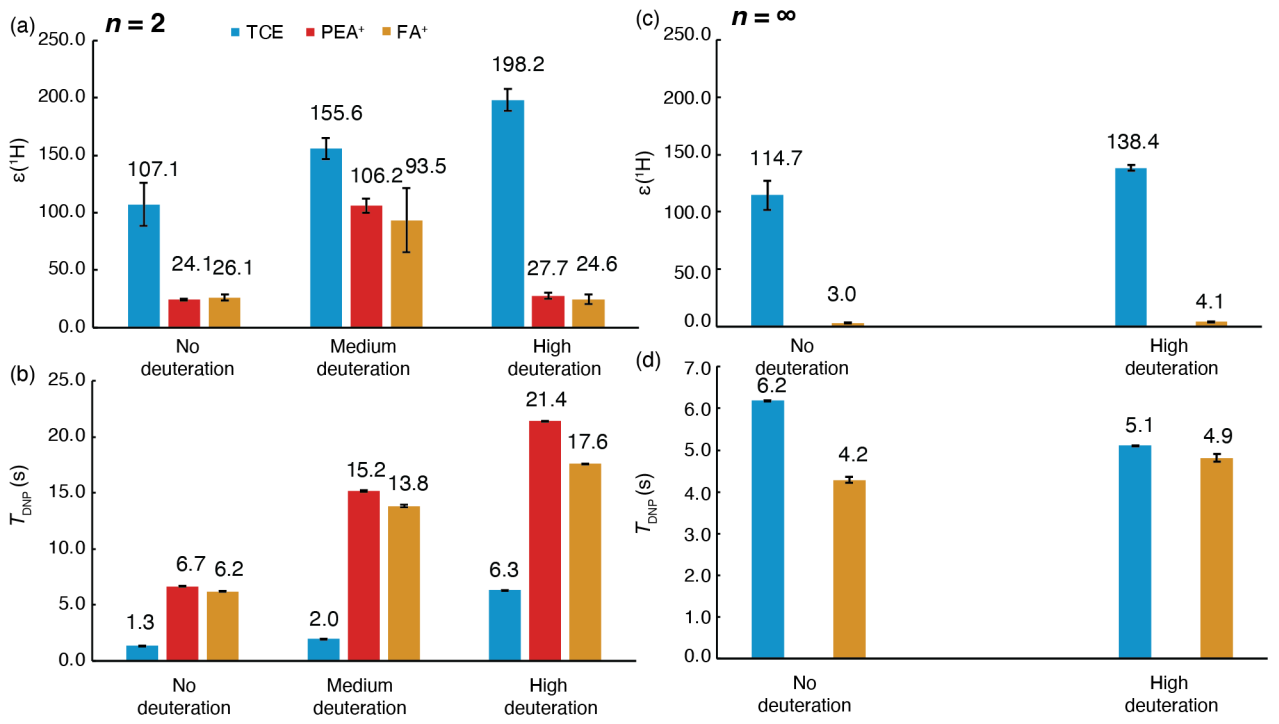

Figure 4-4. ^{1}H DNP enhancement factors and polarization build-up constants (T_{DNP}) as a function of deuteration level for (a, b) n = 2 $PEA_2FAPb_2I_7$, and (c, d) n = ∞ $FAPbI_3$. Medium deuteration for n = 2 is achieved using 60% d_3-PEAI and 50% d_4-FAI. High deuteration for n = 2 is achieved using 80% d_3-PEAI and 85% d_5-FAI. High deuteration for $FAPbI_3$ is achieved using 85% d_5-FA.

To determine, and mitigate, the effect of fast ^{1}H relaxation by the dynamic FA^+ cation, we synthesized the n = 2 perovskite having deuterated the FA^+ cation to different degrees. Note that since the -NH_3 hydrogens in PEA^+ could exchange with FA^+ during synthesis, these were also deuterated. Deuteration of the DNP matrix to decrease the ^{1}H heat capacity is well established,[113, 443, 444] while deuteration of fast-relaxing methyl groups in proteins[445] or on the surfaces of heterogeneous catalysts[446] has also previously been shown to improve DNP performance. Figure 4-4a shows how with increasing deuteration of FA^+, the enhancement of the solvent increases progressively, to reach levels similar to the factors of 177 – 215 achieved for n = 1. This indicates that dissipation of hyperpolarization in the fast-relaxing perovskite phase is the primary factor limiting the solvent enhancement in the n = 2 formulations. The concomitant increase in the T_{DNP} constants for the perovskite corroborates this observation (Figure 4-4b), since the ratio of fast-relaxing FA^+ protons to slower relaxing PEA^+ protons decreases. For the sample with medium deuteration, the enhancement of the perovskite signals increases by a factor of 4, to over 100 for the PEA^+, as compared to the non-deuterated sample. This arises from the lower proportion of the fast-relaxing cations which slows the average T_1 relaxation, increasing the spin-diffusion length and the amount of hyperpolarization that can accumulate both in the solvent and the perovskites. Interestingly, the highly deuterated sample exhibits even higher solvent enhancements, but lower enhancements for the perovskite, comparable to the non-deuterated n = 2 sample. This can be explained by a reduction in ^{1}H spin-diffusion efficiency at the highest deuteration level, due to the low ^{1}H concentration, which hampers propagation of polarization into the perovskite. In particular, when the FA^+ cation is highly deuterated, the perovskite layer acts as a barrier to ^{1}H spin diffusion. Furthermore, since the layers are likely to be aligned with the platelet morphology, we speculate that polarization from the majority of the hyperpolarized solvent must pass through FA^+ layers. Therefore, although the high deuteration of FA^+ moieties increases the perovskite T_{DNP} and reduces polarization loss by relaxation, the overall effect with diminished spin-diffusion gives similar enhancements to those of the non-deuterated n = 2 composition.

Applying a similar deuteration strategy to pure $FAPbI_3$ is less successful. The solvent enhancement is increased to some extent, but not as much as for n = 2 (Figure 4-4c); this is ascribed to the fact that the T_1 relaxation of the perovskite remains fast (T_{DNP} = 4 s, Figure 4-4d), and therefore, although the concentration of the relaxation sinks is reduced, the perovskite does still act as a sink for the solvent hyperpolarization. Greater microwave absorption by n = ∞ than n = 2 reducing the efficiency of saturating the ESR transitions could also play a role, although the sample heating remains similar. The low enhancement for the perovskite itself is expected because only the fast-relaxing cations with residual protonation can be observed.

Although these DNP experiments significantly improve the NMR sensitivity, they were performed with conventional DNP hardware using 3.2 mm outer diameter sample containers (rotors) that require a high sample mass of at least 50 mg, whereas a typical thin-film device contains only ~1 mg of perovskite. Very recently, state-of-the-art DNP hardware has been developed using 0.7 mm outer

diameter rotors which require only 1 – 2 mg of sample, while enabling faster magic-angle spinning that improves resolution;[447] sensitivity and resolution is further improved by the use of a high magnetic field of 21 T, compared to 9.4 T used above. We first tested the DNP using this system on a mechanosynthesized n = 1 perovskite sample, as studied above, wetted with a 32 mM solution of the HyTEK-2 biradical[100] in TCE, which has been shown to perform significantly better than TEKPol at high field with fast spinning.[447] As shown in Figure 4-5a, the TCE and PEA^+ signals exhibit enhancement factors of 125 and 35, respectively. Although solvent enhancements up to 200 have been demonstrated with this formulation in pure frozen solutions,[447] the sample enhancement is nevertheless similar to that obtained in the more conventional DNP experiments at 9.4 T above, validating the effectiveness of the experimental setup. We note that a slightly lower sample temperature of 111 K was observed (cf. 119 K at 9.4 T), possibly due to different microwave absorption at higher frequency and/or more efficient cooling of the smaller rotor.

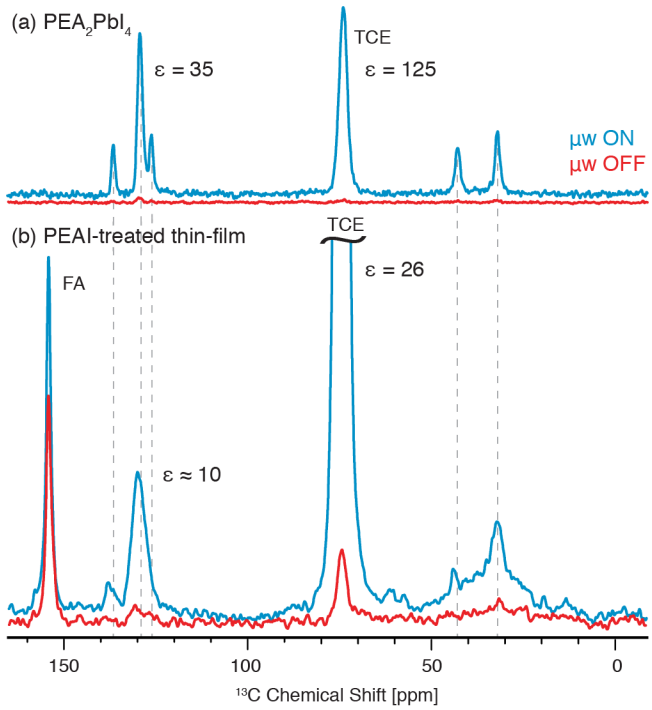

Figure 4-5. DNP enhanced $^1H \rightarrow ^{13}C$ spectra at ~110 K and 21 T of (a) mechanosynthesized n = 1 PEA_2PbI_4 recorded for 2 minutes (20 minutes for microwave off) at 50 kHz MAS, (b) a PEAI-treated single thin-film of deuterated $FAPbI_3$ recorded for one day at 40 kHz MAS.

We then turned to the challenge of studying a technologically relevant surface coating on a thin film. Phenylethylammonium iodide (PEAI) is one of the most widely used passivating agents[218, 341, 448, 449] for perovskite thin-films owing to its bulky nature that facilitates the formation of 2D- perovskite while providing high stability to the material.[341, 450] Here, a ~500 nm layer of deuterated $FAPbI_3$ was spin-coated onto a glass slide (2 × 2 cm^2) and passivated with a thin (~20 nm) surface layer of PEAI, followed by annealing at 100°C. The film was then scraped off (to yield about 0.8 mg) and packed into a 0.7 mm rotor to which the radical-containing solution was then added by centrifugation. The sample is estimated to contain a total of about 6 μg (50 nmol) of PEA^+. Figure 4-5b shows that the PEA^+ signals can clearly be seen in the resulting DNP-enhanced $^1H \rightarrow ^{13}C$ spectrum obtained in 27 hours, whereas even the most intense peak can barely be seen without DNP, giving an estimated enhancement for the PEA^+ layer by a factor ~10 (we therefore estimate that it would have taken ~100 days to acquire this spectrum with the same signal-to-noise ratio without DNP). The FA^+ enhancement is minimal, consistent with expectations from the experiments on deuterated mechanosynthesized $FAPbI_3$. The high PEA^+ enhancement and low FA^+ enhancement are also evident in the ^1H NMR spectrum (Figure 4-11), however the resolution is insufficient to interpret the structure, even at 40 kHz MAS.

Comparing the observed PEA^+ carbon-13 shifts (Figure 4-5 and Figure 4-9) we note that there is a significant change between the PEAI salt and the n = 1 perovskite, reflecting the substantial structural transformation.[302] The PEA^+ signals observed in the spectra of the surface-coated thin film shown in Figure 4-5 align most closely with those for the layered perovskites, indicating that after the surface treatment, the PEA^+ adopts the layered structure, in line with previous reports.[341, 346, 449, 450] However, the peaks are significantly broader, indicating a broader distribution of local environments and disorder in the thin-film coating. This is consistent with a mixture of n = 1 and higher order homologues,[214] as well as the nanoscale thickness of the passivating layer, meaning that most of the material is within ~10 nm of the surface or the perovskite interface, which can slightly modify the local structure. In addition, a slight shift of ~1 ppm is observed for the carbon closest to the perovskite layer (Figure 4-9). This may correspond to a slightly different

binding of the organic spacers to the inorganic layers, or a slight difference in the electronic structure of the inorganic layers, in the nanoscale coating layer as compared to the bulk layered perovskite.

4.3 Conclusions

In conclusion, we have identified the factors that previously limited DNP efficiency in hybrid perovskites. In particular, we find that the primary impediment to hyperpolarization is the fast ^{1}H relaxation of the dynamic cation, while microwave absorption by the sample is also detrimental due to both sample heating and reduced saturation efficiency. We have shown that this can be mitigated by deuterating the cation, which then enables large DNP enhancements to develop on both the DNP matrix and target organic species present at low concentrations in the sample. We have further demonstrated that DNP can be favorably applied to two-dimensional layered perovskites, with the high surface-to-volume ratio that can arise from platelet morphologies being particularly beneficial.

There is plenty of further scope to improve the enhancement by optimizing the impregnation protocols, which could be further combined with isotopic labelling to achieve ultimate sensitivity.[451-453] This will then enable, for example, multi-dimensional correlation experiments to provide information about connectivity and spatial proximities.

Here, efficient DNP with deuterated samples enabled the observation of the ^{13}C PEA^{+} signals from the approximately 6 µg of surface coating on a single $FAPbI_3$ perovskite thin-film, by combining with cutting-edge DNP hardware for small-diameter rotors at high field. The spectra of the thin-film immediately reveal that while the PEA^{+} structure most strongly resembles that in a layered perovskite, there is a greater distribution of local environments and subtle differences in the environment near the perovskite surface. This work extends DNP enhanced solid-state methods to a new class of semiconducting photovoltaic materials, and therefore paves the way to characterize the local structure of additives and surface treatments for technologically relevant perovskite thin-film compositions.

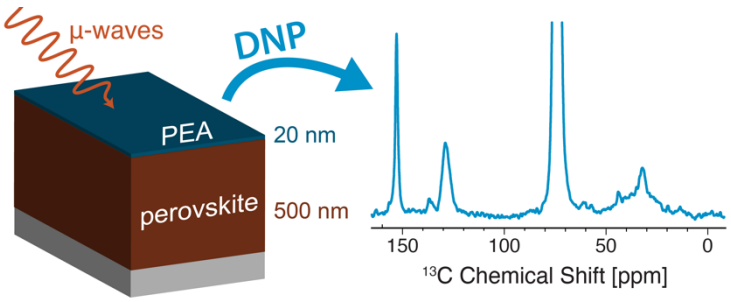

Figure 4-6. Schematic illustration of DNP on a single perovskite thin-film.

4.4 Appendix

Table 4-1. DNP build-up time constants, T_{DNP}, measured from the $^{1}H \rightarrow ^{13}C$ CP spectra for the solvent and perovskite signals in each material used in this chapter.

Perovskite Composition	PEA^+ (s)	FA^+ (s)	TCE (s)
$FAPbI_3$ ($n = \infty$)	-	4.3 ± 0.1	6.194 ± 0.002
d_5-$FAPbI_3$ ($n = \infty$)	-	4.8 ± 0.1	5.105 ± 0.001
PEA_2PbI_4 ($n = 1$)	102.1 ± 0.4	-	7.002 ± 0.004
$PEA_2FAPb_2I_7$ ($n = 2$)	6.66 ± 0.01	6.19 ± 0.03	1.335 ± 0.003
$(d_3\text{-}PEA)_2(d_4\text{-}FA)Pb_2I_7$ ($n = 2$)	15.2 ± 0.1	13.8 ± 0.1	1.94 ± 0.06
$(d_3\text{-}PEA)_2(d_5\text{-}FA)Pb_2I_7$ ($n = 2$)	21.4 ± 0.1	17.6 ± 0.1	6.34 ± 0.05

Table 4-2. Experimental parameters used for the spectra shown in Figure 4-5

Sample	Recycle delay (s)	Scans	Experiment time
PEAI-treated thin-film (μw on)	5	19180	27 h
PEAI-treated thin-film (μw off)	5	18176	26 h
PEA_2PbI_4 (μw on)	30	4	2 mins
PEA_2PbI_4 (μw off)	30	40	20 mins

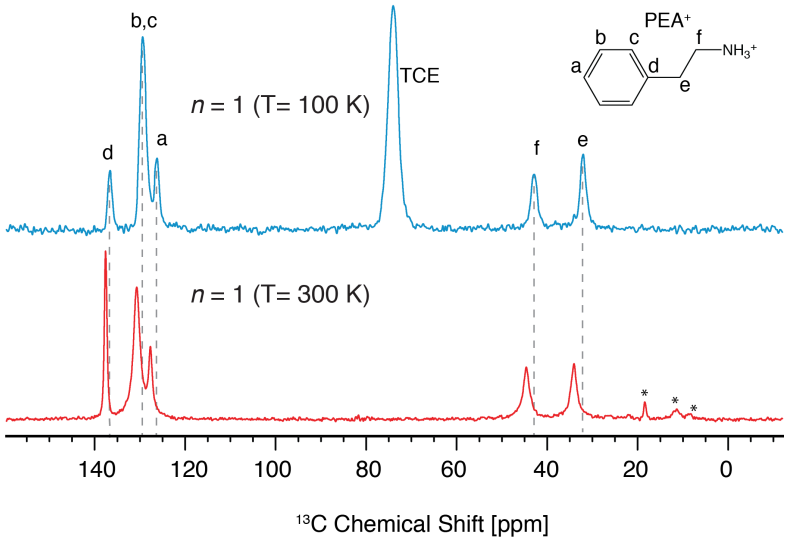

Figure 4-7. $^{1}H \rightarrow ^{13}C$ cross polarization (CP) spectra of PEA_2PbI_4 ($n = 1$) at the indicated temperatures. Asterisks (*) denote spinning sidebands. There are minor changes in the shifts as a function of temperature, therefore we make comparisons at the same temperature.

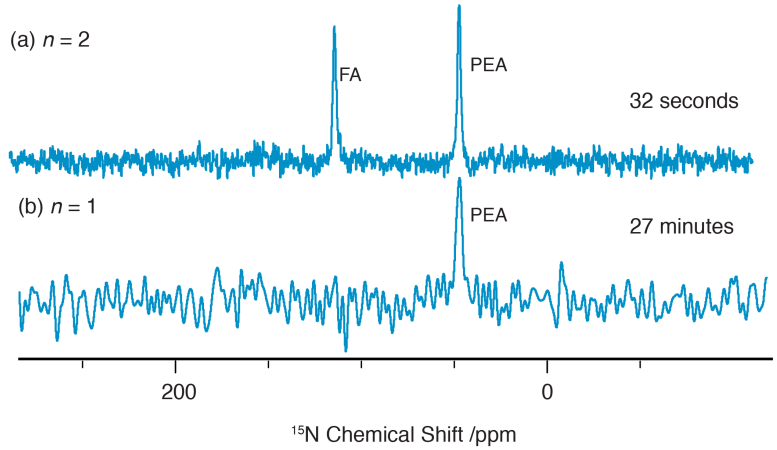

Figure 4-8. DNP enhanced $^{1}H \rightarrow ^{15}N$ CP spectra at natural abundance with 16 scans (a) n = 2 $(d_3\text{-PEA})_2(d_4\text{-FA})Pb_2I_7$ with a 2 s recycle delay (b) n = 1 PEA_2PbI_4 with a 100 s recycle delay.

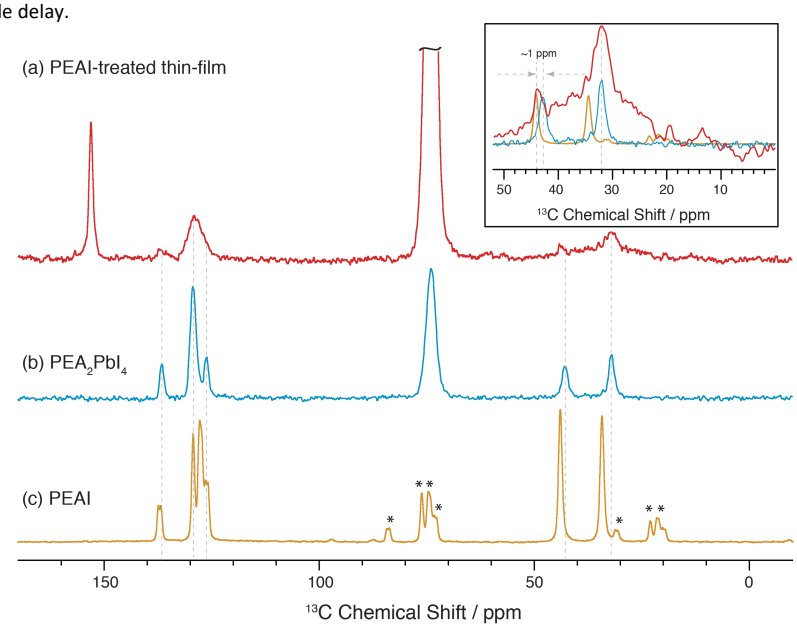

Figure 4-9. DNP enhanced $^{1}H \rightarrow ^{13}C$ spectra at ~110 K and 21 T of (a) a PEAI-treated single thin-film of deuterated $FAPbI_3$ recorded for one day at 40 kHz MAS, (b) mechanosynthesized n = 1 PEA_2PbI_4 recorded for 2 minutes at 50 kHz MAS and (c) PEAI precursor at 12 kHz MAS and ~100 K. Asterisks denote spinning sidebands. The inset shows the zoomed spectra between 0–50 ppm to highlight the relative shifts.

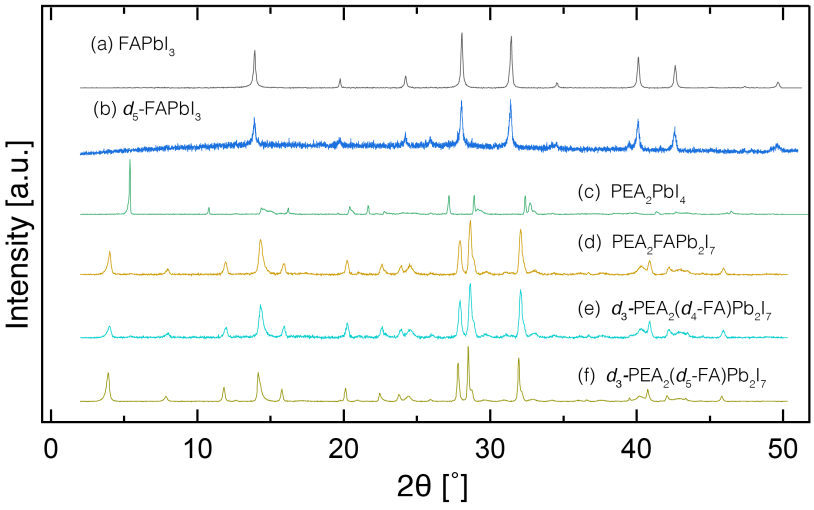

Figure 4-10. Powder XRD diffractograms of mechanosynthesized perovskite compositions used in this work. (e) and (f) correspond to medium- and high-deuteration samples respectively.

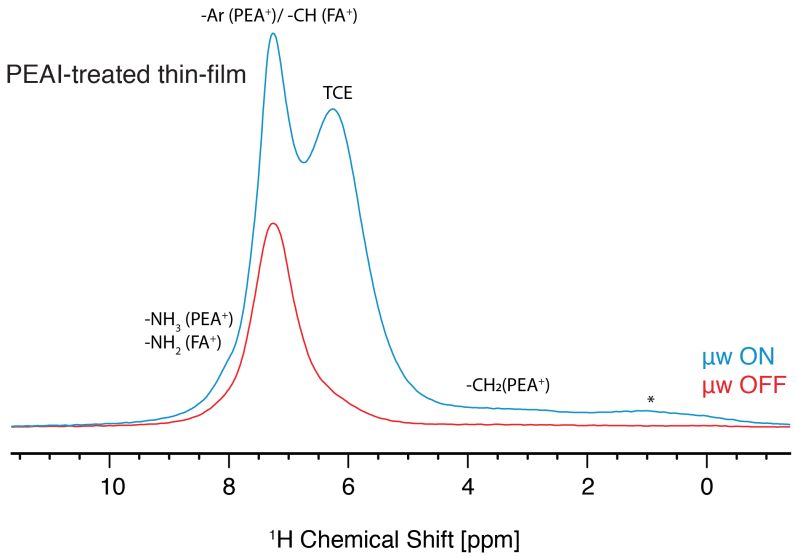

Figure 4-11. Echo-detected ^{1}H NMR spectra of a PEAI-treated thin film at 21.1 T, 40 kHz MAS under microwave on (~111 K) and microwave off (100 K) conditions. The asterisk (*) denotes the residual solvent impurity. Ar = aromatic ^{1}H signals.

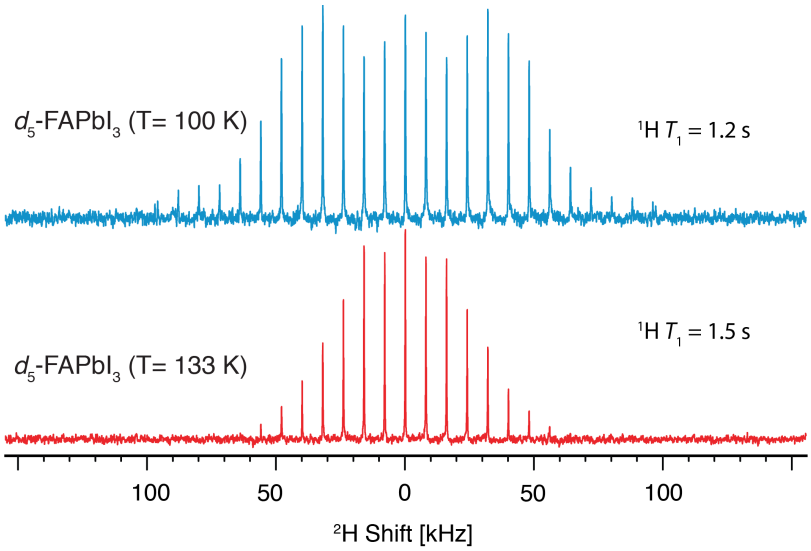

Figure 4-12. Bloch decay ^{2}H spectra of d_5-$FAPbI_3$ at 9.4 T and 8 kHz MAS at the indicated temperatures.

Chapter 5 Conclusions

5.1 Summary

In summary, this thesis presents methods to solve the structure and dynamics in perovskite materials. This has been possible with the use of solid-state NMR, NMR crystallography, and dynamic nuclear polarization (DNP).

Structure: Several examples of using NMR to address structural problems in hybrid perovskites have been shown. The atomic-level structure of DMA^+-doped $CsPbI_3$ perovskite was determined using MAS NMR for samples prepared using two different approaches: (a) solution processing and (b) mechanosynthesis. Mixed cation $Cs_xDMA_{1-x}PbI_3$ was formed when it is kinetically trapped by rapid antisolvent-induced crystallization. Solid-solutions are found to be thermodynamically unstable and synthesis under thermodynamic control leads to segregated phase of $DMAPbI_3$ and $CsPbI_3$. In a second example, MAS NMR was combined with computational methods to give the structure of the organic layer in Ruddlesden–Popper hybrid perovskites. In particular, NMR crystallography determined the structure of layered hybrid perovskites for a mixed-spacer model composed of 2-phenylethylammonium (PEA^+) and 2-(perfluorophenyl)ethylammonium (FEA^+) moieties, revealing nanoscale phase segregation. This system showed promising performance in solar cells with PCE exceeding 21% and enhanced operational stability.

Further, an NMR-driven atomic-level picture in current state-of-the-art hybrid and inorganic perovskites was presented. These studies have extensively used mechanosynthesis to introduce and thoroughly investigate systematic changes in the perovskite compositions. Once the structural hypothesis was confirmed, experiments were run on scratched thin films used for the perovskite solar cells to validate the applicability of the conclusions based on mechanosynthesised samples. In this manner, the mechanistic insights derived from these structures have guided these studies to achieve one of the highest-performing perovskites solar cells available in the literature today. In this device, small amounts of formate and methylammonium were added to the precursor solution. The defect-passivating role of formate ions in $FAPbI_3$ was confirmed and the amount of MA^+ was detected and quantified, which was reflected in the modulation of the band gap of the material. In the following work, MASCN-assisted $FAPbI_3$ perovskite growth was studied as it reduced the phase transition temperature of the material and it was hypothesized that thiocyanate initiated the phase transition of the material to the photoactive phase via strong coordination with the perovskite surface. In this work, the incorporation of a trace amount of MA^+ ions in the lattice was quantified. Further, their atomic-scale proximities with FA^+ ions were established. In the end, intermediate-phase engineered $CsPbBr_3$ inorganic perovskite growth was studied. Initially, the possibility of incorporation of FA^+ ions in the $CsPbBr_3$ lattice was systematically investigated using mechanosynthesised compositions to build a hypothesis. Further, the effect of temperature was studied in combination with solution-state NMR. Then, a structural model emerged from these NMR results, thus providing the link to the improved interfacial contacts in the inorganic perovskite solar cell.

Dynamics: Cation dynamics in contemporary perovskite compositions was investigated using quadrupolar NMR relaxometry. The variable temperature relaxometry data was then combined with rotational diffusion model to determine activation energies (E_a) and correlation times (τ_c) at room temperature, about each unique principal axis of the cation. All cations (FA^+, MA^+ and GUA^+) were found to have at least one component of rotation on picosecond timescale at room temperature, with MA^+ and GUA^+ also having a faster and a slower component respectively. Further, we found that cation alloying did not induce any change in the underlying cation dynamics, suggesting the dynamics are more dependent on the inorganic lattice. In particular, the FA^+ rotational energy landscape was found to be invariant across all multi-cation compositions i.e., $FAPbI_3$, $FA_xCs_{1-x-y}MA_yPbI_3$, and $FA_xMA_{1-x}PbI_3$ when sufficiently above with phase transition temperature. In addition, an unusual relaxation behavior for deuterium nuclei in MA^+ ion was observed while investigating dynamics in $FA_xMA_{1-x}PbI_3$. This behavior was found to be result of the MA^+ physical diffusion.

DNP: DNP methods were developed to determine the structure of the surface layer on a perovskite thin-film. In this work, the factors that limit DNP performance in hybrid perovskite were systematically investigated using mechanosynthesized low-dimensional perovskites. Starting with the possible hypotheses of microwave absorption, fast-relaxation and morphology, fast relaxation was found to have a major impact on the overall enhancement, while the others played a secondary role. Further, this fast relaxation was tailored favorably by deuteration to improve the enhancement factor up to 100. This method was then harnessed to determine the surface structure of an extremely mass-limited passivation layer on a single thin-film.

5.2 Outlook

The perovskite community has studied a huge number of formulations to improve the functional properties of hybrid perovskites. This gigantic effort in the last decade can be rationalized in terms of improvement in electronic and structural properties. However, the atomic-level mechanism of these improvements has been poorly understood, with a lack of definite underlying principles for designing more effective formulations. As I have demonstrated in this thesis, conventional solid state NMR methods can be utilized to test various synthetic approaches and their effect on structure, which can then be compared to rationalize the fundamental principles. Further methodological development will enable NMR to address the remaining fundamental problems in this fast-growing field of materials science; here, I present some examples of potential future directions.

The foremost area involves effective combination of DNP with light illumination at high magnetic fields, which opens the door for real-time monitoring of light-induced phenomena in the material, such as quantifying the amount of degraded species, the kinetics, and their lifetimes. Today, light-induced phenomena are monitored primarily using time revolved photoluminescence (PL) spectra.[454-459] In particular, light-induced phase segregation in mixed halide perovskite films/nanocrystals has been well established. Various models have been developed to rationalize this segregation and its reversibility, which are based on thermodynamics,[345, 455, 460-463] polaron-induced lattice strain,[461, 464, 465] or interaction of carrier gradients with point defects in the materials.[466-468] Moreover, some models also predict dependence on external parameters such as temperature and light illumination.[345, 462, 465, 466] However, the fundamental question of what exactly induces this segregation is not well understood. NMR in combination with light can potentially answer these fundamental questions. In addition, various hypotheses present in the current literature today need to be confirmed with their link to the atomic-level structure of the material, such as suppression of light induced phase segregation in the presence of Cs^{+}[192, 469, 470] and Cl^{-}[471] ions. Further, these methodological advancements can be applied to low dimensional mixed halide perovskites as they are also shown to be resilient against halide-ion mobility.[472]

Another important topic is the crystallization of perovskites, particularly $FAPbI_3$, which is strikingly correlated with the perovskite stability.[473, 474] Studies have proposed an intermediate phase theory whereby $FAPbI_3$ passes through various intermediate polytypes on crystallization (from 2H/δ→4H→6H→8H→3C/α) as shown in Figure 5-1.[473] In particular, the 8H-phase is thought to help in understanding the roles of doping cations and anions within the framework of compositional engineering.[473] These studies have used single crystals to access structural parameters;[473] however, these polytypes have not been thoroughly investigated for polycrystalline thin-films or powdered samples, particularly with atomic-level probes. I believe that a thorough investigation on thin-films samples can shed light on these intermediate polytypes. In particular, ^{13}C or ^{207}Pb NMR can be very effective in combination with NMR crystallography.

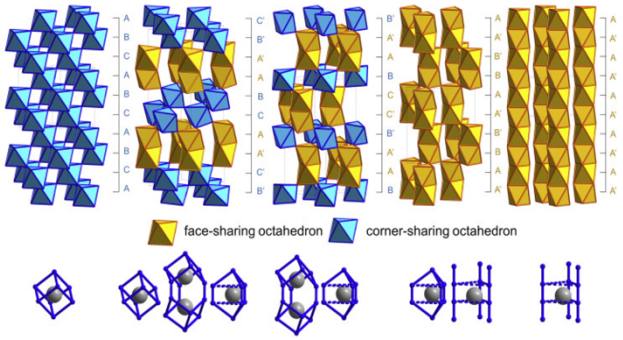

Figure 5-1 Structural evolution of $FAPbX_3$ single crystals. Reproduced with permission from the original work.[473]

This thesis presents an investigation of the dynamics of most prototypical cations in various contemporary perovskite compositions. Application of this method can be easily envisaged on recently discovered new molecular cations such as dimethylammonium (DMA^{+})[264, 265, 428] and methylenediammonium (MDA^{+}).[329, 395] These two cations have been shown to play an important role in improving the overall optoelectronic properties of halide perovskites. The effect of bromine incorporation on the cation dynamics is another important question, as this correlates with longer carrier lifetimes.[475] Introduction of bromine in the $FAPbI_3$ lattice has been shown to slow down the formamidinium rotation from low temperature (80–100 K) quasi-elastic neutron scattering experiments.[475] However, as $FAPbI_3$ undergoes well known phase transitions and adopts a different structural phase at room temperature,[182, 183] the extrapolation to room temperature is potentially not valid, especially since the dynamics are strongly correlated with the symmetry of the inorganic lattice, as observed experimentally in this thesis.

In this thesis impregnation DNP was exploited with only one formulation, i.e., 16 mM TEKPOl in TCE. However, other radical-solvent combinations can be tested and corresponding enhancements can be compared in the future. This will not only help in achieving optimum enhancement but will also help in the understanding the nature of the perovskite surface properties. Further, iodide based inorganic perovskite are least resistant to ambient air, as mentioned in the introduction, and are therefore often treated with surface passivation. Therefore, DNP can be extended to inorganic perovskites, where it can help access the surface structure of the passivation layer.[256-258] In these cases, optimizing and applying methods such as pulse cooling will be beneficial. These methods can then be extended to tin-based perovskites.

Introduction of paramagnetic metal-ion dopants (Mn^{2+} and Gd^{3+}) increases the luminescence and stability of halide perovskites.[476-482] In the past, ^{133}Cs and ^{1}H paramagnetic relaxation enhancement (PRE) has shown that these paramagnetic dopants are incorporated into the perovskite structure.[202, 204] Therefore, these high-spin paramagnetic dopants could be used as polarizing agents for DNP. In this case the achieved enhancements and their correlation with the doping concentration, particle size, microwave absorption, and build-up times can be established to help develop the understanding of metal-ion DNP in general and for these systems in particular.

References

1. Askeland, D. R.; Wright, W. J., *Essentials of materials science and engineering*. Cengage Learning: 2018.
2. Callister, W. D.; Rethwisch, D. G., *Materials science and engineering: an introduction*. Wiley New York: 2018; Vol. 9.
3. Smith, W. F., Principles of materials science and engineering. **1986**.
4. Borchardt-Ott, W., *Crystallography: an introduction*. Springer Science & Business Media: 2011.
5. Giacovazzo, C.; Monaco, H. L.; Artioli, G.; Viterbo, D.; Milanesio, M.; Gilli, G.; Gilli, P.; Zanotti, G.; Ferraris, G.; Catti, M., Fundamentals of crystallography. **2011**.
6. Ladd, M. F. C.; Palmer, R. A.; Palmer, R. A., *Structure determination by X-ray crystallography*. Springer: 1977; Vol. 233.
7. Czichos, H.; Saito, T.; Smith, L., *Springer handbook of materials measurement methods*. Springer: 2006; Vol. 978.
8. O'Connor, D. J.; Sexton, B. A.; Smart, R. S., *Surface analysis methods in materials science*. Springer Science & Business Media: 2013; Vol. 23.
9. Hirsch, P. B., *Topics in Electron Diffraction and microscopy of materials*. CRC Press: 1999.
10. Andrew, E.; Bradbury, A.; Eades, R., Removal of dipolar broadening of nuclear magnetic resonance spectra of solids by specimen rotation. *Nature* **1959,** *183* (4678), 1802–1803.
11. Lowe, I., Free induction decays of rotating solids. *Phys. Rev. Lett.* **1959,** *2* (7), 285.
12. Maricq, M. M.; Waugh, J. S., NMR in rotating solids. *J. Chem. Phys.* **1979,** *70* (7), 3300–3316.
13. Pecher, O.; Carretero-González, J.; Griffith, K. J.; Grey, C. P., Materials' Methods: NMR in Battery Research. *Chem. Mater.* **2017,** *29* (1), 213–242.
14. Pecher, O.; Vyalikh, A.; Grey, C. P., Challenges and new opportunities of in situ NMR characterization of electrochemical processes. *AIP Conf Proc* . **2016,** *1765* (1), 020011.
15. Marom, R.; Amalraj, S. F.; Leifer, N.; Jacob, D.; Aurbach, D., A review of advanced and practical lithium battery materials. *J. Mater. Chem.* **2011,** *21* (27), 9938–9954.
16. Morales, D. J.; Greenbaum, S., NMR Investigations of Crystalline and Glassy Solid Electrolytes for Lithium Batteries: A Brief Review. *Int. J. Mol. Sci.* **2020,** *21* (9), 3402.
17. Grey, C. P.; Lee, Y. J., Lithium MAS NMR studies of cathode materials for lithium-ion batteries. *Solid State Sci.* **2003,** *5* (6), 883–894.
18. Grey, C. P.; Dupré, N., NMR Studies of Cathode Materials for Lithium-Ion Rechargeable Batteries. *Chem. Rev.* **2004,** *104* (10), 4493–4512.
19. Oschatz, M.; Borchardt, L.; Hippauf, F.; Nickel, W.; Kaskel, S.; Brunner, E., Chapter Four - Interactions Between Electrolytes and Carbon-Based Materials—NMR Studies on Electrical Double-Layer Capacitors, Lithium-Ion Batteries, and Fuel Cells. In *Annual Reports on NMR Spectroscopy*, Webb, G. A., Ed. Academic Press: 2016; Vol. 87, pp 237–318.
20. Kuhn, A.; Kunze, M.; Sreeraj, P.; Wiemhöfer, H. D.; Thangadurai, V.; Wilkening, M.; Heitjans, P., NMR relaxometry as a versatile tool to study Li ion dynamics in potential battery materials. *Solid State Nucl. Mag.* **2012,** *42*, 2–8.
21. Dahlman, C. J.; Kubicki, D. J.; Reddy, G. N. M., Interfaces in metal halide perovskites probed by solid-state NMR spectroscopy. *J. Mater. Chem. A* **2021,** *9* (35), 19206–19244.
22. Kubicki, D. J.; Stranks, S. D.; Grey, C. P.; Emsley, L., NMR spectroscopy probes microstructure, dynamics and doping of metal halide perovskites. *Nat. Rev. Chem.* **2021,** *5* (9), 624–645.
23. Franssen, W. M. J.; Kentgens, A. P. M., Solid–state NMR of hybrid halide perovskites. *Solid State Nucl. Mag.* **2019,** *100*, 36–44.
24. Piveteau, L.; Morad, V.; Kovalenko, M. V., Solid-State NMR and NQR Spectroscopy of Lead-Halide Perovskite Materials. *J. Am. Chem. Soc.* **2020,** *142* (46), 19413–19437.
25. Pfleiderer, B.; Xu, P.; Ackerman, J. L.; Garrido, L., Study of aging of silicone rubber biomaterials with NMR. *J. Biomed. Mater. Res.* **1995,** *29* (9), 1129–1140.
26. G.P. Drobny; J.R. Long; T. Karlsson; W. Shaw; J. Popham; N. Oyler; P. Bower; J. Stringer; D. Gregory; M. Mehta; Stayton, P. S., Structural Studies of Biomaterials Using Double-Quantum Solid-State NMR Spectroscopy. *Annu. Rev. Phys. Chem.* **2003,** *54* (1), 531–571.
27. Hrkach, J. S.; Peracchia, M. T.; Bomb, A.; Lotan, n.; Langer, R., Nanotechnology for biomaterials engineering: structural characterization of amphiphilic polymeric nanoparticles by 1H NMR spectroscopy. *Biomaterials* **1997,** *18* (1), 27–30.
28. Qi, G.; Wang, Q.; Xu, J.; Deng, F., Solid-state NMR studies of internuclear correlations for characterizing catalytic materials. *Chem. Soc. Rev.* **2021,** *50* (15), 8382–8399.
29. Xu, J.; Wang, Q.; Li, S.; Deng, F., *Solid-state NMR in zeolite catalysis*. Springer: 2019; Vol. 103.
30. Deng, F.; Yang, J.; Ye, C., Solid state nmr characterization of solid surface of heterogeneous catalysts. In *Modern Magnetic Resonance*, Springer: 2008; pp 205–211.
31. Matzkanin, G. A., A review of nondestructive characterization of composites using NMR. *Nondestructive characterization of materials* **1989**, 655–669.
32. Jelinski, L. W., Solid state deuterium NMR studies of polymer chain dynamics. *Annu. Rev. Mater. Sci* **1985,** *15* (1), 359–377.
33. Adams, A., Non-destructive analysis of polymers and polymer-based materials by compact NMR. *Magn. Reson. Imaging* **2019,** *56*, 119–125.
34. Spiess, H., Structure and dynamics of solid polymers from 2D-and 3D-NMR. *Chem. Rev.* **1991,** *91* (7), 1321–1338.
35. Cheng, H.; Early, T. A. In *NMR Studies of polymeric materials - an overview*, Macromolecular Symposia, Wiley Online Library: 1994; pp 1-14.

36. Blümich, B.; Blümler, P., NMR imaging of polymer materials. *Die Makromolekulare Chemie: Macromolecular Chemistry and Physics* **1993,** *194* (8), 2133–2161.
37. Hoffmann, H. C.; Debowski, M.; Müller, P.; Paasch, S.; Senkovska, I.; Kaskel, S.; Brunner, E., Solid-State NMR Spectroscopy of Metal–Organic Framework Compounds (MOFs). *Materials* **2012,** *5* (12), 2537–2572.
38. Sutrisno, A.; Huang, Y., Solid-state NMR: A powerful tool for characterization of metal–organic frameworks. *Solid State Nucl. Mag.* **2013,** *49-50*, 1–11.
39. Brunner, E.; Rauche, M., Solid-state NMR spectroscopy: an advancing tool to analyse the structure and properties of metal–organic frameworks. *Chem. Sci.* **2020,** *11* (17), 4297–4304.
40. Lucier, B. E. G.; Chen, S.; Huang, Y., Characterization of Metal–Organic Frameworks: Unlocking the Potential of Solid-State NMR. *Acc. Chem. Res.* **2018,** *51* (2), 319–330.
41. Fu, Y.; Guan, H.; Yin, J.; Kong, X., Probing molecular motions in metal-organic frameworks with solid-state NMR. *Coord. Chem. Rev.* **2021,** *427*, 213563.
42. Witherspoon, V. J.; Xu, J.; Reimer, J. A., Solid-State NMR Investigations of Carbon Dioxide Gas in Metal–Organic Frameworks: Insights into Molecular Motion and Adsorptive Behavior. *Chem. Rev.* **2018,** *118* (20), 10033–10048.
43. He, P.; Lucier, B. E. G.; Terskikh, V. V.; Shi, Q.; Dong, J.; Chu, Y.; Zheng, A.; Sutrisno, A.; Huang, Y., Spies Within Metal-Organic Frameworks: Investigating Metal Centers Using Solid-State NMR. *J. Phys. Chem. C* **2014,** *118* (41), 23728–23744.
44. Bertmer, M., Chapter One - Solid-state NMR of small molecule adsorption in metal–organic frameworks (MOFs). In *Annual Reports on NMR Spectroscopy*, Atta ur, R., Ed. Academic Press: 2020; Vol. 101, pp 1–64.
45. Rottstegge, J.; Wilhelm, M.; Spiess, H. W., Solid state NMR investigations on the role of organic admixtures on the hydration of cement pastes. *Cem. Concr. Compos.* **2006,** *28* (5), 417–426.
46. Walkley, B.; Provis, J. L., Solid-state nuclear magnetic resonance spectroscopy of cements. *Materials Today Advances* **2019,** *1*, 100007.
47. Brunet, F.; Charpentier, T.; Chao, C. N.; Peycelon, H.; Nonat, A., Characterization by solid-state NMR and selective dissolution techniques of anhydrous and hydrated CEM V cement pastes. *Cem. Concr. Res.* **2010,** *40* (2), 208–219.
48. d'Espinose de Lacaillerie, J.-B.; Barberon, F.; Bresson, B.; Fonollosa, P.; Zanni, H.; Fedorov, V. E.; Naumov, N. G.; Gan, Z., Applicability of natural abundance 33S solid-state NMR to cement chemistry. *Cem. Concr. Res.* **2006,** *36* (9), 1781–1783.
49. Le Saoût, G.; Lécolier, É.; Rivereau, A.; Zanni, H., Study of oilwell cements by solid-state NMR. *Comptes Rendus Chimie* **2004,** *7* (3), 383–388.
50. Smith, S. A.; Palke, W. E.; Gerig, J. T., The Hamiltonians of NMR. Part III. *Concepts Magn. Reson.* **1993,** *5* (2), 151–177.
51. Smith, S. A.; Palke, W. E.; Gerig, J. T., The Hamiltonians of NMR. Part II. *Concepts Magn. Reson.* **1992,** *4* (3), 181–204.
52. Smith, S. A.; Palke, W. E.; Gerig, J. T., The Hamiltonians of NMR. part I. *Concepts Magn. Reson.* **1992,** *4* (2), 107–144.
53. Duer, M. J., *Solid state NMR spectroscopy: principles and applications*. John Wiley & Sons: 2008.
54. Harris, R. K., *Nuclear Magnetic Resonance Spectroscopy: A Physicochemical View*. Longman Scientific & Technical: 1986.
55. Apperley, D. C.; Harris, R. K.; Hodgkinson, P., *Solid-state NMR: Basic principles and practice*. Momentum Press: 2012.
56. Moutzouri, P.; de Almeida, B. S.; Torodii, D.; Emsley, L., Pure Isotropic Proton Solid State NMR. *J. Am. Chem. Soc.* **2021,** *143* (26), 9834–9841.
57. de Almeida, B. S.; Moutzouri, P.; Stevanato, G.; Emsley, L., Theory and simulations of homonuclear three-spin systems in rotating solids. *J. Chem. Phys.* **2021,** *155* (8).
58. Lacabanne, D.; Boudet, J.; Malar, A. A.; Wu, P. Z.; Cadalbert, R.; Salmon, L.; Alain, F. H. T.; Meier, B. H.; Wiegand, T., Protein Side-Chain-DNA Contacts Probed by Fast Magic-Angle Spinning NMR. *J. Phys. Chem. B* **2020,** *124* (49), 11089–11097.
59. Man, P. P., Quadrupole couplings in nuclear magnetic resonance, general. *Encyclopedia of Analytical Chemistry* **2000,** *10*, 9780470027318.
60. Wasylishen, R. E.; Ashbrook, S. E.; Wimperis, S., *NMR of quadrupolar nuclei in solid materials*. John Wiley & Sons: 2012.
61. Bryce, D. L., Solid-state NMR of quadrupolar nuclei: Selected new methods and applications. **2022**.
62. Abragam, A., *The principles of nuclear magnetism*. Oxford university press: 1961.
63. Keeler, J., *Understanding NMR spectroscopy*. John Wiley & Sons: 2010.
64. Smith, S. A.; Palke, W. E.; Gerig, J. T., The hamiltonians of NMR. Part IV: NMR relaxation. *Concepts Magn. Reson.* **1994,** *6* (2), 137–162.
65. Levitt, M. H., *Spin dynamics: basics of nuclear magnetic resonance*. John Wiley & Sons: 2013.
66. Józef, K.; Lena, M., *Nuclear spin relaxation in liquids: theory, experiments, and applications*. CRC press: 2017.
67. Werbelow, L. G., Relaxation theory for quadrupolar nuclei. *eMagRes* **2007**.
68. Blumberg, W., Nuclear spin-lattice relaxation caused by paramagnetic impurities. *Phys. Rev.* **1960,** *119* (1), 79.
69. Hayashi, S., Nuclear Spin-Lattice Relaxations Caused by Paramagnetic Impurities in Layered Silicates: Effect of Magic Angle Spinning. *Bull. Magn. Reson.* **1995,** *17*, 300–301.
70. Lesage, A.; Bardet, M.; Emsley, L., Through-Bond Carbon−Carbon Connectivities in Disordered Solids by NMR. *J. Am. Chem. Soc.* **1999,** *121* (47), 10987–10993.
71. Walker, T. G. In *Fundamentals of spin-exchange optical pumping*, Journal of Physics: Conference Series, IOP Publishing: 2011; p 012001.
72. Duckett, S. B.; Mewis, R. E., Application of para hydrogen induced polarization techniques in NMR spectroscopy and imaging. *Acc. Chem. Res.* **2012,** *45* (8), 1247–1257.
73. Lawler, R. G., Chemically induced dynamic nuclear polarization (CIDNP). II. Radical-pair model. *Acc. Chem. Res.* **1972,** *5* (1), 25–33.
74. Overhauser, A. W., Polarization of nuclei in metals. *Phys. Rev.* **1953,** *92* (2), 411.

75. Carver, T. R.; Slichter, C. P., Polarization of nuclear spins in metals. *Phys. Rev.* **1953,** *92* (1), 212.
76. Hall, D. A.; Maus, D. C.; Gerfen, G. J.; Inati, S. J.; Becerra, L. R.; Dahlquist, F. W.; Griffin, R. G., Polarization-enhanced NMR spectroscopy of biomolecules in frozen solution. *Science* **1997,** *276* (5314), 930–932.
77. Becerra, L. R.; Gerfen, G. J.; Temkin, R. J.; Singel, D. J.; Griffin, R. G., Dynamic nuclear polarization with a cyclotron resonance maser at 5 T. *Phys. Rev. Lett.* **1993,** *71* (21), 3561.
78. Ni, Q. Z.; Daviso, E.; Can, T. V.; Markhasin, E.; Jawla, S. K.; Swager, T. M.; Temkin, R. J.; Herzfeld, J.; Griffin, R. G., High Frequency Dynamic Nuclear Polarization. *Acc. Chem. Res.* **2013,** *46* (9), 1933–1941.
79. Maly, T.; Debelouchina, G. T.; Bajaj, V. S.; Hu, K.-N.; Joo, C.-G.; Mak–Jurkauskas, M. L.; Sirigiri, J. R.; Wel, P. C. A. v. d.; Herzfeld, J.; Temkin, R. J.; Griffin, R. G., Dynamic nuclear polarization at high magnetic fields. *J. Chem. Phys.* **2008,** *128* (5), 052211.
80. Haber, S.; Leskes, M., Dynamic Nuclear Polarization in battery materials. *Solid State Nucl. Mag.* **2022,** *117*, 101763.
81. Kaushik, M.; Bahrenberg, T.; Can, T. V.; Caporini, M. A.; Silvers, R.; Heiliger, J.; Smith, A. A.; Schwalbe, H.; Griffin, R. G.; Corzilius, B., Gd (III) and Mn (II) complexes for dynamic nuclear polarization: small molecular chelate polarizing agents and applications with site-directed spin labeling of proteins. *Phys. Chem. Chem. Phys.* **2016,** *18* (39), 27205–27218.
82. Pinon, A. C.; Schlagnitweit, J.; Berruyer, P.; Rossini, A. J.; Lelli, M.; Socie, E.; Tang, M.; Pham, T.; Lesage, A.; Schantz, S.; Emsley, L., Measuring Nano- to Microstructures from Relayed Dynamic Nuclear Polarization NMR. *J. Phys. Chem. C* **2017,** *121* (29), 15993–16005.
83. Rossini, A. J., Materials Characterization by Dynamic Nuclear Polarization-Enhanced Solid-State NMR Spectroscopy. *J. Phys. Chem. Lett.* **2018,** *9* (17), 5150–5159.
84. Rossini, A. J.; Zagdoun, A.; Lelli, M.; Lesage, A.; Copéret, C.; Emsley, L., Dynamic Nuclear Polarization Surface Enhanced NMR Spectroscopy. *Acc. Chem. Res.* **2013,** *46* (9), 1942–1951.
85. Rossini, A. J.; Zagdoun, A.; Hegner, F.; Schwarzwälder, M.; Gajan, D.; Copéret, C.; Lesage, A.; Emsley, L., Dynamic Nuclear Polarization NMR Spectroscopy of Microcrystalline Solids. *J. Am. Chem. Soc.* **2012,** *134* (40), 16899–16908.
86. Zhao, L.; Pinon, A. C.; Emsley, L.; Rossini, A. J., DNP-enhanced solid-state NMR spectroscopy of active pharmaceutical ingredients. *Magn. Reson. Chem.* **2018,** *56* (7), 583–609.
87. Hu, K.-N.; Bajaj, V. S.; Rosay, M.; Griffin, R. G., High-frequency dynamic nuclear polarization using mixtures of TEMPO and trityl radicals. *J. Chem. Phys.* **2007,** *126* (4), 044512.
88. Hu, K.-N.; Debelouchina, G. T.; Smith, A. A.; Griffin, R. G., Quantum mechanical theory of dynamic nuclear polarization in solid dielectrics. *J. Chem. Phys.* **2011,** *134* (12), 125105.
89. Can, T. V.; Caporini, M. A.; Mentink-Vigier, F.; Corzilius, B.; Walish, J. J.; Rosay, M.; Maas, W. E.; Baldus, M.; Vega, S.; Swager, T. M.; Griffin, R. G., Overhauser effects in insulating solids. *J. Chem. Phys.* **2014,** *141* (6), 064202.
90. Shimon, D.; Hovav, Y.; Feintuch, A.; Goldfarb, D.; Vega, S., Dynamic nuclear polarization in the solid state: a transition between the cross effect and the solid effect. *Phys. Chem. Chem. Phys.* **2012,** *14* (16), 5729–5743.
91. Hovav, Y.; Feintuch, A.; Vega, S., Theoretical aspects of dynamic nuclear polarization in the solid state – The cross effect. *J. Magn. Reson.* **2012,** *214*, 29–41.
92. Hovav, Y.; Feintuch, A.; Vega, S., Theoretical aspects of dynamic nuclear polarization in the solid state – The solid effect. *J. Magn. Reson.* **2010,** *207* (2), 176–189.
93. Kundu, K.; Feintuch, A.; Vega, S., Theoretical Aspects of the Cross Effect Enhancement of Nuclear Polarization under Static Dynamic Nuclear Polarization Conditions. *J. Phys. Chem. Lett.* **2019,** *10* (8), 1769–1778.
94. Lilly Thankamony, A. S.; Wittmann, J. J.; Kaushik, M.; Corzilius, B., Dynamic nuclear polarization for sensitivity enhancement in modern solid-state NMR. *Prog. Nucl. Mag. Res. Sp.* **2017,** *102-103*, 120–195.
95. Thurber, K. R.; Tycko, R., Theory for cross effect dynamic nuclear polarization under magic-angle spinning in solid state nuclear magnetic resonance: The importance of level crossings. *J. Chem. Phys.* **2012,** *137* (8), 084508.
96. Rossini, A. J.; Zagdoun, A.; Lelli, M.; Gajan, D.; Rascón, F.; Rosay, M.; Maas, W. E.; Copéret, C.; Lesage, A.; Emsley, L., One hundred fold overall sensitivity enhancements for Silicon-29 NMR spectroscopy of surfaces by dynamic nuclear polarization with CPMG acquisition. *Chem. Sci.* **2012,** *3* (1), 108–115.
97. Hediger, S.; Lee, D.; Mentink-Vigier, F.; de Paëpe, G., MAS-DNP Enhancements: Hyperpolarization, Depolarization, and Absolute Sensitivity. *eMagRes* **2018,** *7*, 105–116.
98. Mentink-Vigier, F.; Paul, S.; Lee, D.; Feintuch, A.; Hediger, S.; Vega, S.; De Paëpe, G., Nuclear depolarization and absolute sensitivity in magic-angle spinning cross effect dynamic nuclear polarization. *Phys. Chem. Chem. Phys.* **2015,** *17* (34), 21824–21836.
99. Mentink-Vigier, F.; Mathies, G.; Liu, Y.; Barra, A.-L.; Caporini, M. A.; Lee, D.; Hediger, S.; G. Griffin, R.; De Paëpe, G., Efficient cross-effect dynamic nuclear polarization without depolarization in high-resolution MAS NMR. *Chem. Sci.* **2017,** *8* (12), 8150–8163.
100. Wisser, D.; Karthikeyan, G.; Lund, A.; Casano, G.; Karoui, H.; Yulikov, M.; Menzildjian, G.; Pinon, A. C.; Purea, A.; Engelke, F.; Chaudhari, S. R.; Kubicki, D.; Rossini, A. J.; Moroz, I. B.; Gajan, D.; Copéret, C.; Jeschke, G.; Lelli, M.; Emsley, L.; Lesage, A.; Ouari, O., BDPA-Nitroxide Biradicals Tailored for Efficient Dynamic Nuclear Polarization Enhanced Solid-State NMR at Magnetic Fields up to 21.1 T. *J. Am. Chem. Soc.* **2018,** *140* (41), 13340–13349.
101. Song, C.; Hu, K.-N.; Joo, C.-G.; Swager, T. M.; Griffin, R. G., TOTAPOL: a biradical polarizing agent for dynamic nuclear polarization experiments in aqueous media. *J. Am. Chem. Soc.* **2006,** *128* (35), 11385–11390.
102. Kubicki, D. J.; Casano, G.; Schwarzwälder, M.; Abel, S.; Sauvée, C.; Ganesan, K.; Yulikov, M.; Rossini, A. J.; Jeschke, G.; Copéret, C., Rational design of dinitroxide biradicals for efficient cross-effect dynamic nuclear polarization. *Chem. Sci.* **2016,** *7* (1), 550–558.
103. Casano, G.; Karoui, H.; Ouari, O., Polarizing agents: evolution and outlook in free radical development for DNP. *Handbook of High Field Dynamic Nuclear Polarization* **2019,** *103*.

104. Ysacco, C.; Karoui, H.; Casano, G.; Le Moigne, F.; Combes, S.; Rockenbauer, A.; Rosay, M.; Maas, W.; Ouari, O.; Tordo, P., Dinitroxides for Solid State Dynamic Nuclear Polarization. *Appl. Magn. Reson.* **2012,** *43* (1), 251–261.
105. Zagdoun, A.; Casano, G.; Ouari, O.; Schwarzwälder, M.; Rossini, A. J.; Aussenac, F.; Yulikov, M.; Jeschke, G.; Copéret, C.; Lesage, A.; Tordo, P.; Emsley, L., Large Molecular Weight Nitroxide Biradicals Providing Efficient Dynamic Nuclear Polarization at Temperatures up to 200 K. *J. Am. Chem. Soc.* **2013,** *135* (34), 12790–12797.
106. Rosay, M.; Blank, M.; Engelke, F., Instrumentation for solid-state dynamic nuclear polarization with magic angle spinning NMR. *J. Magn. Reson.* **2016,** *264*, 88–98.
107. Suter, D.; Ernst, R., Spin diffusion in resolved solid-state NMR spectra. *Phys. Rev. B* **1985,** *32* (9), 5608.
108. Ernst, M.; Meier, B. H., Spin diffusion in solids. *Studies in Physical and Theoretical Chemistry* **1998,** *84*, 83–122.
109. Zhang, S.; Meier, B.; Ernst, R., Local monitoring of proton spin diffusion in static and rotating samples via spy detection. *Solid State Nucl. Mag.* **1993,** *1* (6), 313–320.
110. Kubo, A.; McDowell, C. A., Spectral spin diffusion in polycrystalline solids under magic-angle spinning. *J. Chem. Soc., Faraday trans. I: Phys. Chem. Cond. Phases* **1988,** *84* (11), 3713–3730.
111. Bloembergen, N., On the interaction of nuclear spins in a crystalline lattice. *Physica* **1949,** *15* (3-4), 386–426.
112. Khutsishvili, G. R., Spin diffusion. *Soviet Physics Uspekhi* **1966,** *8* (5), 743.
113. Prisco, N. A.; Pinon, A. C.; Emsley, L.; Chmelka, B. F., Scaling analyses for hyperpolarization transfer across a spin-diffusion barrier and into bulk solid media. *Phys. Chem. Chem. Phys.* **2021,** *23* (2), 1006–1020.
114. Girifalco, L. A., *Statistical mechanics of solids*. OUP USA: 2003; Vol. 58.
115. Seidel, K.; Etzkorn, M.; Sonnenberg, L.; Griesinger, C.; Sebald, A.; Baldus, M., Studying Molecular 3D Structure and Dynamics by High-Resolution Solid-State NMR: Application to l-Tyrosine-Ethylester. *J. Phys. Chem. A* **2005,** *109* (11), 2436–2442.
116. Elena, B.; Pintacuda, G.; Mifsud, N.; Emsley, L., Molecular Structure Determination in Powders by NMR Crystallography from Proton Spin Diffusion. *J. Am. Chem. Soc.* **2006,** *128* (29), 9555–9560.
117. Edzes, H. T.; Bernards, J. P. C., Two-dimensional exchange NMR in static powders: interchain carbon-13 spin exchange in crystalline polyethylene. *J. Am. Chem. Soc.* **1984,** *106* (5), 1515–1517.
118. Manolikas, T.; Herrmann, T.; Meier, B. H., Protein Structure Determination from 13C Spin-Diffusion Solid-State NMR Spectroscopy. *J. Am. Chem. Soc.* **2008,** *130* (12), 3959–3966.
119. Clauss, J.; Schmidt-Rohr, K.; Spiess, H. W., Determination of domain sizes in heterogeneous polymers by solid-state NMR. *Acta Polymerica* **1993,** *44* (1), 1–17.
120. Caravatti, P.; Neuenschwander, P.; Ernst, R. R., Characterization of heterogeneous polymer blends by two-dimensional proton spin diffusion spectroscopy. *Macromolecules* **1985,** *18* (1), 119–122.
121. Schmidt-Rohr, K.; Clauss, J.; Spiess, H. W., Correlation of structure, mobility, and morphological information in heterogeneous polymer materials by two-dimensional wideline-separation NMR spectroscopy. *Macromolecules* **1992,** *25* (12), 3273–3277.
122. Schmidt-Rohr, K.; Clauss, J.; Blümich, B.; Spiess, H. W., Miscibility of polymer blends investigated by 1H spin diffusion and 13C NMR detection. *Magn. Reson. Chem.* **1990,** *28* (13), S3–S9.
123. van der Wel, P. C.; Hu, K.-N.; Lewandowski, J.; Griffin, R. G., Dynamic nuclear polarization of amyloidogenic peptide nanocrystals: GNNQQNY, a core segment of the yeast prion protein Sup35p. *J. Am. Chem. Soc.* **2006,** *128* (33), 10840–10846.
124. Lesage, A.; Lelli, M.; Gajan, D.; Caporini, M. A.; Vitzthum, V.; Miéville, P.; Alauzun, J.; Roussey, A.; Thieuleux, C.; Mehdi, A.; Bodenhausen, G.; Coperet, C.; Emsley, L., Surface Enhanced NMR Spectroscopy by Dynamic Nuclear Polarization. *J. Am. Chem. Soc.* **2010,** *132* (44), 15459–15461.
125. Walder, B. J.; Berk, C.; Liao, W.-C.; Rossini, A. J.; Schwarzwälder, M.; Pradere, U.; Hall, J.; Lesage, A.; Copéret, C.; Emsley, L., One- and Two-Dimensional High-Resolution NMR from Flat Surfaces. *ACS Cent. Sci.* **2019,** *5* (3), 515–523.
126. Vitzthum, V.; Miéville, P.; Carnevale, D.; Caporini, M. A.; Gajan, D.; Copéret, C.; Lelli, M.; Zagdoun, A.; Rossini, A. J.; Lesage, A.; Emsley, L.; Bodenhausen, G., Dynamic nuclear polarization of quadrupolar nuclei using cross polarization from protons: surface-enhanced aluminium-27 NMR. *Chem. Commun.* **2012,** *48* (14), 1988–1990.
127. Blanc, F.; Copéret, C.; Lesage, A.; Emsley, L., High resolution solid state NMR spectroscopy in surface organometallic chemistry: access to molecular understanding of active sites of well-defined heterogeneous catalysts. *Chem. Soc. Rev.* **2008,** *37* (3), 518–526.
128. Kobayashi, T.; Perras, F. A.; Chaudhary, U.; Slowing, I. I.; Huang, W.; Sadow, A. D.; Pruski, M., Improved strategies for DNP-enhanced 2D 1H-X heteronuclear correlation spectroscopy of surfaces. *Solid State Nucl. Mag.* **2017,** *87*, 38–44.
129. Kobayashi, T.; Perras, F. A.; Slowing, I. I.; Sadow, A. D.; Pruski, M., Dynamic Nuclear Polarization Solid-State NMR in Heterogeneous Catalysis Research. *ACS Catal.* **2015,** *5* (12), 7055–7062.
130. Somorjai, G. A.; Frei, H.; Park, J. Y., Advancing the frontiers in nanocatalysis, biointerfaces, and renewable energy conversion by innovations of surface techniques. *J. Am. Chem. Soc.* **2009,** *131* (46), 16589–16605.
131. Moran, R. F.; Dawson, D. M.; Ashbrook, S. E., Exploiting NMR spectroscopy for the study of disorder in solids. *Int. Rev. Phys. Chem.* **2017,** *36* (1), 39–115.
132. Berruyer, P.; Emsley, L.; Lesage, A., DNP in Materials Science: Touching the Surface. In *eMagRes*, 2018; pp 93–104.
133. Eaton, G. R.; Eaton, S. S.; Barr, D. P.; Weber, R. T., *Quantitative EPR*. Springer Science & Business Media: 2010.
134. Kubicki, D. J.; Rossini, A. J.; Purea, A.; Zagdoun, A.; Ouari, O.; Tordo, P.; Engelke, F.; Lesage, A.; Emsley, L., Amplifying Dynamic Nuclear Polarization of Frozen Solutions by Incorporating Dielectric Particles. *J. Am. Chem. Soc.* **2014,** *136* (44), 15711–15718.
135. Björgvinsdóttir, S.; Moutzouri, P.; Berruyer, P.; Hope, M. A.; Emsley, L., Sensitivity Enhancements in Lithium Titanates by Incipient Wetness Impregnation DNP NMR. *J. Phys. Chem. C* **2020,** *124* (30), 16524–16528.

136. Michaelis, V. K.; Corzilius, B. r.; Smith, A. A.; Griffin, R. G., Dynamic nuclear polarization of 17O: direct polarization. *J. Phys. Chem. B* **2013,** *117* (48), 14894–14906.
137. Blanc, F.; Sperrin, L.; Jefferson, D. A.; Pawsey, S.; Rosay, M.; Grey, C. P., Dynamic nuclear polarization enhanced natural abundance 17O spectroscopy. *J. Am. Chem. Soc.* **2013,** *135* (8), 2975–2978.
138. Perras, F. A.; Kobayashi, T.; Pruski, M., Growing Signals from the Noise: Challenging Nuclei in Materials DNP. In *eMagRes*, pp 35–50.
139. Bertarello, A.; Berruyer, P.; Artelsmair, M.; Elmore, C. S.; Heydarkhan-Hagvall, S.; Schade, M.; Chiarparin, E.; Schantz, S.; Emsley, L., In-Cell Quantification of Drugs by Magic-Angle Spinning Dynamic Nuclear Polarization NMR. *J. Am. Chem. Soc.* **2022,** *144* (15), 6734–6741.
140. Lelli, M.; Gajan, D.; Lesage, A.; Caporini, M. A.; Vitzthum, V.; Miéville, P.; Héroguel, F.; Rascón, F.; Roussey, A.; Thieuleux, C., Fast characterization of functionalized silica materials by silicon-29 surface-enhanced NMR spectroscopy using dynamic nuclear polarization. *J. Am. Chem. Soc.* **2011,** *133* (7), 2104–2107.
141. Valla, M.; Rossini, A. J.; Caillot, M.; Chizallet, C.; Raybaud, P.; Digne, M.; Chaumonnot, A.; Lesage, A.; Emsley, L.; van Bokhoven, J. A.; Copéret, C., Atomic Description of the Interface between Silica and Alumina in Aluminosilicates through Dynamic Nuclear Polarization Surface-Enhanced NMR Spectroscopy and First-Principles Calculations. *J. Am. Chem. Soc.* **2015,** *137* (33), 10710–10719.
142. Perras, F. A.; Padmos, J. D.; Johnson, R. L.; Wang, L.-L.; Schwartz, T. J.; Kobayashi, T.; Horton, J. H.; Dumesic, J. A.; Shanks, B. H.; Johnson, D. D., Characterizing substrate–surface interactions on alumina-supported metal catalysts by dynamic nuclear polarization-enhanced double-resonance NMR spectroscopy. *J. Am. Chem. Soc.* **2017,** *139* (7), 2702–2709.
143. Lee, D.; Takahashi, H.; Thankamony, A. S. L.; Dacquin, J.-P.; Bardet, M.; Lafon, O.; De Paëpe, G., Enhanced Solid-State NMR Correlation Spectroscopy of Quadrupolar Nuclei Using Dynamic Nuclear Polarization. *J. Am. Chem. Soc.* **2012,** *134* (45), 18491–18494.
144. Segura Lecina, O.; Hope, M. A.; Venkatesh, A.; Björgvinsdóttir, S.; Rossi, K.; Loiudice, A.; Emsley, L.; Buonsanti, R., Colloidal-ALD-Grown Hybrid Shells Nucleate via a Ligand–Precursor Complex. *J. Am. Chem. Soc.* **2022,** *144* (9), 3998–4008.
145. Perras, F. A.; Kobayashi, T.; Pruski, M., PRESTO polarization transfer to quadrupolar nuclei: implications for dynamic nuclear polarization. *Phys. Chem. Chem. Phys.* **2015,** *17* (35), 22616–22622.
146. Perras, F. A.; Kobayashi, T.; Pruski, M., Natural abundance 17O DNP two-dimensional and surface-enhanced NMR spectroscopy. *J. Am. Chem. Soc.* **2015,** *137* (26), 8336–8339.
147. Perras, F. A.; Wang, Z.; Naik, P.; Slowing, I. I.; Pruski, M., Inside Cover: Natural Abundance 17O DNP NMR Provides Precise O− H Distances and Insights into the Brønsted Acidity of Heterogeneous Catalysts (Angew. Chem. Int. Ed. 31/2017). *Angew. Chem. Int. Ed.* **2017,** *56* (31), 8906–8906.
148. Thankamony, A. S.; Knoche, S.; Bothe, S.; Drochner, A.; Jagtap, A. P.; Sigurdsson, S. T.; Vogel, H.; Etzold, B. J.; Gutmann, T.; Buntkowsky, G., Characterization of V–Mo–W Mixed Oxide Catalyst Surface Species by 51V Solid-State Dynamic Nuclear Polarization NMR. *J. Phys. Chem. C* **2017,** *121* (38), 20857–20864.
149. Hope, M. A.; Halat, D. M.; Magusin, P. C.; Paul, S.; Peng, L.; Grey, C. P., Surface-selective direct 17 O DNP NMR of CeO 2 nanoparticles. *Chem. Commun.* **2017,** *53* (13), 2142–2145.
150. Björgvinsdóttir, S.; Walder, B. J.; Pinon, A. C.; Emsley, L., Bulk Nuclear Hyperpolarization of Inorganic Solids by Relay from the Surface. *J. Am. Chem. Soc.* **2018,** *140* (25), 7946–7951.
151. Björgvinsdóttir, S.; Walder, B. J.; Matthey, N.; Emsley, L., Maximizing nuclear hyperpolarization in pulse cooling under MAS. *J. Magn. Reson.* **2019,** *300*, 142–148.
152. Rossini, A. J.; Zagdoun, A.; Lelli, M.; Canivet, J.; Aguado, S.; Ouari, O.; Tordo, P.; Rosay, M.; Maas, W. E.; Copéret, C., Dynamic nuclear polarization enhanced solid‐state NMR spectroscopy of functionalized metal‐organic frameworks. *Angew. Chem. Int. Ed.* **2012,** *51* (1), 123‐127.
153. Kobayashi, T.; Perras, F. A.; Goh, T. W.; Metz, T. L.; Huang, W.; Pruski, M., DNP-enhanced ultrawideline solid-state NMR spectroscopy: Studies of platinum in metal–organic frameworks. *J. Phys. Chem. Lett.* **2016,** *7* (13), 2322–2327.
154. Rossini, A. J.; Widdifield, C. M.; Zagdoun, A.; Lelli, M.; Schwarzwalder, M.; Coperet, C.; Lesage, A.; Emsley, L., Dynamic nuclear polarization enhanced NMR spectroscopy for pharmaceutical formulations. *J. Am. Chem. Soc.* **2014,** *136* (6), 2324–2334.
155. Lafon, O.; Thankamony, A. S. L.; Kobayashi, T.; Carnevale, D.; Vitzthum, V.; Slowing, I. I.; Kandel, K.; Vezin, H.; Amoureux, J.-P.; Bodenhausen, G., Mesoporous silica nanoparticles loaded with surfactant: low temperature magic angle spinning 13C and 29Si NMR enhanced by dynamic nuclear polarization. *J. Phys. Chem. C* **2013,** *117* (3), 1375–1382.
156. Gunther, W. R.; Michaelis, V. K.; Caporini, M. A.; Griffin, R. G.; Román-Leshkov, Y., Dynamic Nuclear Polarization NMR Enables the Analysis of Sn-Beta Zeolite Prepared with Natural Abundance ^{119}Sn Precursors. *J. Am. Chem. Soc.* **2014,** *136* (17), 6219–6222.
157. Wolf, P.; Valla, M.; Nunez-Zarur, F.; Comas-Vives, A.; Rossini, A. J.; Firth, C.; Kallas, H.; Lesage, A.; Emsley, L.; Coperet, C., Correlating synthetic methods, morphology, atomic-level structure, and catalytic activity of Sn-β catalysts. *ACS Catal.* **2016,** *6* (7), 4047–4063.
158. Wolf, P.; Valla, M.; Rossini, A. J.; Comas-Vives, A.; Núñez-Zarur, F.; Malaman, B.; Lesage, A.; Emsley, L.; Copéret, C.; Hermans, I., NMR Signatures of the Active Sites in Sn-β Zeolite. *Angew. Chem. Int. Ed.* **2014,** *53* (38), 10179–10183.
159. Kumar, A.; Walder, B. J.; Kunhi Mohamed, A.; Hofstetter, A.; Srinivasan, B.; Rossini, A. J.; Scrivener, K.; Emsley, L.; Bowen, P., The atomic-level structure of cementitious calcium silicate hydrate. *J. Phys. Chem. C* **2017,** *121* (32), 17188–17196.
160. Leroy, C.; Aussenac, F.; Bonhomme-Coury, L.; Osaka, A.; Hayakawa, S.; Babonneau, F.; Coelho-Diogo, C.; Bonhomme, C., Hydroxyapatites: key structural questions and answers from dynamic nuclear polarization. *Anal. Chem.* **2017,** *89* (19), 10201–10207.

161. Viger-Gravel, J.; Lan, W.; Pinon, A. C.; Berruyer, P.; Emsley, L.; Bardet, M.; Luterbacher, J., Topology of Pretreated Wood Fibers Using Dynamic Nuclear Polarization. *J. Phys. Chem. C* **2019,** *123* (50), 30407–30415.
162. Chakhmouradian, A. R.; Woodward, P. M., Celebrating 175 years of perovskite research: a tribute to Roger H. Mitchell. *Phys. Chem. Miner.* **2014,** *41* (6), 387–391.
163. Yuan, Y.; Xiao, Z.; Yang, B.; Huang, J., Arising applications of ferroelectric materials in photovoltaic devices. *J. Mater. Chem. A* **2014,** *2* (17), 6027–6041.
164. Wells, H. L., Über die cäsium‐ und kalium‐bleihalogenide. *Zeitschrift für anorganische Chemie* **1893,** *3* (1), 195‐210.
165. Kojima, A.; Teshima, K.; Shirai, Y.; Miyasaka, T., Organometal Halide Perovskites as Visible-Light Sensitizers for Photovoltaic Cells. *J. Am. Chem. Soc.* **2009,** *131* (17), 6050–6051.
166. Best Research-Cell Efficiencies (NREL, accessed 13 July 2022) https://www.nrel.gov/pv/assets/pdfs/best-research-cell-efficiencies-rev220630.pdf.
167. Stoumpos, C. C.; Kanatzidis, M. G., The Renaissance of Halide Perovskites and Their Evolution as Emerging Semiconductors. *Acc. Chem. Res.* **2015,** *48* (10), 2791–2802.
168. Stoumpos, C. C.; Malliakas, C. D.; Kanatzidis, M. G., Semiconducting Tin and Lead Iodide Perovskites with Organic Cations: Phase Transitions, High Mobilities, and Near-Infrared Photoluminescent Properties. *Inorg. Chem.* **2013,** *52*, 9019–9038.
169. Eperon, G. E.; Paterno, G. M.; Sutton, R. J.; Zampetti, A.; Haghighirad, A. A.; Cacialli, F.; Snaith, H. J., Inorganic Caesium Lead Iodide Perovskite Solar Cells. *J. Mater. Chem. A* **2015,** *3*, 19688–19695.
170. Grätzel, M., The light and shade of perovskite solar cells. *Nat. Mater.* **2014,** *13* (9), 838–842.
171. Jeong, J.; Kim, M.; Seo, J.; Lu, H.; Ahlawat, P.; Mishra, A.; Yang, Y.; Hope, M. A.; Eickemeyer, F. T.; Kim, M.; Yoon, Y. J.; Choi, I. W.; Darwich, B. P.; Choi, S. J.; Jo, Y.; Lee, J. H.; Walker, B.; Zakeeruddin, S. M.; Emsley, L.; Rothlisberger, U.; Hagfeldt, A.; Kim, D. S.; Grätzel, M.; Kim, J. Y., Pseudo-halide anion engineering for α-$FAPbI_3$ perovskite solar cells. *Nature* **2021,** *592* (7854), 381–385.
172. Jena, A. K.; Kulkarni, A.; Miyasaka, T., Halide Perovskite Photovoltaics: Background, Status, and Future Prospects. *Chem. Rev.* **2019,** *119* (5), 3036–3103.
173. Manser, J. S.; Christians, J. A.; Kamat, P. V., Intriguing Optoelectronic Properties of Metal Halide Perovskites. *Chem. Rev.* **2016,** *116*, 12956–13008.
174. Fu, Y.; Zhu, H.; Chen, J.; Hautzinger, M. P.; Zhu, X. Y.; Jin, S., Metal halide perovskite nanostructures for optoelectronic applications and the study of physical properties. *Nat. Rev. Mater.* **2019,** *4* (3), 169–188.
175. Hirotsu, S., Experimental studies of structural phase transitions in CsPbCl3. *J. Phys. Soc. Jpn.* **1971,** *31* (2), 552–560.
176. Plesko, S.; Kind, R.; Roos, J., Structural phase transitions in CsPbCl3 and RbCdCl3. *J. Phys. Soc. Jpn.* **1978,** *45* (2), 553–557.
177. Cohen, M.; Young, K.; Chang, T. T.; Brower Jr, W., Phase transitions in CsPbCl3. *J. Appl. Phys.* **1971,** *42* (13), 5267–5272.
178. Hidaka, M.; Okamoto, Y.; Zikumaru, Y., Structural phase transition of CsPbCl3 below room temperature. *Phys. Status Solidi A* **1983,** *79* (1), 263–269.
179. Svirskas, Š.; Balčiūnas, S.; Šimėnas, M.; Usevičius, G.; Kinka, M.; Velička, M.; Kubicki, D.; Castillo, M. E.; Karabanov, A.; Shvartsman, V. V.; de Rosário Soares, M.; Šablinskas, V.; Salak, A. N.; Lupascu, D. C.; Banys, J., Phase transitions, screening and dielectric response of CsPbBr3. *J. Mater. Chem. A* **2020,** *8* (28), 14015–14022.
180. Hirotsu, S.; Harada, J.; Iizumi, M.; Gesi, K., Structural phase transitions in CsPbBr3. *J. Phys. Soc. Jpn.* **1974,** *37* (5), 1393–1398.
181. Sharma, V. K.; Mukhopadhyay, R.; Mohanty, A.; García Sakai, V.; Tyagi, M.; Sarma, D. D., Influence of the Halide Ion on the A-Site Dynamics in FAPbX3 (X = Br and Cl). *J. Phys. Chem. C* **2022,** *126* (16), 7158–7168.
182. Fabini, D. H.; Siaw, T. A.; Stoumpos, C. C.; Laurita, G.; Olds, D.; Page, K.; Hu, J. G.; Kanatzidis, M. G.; Han, S.; Seshadri, R., Universal Dynamics of Molecular Reorientation in Hybrid Lead Iodide Perovskites. *J. Am. Chem. Soc.* **2017,** *139*, 16875–16884.
183. Fabini, D. H.; Stoumpos, C. C.; Laurita, G.; Kaltzoglou, A.; Kontos, A. G.; Falaras, P.; Kanatzidis, M. G.; Seshadri, R., Reentrant Structural and Optical Properties and Large Positive Thermal Expansion in Perovskite Formamidinium Lead Iodide. *Angew. Chem. Int. Ed.* **2016,** *55* (49), 15392–15396.
184. Eperon, G. E.; Stranks, S. D.; Menelaou, C.; Johnston, M. B.; Herz, L.; Snaith, H., Formamidinium Lead Trihalide: A Broadly Tunable Perovskite for Efficient Planar Heterojunction Solar Cells. *Energy Environ. Sci.* **2014,** *7*, 982–988.
185. Bernard, G. M.; Wasylishen, R. E.; Ratcliffe, C. I.; Terskikh, V.; Wu, Q.; Buriak, J. M.; Hauger, T., Methylammonium Cation Dynamics in Methylammonium Lead Halide Perovskites: A Solid-State NMR Perspective. *J. Phys. Chem. A* **2018,** *122* (6), 1560–1573.
186. Wasylishen, R.; Knop, O.; Macdonald, J., Cation Rotation in Methylammonium Lead Halides. *Solid State Commun.* **1985,** *56*, 581.
187. Li, Z.; Yang, M.; Park, J. S.; Wei, S. H.; Berry, J. J.; Zhu, K., Stabilizing Perovskite Structures by Tuning Tolerance Factor: Formation of Formamidinium and Cesium Lead Iodide Solid-State Alloys. *Chem. Mater.* **2016,** *28*, 284–292.
188. Kieslich, G.; Sun, S. J.; Cheetham, A. K., Solid-state principles applied to organic-inorganic perovskites: new tricks for an old dog. *Chem. Sci.* **2014,** *5* (12), 4712–4715.
189. Rong, Y.; Hu, Y.; Mei, A.; Tan, H.; Saidaminov, M. I.; Seok, S. I.; McGehee, M. D.; Sargent, E. H.; Han, H., Challenges for commercializing perovskite solar cells. *Science* **2018,** *361* (6408).
190. Lu, H.; Krishna, A.; Zakeeruddin, S. M.; Gratzel, M.; Hagfeldt, A., Compositional and Interface Engineering of Organic-Inorganic Lead Halide Perovskite Solar Cells. *iScience* **2020,** *23* (8), 101359.
191. Chen, B.; Wang, S.; Song, Y.; Li, C.; Hao, F., A critical review on the moisture stability of halide perovskite films and solar cells. *J. Chem. Eng.* **2022,** *430*, 132701.
192. Nandi, P.; Li, Z.; Kim, Y.; Ahn, T. K.; Park, N. G.; Shin, H., Stabilizing Mixed Halide Lead Perovskites against Photoinduced Phase Segregation by A-Site Cation Alloying. *ACS Energy Lett.* **2021,** *6* (3), 837–847.

193. Pitaro, M.; Tekelenburg, E. K.; Shao, S.; Loi, M. A., Tin Halide Perovskites: From Fundamental Properties to Solar Cells. *Adv. Mater.* **2022,** *34* (1), 2105844.
194. Aftab, A.; Ahmad, M. I., A review of stability and progress in tin halide perovskite solar cell. *Solar Energy* **2021,** *216*, 26–47.
195. Hoefler, S. F.; Trimmel, G.; Rath, T., Progress on lead-free metal halide perovskites for photovoltaic applications: a review. *Monatsh. Chem.* **2017,** *148* (5), 795–826.
196. Zhang, M.; Zhang, Z.; Cao, H.; Zhang, T.; Yu, H.; Du, J.; Shen, Y.; Zhang, X.-L.; Zhu, J.; Chen, P.; Wang, M., Recent progress in inorganic tin perovskite solar cells. *Mater. Today Energy* **2022,** *23*, 100891.
197. Cao, J.; Yan, F., Recent progress in tin-based perovskite solar cells. *Energy Environ. Sci.* **2021,** *14* (3), 1286–1325.
198. Yu, B.-B.; Chen, Z.; Zhu, Y.; Wang, Y.; Han, B.; Chen, G.; Zhang, X.; Du, Z.; He, Z., Heterogeneous 2D/3D Tin-Halides Perovskite Solar Cells with Certified Conversion Efficiency Breaking 14%. *Adv. Mater.* **2021,** *33* (36), 2102055.
199. Xu, Q.; Eguchi, T.; Nakayama, H.; Nakamura, N.; Kishita, M., Molecular Motions and Phase-Transitions in Solid $CH_3NH_3PbCl_3$, $CH_3NH_3PbBr_3$, $CH_3NH_3PbI_3$, as Studied by NMR and NQR. *Z Naturforsch A* **1991,** *46* (3), 240–246.
200. Kubicki, D. J.; Prochowicz, D.; Hofstetter, A.; Zakeeruddin, S. M.; Grätzel, M.; Emsley, L., Phase Segregation in Cs-, Rb- and K-Doped Mixed-Cation $(MA)_x(FA)_{1-x}PbI_3$ Hybrid Perovskites from Solid-State NMR. *J. Am. Chem. Soc.* **2017,** *139*, 14173–14180.
201. Kubicki, D. J.; Prochowicz, D.; Hofstetter, A.; Zakeeruddin, S. M.; Grätzel, M.; Emsley, L., Phase Segregation in Potassium-Doped Lead Halide Perovskites from ^{39}K Solid-State NMR at 21.1 T. *J. Am. Chem. Soc.* **2018,** *140* (23), 7232–7238.
202. Kubicki, D. J.; Prochowicz, D.; Pinon, A.; Stevanato, G.; Hofstetter, A.; Zakeeruddin, S. M.; Grätzel, M.; Emsley, L., Doping and Phase Segregation in Mn^{2+} - and Co^{2+} -Doped Lead Halide Perovskites from ^{133}Cs and ^{1}H NMR Relaxation Enhancement. *J. Mater. Chem. A* **2019,** *7*, 2326–2333.
203. Rosales, B. A.; Men, L.; Cady, S. D.; Hanrahan, M. P.; Rossini, A. J.; Vela, J., Persistent Dopants and Phase Segregation in Organolead Mixed-Halide Perovskites. *Chem. Mater.* **2016,** *28* (19), 6848–6859.
204. Xiang, W. C.; Wang, Z. W.; Kubicki, D. J.; Tress, W.; Luo, J. S.; Prochowicz, D.; Akin, S.; Emsley, L.; Zhou, J. T.; Dietler, G.; Gratzel, M.; Hagfeldt, A., Europium-Doped $CsPbI_2Br$ for Stable and Highly Efficient Inorganic Perovskite Solar Cells. *Joule* **2019,** *3* (1), 205–214.
205. Zhang, J. H.; Wang, Z. W.; Mishra, A.; Yu, M. L.; Shasti, M.; Tress, W.; Kubicki, D. J.; Avalos, C. E.; Lu, H. Z.; Liu, Y. H.; Carlsen, B. I.; Agarwalla, A.; Wang, Z. S.; Xiang, W. C.; Emsley, L.; Zhang, Z. H.; Gratzel, M.; Guo, W. L.; Hagfeldt, A., Intermediate Phase Enhances Inorganic Perovskite and Metal Oxide Interface for Efficient Photovoltaics. *Joule* **2020,** *4* (1), 222–234.
206. Senocrate, A.; Moudrakovski, I.; Maier, J., Short-range ion dynamics in methylammonium lead iodide by multinuclear solid state NMR and ^{127}I NQR. *Phys. Chem. Chem. Phys.* **2018,** *20* (30), 20043–20055.
207. Kubicki, D. J.; Prochowicz, D.; Hofstetter, A.; Péchy, P.; Zakeeruddin, S. M.; Grätzel, M.; Emsley, L., Cation Dynamics in Mixed-Cation $(MA)_x(FA)_{1-x}PbI_3$ Hybrid Perovskites from Solid-State NMR. *J. Am. Chem. Soc.* **2017,** *139* (29), 10055–10061.
208. Alanazi, A. Q.; Kubicki, D. J.; Prochowicz, D.; Alharbi, E. A.; Bouduban, M. E. F.; Jahanbakhshi, F.; Mladenović, M.; Milić, J. V.; Giordano, F.; Ren, D.; Alyamani, A. Y.; Albrithen, H.; Albadri, A.; Alotaibi, M. H.; Moser, J. E.; Zakeeruddin, S. M.; Rothlisberger, U.; Emsley, L.; Grätzel, M., Atomic-Level Microstructure of Efficient Formamidinium-Based Perovskite Solar Cells Stabilized by 5-Ammonium Valeric Acid Iodide Revealed by Multinuclear and Two-Dimensional Solid-State NMR. *J. Am. Chem. Soc.* **2019,** *141* (44), 17659–17669.
209. Hanrahan, M. P.; Men, L.; Rosales, B. A.; Vela, J.; Rossini, A. J., Sensitivity-Enhanced ^{207}Pb Solid-State NMR Spectroscopy for the Rapid, Non-Destructive Characterization of Organolead Halide Perovskites. *Chem. Mater.* **2018,** *30* (20), 7005–7015.
210. Karmakar, A.; Dodd, M. S.; Zhang, X.; Oakley, M. S.; Klobukowski, M.; Michaelis, V. K., Mechanochemical synthesis of 0D and 3D cesium lead mixed halide perovskites. *Chem. Commun.* **2019,** *55* (35), 5079–5082.
211. Karmakar, A.; Askar, A. M.; Bernard, G. M.; Terskikh, V. V.; Ha, M.; Patel, S.; Shankar, K.; Michaelis, V. K., Mechanochemical Synthesis of Methylammonium Lead Mixed–Halide Perovskites: Unraveling the Solid-Solution Behavior Using Solid-State NMR. *Chem. Mater.* **2018,** *30* (7), 2309–2321.
212. Askar, A. M.; Karmakar, A.; Bernard, G. M.; Ha, M.; Terskikh, V. V.; Wiltshire, B. D.; Patel, S.; Fleet, J.; Shankar, K.; Michaelis, V. K., Composition-Tunable Formamidinium Lead Mixed Halide Perovskites via Solvent-Free Mechanochemical Synthesis: Decoding the Pb Environments Using Solid-State NMR Spectroscopy. *J. Phys. Chem. Lett.* **2018,** *9* (10), 2671–2677.
213. Chen, Y.; Smock, S. R.; Flintgruber, A. H.; Perras, F. A.; Brutchey, R. L.; Rossini, A. J., Surface Termination of $CsPbBr_3$ Perovskite Quantum Dots Determined by Solid-State NMR Spectroscopy. *J. Am. Chem. Soc.* **2020,** *142* (13), 6117–6127.
214. Milić, J. V.; Im, J.; Kubicki, D. J.; Ummadisingu, A.; Seo, J.; Li, Y.; Ruiz Preciado, M. A.; Dar, M. I.; Zakeeruddin, S. M.; Emsley, L.; Grätzel, M., Supramolecular Engineering for Formamidinium Based Layered 2D Perovskite Solar Cells: Structural Complexity and Dynamics Revealed by Solid State NMR Spectroscopy. *Adv. Energy Mater.* **2019,** *9*, 1900284.
215. Ruiz-Preciado, M. A.; Kubicki, D. J.; Hofstetter, A.; McGovern, L.; Futscher, M. H.; Ummadisingu, A.; Gershoni-Poranne, R.; Zakeeruddin, S. M.; Ehrler, B.; Emsley, L.; Milić, J. V.; Grätzel, M., Supramolecular Modulation of Hybrid Perovskite Solar Cells via Bifunctional Halogen Bonding Revealed by Two-Dimensional ^{19}F Solid-State NMR Spectroscopy. *J. Am. Chem. Soc.* **2020,** *142* (3), 1645–1654.
216. Grüninger, H.; Bokdam, M.; Leupold, N.; Tinnemans, P.; Moos, R.; De Wijs, G. A.; Panzer, F.; Kentgens, A. P. M., Microscopic (Dis)order and Dynamics of Cations in Mixed FA/MA Lead Halide Perovskites. *J. Phys. Chem. C* **2021,** *125* (3), 1742–1753.
217. Rosales, B. A.; Hanrahan, M. P.; Boote, B. W.; Rossini, A. J.; Smith, E. A.; Vela, J., Lead Halide Perovskites: Challenges and Opportunities in Advanced Synthesis and Spectroscopy. *ACS Energy Lett.* **2017,** *2* (4), 906–914.
218. Smith, I. C.; Hoke, E. T.; Solis-Ibarra, D.; McGehee, M. D.; Karunadasa, H. I., A Layered Hybrid Perovskite Solar-Cell Absorber with Enhanced Moisture Stability. *Angew. Chem.* **2014,** *126*, 11232–11235.
219. Chen, Y.; Sun, Y.; Peng, J.; Tang, J.; Zheng, K.; Liang, Z., 2D Ruddlesden-Popper Perovskites for Optoelectronics. *Adv Mater* **2018,** *30* (2).

220. Mao, L.; Ke, W.; Pedesseau, L.; Wu, Y.; Katan, C.; Even, J.; Wasielewski, M. R.; Stoumpos, C. C.; Kanatzidis, M. G., Hybrid Dion–Jacobson 2D Lead Iodide Perovskites. *J. Am. Chem. Soc.* **2018,** *140* (10), 3775–3783.
221. Li, X.; Hoffman, J. M.; Kanatzidis, M. G., The 2D Halide Perovskite Rulebook: How the Spacer Influences Everything from the Structure to Optoelectronic Device Efficiency. *Chem. Rev.* **2021,** *121* (4), 2230–2291.
222. Jahanbakhshi, F.; Mladenović, M.; Dankl, M.; Boziki, A.; Ahlawat, P.; Rothlisberger, U., Organic Spacers in 2D Perovskites: General Trends and Structure-Property Relationships from Computational Studies. *Helv. Chim. Acta* **2021,** *104* (4), e2000232.
223. Kim, E.-B.; Akhtar, M. S.; Shin, H.-S.; Ameen, S.; Nazeeruddin, M. K., A review on two-dimensional (2D) and 2D-3D multidimensional perovskite solar cells: Perovskites structures, stability, and photovoltaic performances. *J. Photochem. Photobiol. C: Photochem. Rev.* **2021,** *48*, 100405.
224. Mao, L.; Stoumpos, C. C.; Kanatzidis, M. G., Two-Dimensional Hybrid Halide Perovskites: Principles and Promises. *J. Am. Chem. Soc.* **2019,** *141* (3), 1171–1190.
225. Leung, T. L.; Ahmad, I.; Syed, A. A.; Ng, A. M. C.; Popović, J.; Djurišić, A. B., Stability of 2D and quasi-2D perovskite materials and devices. *Commun. Mater.* **2022,** *3* (1), 63.
226. Milić, J. V.; Zakeeruddin, S. M.; Grätzel, M., Layered Hybrid Formamidinium Lead Iodide Perovskites: Challenges and Opportunities. *Acc. Chem. Res.* **2021,** *54* (12), 2729–2740.
227. Milić, J. V., Multifunctional layered hybrid perovskites. *J. Mater. Chem. C* **2021,** *9* (35), 11428–11443.
228. Yan, L.; Hu, J.; You, W., Non-Covalent Interactions in Organic/Inorganic Hybrid 2D Perovskites. In *Hybrid Organic Inorganic Perovskites*, World Scientific pp 153–193.
229. Hu, J.; Yan, L.; You, W., Two-Dimensional Organic-Inorganic Hybrid Perovskites: A New Platform for Optoelectronic Applications. *Adv. Mater.* **2018,** *30* (48), e1802041.
230. Smith, M. D.; Crace, E. J.; Jaffe, A.; Karunadasa, H. I., The Diversity of Layered Halide Perovskites. *Annu. Rev. Mater. Res.* **2018,** *48* (1), 111–136.
231. Smith, M. D.; Connor, B. A.; Karunadasa, H. I., Tuning the Luminescence of Layered Halide Perovskites. *Chem. Rev.* **2019,** *119* (5), 3104–3139.
232. Ball, M. L.; Milić, J. V.; Loo, Y.-L., The Emerging Role of Halogen Bonding in Hybrid Perovskite Photovoltaics. *Chem. Mater.* **2022,** *34* (6), 2495–2502.
233. Smecca, E.; Numata, Y.; Deretzis, I.; Pellegrino, G.; Boninelli, S.; Miyasaka, T.; La Magna, A.; Alberti, A., Stability of solution-processed MAPbI 3 and FAPbI 3 layers. *Phys. Chem. Chem. Phys.* **2016,** *18* (19), 13413–13422.
234. Conings, B.; Drijkoningen, J.; Gauquelin, N.; Babayigit, A.; D'Haen, J.; D'Olieslaeger, L.; Ethirajan, A.; Verbeeck, J.; Manca, J.; Mosconi, E., Intrinsic thermal instability of methylammonium lead trihalide perovskite. *Adv. Energy Mater.* **2015,** *5* (15), 1500477.
235. Berhe, T. A.; Su, W.-N.; Chen, C.-H.; Pan, C.-J.; Cheng, J.-H.; Chen, H.-M.; Tsai, M.-C.; Chen, L.-Y.; Dubale, A. A.; Hwang, B.-J., Organometal halide perovskite solar cells: degradation and stability. *Energy Environ. Sci.* **2016,** *9* (2), 323–356.
236. Dualeh, A.; Gao, P.; Seok, S. I.; Nazeeruddin, M. K.; Grätzel, M., Thermal behavior of methylammonium lead-trihalide perovskite photovoltaic light harvesters. *Chem. Mater.* **2014,** *26* (21), 6160–6164.
237. Boyd, C. C.; Cheacharoen, R.; Leijtens, T.; McGehee, M. D., Understanding degradation mechanisms and improving stability of perovskite photovoltaics. *Chem. Rev.* **2018,** *119* (5), 3418–3451.
238. Swarnkar, A.; Marshall, A. R.; Sanehira, E. M.; Chernomordik, B. D.; Moore, D. T.; Christians, J. A.; Chakrabarti, T.; Luther, J. M., Quantum dot–induced phase stabilization of α-CsPbI3 perovskite for high-efficiency photovoltaics. *Science* **2016,** *354* (6308), 92–95.
239. Lim, S.; Kim, J.; Park, J. Y.; Min, J.-w.; Yun, S.; Park, T.; Kim, Y.; Choi, J., Suppressed degradation and enhanced performance of CsPbI3 perovskite quantum dot solar cells via engineering of electron transport layers. *ACS Appl. Mater. Inter.* **2021,** *13* (5), 6119–6129.
240. Wang, Y.; Dar, M. I.; Ono, L. K.; Zhang, T. Y.; Kan, M.; Li, Y. W.; Zhang, L. J.; Wang, X. T.; Yang, Y. G.; Gao, X. Y.; Qi, Y. B.; Gratzel, M.; Zhao, Y. X., Thermodynamically stabilized β-$CsPbI_3$–based perovskite solar cells with efficiencies > 18%. *Science* **2019,** *365* (6453), 591.
241. Ye, Q.; Zhao, Y.; Mu, S.; Ma, F.; Gao, F.; Chu, Z.; Yin, Z.; Gao, P.; Zhang, X.; You, J., Cesium lead inorganic solar cell with efficiency beyond 18% via reduced charge recombination. *Adv. Mater.* **2019,** *31* (49), 1905143.
242. Liu, C.; Li, W. Z.; Zhang, C. L.; Ma, Y. P.; Fan, J. D.; Mai, Y. H., All-Inorganic $CsPbI_2Br$ Perovskite Solar Cells with High Efficiency Exceeding 13%. *J. Am. Chem. Soc.* **2018,** *140* (11), 3825–3828.
243. Yoon, S. M.; Min, H.; Kim, J. B.; Kim, G.; Lee, K. S.; Seok, S. I., Surface Engineering of Ambient-Air-Processed Cesium Lead Triiodide Layers for Efficient Solar Cells. *Joule* **2021,** *5* (1), 183–196.
244. Liang, J.; Qi, Y., Recent progress on all-inorganic metal halide perovskite solar cells. *Mater. Today Nano* **2021,** *16*, 100143.
245. Shockley, W.; Queisser, H. J., Detailed balance limit of efficiency of p‐n junction solar cells. *J. Appl. Phys.* **1961,** *32* (3), 510‐519.
246. Steele, J. A.; Jin, H.; Dovgaliuk, I.; Berger, R. F.; Braeckevelt, T.; Yuan, H.; Martin, C.; Solano, E.; Lejaeghere, K.; Rogge, S. M., Thermal unequilibrium of strained black CsPbI3 thin films. *Science* **2019,** *365* (6454), 679–684.
247. Bian, H.; Bai, D. L.; Jin, Z. W.; Wang, K.; Liang, L.; Wang, H. R.; Zhang, J. R.; Wang, Q.; Liu, S. Z., Graded Bandgap CsPbI2+xBr1-x Perovskite Solar Cells with a Stabilized Efficiency of 14.4%. *Joule* **2018,** *2* (8), 1500–1510.
248. Liang, J.; Zhao, P. Y.; Wang, C. X.; Wang, Y. R.; Hu, Y.; Zhu, G. Y.; Ma, L. B.; Liu, J.; Jin, Z., $CsPb_{0.9}Sn_{0.1}IBr_2$ Based All-Inorganic Perovskite Solar Cells with Exceptional Efficiency and Stability. *J. Am. Chem. Soc.* **2017,** *139* (40), 14009–14012.
249. Fu, L.; Zhang, Y. N.; Chang, B. H.; Li, B.; Zhou, S. J.; Zhang, L. Y.; Yin, L. W., A fluorine-modulated bulk-phase heterojunction and tolerance factor for enhanced performance and structure stability of cesium lead halide perovskite solar cells. *J. Mater. Chem. A* **2018,** *6* (27), 13263–13270.

250. Ramadan, A. J.; Rochford, L. A.; Fearn, S.; Snaith, H. J., Processing Solvent-Dependent Electronic and Structural Properties of Cesium Lead Triiodide Thin Films. *J. Phys. Chem. Lett.* **2017,** *8* (17), 4172–4176.
251. Wang, P. Y.; Zhang, X. W.; Zhou, Y. Q.; Jiang, Q.; Ye, Q. F.; Chu, Z. M.; Li, X. X.; Yang, X. L.; Yin, Z. G.; You, J. B., Solvent-controlled growth of inorganic perovskite films in dry environment for efficient and stable solar cells. *Nat. Commun.* **2018,** *9*.
252. Hu, Y. Q.; Bai, F.; Liu, X. B.; Ji, Q. M.; Miao, X. L.; Qiu, T.; Zhang, S. F., Bismuth Incorporation Stabilized α-$CsPbI_3$ for Fully Inorganic Perovskite Solar Cells. *ACS Energy Lett.* **2017,** *2* (10), 2219–2227.
253. Ge, S. P.; Wang, Y. H.; Xiang, Z. C.; Cui, Y. M., Reset Voltage-Dependent Multilevel Resistive Switching Behavior in $CsPb_{1-x}B_xI_3$ Perovskite-Based Memory Device. *ACS Appl. Mater. Inter.* **2018,** *10* (29), 24620–24626.
254. Xiang, S. S.; Li, W. P.; Wei, Y.; Liu, J. M.; Liu, H. C.; Zhu, L. Q.; Chen, H. N., The synergistic effect of non-stoichiometry and Sb-doping on air-stable α-$CsPbI_3$ for efficient carbon-based perovskite solar cells. *Nanoscale* **2018,** *10* (21), 9996–10004.
255. Jena, A. K.; Kulkarni, A.; Sanehira, Y.; Ikegami, M.; Miyasaka, T., Stabilization of α-$CsPbI_3$ in Ambient Room Temperature Conditions by Incorporating Eu into $CsPbI_3$. *Chem. Mater.* **2018,** *30* (19), 6668–6674.
256. Wang, Y.; Zhang, T. Y.; Kan, M.; Li, Y. H.; Wang, T.; Zhao, Y. X., Efficient α-$CsPbI_3$ Photovoltaics with Surface Terminated Organic Cations. *Joule* **2018,** *2* (10), 2065–2075.
257. Wang, Y.; Zhang, T. Y.; Kan, M.; Zhao, Y. X., Bifunctional Stabilization of All-Inorganic α-$CsPbI_3$ Perovskite for 17% Efficiency Photovoltaics. *J. Am. Chem. Soc.* **2018,** *140* (39), 12345–12348.
258. Zhang, T. Y.; Dar, M. I.; Li, G.; Xu, F.; Guo, N. J.; Gratzel, M.; Zhao, Y. X., Bication lead iodide 2D perovskite component to stabilize inorganic α-$CsPbI_3$ perovskite phase for high-efficiency solar cells. *Sci. Adv.* **2017,** *3* (9).
259. Daub, M.; Hillebrecht, H., On the Demystification of "$HPbI_3$" and the Peculiarities of the Non‐innocent Solvents H_2O and DMF. *Zeitschrift für anorganische und allgemeine Chemie* **2018,** *644* (22), 1393–1400.
260. Ke, W. J.; Spanopoulos, I.; Stoumpos, C. C.; Kanatzidis, M. G., Myths and reality of $HPbI_3$ in halide perovskite solar cells. *Nat. Commun.* **2018,** *9*.
261. Bian, H.; Wang, H.; Li, Z.; Zhou, F.; Xu, Y.; Zhang, H.; Wang, Q.; Ding, L.; Liu, S.; Jin, Z., Unveiling the effects of hydrolysis‐derived DMAI/$DMAPbI_x$ intermediate compound on the performance of $CsPbI_3$ solar cells. *Adv. Sci.* **2020,** *7* (9), 1902868.
262. Chen, H.; Wei, Q.; Saidaminov, M. I.; Wang, F.; Johnston, A.; Hou, Y.; Peng, Z.; Xu, K.; Zhou, W.; Liu, Z., Efficient and stable inverted perovskite solar cells incorporating secondary amines. *Adv. Mater.* **2019,** *31* (46), 1903559.
263. Wang, Y.; Liu, X.; Zhang, T.; Wang, X.; Kan, M.; Shi, J.; Zhao, Y., The role of dimethylammonium iodide in $CsPbI_3$ perovskite fabrication: additive or dopant? *Angew. Chem.* **2019,** *131* (46), 16844–16849.
264. Eperon, G. E.; Stone, K. H.; Mundt, L. E.; Schloemer, T. H.; Habisreutinger, S. N.; Dunfield, S. P.; Schelhas, L. T.; Berry, J. J.; Moore, D. T., The Role of Dimethylammonium in Bandgap Modulation for Stable Halide Perovskites. *ACS Energy Lett.* **2020,** *5* (6), 1856–1864.
265. Hu, Y.; Yan, Z.; Li, M.; Wen, X.; Yang, Y.; Choy, W. C.; Lu, H., Observing the stability evolution of β-$DMA_xCs_{1-x}PbI_2Br$ through precursor incubation. *Org. Electron.* **2020,** *84*, 105800.
266. Marshall, A. R.; Sansom, H. C.; McCarthy, M. M.; Warby, J. H.; Ashton, O. J.; Wenger, B.; Snaith, H. J., Dimethylammonium: An A‐Site Cation for Modifying CsPbI3. *Sol. RRL* **2021,** *5* (1), 2000599.
267. Fan, Y.; Wang, X.; Miao, Y.; Zhao, Y., The Chemical Design in High-Performance Lead Halide Perovskite: Additive vs Dopant? *J. Phys. Chem. Lett.* **2021,** *12* (48), 11636–11644.
268. Prochowicz, D.; Saski, M.; Yadav, P.; Gratzel, M.; Lewinski, J., Mechanoperovskites for Photovoltaic Applications: Preparation, Characterization, and Device Fabrication. *Acc. Chem. Res.* **2019,** *52* (11), 3233–3243.
269. Pines, A.; Gibby, M. G.; Waugh, J. S., Proton‐enhanced NMR of dilute spins in solids. *J. Chem. Phys.* **1973,** *59* (2), 569–590.
270. Ummadisingu, A.; Mishra, A.; Kubicki, D. J.; LaGrange, T.; Dučinskas, A.; Siczek, M.; Bury, W.; Milić, J. V.; Grätzel, M.; Emsley, L., Multi-Length Scale Structure of 2D/3D Dion–Jacobson Hybrid Perovskites Based on an Aromatic Diammonium Spacer. *Small* **2022,** *18* (5), 2104287.
271. Boziki, A.; Kubicki, D. J.; Mishra, A.; Meloni, S.; Emsley, L.; Grätzel, M.; Rothlisberger, U., Atomistic Origins of the Limited Phase Stability of Cs^+-Rich $FA_xCs_{(1-x)}PbI_3$ Mixtures. *Chem. Mater.* **2020,** *32* (6), 2605–2614.
272. Kubicki, D. J.; Prochowicz, D.; Hofstetter, A.; Saski, M.; Yadav, P.; Bi, D.; Pellet, N.; Lewiński, J.; Zakeeruddin, S. M.; Grätzel, M.; Emsley, L., Formation of Stable Mixed Guanidinium–Methylammonium Phases with Exceptionally Long Carrier Lifetimes for High-Efficiency Lead Iodide-Based Perovskite Photovoltaics. *J. Am. Chem. Soc.* **2018,** *140* (9), 3345–3351.
273. Nazarenko, O.; Kotyrba, M. R.; Wörle, M.; Cuervo-Reyes, E.; Yakunin, S.; Kovalenko, M. V., Luminescent and Photoconductive Layered Lead Halide Perovskite Compounds Comprising Mixtures of Cesium and Guanidinium Cations. *Inorg. Chem.* **2017,** *56* (19), 11552–11564.
274. Tsai, H.; Nie, W.; Blancon, J.-C.; Stoumpos, C. C.; Asadpour, R.; Harutyunyan, B.; Neukirch, A. J.; Verduzco, R.; Crochet, J. J.; Tretiak, S., High-efficiency two-dimensional Ruddlesden–Popper perovskite solar cells. *Nature* **2016,** *536* (7616), 312–316.
275. Grancini, G.; Nazeeruddin, M. K., Dimensional tailoring of hybrid perovskites for photovoltaics. *Nat. Rev. Mater.* **2019,** *4* (1), 4–22.
276. Saparov, B.; Mitzi, D. B., Organic–Inorganic Perovskites: Structural Versatility for Functional Materials Design. *Chem. Rev.* **2016,** *116* (7), 4558–4596.
277. Grancini, G.; Roldán-Carmona, C.; Zimmermann, I.; Mosconi, E.; Lee, X.; Martineau, D.; Narbey, S.; Oswald, F.; De Angelis, F.; Graetzel, M., One-Year stable perovskite solar cells by 2D/3D interface engineering. *Nat. Commun.* **2017,** *8* (1), 1–8.
278. Li, X.; Guo, P.; Kepenekian, M.; Hadar, I.; Katan, C.; Even, J.; Stoumpos, C. C.; Schaller, R. D.; Kanatzidis, M. G., Small cyclic diammonium cation templated (110)-oriented 2D halide (X= I, Br, Cl) perovskites with white-light emission. *Chem. Mater.* **2019,** *31* (9), 3582–3590.

279. Ashari-Astani, N.; Jahanbakhshi, F.; Mladenović, M.; Alanazi, A. Q.; Ahmadabadi, I.; Ejtehadi, M. R.; Dar, M. I.; Grätzel, M.; Rothlisberger, U., Ruddlesden–Popper Phases of Methylammonium-Based Two-Dimensional Perovskites with 5-Ammonium Valeric Acid AVA2MAn–1PbnI3n+1 with n= 1, 2, and 3. *J. Phys. Chem. Lett.* **2019,** *10* (13), 3543–3549.
280. Jahanbakhshi, F.; Mladenović, M.; Kneschaurek, E.; Merten, L.; Gélvez-Rueda, M. C.; Ahlawat, P.; Li, Y.; Dučinskas, A.; Hinderhofer, A.; Dar, M. I., Unravelling the structural complexity and photophysical properties of adamantyl-based layered hybrid perovskites. *J. Mater. Chem. A* **2020,** *8* (34), 17732–17740.
281. Bi, D.; Li, X.; Milić, J. V.; Kubicki, D. J.; Pellet, N.; Luo, J.; LaGrange, T.; Mettraux, P.; Emsley, L.; Zakeeruddin, S. M.; Grätzel, M., Multifunctional Molecular Modulators for Perovskite Solar Cells with over 20% Efficiency and High Operational Stability. *Nat. Commun.* **2018,** *9*, 4482.
282. Abate, A.; Saliba, M.; Hollman, D. J.; Stranks, S. D.; Wojciechowski, K.; Avolio, R.; Grancini, G.; Petrozza, A.; Snaith, H. J., Supramolecular halogen bond passivation of organic–inorganic halide perovskite solar cells. *Nano. Lett.* **2014,** *14* (6), 3247–3254.
283. Mitzi, D. B.; Medeiros, D. R.; Malenfant, P. R., Intercalated organic− inorganic perovskites stabilized by fluoroaryl− aryl interactions. *Inorg. Chem.* **2002,** *41* (8), 2134–2145.
284. Hu, J.; Oswald, I. W.; Hu, H.; Stuard, S. J.; Nahid, M. M.; Yan, L.; Chen, Z.; Ade, H.; Neilson, J. R.; You, W., Aryl-perfluoroaryl interaction in two-dimensional organic–inorganic hybrid perovskites boosts stability and photovoltaic efficiency. *ACS Mater. Lett.* **2019,** *1* (1), 171–176.
285. Li, Y.; Milić, J. V.; Ummadisingu, A.; Seo, J.-Y.; Im, J.-H.; Kim, H.-S.; Liu, Y.; Dar, M. I.; Zakeeruddin, S. M.; Wang, P.; Hagfeldt, A.; Grätzel, M., Bifunctional Organic Spacers for Formamidinium-Based Hybrid Dion–Jacobson Two-Dimensional Perovskite Solar Cells. *Nano. Lett.* **2019,** *19* (1), 150–157.
286. Gélvez-Rueda, M. C.; Ahlawat, P.; Merten, L.; Jahanbakhshi, F.; Mladenović, M.; Hinderhofer, A.; Dar, M. I.; Li, Y.; Dučinskas, A.; Carlsen, B.; Tress, W.; Ummadisingu, A.; Zakeeruddin, S. M.; Schreiber, F.; Hagfeldt, A.; Rothlisberger, U.; Grozema, F. C.; Milić, J. V.; Graetzel, M., Formamidinium-Based Dion-Jacobson Layered Hybrid Perovskites: Structural Complexity and Optoelectronic Properties. *Adv. Funct. Mater.* **2020,** *30* (38), 2003428.
287. Alharbi, E. A.; Alyamani, A. Y.; Kubicki, D. J.; Uhl, A. R.; Walder, B. J.; Alanazi, A. Q.; Luo, J.; Burgos-Caminal, A.; Albadri, A.; Albrithen, H.; Alotaibi, M. H.; Moser, J.-E.; Zakeeruddin, S. M.; Giordano, F.; Emsley, L.; Grätzel, M., Atomic-level passivation mechanism of ammonium salts enabling highly efficient perovskite solar cells. *Nat. Commun.* **2019,** *10* (1), 3008.
288. Franssen, W. M. J.; van Es, S. G. D.; Dervişoğlu, R.; de Wijs, G. A.; Kentgens, A. P. M., Symmetry, Dynamics, and Defects in Methylammonium Lead Halide Perovskites. *J. Phys. Chem. Lett.* **2017,** *8* (1), 61–66.
289. Bryce, D., NMR crystallography: structure and properties of materials from solid-state nuclear magnetic resonance observables. *IUCrJ* **2017,** *4* (4), 350–359.
290. Mitzi, D. B.; Medeiros, D. R.; Malenfant, P. R. L., Intercalated Organic−Inorganic Perovskites Stabilized by Fluoroaryl−Aryl Interactions. *Inorg. Chem.* **2002,** *41* (8), 2134–2145.
291. Chen, P.; Bai, Y.; Wang, S.; Lyu, M.; Yun, J.-H.; Wang, L., In Situ Growth of 2D Perovskite Capping Layer for Stable and Efficient Perovskite Solar Cells. *Adv. Funct. Mater.* **2018,** *28* (17), 1706923.
292. Xu, Z.; Mitzi, D. B., SnI42--Based Hybrid Perovskites Templated by Multiple Organic Cations: Combining Organic Functionalities through Noncovalent Interactions. *Chem. Mater.* **2003,** *15* (19), 3632–3637.
293. Kim, K. S.; Tarakeshwar, P.; Lee, J. Y., Molecular Clusters of π-Systems: Theoretical Studies of Structures, Spectra, and Origin of Interaction Energies. *Chem. Rev.* **2000,** *100* (11), 4145–4186.
294. Sutton, C.; Risko, C.; Brédas, J.-L., Noncovalent Intermolecular Interactions in Organic Electronic Materials: Implications for the Molecular Packing vs Electronic Properties of Acenes. *Chem. Mater.* **2016,** *28* (1), 3–16.
295. Giese, M.; Albrecht, M.; Rissanen, K., Anion−π Interactions with Fluoroarenes. *Chem. Rev.* **2015,** *115* (16), 8867–8895.
296. Wang, R.; Mujahid, M.; Duan, Y.; Wang, Z.-K.; Xue, J.; Yang, Y., A Review of Perovskites Solar Cell Stability. *Adv. Funct. Mater.* **2019,** *29* (47), 1808843.
297. Prochowicz, D.; Franckevicius, M.; Cieslak, A. M.; Zakeeruddin, S. M.; Gratzel, M.; Lewinski, J., Mechanosynthesis of the hybrid perovskite $CH_3NH_3PbI_3$: characterization and the corresponding solar cell efficiency. *J. Mater. Chem. A* **2015,** *3* (41), 20772–20777.
298. Hong, L.; Milić, J. V.; Ahlawat, P.; Mladenović, M.; Kubicki, D. J.; Jahanabkhshi, F.; Ren, D.; Gélvez‐Rueda, M. C.; Ruiz‐Preciado, M. A.; Ummadisingu, A., Guanine‐stabilized formamidinium lead iodide perovskites. *Angew. Chem. Int. Ed.* **2020,** *59* (12), 4691–4697.
299. Liu, Y.; Akin, S.; Pan, L.; Uchida, R.; Arora, N.; Milić, J. V.; Hinderhofer, A.; Schreiber, F.; Uhl, A. R.; Zakeeruddin, S. M.; Hagfeldt, A.; Dar, M. I.; Grätzel, M., Ultrahydrophobic 3D/2D fluoroarene bilayer-based water-resistant perovskite solar cells with efficiencies exceeding 22%. *Sci. Adv.* **2019,** *5* (6), eaaw2543.
300. Weller, M. T.; Weber, O. J.; Frost, J. M.; Walsh, A., Cubic Perovskite Structure of Black Formamidinium Lead Iodide, α-[HC(NH2)2]PbI3, at 298 K. *J. Phys. Chem. Lett.* **2015,** *6* (16), 3209–3212.
301. Binek, A.; Hanusch, F. C.; Docampo, P.; Bein, T., Stabilization of the Trigonal High-Temperature Phase of Formamidinium Lead Iodide. *J. Phys. Chem. Lett.* **2015,** *6* (7), 1249–1253.
302. Hope, M. A.; Nakamura, T.; Ahlawat, P.; Mishra, A.; Cordova, M.; Jahanbakhshi, F.; Mladenović, M.; Runjhun, R.; Merten, L.; Hinderhofer, A.; Carlsen, B. I.; Kubicki, D. J.; Gershoni-Poranne, R.; Schneeberger, T.; Carbone, L. C.; Liu, Y.; Zakeeruddin, S. M.; Lewinski, J.; Hagfeldt, A.; Schreiber, F.; Rothlisberger, U.; Grätzel, M.; Milić, J. V.; Emsley, L., Nanoscale Phase Segregation in Supramolecular π-Templating for Hybrid Perovskite Photovoltaics from NMR Crystallography. *J. Am. Chem. Soc.* **2021,** *143* (3), 1529–1538.

303. Krishna, A.; Akhavan Kazemi, M. A.; Sliwa, M.; Reddy, G. N. M.; Delevoye, L.; Lafon, O.; Felten, A.; Do, M. T.; Gottis, S.; Sauvage, F., Defect Passivation via the Incorporation of Tetrapropylammonium Cation Leading to Stability Enhancement in Lead Halide Perovskite. *Adv. Funct. Mater.* **2020,** *30* (13), 1909737.
304. Du, K.-z.; Tu, Q.; Zhang, X.; Han, Q.; Liu, J.; Zauscher, S.; Mitzi, D. B., Two-Dimensional Lead(II) Halide-Based Hybrid Perovskites Templated by Acene Alkylamines: Crystal Structures, Optical Properties, and Piezoelectricity. *Inorg. Chem.* **2017,** *56* (15), 9291–9302.
305. Hogben, M. G.; Graham, W. A., Chemical shifts and coupling constants in pentafluorophenyl derivatives. I. Correlations of chemical shifts, coupling constants, and. pi.-electronic interactions. *J. Am. Chem. Soc.* **1969,** *91* (2), 283–291.
306. Safont-Sempere, M. M.; Fernández, G.; Würthner, F., Self-sorting phenomena in complex supramolecular systems. *Chem. Rev.* **2011,** *111* (9), 5784–5814.
307. Straus, D. B.; Iotov, N.; Gau, M. R.; Zhao, Q.; Carroll, P. J.; Kagan, C. R., Longer cations increase energetic disorder in excitonic 2D hybrid perovskites. *J. Phys. Chem. Lett.* **2019,** *10* (6), 1198–1205.
308. Slavney, A. H.; Smaha, R. W.; Smith, I. C.; Jaffe, A.; Umeyama, D.; Karunadasa, H. I., Chemical approaches to addressing the instability and toxicity of lead–halide perovskite absorbers. *Inorg. Chem.* **2017,** *56* (1), 46–55.
309. Engel, E. A.; Anelli, A.; Hofstetter, A.; Paruzzo, F.; Emsley, L.; Ceriotti, M., A Bayesian approach to NMR crystal structure determination. *Phys. Chem. Chem. Phys.* **2019,** *21* (42), 23385–23400.
310. Domanski, K.; Roose, B.; Matsui, T.; Saliba, M.; Turren-Cruz, S. H.; Correa-Baena, J. P.; Roldan-Carmona, C.; Richardson, G.; Foster, J. M.; De Angelis, F.; Ball, J. M.; Petrozza, A.; Mine, N.; Nazeeruddin, M. K.; Tress, W.; Gratzel, M.; Steiner, U.; Hagfeldt, A.; Abate, A., Migration of cations induces reversible performance losses over day/night cycling in perovskite solar cells. *Energy Environ. Sci.* **2017,** *10* (2), 604–613.
311. Domanski, K.; Alharbi, E. A.; Hagfeldt, A.; Gratzel, M.; Tress, W., Systematic investigation of the impact of operation conditions on the degradation behaviour of perovskite solar cells. *Nat. Energy* **2018,** *3* (1), 61–67.
312. Giannozzi, P.; Baroni, S.; Bonini, N.; Calandra, M.; Car, R.; Cavazzoni, C.; Ceresoli, D.; Chiarotti, G. L.; Cococcioni, M.; Dabo, I.; Dal Corso, A.; de Gironcoli, S.; Fabris, S.; Fratesi, G.; Gebauer, R.; Gerstmann, U.; Gougoussis, C.; Kokalj, A.; Lazzeri, M.; Martin-Samos, L.; Marzari, N.; Mauri, F.; Mazzarello, R.; Paolini, S.; Pasquarello, A.; Paulatto, L.; Sbraccia, C.; Scandolo, S.; Sclauzero, G.; Seitsonen, A. P.; Smogunov, A.; Umari, P.; Wentzcovitch, R. M., QUANTUM ESPRESSO: a modular and open-source software project for quantum simulations of materials. *J. Condens. Matter Phys.* **2009,** *21* (39), 395502.
313. Perdew, J. P.; Ruzsinszky, A.; Csonka, G. I.; Vydrov, O. A.; Scuseria, G. E.; Constantin, L. A.; Zhou, X.; Burke, K., Restoring the Density-Gradient Expansion for Exchange in Solids and Surfaces. *Phys. Rev. Lett.* **2008,** *100* (13), 136406.
314. Grimme, S., Semiempirical GGA-type density functional constructed with a long-range dispersion correction. *J. Comput. Chem.* **2006,** *27* (15), 1787–1799.
315. Pack, J. D.; Monkhorst, H. J., "Special points for Brillouin-zone integrations"---a reply. *Phys. Rev. B* **1977,** *16* (4), 1748–1749.
316. Pickard, C. J.; Mauri, F., All-electron magnetic response with pseudopotentials: NMR chemical shifts. *Phys. Rev. B* **2001,** *63* (24), 245101.
317. Yates, J. R.; Pickard, C. J.; Mauri, F., Calculation of NMR chemical shifts for extended systems using ultrasoft pseudopotentials. *Phys. Rev. B* **2007,** *76* (2), 024401.
318. Momma, K.; Izumi, F., VESTA 3 for three-dimensional visualization of crystal, volumetric and morphology data. *J. Appl. Crystallogr.* **2011,** *44* (6), 1272–1276.
319. Szell, P. M. J.; Gabriel, S. A.; Gill, R. D. D.; Wan, S. Y. H.; Gabidullin, B.; Bryce, D. L., 13C and 19F solid-state NMR and X-ray crystallographic study of halogen-bonded frameworks featuring nitrogen-containing heterocycles. *Acta Crystallogr. C* **2017,** *73* (3), 157–167.
320. Viger-Gravel, J.; Avalos, C. E.; Kubicki, D. J.; Gajan, D.; Lelli, M.; Ouari, O.; Lesage, A.; Emsley, L., 19F Magic Angle Spinning Dynamic Nuclear Polarization Enhanced NMR Spectroscopy. *Angew. Chem. Int. Ed.* **2019,** *58* (22), 7249–7253.
321. Robbins, A. J.; Ng, W. T. K.; Jochym, D.; Keal, T. W.; Clark, S. J.; Tozer, D. J.; Hodgkinson, P., Combining insights from solid-state NMR and first principles calculation: applications to the 19F NMR of octafluoronaphthalene. *Phys. Chem. Chem. Phys.* **2007,** *9* (19), 2389–2396.
322. Pellet, N.; Gao, P.; Gregori, G.; Yang, T. Y.; Nazeeruddin, M. K.; Maier, J.; Grätzel, M., Mixed-organic-cation perovskite photovoltaics for enhanced solar-light harvesting. *Angew. Chem. Int. Ed.* **2014,** *53*, 3151–3157.
323. Eperon, G. E.; Stranks, S. D.; Menelaou, C.; Johnston, M. B.; Herz, L. M.; Snaith, H. J., Formamidinium Lead Trihalide: A Broadly Tunable Perovskite for Efficient Planar Heterojunction Solar Cells. *Energy Environ. Sci.* **2014,** *7*, 982–988.
324. Jeon, N. J.; Noh, J. H.; Yang, W. S.; Kim, Y. C.; Ryu, S.; Seo, J.; Seok, S. I., Compositional engineering of perovskite materials for high-performance solar cells. *Nature* **2015,** *517* (7535), 476.
325. Lu, H.; Liu, Y.; Ahlawat, P.; Mishra, A.; Tress, W. R.; Eickemeyer, F. T.; Yang, Y.; Fu, F.; Wang, Z.; Avalos, C. E.; Carlsen, B. I.; Agarwalla, A.; Zhang, X.; Li, X.; Zhan, Y.; Zakeeruddin, S. M.; Emsley, L.; Rothlisberger, U.; Zheng, L.; Hagfeldt, A.; Grätzel, M., Vapor-assisted deposition of highly efficient, stable black-phase $FAPbI_3$ perovskite solar cells. *Science* **2020,** *370* (6512), eabb8985.
326. Saliba, M.; Matsui, T.; Seo, J.-Y.; Domanski, K.; Correa-Baena, J.-P.; Nazeeruddin, M. K.; Zakeeruddin, S. M.; Tress, W.; Abate, A.; Hagfeldt, A.; Grätzel, M., Cesium-containing triple cation perovskite solar cells: improved stability, reproducibility and high efficiency. *Energy Environ. Sci.* **2016,** *9* (6), 1989–1997.
327. Stranks, S. D.; Eperon, G. E.; Grancini, G.; Menelaou, C.; Alcocer, M. J. P.; Leijtens, T.; Herz, L. M.; Petrozza, A.; Snaith, H. J., Electron-Hole Diffusion Lengths Exceeding 1 Micrometer in an Organometal Trihalide Perovskite Absorber. *Science* **2013,** *342* (6156), 341–344.

328. Kim, M.; Kim, G.-H.; Lee, T. K.; Choi, I. W.; Choi, H. W.; Jo, Y.; Yoon, Y. J.; Kim, J. W.; Lee, J.; Huh, D.; Lee, H.; Kwak, S. K.; Kim, J. Y.; Kim, D. S., Methylammonium Chloride Induces Intermediate Phase Stabilization for Efficient Perovskite Solar Cells. *Joule* **2019,** *3* (9), 2179–2192.
329. Min, H.; Kim, M.; Lee, S. U.; Kim, H.; Kim, G.; Choi, K.; Lee, J. H.; Seok, S. I., Efficient, stable solar cells by using inherent bandgap of alpha-phase formamidinium lead iodide. *Science* **2019,** *366* (6466), 749.
330. Yang, S.; Liu, W.; Zuo, L.; Zhang, X.; Ye, T.; Chen, J.; Li, C.-Z.; Wu, G.; Chen, H., Thiocyanate assisted performance enhancement of formamidinium based planar perovskite solar cells through a single one-step solution process. *J. Mater. Chem. A* **2016,** *4* (24), 9430–9436.
331. Kim, D. H.; Muzzillo, C. P.; Tong, J.; Palmstrom, A. F.; Larson, B. W.; Choi, C.; Harvey, S. P.; Glynn, S.; Whitaker, J. B.; Zhang, F.; Li, Z.; Lu, H.; van Hest, M. F. A. M.; Berry, J. J.; Mansfield, L. M.; Huang, Y.; Yan, Y.; Zhu, K., Bimolecular Additives Improve Wide-Band-Gap Perovskites for Efficient Tandem Solar Cells with CIGS. *Joule* **2019,** *3* (7), 1734–1745.
332. Kim, D.; Jung, H. J.; Park, I. J.; Larson, B. W.; Dunfield, S. P.; Xiao, C.; Kim, J.; Tong, J.; Boonmongkolras, P.; Ji, S. G.; Zhang, F.; Pae, S. R.; Kim, M.; Kang, S. B.; Dravid, V.; Berry, J. J.; Kim, J. Y.; Zhu, K.; Kim, D. H.; Shin, B., Efficient, stable silicon tandem cells enabled by anion-engineered wide-bandgap perovskites. *Science* **2020,** *368* (6487), 155–160.
333. Walker, B.; Kim, G.-H.; Kim, J. Y., Pseudohalides in Lead-Based Perovskite Semiconductors. *Adv. Mater.* **2019,** *31* (20), 1807029.
334. Moore, D. T.; Tan, K. W.; Sai, H.; Barteau, K. P.; Wiesner, U.; Estroff, L. A., Direct Crystallization Route to Methylammonium Lead Iodide Perovskite from an Ionic Liquid. *Chem. Mater.* **2015,** *27* (9), 3197–3199.
335. Seo, J.-Y.; Matsui, T.; Luo, J.; Correa-Baena, J.-P.; Giordano, F.; Saliba, M.; Schenk, K.; Ummadisingu, A.; Domanski, K.; Hadadian, M.; Hagfeldt, A.; Zakeeruddin, S. M.; Steiner, U.; Grätzel, M.; Abate, A., Ionic Liquid Control Crystal Growth to Enhance Planar Perovskite Solar Cells Efficiency. *Adv. Energy Mater.* **2016,** *6* (20), 1600767.
336. Nayak, P. K.; Moore, D. T.; Wenger, B.; Nayak, S.; Haghighirad, A. A.; Fineberg, A.; Noel, N. K.; Reid, O. G.; Rumbles, G.; Kukura, P.; Vincent, K. A.; Snaith, H. J., Mechanism for rapid growth of organic–inorganic halide perovskite crystals. *Nat. Commun.* **2016,** *7* (1), 13303.
337. Meng, L.; Wei, Q.; Yang, Z.; Yang, D.; Feng, J.; Ren, X.; Liu, Y.; Liu, S., Improved perovskite solar cell efficiency by tuning the colloidal size and free ion concentration in precursor solution using formic acid additive. *J. Energy Chem.* **2020,** *41*, 43–51.
338. Khan, Y.; Ahn, Y.; Lee, H.; Jeong, J.; Shin, Y. S.; Lee, J. S.; Kwon, J. H.; Kim, J. Y.; Kim, H. S.; Seo, J. H.; Walker, B., Waterproof perovskites: high fluorescence quantum yield and stability from a methylammonium lead bromide/formate mixture in water. *J. Mater. Chem. C* **2020,** *8* (17), 5873–5881.
339. Saliba, M.; Matsui, T.; Domanski, K.; Seo, J.-Y.; Ummadisingu, A.; Zakeeruddin, S. M.; Correa-Baena, J.-P.; Tress, W. R.; Abate, A.; Hagfeldt, A.; Grätzel, M., Incorporation of rubidium cations into perovskite solar cells improves photovoltaic performance. *Science* **2016,** *354* (6309), 206–209.
340. Yang, W. S.; Park, B. W.; Jung, E. H.; Jeon, N. J.; Kim, Y. C.; Lee, D. U.; Shin, S. S.; Seo, J.; Kim, E. K.; Noh, J. H.; Seok, S. I., Iodide management in formamidinium-lead-halide-based perovskite layers for efficient solar cells. *Science* **2017,** *356* (6345), 1376.
341. Jiang, Q.; Zhao, Y.; Zhang, X.; Yang, X.; Chen, Y.; Chu, Z.; Ye, Q.; Li, X.; Yin, Z.; You, J., Surface passivation of perovskite film for efficient solar cells. *Nat. Photon* **2019,** *13* (7), 460–466.
342. Jung, E. H.; Jeon, N. J.; Park, E. Y.; Moon, C. S.; Shin, T. J.; Yang, T. Y.; Noh, J. H.; Seo, J., Efficient, stable and scalable perovskite solar cells using poly(3-hexylthiophene). *Nature* **2019,** *567* (7749), 511.
343. Wang, Z.; Lin, Q.; Wenger, B.; Christoforo, M. G.; Lin, Y.-H.; Klug, M. T.; Johnston, M. B.; Herz, L. M.; Snaith, H. J., High irradiance performance of metal halide perovskites for concentrator photovoltaics. *Nat. Energy* **2018,** *3* (10), 855–861.
344. Turren-Cruz, S.-H.; Hagfeldt, A.; Saliba, M., Methylammonium-free, high-performance, and stable perovskite solar cells on a planar architecture. *Science* **2018,** *362* (6413), 449–453.
345. Draguta, S.; Sharia, O.; Yoon, S. J.; Brennan, M. C.; Morozov, Y. V.; Manser, J. S.; Kamat, P. V.; Schneider, W. F.; Kuno, M., Rationalizing the light-induced phase separation of mixed halide organic–inorganic perovskites. *Nat. Commun.* **2017,** *8* (1), 200.
346. Lee, J.-W.; Dai, Z.; Han, T.-H.; Choi, C.; Chang, S.-Y.; Lee, S.-J.; De Marco, N.; Zhao, H.; Sun, P.; Huang, Y.; Yang, Y., 2D perovskite stabilized phase-pure formamidinium perovskite solar cells. *Nat. Commun.* **2018,** *9* (1), 3021.
347. Fu, Y.; Wu, T.; Wang, J.; Zhai, J.; Shearer, M. J.; Zhao, Y.; Hamers, R. J.; Kan, E.; Deng, K.; Zhu, X. Y.; Jin, S., Stabilization of the Metastable Lead Iodide Perovskite Phase via Surface Functionalization. *Nano. Lett.* **2017,** *17* (7), 4405–4414.
348. Wang, J.; Luo, S.; Lin, Y.; Chen, Y.; Deng, Y.; Li, Z.; Meng, K.; Chen, G.; Huang, T.; Xiao, S.; Huang, H.; Zhou, C.; Ding, L.; He, J.; Huang, J.; Yuan, Y., Templated growth of oriented layered hybrid perovskites on 3D-like perovskites. *Nat. Commun.* **2020,** *11* (1), 582.
349. Chen, Y.; Lei, Y.; Li, Y.; Yu, Y.; Cai, J.; Chiu, M.-H.; Rao, R.; Gu, Y.; Wang, C.; Choi, W.; Hu, H.; Wang, C.; Li, Y.; Song, J.; Zhang, J.; Qi, B.; Lin, M.; Zhang, Z.; Islam, A. E.; Maruyama, B.; Dayeh, S.; Li, L.-J.; Yang, K.; Lo, Y.-H.; Xu, S., Strain engineering and epitaxial stabilization of halide perovskites. *Nature* **2020,** *577* (7789), 209–215.
350. Turkevych, I.; Kazaoui, S.; Belich, N. A.; Grishko, A. Y.; Fateev, S. A.; Petrov, A. A.; Urano, T.; Aramaki, S.; Kosar, S.; Kondo, M.; Goodilin, E. A.; Graetzel, M.; Tarasov, A. B., Strategic advantages of reactive polyiodide melts for scalable perovskite photovoltaics. *Nat. Nanotechnol.* **2019,** *14* (1), 57–63.
351. Dong, Q.; Fang, Y.; Shao, Y.; Mulligan, P.; Qiu, J.; Cao, L.; Huang, J., Electron-hole diffusion lengths > 175 μm in solution-grown CH3NH3PbI3 single crystals. *Science* **2015,** *347* (6225), 967–970.
352. Polman, A.; Knight, M.; Garnett, E. C.; Ehrler, B.; Sinke, W. C., Photovoltaic materials: Present efficiencies and future challenges. *Science* **2016,** *352* (6283), aad4424.

353. Lin, K.; Xing, J.; Quan, L. N.; de Arquer, F. P. G.; Gong, X.; Lu, J.; Xie, L.; Zhao, W.; Zhang, D.; Yan, C.; Li, W.; Liu, X.; Lu, Y.; Kirman, J.; Sargent, E. H.; Xiong, Q.; Wei, Z., Perovskite light-emitting diodes with external quantum efficiency exceeding 20 per cent. *Nature* **2018,** *562* (7726), 245–248.
354. Kim, H.-S.; Lee, C.-R.; Im, J.-H.; Lee, K.-B.; Moehl, T.; Marchioro, A.; Moon, S.-J.; Humphry-Baker, R.; Yum, J.-H.; Moser, J. E.; Grätzel, M.; Park, N.-G., Lead Iodide Perovskite Sensitized All-Solid-State Submicron Thin Film Mesoscopic Solar Cell with Efficiency Exceeding 9%. *Sci. Rep.* **2012,** *2* (1), 591.
355. Lee, M. M.; Teuscher, J.; Miyasaka, T.; Murakami, T. N.; Snaith, H. J., Efficient Hybrid Solar Cells Based on Meso-Superstructured Organometal Halide Perovskites. *Science* **2012,** *338* (6107), 643–647.
356. Burschka, J.; Pellet, N.; Moon, S.-J.; Humphry-Baker, R.; Gao, P.; Nazeeruddin, M. K.; Grätzel, M., Sequential deposition as a route to high-performance perovskite-sensitized solar cells. *Nature* **2013,** *499* (7458), 316–319.
357. Liu, M.; Johnston, M. B.; Snaith, H. J., Efficient planar heterojunction perovskite solar cells by vapour deposition. *Nature* **2013,** *501* (7467), 395–398.
358. Service, R. F., Cesium fortifies next-generation solar cells. *Science* **2016,** *351* (6269), 113–114.
359. Zhou, Y.; Zhao, Y., Chemical stability and instability of inorganic halide perovskites. *Energy Environ. Sci.* **2019,** *12* (5), 1495–1511.
360. Zhou, H.; Chen, Q.; Li, G.; Luo, S.; Song, T.-b.; Duan, H.-S.; Hong, Z.; You, J.; Liu, Y.; Yang, Y., Interface engineering of highly efficient perovskite solar cells. *Science* **2014,** *345* (6196), 542–546.
361. Tan, H.; Jain, A.; Voznyy, O.; Lan, X.; García de Arquer, F. P.; Fan, J. Z.; Quintero-Bermudez, R.; Yuan, M.; Zhang, B.; Zhao, Y.; Fan, F.; Li, P.; Quan, L. N.; Zhao, Y.; Lu, Z.-H.; Yang, Z.; Hoogland, S.; Sargent, E. H., Efficient and stable solution-processed planar perovskite solar cells via contact passivation. *Science* **2017,** *355* (6326), 722–726.
362. Li, X.; Ibrahim Dar, M.; Yi, C.; Luo, J.; Tschumi, M.; Zakeeruddin, S. M.; Nazeeruddin, M. K.; Han, H.; Grätzel, M., Improved performance and stability of perovskite solar cells by crystal crosslinking with alkylphosphonic acid ω-ammonium chlorides. *Nat. Chem.* **2015,** *7* (9), 703–711.
363. Zhang, T.; Dar, M. I.; Li, G.; Xu, F.; Guo, N.; Grätzel, M.; Zhao, Y., Bication lead iodide 2D perovskite component to stabilize inorganic α-$CsPbI_3$ perovskite phase for high-efficiency solar cells. *Sci. Adv.* **2017,** *3* (9), e1700841.
364. Fan, L.-Q.; Wu, J.-H., NH4PbI3. *Acta Crystallogr. E* **2007,** *63* (11), i189.
365. Sheikh, T.; Nag, A., Mn Doping in Centimeter-Sized Layered 2D Butylammonium Lead Bromide (BA2PbBr4) Single Crystals and Their Optical Properties. *J. Phys. Chem. C* **2019,** *123* (14), 9420–9427.
366. Alanazi, A. Q.; Almalki, M. H.; Mishra, A.; Kubicki, D. J.; Wang, Z.; Merten, L.; Eickemeyer, F. T.; Zhang, H.; Ren, D.; Alyamani, A. Y.; Albrithen, H.; Albadri, A.; Alotaibi, M. H.; Hinderhofer, A.; Zakeeruddin, S. M.; Schreiber, F.; Hagfeldt, A.; Emsley, L.; Milić, J. V.; Graetzel, M., Benzylammonium-Mediated Formamidinium Lead Iodide Perovskite Phase Stabilization for Photovoltaics. *Adv. Funct. Mater.* **2021,** *31* (30), 2101163.
367. Su, T. S.; Eickemeyer, F. T.; Hope, M. A.; Jahanbakhshi, F.; Mladenovic, M.; Li, J.; Zhou, Z. W.; Mishra, A.; Yum, J. H.; Ren, D.; Krishna, A.; Ouellette, O.; Wei, T. C.; Zhou, H.; Huang, H. H.; Mensi, M. D.; Sivula, K.; Zakeeruddin, S. M.; Milic, J. V.; Hagfeldt, A.; Rothlisberger, U.; Emsley, L.; Zhang, H.; Gratzel, M., Crown Ether Modulation Enables over 23% Efficient Formamidinium-Based Perovskite Solar Cells. *J. Am. Chem. Soc.* **2020,** *142* (47), 19980–19991.
368. Mishra, A.; Hope, M. A.; Almalki, M.; Pfeifer, L.; Zakeeruddin, S. M.; Grätzel, M.; Emsley, L., Dynamic Nuclear Polarization Enables NMR of Surface Passivating Agents on Hybrid Perovskite Thin Films. *J. Am. Chem. Soc.* **2022,** *144* (33), 15175–15184.
369. Mishra, A.; Ahlawat, P.; Fish, G. C.; Jahanbakhshi, F.; Mladenović, M.; Almalki, M.; Ruiz-Preciado, M. A.; Gelvéz-Rueda, M. C.; Kubicki, D. J.; Schouwink, P. A.; Dufoulon, V.; Schneeberger, T.; Aslanzadeh, A.; Grozema, F. C.; Zakeeruddin, S. M.; Moser, J.-E.; Rothlisberger, U.; Emsley, L.; Milić, J. V.; Grätzel, M., Naphthalenediimide/Formamidinium-Based Low-Dimensional Perovskites. *Chem. Mater.* **2021,** *33* (16), 6412–6420.
370. Anusca, I.; Balciunas, S.; Gemeiner, P.; Svirskas, S.; Sanlialp, M.; Lackner, G.; Fettkenhauer, C.; Belovickis, J.; Samulionis, V.; Ivanov, M.; Dkhil, B.; Banys, J.; Shvartsman, V. V.; Lupascu, D. C., Dielectric Response: Answer to Many Questions in the Methylammonium Lead Halide Solar Cell Absorbers. *Adv. Energy Mater.* **2017,** *7* (19).
371. Juarez-Perez, E. J.; Sanchez, R. S.; Badia, L.; Garcia-Belmonte, G.; Kang, Y. S.; Mora-Sero, I.; Bisquert, J., Photoinduced Giant Dielectric Constant in Lead Halide Perovskite Solar Cells. *J. Phys. Chem. Lett.* **2014,** *5* (13), 2390–2394.
372. La-o-vorakiat, C.; Xia, H. X.; Kadro, J.; Salim, T.; Zhao, D. M.; Ahmed, T.; Lam, Y. M.; Zhu, J. X.; Marcus, R. A.; Michel-Beyerle, M. E.; Chia, E. E. M., Phonon Mode Transformation Across the Orthohombic-Tetragonal Phase Transition in a Lead Iodide Perovskite $CH_3NH_3PbI_3$: A Terahertz Time-Domain Spectroscopy Approach. *J. Phys. Chem. Lett.* **2016,** *7* (1), 1–6.
373. Wright, A. D.; Verdi, C.; Milot, R. L.; Eperon, G. E.; Perez-Osorio, M. A.; Snaith, H. J.; Giustino, F.; Johnston, M. B.; Herz, L. M., Electron-phonon coupling in hybrid lead halide perovskites. *Nat. Commun.* **2016,** *7*.
374. Mozur, E. M.; Neilson, J. R., Cation Dynamics in Hybrid Halide Perovskites. *Annu. Rev. Mater. Res.* **2021,** *51* (1), 269–291.
375. Liu, S.; Guo, R.; Xie, F., The effects of organic cation rotation in hybrid Organic-Inorganic Perovskites: A critical review. *Mater. Des.* **2022,** *221*, 110951.
376. Lee, J. W.; Tan, S.; Seok, S. I.; Yang, Y.; Park, N. G., Rethinking the A cation in halide perovskites. *Science* **2022,** *375* (6583), 835.
377. Lee, J. W.; Seo, S.; Nandi, P.; Jung, H. S.; Park, N. G.; Shin, H., Dynamic structural property of organic-inorganic metal halide perovskite. *iScience* **2021,** *24* (1).
378. Herz, L. M., How Lattice Dynamics Moderate the Electronic Properties of Metal-Halide Perovskites. *J. Phys. Chem. Lett.* **2018,** *9* (23), 6853–6863.

379. Crothers, T. W.; Milot, R. L.; Patel, J. B.; Parrott, E. S.; Schlipf, J.; Muller-Buschbaum, P.; Johnston, M. B.; Herz, L. M., Photon Reabsorption Masks Intrinsic Bimolecular Charge-Carrier Recombination in $CH_3NH_3PbI_3$ Perovskite. *Nano. Lett.* **2017,** *17* (9), 5782–5789.
380. Sendner, M.; Nayak, P. K.; Egger, D. A.; Beck, S.; Muller, C.; Epding, B.; Kowalsky, W.; Kronik, L.; Snaith, H. J.; Pucci, A.; Lovrincic, R., Optical phonons in methylammonium lead halide perovskites and implications for charge transport. *Mater. Horiz.* **2016,** *3* (6), 613–620.
381. Chen, T. R.; Chen, W. L.; Foley, B. J.; Lee, J.; Ruff, J. P. C.; Ko, J. Y. P.; Brown, C. M.; Harriger, L. W.; Zhang, D. P.; Park, C. W.; Yoon, M.; Chang, Y. M.; Choi, J. J.; Lee, S. H., Origin of long lifetime of band-edge charge carriers in organic-inorganic lead iodide perovskites. *P. Natl. Acad. Sci. USA* **2017,** *114* (29), 7519–7524.
382. Ambrosio, F.; Meggiolaro, D.; Mosconi, E.; De Angelis, F., Charge Localization, Stabilization, and Hopping in Lead Halide Perovskites: Competition between Polaron Stabilization and Cation Disorder. *ACS Energy Lett.* **2019,** *4* (8), 2013–2020.
383. Gelvez-Rueda, M. C.; Cao, D. H.; Patwardhan, S.; Renaud, N.; Stoumpos, C. C.; Schatz, G. C.; Hupp, J. T.; Farha, O. K.; Savenije, T. J.; Kanatzidis, M. G.; Grozema, F. C., Effect of Cation Rotation on Charge Dynamics in Hybrid Lead Halide Perovskites. *J. Phys. Chem. C* **2016,** *120* (30), 16577–16585.
384. Frost, J. M.; Butler, K. T.; Brivio, F.; Hendon, C. H.; van Schilfgaarde, M.; Walsh, A., Atomistic Origins of High-Performance in Hybrid Halide Perovskite Solar Cells. *Nano. Lett.* **2014,** *14* (5), 2584–2590.
385. Zhu, X. Y.; Podzorov, V., Charge Carriers in Hybrid Organic-Inorganic Lead Halide Perovskites Might Be Protected as Large Polarons. *J. Phys. Chem. Lett.* **2015,** *6* (23), 4758–4761.
386. Kim, M.; Im, J.; Freeman, A. J.; Ihm, J.; Jin, H., Switchable S=1/2 and J=1/2 Rashba bands in ferroelectric halide perovskites. *P. Natl. Acad. Sci. USA* **2014,** *111* (19), 6900–6904.
387. Leguy, A. M.; Frost, J. M.; McMahon, A. P.; Sakai, V. G.; Kockelmann, W.; Law, C.; Li, X.; Foglia, F.; Walsh, A.; O'regan, B. C.; Nelson, J.; Carbral, J. T.; Barnes, P. R. F., The Dynamics of Methylammonium Ions in Hybrid Organic–Inorganic Perovskite Solar Cells. *Nat. Commun.* **2015,** *6*, 7124.
388. Swainson, I. P.; Stock, C.; Parker, S. F.; Van Eijck, L.; Russina, M.; Taylor, J. W., From soft harmonic phonons to fast relaxational dynamics in $CH_3NH_3PbBr_3$. *Phys. Rev. B* **2015,** *92* (10).
389. Chen, T.; Foley, B. J.; Ipek, B.; Tyagi, M.; Copley, J. R. D.; Brown, C. M.; Choi, J. J.; Lee, S. H., Rotational dynamics of organic cations in the $CH_3NH_3PbI_3$ perovskite. *Phys. Chem. Chem. Phys.* **2015,** *17* (46), 31278–31286.
390. Druzbicki, K.; Pinna, R. S.; Rudic, S.; Jura, M.; Gorini, G.; Fernandez-Alonso, F., Unexpected Cation Dynamics in the Low-Temperature Phase of Methylammonium Lead Iodide: The Need for Improved Models. *J. Phys. Chem. Lett.* **2016,** *7* (22), 4701–4709.
391. Li, B.; Kawakita, Y.; Liu, Y. C.; Wang, M. C.; Matsuura, M.; Shibata, K.; Ohira-Kawamura, S.; Yamada, T.; Lin, S. C.; Nakajima, K. J.; Liu, S. Z., Polar rotor scattering as atomic-level origin of low mobility and thermal conductivity of perovskite $CH_3NH_3PbI_3$. *Nat. Commun.* **2017,** *8*.
392. Poglitsch, A.; Weber, D., Dynamic disorder in methylammoniumtrihalogenoplumbates (II) observed by millimeter-wave spectroscopy. *J. Chem. Phys.* **1987,** *87*, 6373–6378.
393. Bakulin, A. A.; Selig, O.; Bakker, H. J.; Rezus, Y. L. A.; Muller, C.; Glaser, T.; Lovrincic, R.; Sun, Z. H.; Chen, Z. Y.; Walsh, A.; Frost, J. M.; Jansen, T. L. C., Real-Time Observation of Organic Cation Reorientation in Methylammonium Lead Iodide Perovskites. *J. Phys. Chem. Lett.* **2015,** *6* (18), 3663–3669.
394. Selig, O.; Sadhanala, A.; Muller, C.; Lovrincic, R.; Chen, Z.; Rezus, Y. L. A.; Frost, J. M.; Jansen, T. L. C.; Bakulin, A. A., Organic Cation Rotation and Immobilization in Pure and Mixed Methylammonium Lead-Halide Perovskites. *J. Am. Chem. Soc.* **2017,** *139* (11), 4068–4074.
395. Kim, G.; Min, H.; Lee, K. S.; Lee, D. Y.; Yoon, S. M.; Seok, S. I., Impact of strain relaxation on performance of alpha-formamidinium lead iodide perovskite solar cells. *Science* **2020,** *370* (6512), 108.
396. Taylor, V. C. A.; Tiwari, D.; Duchi, M.; Donaldson, P. M.; Clark, I. P.; Fermin, D. J.; Oliver, T. A. A., Investigating the Role of the Organic Cation in Formamidinium Lead Iodide Perovskite Using Ultrafast Spectroscopy. *J. Phys. Chem. Lett.* **2018,** *9* (4), 895–901.
397. Druzbicki, K.; Laven, R.; Armstrong, J.; Malavasi, L.; Fernandez-Alonso, F.; Karlsson, M., Cation Dynamics and Structural Stabilization in Formamidinium Lead Iodide Perovskites. *J. Phys. Chem. Lett.* **2021,** *12* (14), 3503–3508.
398. Mozur, E. M.; Hope, M. A.; Trowbridge, J. C.; Halat, D. M.; Daemen, L. L.; Maughan, A. E.; Prisk, T. R.; Grey, C. P.; Neilson, J. R., Cesium Substitution Disrupts Concerted Cation Dynamics in Formamidinium Hybrid Perovskites. *Chem. Mater.* **2020,** *32* (14), 6266–6277.
399. Bielecki, A.; Burum, D. P., Temperature Dependence of ^{207}Pb MAS Spectra of Solid Lead Nitrate. An Accurate, Sensitive Thermometer for Variable-Temperature MAS. *J. Magn. Reson. (A)* **1995,** *116* (2), 215–220.
400. Nimerovsky, E.; Gupta, R.; Yehl, J.; Li, M. Y.; Polenova, T.; Goldbourt, A., Phase-modulated LA-REDOR: A robust, accurate and efficient solid-state NMR technique for distance measurements between a spin-1/2 and a quadrupole spin. *J. Magn. Reson.* **2014,** *244*, 107–113.
401. Reif, B.; Ashbrook, S. E.; Emsley, L.; Hong, M., Solid-state NMR spectroscopy. *Nat. Rev. Methods Primers* **2021,** *1* (1), 1–23.
402. Min, G.; Yun, Y.; Choi, H. J.; Lee, S.; Joo, J., Hydrogen halide-free synthesis of organohalides for organometal trihalide perovskite solar cells. *J. Ind. Eng. Chem.* **2020,** *89*, 375–382.
403. d'Espinose de la Caillerie, J. B.; Fretigny, C.; Massiot, D., MAS NMR spectra of quadrupolar nuclei in disordered solids: The Czjzek model. *J. Magn. Reson.* **2008,** *192* (2), 244–251.
404. Kawachi, S.; Atsumi, M.; Saito, N.; Ohashi, N.; Murakami, Y.; Yamaura, J.-i., Structural and Thermal Properties in Formamidinium and Cs-Mixed Lead Halides. *J. Phys. Chem. Lett.* **2019,** *10* (22), 6967–6972.
405. Huntress Jr, W. T., The study of anisotropic rotation of molecules in liquids by NMR quadrupolar relaxation. In *Advances in Magnetic and Optical Resonance*, Elsevier: 1970; Vol. 4, pp 1–37.

406. Chen, T.; Foley, B. J.; Park, C.; Brown, C. M.; Harriger, L. W.; Lee, J.; Ruff, J.; Yoon, M.; Choi, J. J.; Lee, S. H., Entropy-driven structural transition and kinetic trapping in formamidinium lead iodide perovskite. *Sci. Adv.* **2016,** *2* (10).
407. Knight, A. J.; Borchert, J.; Oliver, R. D. J.; Patel, J. B.; Radaelli, P. G.; Snaith, H. J.; Johnston, M. B.; Herz, L. M., Halide Segregation in Mixed-Halide Perovskites: Influence of A-Site Cations. *ACS Energy Lett.* **2021,** *6* (2), 799–808.
408. Li, N. X.; Tao, S. X.; Chen, Y. H.; Niu, X. X.; Onwudinanti, C. K.; Hu, C.; Qiu, Z. W.; Xu, Z. Q.; Zheng, G. H. J.; Wang, L. G.; Zhang, Y.; Li, L.; Liu, H. F.; Lun, Y. Z.; Hong, J. W.; Wang, X. Y.; Liu, Y. Q.; Xie, H. P.; Gao, Y. L.; Bai, Y.; Yang, S. H.; Brocks, G.; Chen, Q.; Zhou, H. P., Cation and anion immobilization through chemical bonding enhancement with fluorides for stable halide perovskite solar cells. *Nat. Energy* **2019,** *4* (5), 408–415.
409. Xu, J. X.; Boyd, C. C.; Yu, Z. S. J.; Palmstrom, A. F.; Witter, D. J.; Larson, B. W.; France, R. M.; Werner, J.; Harvey, S. P.; Wolf, E. J.; Weigand, W.; Manzoor, S.; van Hest, M. F. A. M.; Berry, J. J.; Luther, J. M.; Holman, Z. C.; McGehee, M. D., Triple-halide wide-band gap perovskites with suppressed phase segregation for efficient tandems. *Science* **2020,** *367* (6482), 1097.
410. Li, F. Z.; Deng, X.; Qi, F.; Li, Z.; Liu, D. J.; Shen, D.; Qin, M. C.; Wu, S. F.; Lin, F.; Jang, S. H.; Zhang, J.; Lu, X. H.; Lei, D. Y.; Lee, C. S.; Zhu, Z. L.; Jen, A. K. Y., Regulating Surface Termination for Efficient Inverted Perovskite Solar Cells with Greater Than 23% Efficiency. *J. Am. Chem. Soc.* **2020,** *142* (47), 20134–20142.
411. Francisco-Lopez, A.; Charles, B.; Alonso, M. I.; Garriga, M.; Campoy-Quiles, M.; Weller, M. T.; Goni, A. R., Phase Diagram of Methylammonium/Formamidinium Lead Iodide Perovskite Solid Solutions from Temperature-Dependent Photoluminescence and Raman Spectroscopies. *J. Phys. Chem. C* **2020,** *124* (6), 3448–3458.
412. McClung, R. E. D., Spin–Rotation Relaxation Theory. In *eMagRes*, John Wiley & Sons, Ltd.
413. Pell, A. J.; Pintacuda, G.; Grey, C. P., Paramagnetic NMR in solution and the solid state. *Prog. Nucl. Mag. Res. Sp.* **2019,** *111*, 1–271.
414. De Marco, N.; Zhou, H. P.; Chen, Q.; Sun, P. Y.; Liu, Z. H.; Meng, L.; Yao, E. P.; Liu, Y. S.; Schiffer, A.; Yang, Y., Guanidinium: A Route to Enhanced Carrier Lifetime and Open-Circuit Voltage in Hybrid Perovskite Solar Cells. *Nano. Lett.* **2016,** *16* (2), 1009–1016.
415. Gao, L. L.; Li, X. T.; Liu, Y.; Fang, J. J.; Huang, S.; Spanopoulos, I.; Li, X. L.; Wang, Y.; Chen, L.; Yang, G. J.; Kanatzidis, M. G., Incorporated Guanidinium Expands the $CH_3NH_3PbI_3$ Lattice and Enhances Photovoltaic Performance. *ACS Appl. Mater. Inter.* **2020,** *12* (39), 43885–43891.
416. Prochowicz, D.; Tavakoli, M. M.; Alanazi, A. Q.; Trivedi, S.; Dastjerdi, H. T.; Zakeeruddin, S. M.; Gratzel, M.; Yadav, P., Charge Accumulation, Recombination, and Their Associated Time Scale in Efficient $(GUA)_x(MA)_{1-x}PbI_3$-Based Perovskite Solar Cells. *ACS Omega* **2019,** *4* (16), 16840–16846.
417. Jodlowski, A. D.; Roldán-Carmona, C.; Grancini, G.; Salado, M.; Ralaiarisoa, M.; Ahmad, S.; Koch, N.; Camacho, L.; De Miguel, G.; Nazeeruddin, M. K., Large Guanidinium Cation Mixed with Methylammonium in Lead Iodide Perovskites for 19% Efficient Solar Cells. *Nat. Energy* **2017,** *2* (12), 972–979.
418. Giorgi, G.; Fujisawa, J. I.; Segawa, H.; Yamashita, K., Organic-Inorganic Hybrid Lead Iodide Perovskite Featuring Zero Dipole Moment Guanidinium Cations: A Theoretical Analysis. *J. Phys. Chem. C* **2015,** *119* (9), 4694–4701.
419. Oja, T., Nitrogen‐14 nuclear quadrupole resonance study of the guanidinium ion. *J. Chem. Phys.* **1973,** *59* (5), 2668–2675.
420. Ratcliffe, C. I., Nuclear Magnetic-Resonance Studies of Molecular-Motion in Guanidinium Chloride, Bromide, and Iodide. *Can. J. Chem.* **1985,** *63* (6), 1239–1244.
421. Bloembergen, N.; Purcell, E. M.; Pound, R. V., Relaxation Effects in Nuclear Magnetic Resonance Absorption. *Phys. Rev.* **1948,** *73* (7), 679–712.
422. Even, J.; Carignano, M.; Katan, C., Molecular disorder and translation/rotation coupling in the plastic crystal phase of hybrid perovskites. *Nanoscale* **2016,** *8* (12), 6222–6236.
423. Vold, R. L.; Hoatson, G. L., Effects of jump dynamics on solid state nuclear magnetic resonance line shapes and spin relaxation times. *J. Magn. Reson.* **2009,** *198* (1), 57–72.
424. Whitfield, P. S.; Herron, N.; Guise, W. E.; Page, K.; Cheng, Y. Q.; Milas, I.; Crawford, M. K., Structures, Phase Transitions and Tricritical Behavior of the Hybrid Perovskite Methyl Ammonium Lead Iodide. *Sci. Rep.* **2016,** *6*, 35685.
425. Franz, A.; Tobbens, D. M.; Lehmann, F.; Kargell, M.; Schorr, S., The influence of deuteration on the crystal structure of hybrid halide perovskites: a temperature-dependent neutron diffraction study of $FAPbBr_3$. *Acta Crystallogr. B* **2020,** *76* (2), 267-274.
426. Franssen, W. M. J.; Bruijnaers, B. J.; Portengen, V. H. L.; Kentgens, A. P. M., Dimethylammonium Incorporation in Lead Acetate Based $MAPbI_3$ Perovskite Solar Cells. *Chemphyschem* **2018,** *19* (22), 3107–3115.
427. Ray, A.; Martin-Garcia, B.; Moliterni, A.; Casati, N.; Boopathi, K. M.; Spirito, D.; Goldoni, L.; Prato, M.; Giacobbe, C.; Giannini, C.; Di Stasio, F.; Krahne, R.; Manna, L.; Abdelhady, A. L., Mixed Dimethylammonium/Methylammonium Lead Halide Perovskite Crystals for Improved Structural Stability and Enhanced Photodetection. *Adv. Mater.* **2022,** *34* (7).
428. Mishra, A.; Kubicki, D. J.; Boziki, A.; Chavan, R. D.; Dankl, M.; Mladenović, M.; Prochowicz, D.; Grey, C. P.; Rothlisberger, U.; Emsley, L., Interplay of Kinetic and Thermodynamic Reaction Control Explains Incorporation of Dimethylammonium Iodide into $CsPbI_3$. *ACS Energy Lett.* **2022**, 2745–2752.
429. Almora, O.; Aranda, C.; Mas-Marza, E.; Garcia-Belmonte, G., On Mott-Schottky analysis interpretation of capacitance measurements in organometal perovskite solar cells. *Appl. Phys. Lett.* **2016,** *109* (17).
430. Futscher, M. H.; Lee, J. M.; McGovern, L.; Muscarella, L. A.; Wang, T. Y.; Haider, M. I.; Fakharuddin, A.; Schmidt-Mende, L.; Ehrler, B., Quantification of ion migration in $CH_3NH_3PbI_3$ perovskite solar cells by transient capacitance measurements. *Mater. Horiz.* **2019,** *6* (7), 1497–1503.
431. Senocrate, A.; Moudrakovski, I.; Kim, G. Y.; Yang, T. Y.; Gregori, G.; Gratzel, M.; Maier, J., The Nature of Ion Conduction in Methylammonium Lead Iodide: A Multimethod Approach. *Angew. Chem. Int. Ed.* **2017,** *56* (27), 7755–7759.
432. Egger, D. A.; Kronik, L.; Rappe, A. M., Theory of Hydrogen Migration in Organic-Inorganic Halide Perovskites. *Angew. Chem. Int. Ed.* **2015,** *54* (42), 12437–12441.

433. Ceratti, D. R.; Zohar, A.; Kozlov, R.; Dong, H.; Uraltsev, G.; Girshevitz, O.; Pinkas, I.; Avram, L.; Hodes, G.; Cahen, D., Eppur si Muove: Proton Diffusion in Halide Perovskite Single Crystals. *Adv. Mater.* **2020,** *32* (46).
434. Sadhu, S.; Buffeteau, T.; Sandrez, S.; Hirsch, L.; Bassani, D. M., Observing the Migration of Hydrogen Species in Hybrid Perovskite Materials through D/H Isotope Exchange. *J. Am. Chem. Soc.* **2020,** *142* (23), 10431–10437.
435. Chen, Y. F.; Tsai, Y. T.; Hirsch, L.; Bassani, D. M., Kinetic Isotope Effects Provide Experimental Evidence for Proton Tunneling in Methylammonium Lead Triiodide Perovskites. *J. Am. Chem. Soc.* **2017,** *139* (45), 16359–16364.
436. Sturniolo, S.; Green, T. F. G.; Hanson, R. M.; Zilka, M.; Refson, K.; Hodgkinson, P.; Brown, S. P.; Yates, J. R., Visualization and processing of computed solid-state NMR parameters: MagresView and MagresPython. *Solid State Nucl. Mag.* **2016,** *78*, 64–70.
437. Thurber, K. R.; Tycko, R., Measurement of sample temperatures under magic-angle spinning from the chemical shift and spin-lattice relaxation rate of ^{79}Br in KBr powder. *J. Magn. Reson.* **2009,** *196* (1), 84–87.
438. Fung, B. M.; Khitrin, A. K.; Ermolaev, K., An Improved Broadband Decoupling Sequence for Liquid Crystals and Solids. *J. Magn. Reson.* **2000,** *142* (1), 97–101.
439. Yarava, J. R.; Chaudhari, S. R.; Rossini, A. J.; Lesage, A.; Emsley, L., Solvent suppression in DNP enhanced solid state NMR. *J. Magn. Reson.* **2017,** *277*, 149–153.
440. Ripolles, T. S.; Serafini, P.; Redondo-Obispo, C.; Climent-Pascual, E.; Masi, S.; Mora-Seró, I.; Coya, C., Interface Engineering in Perovskite Solar Cells by Low Concentration of Phenylethyl Ammonium Iodide Solution in the Antisolvent Step. *Energy Technol.* **2022,** *10* (3), 2100890.
441. Lee, D. S.; Yun, J. S.; Kim, J.; Soufiani, A. M.; Chen, S.; Cho, Y.; Deng, X.; Seidel, J.; Lim, S.; Huang, S., Passivation of grain boundaries by phenethylammonium in formamidinium-methylammonium lead halide perovskite solar cells. *ACS Energy Lett.* **2018,** *3* (3), 647–654.
442. Wang, Z.; Lin, Q.; Chmiel, F. P.; Sakai, N.; Herz, L. M.; Snaith, H. J., Efficient ambient-air-stable solar cells with 2D–3D heterostructured butylammonium-caesium-formamidinium lead halide perovskites. *Nat. Energy* **2017,** *2* (9), 17135.
443. Rosay, M. M. Sensitivity-enhanced nuclear magnetic resonance of biological solids. Ph.D. Dissertation, Massachusetts Institute of Technology (MIT), Cambridge, USA, 2001.
444. Hu, K.-N.; Yu, H.-h.; Swager, T. M.; Griffin, R. G., Dynamic Nuclear Polarization with Biradicals. *J. Am. Chem. Soc.* **2004,** *126* (35), 10844–10845.
445. Akbey, Ü.; Franks, W. T.; Linden, A.; Lange, S.; Griffin, R. G.; van Rossum, B.-J.; Oschkinat, H., Dynamic Nuclear Polarization of Deuterated Proteins. *Angew. Chem. Int. Ed.* **2010,** *49* (42), 7803–7806.
446. Zagdoun, A.; Rossini, A. J.; Conley, M. P.; Grüning, W. R.; Schwarzwälder, M.; Lelli, M.; Franks, W. T.; Oschkinat, H.; Copéret, C.; Emsley, L.; Lesage, A., Improved Dynamic Nuclear Polarization Surface-Enhanced NMR Spectroscopy through Controlled Incorporation of Deuterated Functional Groups. *Angew. Chem. Int. Ed.* **2013,** *52* (4), 1222–1225.
447. Berruyer, P.; Björgvinsdóttir, S.; Bertarello, A.; Stevanato, G.; Rao, Y.; Karthikeyan, G.; Casano, G.; Ouari, O.; Lelli, M.; Reiter, C.; Engelke, F.; Emsley, L., Dynamic Nuclear Polarization Enhancement of 200 at 21.15 T Enabled by 65 kHz Magic Angle Spinning. *J. Phys. Chem. Lett.* **2020,** *11* (19), 8386–8391.
448. Quan, L. N.; Yuan, M.; Comin, R.; Voznyy, O.; Beauregard, E. M.; Hoogland, S.; Buin, A.; Kirmani, A. R.; Zhao, K.; Amassian, A., Ligand-Stabilized Reduced-Dimensionality Perovskites. *J. Am. Chem. Soc.* **2016,** *138* (8), 2649–2655.
449. Li, N.; Zhu, Z.; Chueh, C. C.; Liu, H.; Peng, B.; Petrone, A.; Li, X.; Wang, L.; Jen, A. K. Y., Mixed Cation $FA_xPEA_{1-x}PbI3$ with Enhanced Phase and Ambient Stability toward High-Performance Perovskite Solar Cells. *Adv. Energy Mater.* **2017,** *7*, 1601307.
450. Cho, K. T.; Grancini, G.; Lee, Y.; Oveisi, E.; Ryu, J.; Almora, O.; Tschumi, M.; Schouwink, P. A.; Seo, G.; Heo, S.; Park, J.; Jang, J.; Paek, S.; Garcia-Belmonte, G.; Nazeeruddin, M. K., Selective growth of layered perovskites for stable and efficient photovoltaics. *Energy Environ. Sci.* **2018,** *11* (4), 952–959.
451. Berruyer, P.; Lelli, M.; Conley, M. P.; Silverio, D. L.; Widdifield, C. M.; Siddiqi, G.; Gajan, D.; Lesage, A.; Copéret, C.; Emsley, L., Three-Dimensional Structure Determination of Surface Sites. *J. Am. Chem. Soc.* **2017,** *139* (2), 849–855.
452. Sangodkar, R. P.; Smith, B. J.; Gajan, D.; Rossini, A. J.; Roberts, L. R.; Funkhouser, G. P.; Lesage, A.; Emsley, L.; Chmelka, B. F., Influences of Dilute Organic Adsorbates on the Hydration of Low-Surface-Area Silicates. *J. Am. Chem. Soc.* **2015,** *137* (25), 8096–8112.
453. Perras, F. A.; Boteju, K. C.; Slowing, II; Sadow, A. D.; Pruski, M., Direct ^{17}O dynamic nuclear polarization of single-site heterogeneous catalysts. *Chem. Commun.* **2018,** *54* (28), 3472–3475.
454. Hoke, E. T.; Slotcavage, D. J.; Dohner, E. R.; Bowring, A. R.; Karunadasa, H. I.; McGehee, M. D., Reversible photo-induced trap formation in mixed-halide hybrid perovskites for photovoltaics. *Chem. Sci.* **2015,** *6* (1), 613–617.
455. Amat, A.; Mosconi, E.; Ronca, E.; Quarti, C.; Umari, P.; Nazeeruddin, M. K.; Gratzel, M.; De Angelis, F., Cation-induced band-gap tuning in organohalide perovskites: interplay of spin–orbit coupling and octahedra tilting. *Nano. Lett.* **2014,** *14* (6), 3608–3616.
456. Slotcavage, D. J.; Karunadasa, H. I.; McGehee, M. D., Light-induced phase segregation in halide-perovskite absorbers. *ACS Energy Lett.* **2016,** *1* (6), 1199–1205.
457. Brennan, M. C.; Draguta, S.; Kamat, P. V.; Kuno, M., Light-induced anion phase segregation in mixed halide perovskites. *ACS Energy Lett.* **2017,** *3* (1), 204–213.
458. Yoon, S. J.; Draguta, S.; Manser, J. S.; Sharia, O.; Schneider, W. F.; Kuno, M.; Kamat, P. V., Tracking iodide and bromide ion segregation in mixed halide lead perovskites during photoirradiation. *ACS Energy Lett.* **2016,** *1* (1), 290–296.
459. Brennan, M. C.; Ruth, A.; Kamat, P. V.; Kuno, M., Photoinduced anion segregation in mixed halide perovskites. *Trends Chem.* **2020,** *2* (4), 282–301.

460. Gottesman, R.; Haltzi, E.; Gouda, L.; Tirosh, S.; Bouhadana, Y.; Zaban, A.; Mosconi, E.; De Angelis, F., Extremely slow photoconductivity response of $CH_3NH_3PbI_3$ perovskites suggesting structural changes under working conditions. *J. Phys. Chem. Lett.* **2014,** *5* (15), 2662–2669.
461. Bischak, C. G.; Wong, A. B.; Lin, E.; Limmer, D. T.; Yang, P.; Ginsberg, N. S., Tunable polaron distortions control the extent of halide demixing in lead halide perovskites. *J. Phys. Chem. Lett.* **2018,** *9* (14), 3998–4005.
462. Ruth, A.; Brennan, M. C.; Draguta, S.; Morozov, Y. V.; Zhukovskyi, M.; Janko, B.; Zapol, P.; Kuno, M., Vacancy-mediated anion photosegregation kinetics in mixed halide hybrid perovskites: coupled kinetic Monte Carlo and optical measurements. *ACS Energy Lett.* **2018,** *3* (10), 2321–2328.
463. Brivio, F.; Caetano, C.; Walsh, A., Thermodynamic origin of photoinstability in the CH3NH3Pb ($I_{1-x}Br_x$) 3 hybrid halide perovskite alloy. *J. Phys. Chem. Lett.* **2016,** *7* (6), 1083–1087.
464. Bischak, C. G.; Hetherington, C. L.; Wu, H.; Aloni, S.; Ogletree, D. F.; Limmer, D. T.; Ginsberg, N. S., Origin of reversible photoinduced phase separation in hybrid perovskites. *Nano. Lett.* **2017,** *17* (2), 1028–1033.
465. Wang, X.; Ling, Y.; Lian, X.; Xin, Y.; Dhungana, K. B.; Perez-Orive, F.; Knox, J.; Chen, Z.; Zhou, Y.; Beery, D., Suppressed phase separation of mixed-halide perovskites confined in endotaxial matrices. *Nat. Commun.* **2019,** *10* (1), 1–7.
466. Knight, A. J.; Wright, A. D.; Patel, J. B.; McMeekin, D. P.; Snaith, H. J.; Johnston, M. B.; Herz, L. M., Electronic traps and phase segregation in lead mixed-halide perovskite. *ACS Energy Lett.* **2018,** *4* (1), 75–84.
467. Barker, A. J.; Sadhanala, A.; Deschler, F.; Gandini, M.; Senanayak, S. P.; Pearce, P. M.; Mosconi, E.; Pearson, A. J.; Wu, Y.; Srimath Kandada, A. R., Defect-assisted photoinduced halide segregation in mixed-halide perovskite thin films. *ACS Energy Lett.* **2017,** *2* (6), 1416–1424.
468. Belisle, R. A.; Bush, K. A.; Bertoluzzi, L.; Gold-Parker, A.; Toney, M. F.; McGehee, M. D., Impact of surfaces on photoinduced halide segregation in mixed-halide perovskites. *ACS Energy Lett.* **2018,** *3* (11), 2694–2700.
469. Dang, H. X.; Wang, K.; Ghasemi, M.; Tang, M.-C.; De Bastiani, M.; Aydin, E.; Dauzon, E.; Barrit, D.; Peng, J.; Smilgies, D.-M., Multi-cation synergy suppresses phase segregation in mixed-halide perovskites. *Joule* **2019,** *3* (7), 1746–1764.
470. Mathew, P. S.; Samu, G. F.; Janáky, C.; Kamat, P. V., Iodine (I) Expulsion at Photoirradiated Mixed Halide Perovskite Interface. Should I Stay or Should I Go? *ACS Energy Lett.* **2020,** *5* (6), 1872–1880.
471. Cho, J.; Kamat, P. V., How Chloride Suppresses Photoinduced Phase Segregation in Mixed Halide Perovskites. *Chem. Mater.* **2020,** *32* (14), 6206–6212.
472. Cho, J.; DuBose, J. T.; Le, A. N. T.; Kamat, P. V., Suppressed Halide Ion Migration in 2D Lead Halide Perovskites. *ACS Mater. Lett.* **2020,** *2* (6), 565–570.
473. Nan, Z.-A.; Chen, L.; Liu, Q.; Wang, S.-H.; Chen, Z.-X.; Kang, S.-Y.; Ji, J.-B.; Tan, Y.-Y.; Hui, Y.; Yan, J.-W., Revealing phase evolution mechanism for stabilizing formamidinium-based lead halide perovskites by a key intermediate phase. *Chem* **2021,** *7* (9), 2513–2526.
474. Gratia, P.; Zimmermann, I.; Schouwink, P.; Yum, J.-H.; Audinot, J.-N.; Sivula, K.; Wirtz, T.; Nazeeruddin, M. K., The Many Faces of Mixed Ion Perovskites: Unraveling and Understanding the Crystallization Process. *ACS Energy Lett.* **2017,** *2* (12), 2686–2693.
475. Johnston, A.; Walters, G.; Saidaminov, M. I.; Huang, Z.; Bertens, K.; Jalarvo, N.; Sargent, E. H., Bromine Incorporation and Suppressed Cation Rotation in Mixed-Halide Perovskites. *ACS Nano* **2020,** *14* (11), 15107–15118.
476. Liu, W.; Lin, Q.; Li, H.; Wu, K.; Robel, I.; Pietryga, J. M.; Klimov, V. I., Mn^{2+}-Doped Lead Halide Perovskite Nanocrystals with Dual-Color Emission Controlled by Halide Content. *J. Am. Chem. Soc.* **2016,** *138* (45), 14954–14961.
477. Parobek, D.; Roman, B. J.; Dong, Y.; Jin, H.; Lee, E.; Sheldon, M.; Son, D. H., Exciton-to-Dopant Energy Transfer in Mn-Doped Cesium Lead Halide Perovskite Nanocrystals. *Nano. Lett.* **2016,** *16* (12), 7376–7380.
478. Zou, S.; Liu, Y.; Li, J.; Liu, C.; Feng, R.; Jiang, F.; Li, Y.; Song, J.; Zeng, H.; Hong, M.; Chen, X., Stabilizing Cesium Lead Halide Perovskite Lattice through Mn(II) Substitution for Air-Stable Light-Emitting Diodes. *J. Am. Chem. Soc.* **2017,** *139* (33), 11443–11450.
479. Akkerman, Q. A.; Meggiolaro, D.; Dang, Z.; De Angelis, F.; Manna, L., Fluorescent Alloy $CsPb_xMn_{1-x}I_3$ Perovskite Nanocrystals with High Structural and Optical Stability. *ACS Energy Lett.* **2017,** *2* (9), 2183–2186.
480. Guvenc, C. M.; Yalcinkaya, Y.; Ozen, S.; Sahin, H.; Demir, M. M., Gd^{3+}-Doped α-$CsPbI_3$ Nanocrystals with Better Phase Stability and Optical Properties. *J. Phys. Chem. C* **2019,** *123* (40), 24865–24872.
481. He, Q.; Mei, E.; Wang, Z.; Liang, X.; Chen, S.; Xiang, W., Ultrastable Gd^{3+} doped $CsPbCl_{1.5}Br_{1.5}$ nanocrystals blue glass for regulated and low thresholds amplified spontaneous emission. *Photonics Res.* **2021,** *9* (10), 1916–1923.
482. Ahmed, G. H.; Yin, J.; Bakr, O. M.; Mohammed, O. F., Near-unity photoluminescence quantum yield in inorganic perovskite nanocrystals by metal-ion doping. *J. Chem. Phys.* **2020,** *152* (2), 020902.

Glossary

NMR	Nuclear magnetic resonance
DNP	Dynamic Nuclear polarization
MAS	Magic angle spinning
SE	Solid effect
CE	Cross effect
OE	Overhauser effect
PSC	Perovskite solar cell
PCE	Power conversion efficiency
PV	Photovoltaics
FA	Formamidinium
MA	Methylammonium
GUA	Guanidinium
DMA	Dimethylammonium
MDA	Methylenediammonium
RP	Ruddlesden-Popper
DJ	Dion-Jacobson
DFT	Density functional theory
XRD	X-ray diffraction
SEM	Scanning electron microscopy
CP	Cross polarization

Curriculum Vitae

Aditya Mishra

adityagsmishra@gmail.com / aditya.mishra@epfl.ch

Current position

2018 – 2022 Ph.D. student, Laboratory of Magnetic Resonance.

Thesis director: David Lyndon Emsley.

École Polytechnique Fédérale de Lausanne (EPFL), Switzerland.

Education

2013 – 2018 BS-MS dual Degree in Physics

Indian Institute of Science Education and Research (IISER), Mohali, India.

Publications

[1] **Mishra, A.**; Hope, M. A.; Grätzel, M.; Emsley, L., A Complete Picture of Cation Dynamics in Hybrid Perovskite Materials using Solid State NMR Spectroscopy. *(submitted)*

[2] **Mishra, A.**; Hope, M. A.; Almalki, M.; Pfeifer, L.; Zakeeruddin, S. M.; Grätzel, M.; Emsley, L., Dynamic Nuclear Polarization Enables NMR of Surface Passivating Agents on Hybrid Perovskite Thin Films. *J. Am. Chem. Soc.* **2022,** *144* (33), 15175–15184.

[3] **Mishra, A.**; Kubicki, D. J.; Boziki, A.; Chavan, R. D.; Dankl, M.; Mladenović, M.; Prochowicz, D.; Grey, C. P.; Rothlisberger, U.; Emsley, L., Interplay of Kinetic and Thermodynamic Reaction Control Explains Incorporation of Dimethylammonium Iodide into CsPbI3. *ACS Energy Lett.* **2022**, 2745-2752.

[4] **Mishra, A.**; Ahlawat, P.; Fish, G. C.; Jahanbakhshi, F.; Mladenović, M.; Almalki, M.; Ruiz-Preciado, M. A.; Gelvéz-Rueda, M. C.; Kubicki, D. J.; Schouwink, P. A.; Dufoulon, V.; Schneeberger, T.; Aslanzadeh, A.; Grozema, F. C.; Zakeeruddin, S. M.; Moser, J.-E.; Rothlisberger, U.; Emsley, L.; Milić, J. V.; Grätzel, M., Naphthalenediimide/Formamidinium-Based Low-Dimensional Perovskites. *Chem. Mater.* **2021,** *33* (16), 6412–6420.

[5] Hope, M. A.*; Nakamura, T.*; Ahlawat, P.*; **Mishra, A.***; Cordova, M.; Jahanbakhshi, F.; Mladenović, M.; Runjhun, R.; Merten, L.; Hinderhofer, A.; Carlsen, B. I.; Kubicki, D. J.; Gershoni-Poranne, R.; Schneeberger, T.; Carbone, L. C.; Liu, Y.; Zakeeruddin, S. M.; Lewinski, J.; Hagfeldt, A.; Schreiber, F.; Rothlisberger, U.; Grätzel, M.; Milić, J. V.; Emsley, L., *J. Am. Chem. Soc.* 2021, 143 (3), 1529–1538. (*denotes equal contribution)

[6] Ummadisingu, A.*; **Mishra, A.***; Kubicki, D. J.; LaGrange, T.; Dučinskas, A.; Siczek, M.; Bury, W.; Milić, J. V.; Grätzel, M.; Emsley, L., Multi-Length Scale Structure of 2D/3D Dion–Jacobson Hybrid Perovskites Based on an Aromatic Diammonium Spacer. *Small* **2022,** *18* (5), 2104287.
(*denotes equal contribution)

[7] Jeong, J.; Kim, M.;Seo, J.; Lu, H.;Ahlawat, P.;**Mishra, A**.; Yang, Y.;Hope, M. A.;Eickemeyer, F. T.; Kim, M.;Yoon, Y. J.;Choi, I. W.;Darwich, B. P.;Choi, S. J.;Jo, Y.; Lee, J. H.;Walker, B.;Zakeeruddin, S. M.;Emsley, L.; Rothlisberger, U.;Hagfeldt, A.;Kim, D. S.;Grätzel, M.;Kim, J. Y., Pseudo-halide anion engineering for α-$FAPbI_3$ perovskite solar cells. *Nature* **2021,** *592* (7854), 381–385.

[8] Lu, H.; Liu, Y.; Ahlawat, P.; **Mishra, A.**; Tress, W. R.; Eickemeyer, F. T.; Yang, Y.; Fu, F.; Wang, Z.; Avalos, C. E.; Carlsen, B. I.; Agarwalla, A.; Zhang, X.; Li, X.; Zhan, Y.; Zakeeruddin, S. M.; Emsley, L.; Rothlisberger, U.; Zheng, L.; Hagfeldt, A.; Grätzel, M., Vapor-assisted deposition of highly efficient, stable black-phase $FAPbI_3$ perovskite solar cells. *Science* **2020,** *370* (6512), eabb8985.

[9] Boziki, A.; Kubicki, D. J.; **Mishra, A.**; Meloni, S.; Emsley, L.; Grätzel, M.; Rothlisberger, U., Atomistic Origins of the Limited Phase Stability of Cs^+-Rich $FA_xCs_{1-x}PbI_3$ Mixtures. *Chem. Mater.* **2020,** *32* (6), 2605–2614.

[10] Zhang, J.; Wang, Z.; **Mishra, A.**; Yu, M.; Shasti, M.; Tress, W.; Kubicki, D. J.; Avalos, C. E.; Lu, H.; Liu, Y.; Carlsen, B. I.; Agarwalla, A.; Wang, Z.; Xiang, W.; Emsley, L.; Zhang, Z.; Grätzel, M.; Guo, W.; Hagfeldt, A., Intermediate Phase Enhances Inorganic Perovskite and Metal Oxide Interface for Efficient Photovoltaics. *Joule* **2020,** *4*, 222.

[11] Alanazi, A. Q.; Almalki, M. H.; **Mishra, A.**; Kubicki, D. J.; Wang, Z.; Merten, L.; Eickemeyer, F. T.; Zhang, H.; Ren, D.; Alyamani, A. Y.; Albrithen, H.; Albadri, A.; Alotaibi, M. H.; Hinderhofer, A.; Zakeeruddin, S. M.; Schreiber, F.; Hagfeldt, A.; Emsley, L.; Milić, J. V.; Graetzel, M., Benzylammonium-Mediated Formamidinium Lead Iodide Perovskite Phase Stabilization for Photovoltaics. *Adv. Funct. Mater.* **2021,** *31* (30), 2101163.

[12] Dučinskas, A.; Kim, G. Y.; Moia, D.; Senocrate, A.; Wang, Y.-R.; Hope, M. A**.; Mishra, A.**; Kubicki, D. J.; Siczek, M.; Bury, W.; Schneeberger, T.; Emsley, L.; Milić, J. V.; Maier, J.; Grätzel, M., Unravelling the Behavior of Dion–Jacobson Layered Hybrid Perovskites in Humid Environments. *ACS Energy Lett.* **2021,** *6* (2), 337–344.

[13] Zhang, H.; Eickemeyer, F. T.; Zhou, Z.; Mladenović, M.; Jahanbakhshi, F.; Merten, L.;Hinderhofer, A.; Hope, M. A.; Ouellette, O.; **Mishra, A.**; Ahlawat, P.; Ren, D.; Su, T.-S.; Krishna, A.; Wang, Z.; Dong, Z.; Guo, J.; Zakeeruddin, S. M.; Schreiber, F.; Hagfeldt, A.; Emsley, L.; Rothlisberger, U.; Milić, J. V.; Grätzel, M., Multimodal host–guest complexation for efficient and stable perovskite photo-voltaics. *Nature Commun.* **2021,** *12* (1), 3383.

[14] Su, T.-S.; Eickemeyer, F. T.; Hope, M. A.; Jahanbakhshi, F.; Mladenović, M.; Li, J.; Zhou, Z.; **Mishra, A**.; Yum, J.-H.; Ren, D.; Krishna, A.; Ouellette, O.; Wei, T.-C.; Zhou, H.; Huang, H.-H.; Mensi, M. D.; Sivula, K.; Zakeeruddin, S. M.; Milić, J. V.; Hagfeldt, A.; Rothlisberger, U.; Emsley, L.; Zhang, H.; Grätzel, M., Crown Ether Modulation Enables over 23% Efficient Formamidinium-Based Perovskite Solar Cells. *J. Am. Chem. Soc.* **2020,** *142* (47), 19980–19991.

[15] Alharbi E.A., Krishna A., Lempesis N., Dankl M., Lois M., Hope M.A., Baumeler T.P., Kakavelakis G., **Mishra A.**, Eickemeyer F., Ouellette O., Chawanpunyawat T., Hagfeldt A., Zakeeruddin S.M., Emsley L., Pfeifer L., Rothelisberger U., Grätzel M., Cooperative Passivation of Perovskite Solar Cells by Alkyldimethylammonium Halide Amphiphiles, *(accepted in Joule).*

Teaching experience

2018 – 2021 École Polytechnique Fédérale de Lausanne (EPFL), Switzerland.

- General physics: thermodynamics.
- General physics: electromagnetism.
- General Physics: mechanics.

Grants and awards

2019 Best poster presentation award, Ampere NMR school.

2019 Student stipend from the EPFL doctoral school to attend Ampere NMR school.

2019 Student stipend from the EPFL doctoral school to attend Alpine conference on magnetic resonance in solids.

2022 Student stipend to attend Chianti workshop.

2022 Student stipend by the EPFL doctoral School to attend Rocky Mountain conference on magnetic resonance.

2022 Student stipend to attend Rocky Mountain conference on magnetic resonance.